Univerzita Karlova v Praze
Matematicko-fyzikální fakulta

HABILITAČNÍ PRÁCE

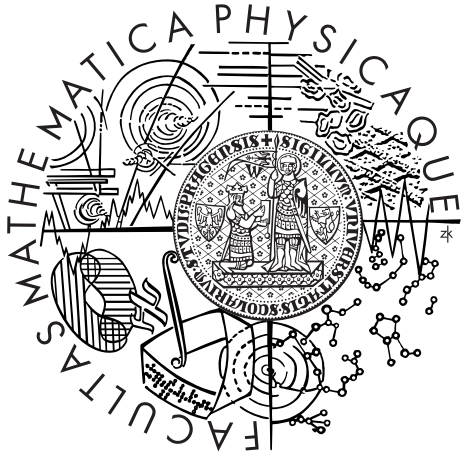

RNDr. Pavel Kocán, Ph.D.

Kombinace tunelové mikroskopie a kinetických simulací pro studium růstu atomárních struktur.

Katedra fyziky povrchů a plazmatu

Praha 2014

Poděkování.

Tato práce je postavena na publikovaných výsledcích, na kterých se podílela řada spoluautorů. Děkuji proto všem kolegům, se kterými jsem měl a mám štěstí spolupracovat, především Ivanovi Ošťádalovi a Pavlovi Sobotíkovi z Katedry fyziky povrchů a plazmatu na MFF UK, Miroslavovi Kotrlovi z Fyzikálního ústavu Akademie věd a prof. Tochiharovi z Kyushu University v Japonsku.

Obsah

Úvod

V posledním desetiletí dosáhly technologie používané v především elektronickém průmyslu přesnosti, na které je rozhodující znalost chování systému na atomární úrovni. Nejkřiklavějším příkladem je miniaturizace tranzistorů, kdy při současných rozměrech (22 nm) rozhodují pozice jednotlivých atomů-dopantů o parametrech konkrétního výrobku [1, 2]. Ze stejného důvodu je zřejmé, že další miniaturizace nebude možná bez využití nových fyzikálních principů. Zde zmíním dvě z možných alternativ současné elektroniky, které souvisejí s obsahem této práce.

První alternativou je doplnění náboje elektronu jako nosiče informace jeho spinem, tzv. spintronika. Spintronické součástky lze rozdělit do dvou kategorií. Zástupce první kategorie - magnetické spintronické součástky - jsou již použity v komerčních výrobcích jako např. ve čtecích hlavách paměťových disků, využívajících spintronický jev - gigantickou magnetorezistanci. Do druhé kategorie patří nemagnetické polovodičové spintronické součástky, jako např. spinový polem řízený tranzistor (SFET) [3]. Spinový tranzistor by byl analogií běžného polem řízeného tranzistoru (FET), ale díky spinové polarizaci balisticky se pohybujících elektronů by bylo možné transportní kanál zavřít bez vytěsnění nosičů, pouze rotací spinu vhodným napětím na hradle. Výhodami SFETu proti dnes používaným tranzistorům typu FET by byly především nižší energetická náročnost a vyšší rychlost.

Nicméně realizace funkčního SFETu zatím stále naráží na absenci vhodného spin-injektujícího materiálu a na problému samotné účinné injekce polarizovaných nosičů. Ukazuje se, že značné množství povrchových struktur vytvořených depozicí kovů na monokrystal křemíku vykazuje spinovou polarizaci elektronů. Využití těchto vrstev by bylo plně kompatibilní se současnými technologiemi, což je pochopitelně jeden z důvodů rostoucího zájmu o jejich studium.

Druhou často zmiňovanou alternativou současných elektronických prvků je využití spontánně narostlých nanostruktur složených z deponovaných atomů nebo molekul coby základních prvků elektronických součástek. Je známo, že snižování dimenze přináší kvalitativně nové fyzikální vlastnosti oproti objemovému materiálu [4]. Např. chování elektronů náležejících jednodimenzionálnímu objektu (nano-drátu) nelze popsat modelem Fermiho kapaliny neinteragujících kvazičástic, protože interakce blízkých elektronů je nevyhnutelná. Je nutné použít model Luttingerovy kapaliny, jehož charakteristickou vlastností je oddělení spinu a náboje. Vize využití spontánně vzniklých nanostruktur v elektronice spočívá v řízeném samo-uspořádání funkčních prvků nesoucích zajímavé fyzikální vlastnosti a jejich

vhodném rovněž samo-organizovaném propojení, které by umožňovalo výměnu informace. K těmto účelům lze využít struktury substrátu a vlastností deponovaných materiálů, často kovových atomů nebo na míru syntetizovaných organických molekul. Růst nanostruktur je vždy souhra mnoha dílčích kinetických procesů [5]. Má-li být růst kontrolovaný a dobře definovaný, je potřeba tyto procesy identifikovat a určit jejich parametry - jinými slovy, je třeba najít kinetický model systému.

Potřeby nových technologií stimulují základní výzkum v oblasti nanostruktur. Dnes je běžné studium na skutečně atomární úrovni, a to díky prudkému vývoji experimentálních technik a možností teoretické či výpočetní fyziky. V reálném prostoru je možné zobrazit nejen atomy a molekuly, ale např. i slabé vodíkové vazby mezi jednotlivými molekulami [6]. Nicméně omezení jsou značná - základní výzkum je obvykle omezen na modelové, silně zjednodušené situace, např. interakce jednotlivých atomů nebo molekul s čistým (v ultra-vysokém vakuu) a velmi dobře definovaným (obvykle monokrystalickým) povrchem pevné látky.

V této práci jsou zahrnuty čtyři oblasti, jejichž spojujícím prvkem je využití monokrystalu křemíku jako podložky. Prvním tématem je růst a samo-uspořádání kovových nano-klastrů na povrchu Si(111)7×7, tato síť klastrů představuje umělý dvoj-dimenzionální (2D) krystal. Následuje studium růstu jedno-dimenzionálních (1D) atomárních řetízků na povrchu Si(100), prototyp 1D uspořádání. Dalším tématem je růst silicidu manganu na povrchu Si(111) ovlivněný nutností dodání křemíku z podložky; v případě nalezení podmínek růstu 2D vrstvy MnSi s minimem defektů by byl takový povrch vhodným kandidátem na spin-injektující materiál. A závěrečným tématem je studium vlastností monovrstvy thallia na povrchu Si(111), motivované výjimečnými vlastnostmi tohoto systému, především rozštěpením spinu vlivem Rashba-Bychkov efektu [7].

Metoda řádkovací tunelové mikroskopie (STM) se od doby jejího objevení r. 1982 [8] (Nobelova cena r. 1986) vyvinula v techniku, bez které se většina laboratoří zabývajících se fyzikou povrchů neobejde. Historicky znamenalo využití techniky STM přechod od pozorování struktury povrchů v reciprokém prostoru k pozorování v prostoru reálném [9]. Původní využití STM jako techniky určení struktury povrchů je ale dnes posunuto do širších oblastí - pomocí STM lze pozorovat atomární procesy v reálném čase, hrot STM je možné použít jako nástroj pro atomární manipulace, nebo např. zobrazovat lokální hustotu elektronických stavů povrchu. Jako příklad současných možností lze uvést úspěšné vytvoření „jedno-atomárního“ transistoru [10] definovaným umístěním jednoho dopujícího atomu fosforu do povrchové vrstvy Si(100) a vytvoření kontaktů o šířce $< 10\,\mathrm{nm}$

umožňujících měření charakteristiky tohoto transistoru.

Nicméně, vzhledem k fyzikální podstatě techniky STM, bývá nezbytné kombinovat její využití s teoretickými metodami. V oblasti strukturní analýzy je obvyklá kombinace s *ab-initio* výpočty založenými většinou na teorii funkcionálu hustoty stavů (DFT) [11]. DFT simulace umožňují energetické porovnání vybraných konfigurací a tudíž nalezení atomární konfigurace s energií minimální. Časový vývoj těchto struktur je dále možno simulovat pomocí molekulární dynamiky - jsou počítány síly působící na jednotlivé atomy a systém se vyvíjí podle Newtonových rovnic s časovým krokem typicky 10^{-15} s. Malý časový krok omezuje výpočty na krátké časové škály, tudíž je metoda nevhodná pro studium růstu komplexnějších nanostruktur nebo tenkých vrstev.

V oblasti, kterou se zabývám v této práci, zaměřené na kinetiku vývoje morfologie, je výhodné jako doplňkovou metodu využít kinetické Monte Carlo (KMC) simulace. Tato metoda využívá náhodná čísla pro statistické řešení kinetických rovnic, ale zároveň zohledňuje detailní lokální uspořádání. Znalost struktury, alespoň částečná, je předpokládána; zajímá nás fyzikální mechanismus vývoje těchto struktur v čase při dané teplotě.

V rámci každé ze čtyř v této práci studovaných problematik je uplatněn podobný postup: nejdříve pomocí STM získat představu o chování systému na atomární úrovni, dále navrhnout co nejjednodušší model vysvětlující pozorované chování a nakonec tento model otestovat pomocí KMC simulací. Cílem tedy v každém případě bylo extrahování podstatných procesů určujících chování systému. V každé ze čtyř kapitol této práce se snažím pomocí komentářů a vybraných vložených publikací nastínit a obhájit tuto cestu - od prvních pozorování přes detailní studium problému k jednoduchému modelu popisujícímu podstatné vlastnosti daného systému.

Poznámka k členění práce. Tato habilitační práce je rozdělena do čtyř kapitol zabývajících se problematikami zmíněnými výše. Každá kapitola obsahuje úvodní komentář k vloženým publikacím, které se týkají dané problematiky, a dále shrnutí prací na ně navazujících, pocházejících především z nezávislých pracovišť. Literatura a samotné komentované práce jsou pro přehlednost uváděny zvlášť u každé kapitoly. Aplikace KMC simulací pro růst tenkých vrstev není úplně běžná a během prací zde shrnutých došlo ke specifickým úpravám této techniky. Proto je tato práce rozšířena o dodatek, stručně nastiňující princip použité techniky a její zasazení do širšího kontextu.

Literatura

[1] S. Roy and A. Asenov, "Where do the dopants go?," *Science*, vol. 309, p. 388, 2005.

[2] M. Pierre, R. Wacquez, X. Jehl, M. Sanquer, M. Vinet, and O. Cueto, "Single-donor ionization energies in a nanoscale CMOS channel.," *Nat. Nanotechnol.*, vol. 5, pp. 133–7, Feb. 2010.

[3] S. Datta and B. Das, "Electronic analog of the electro-optic modulator," *Appl. Phys. Lett.*, vol. 56, no. 7, p. 665, 1990.

[4] H.-E. Schaefer, *Nanoscience - The Science of the Small in Physics, Engineering, Chemistry, Biology and Medicine*. Springer, 2010.

[5] Z. Zhang and M. Lagally, "Atomistic Processes in the Early Stages of Thin-Film Growth," *Science*, vol. 276, pp. 377–83, Apr. 1997.

[6] J. Zhang, P. Chen, B. Yuan, W. Ji, Z. Cheng, and X. Qiu, "Real-space identification of intermolecular bonding with atomic force microscopy.," *Science*, vol. 342, pp. 611–4, Nov. 2013.

[7] Y. Bychkov and E. Rashba, "Properties of a 2D electron gas with lifted spectral degeneracy," *JETP lett*, vol. 39, no. 2, p. 78, 1984.

[8] G. Binnig, H. Rohrer, C. Gerber, and E. Weibel, "7×7 reconstruction on Si(111) resolved in real space," *Phys. Rev. Lett.*, vol. 50, p. 120, 1983.

[9] M. Lagally, "Transition from reciprocal-space to real-space surface science-advent of the scanning tunneling microscope," *Journal of Vac. Sci. & Technol. A*, vol. 21, pp. S54–S63, SEP-OCT 2003.

[10] M. Fuechsle, J. A. Miwa, S. Mahapatra, H. Ryu, S. Lee, O. Warschkow, L. C. L. Hollenberg, G. Klimeck, and M. Y. Simmons, "A single-atom transistor," *Nature Nanotechnol.*, vol. 7, pp. 242–246, APR 2012.

[11] R. O. Jones and O. Gunnarson, "The density functional formalism, its applications and prospects," *Revs of Mod. Phys.*, vol. 61, p. 689, 1989.

1. Růst atomárních klastrů na povrchu Si(111)

1.1 Specifika povrchu Si(111)

Povrch křemíkového monokrystalu s orientací (111) vytváří během chladnutí z vyšších teplot ($\sim$ 900 °C) obdivovanou rekonstrukci 7×7. Určení její struktury bylo prubířským kamenem povrchových analýz a významnou roli sehrálo objevení techniky STM [1]. Přestože první pozorování této rekonstrukce pomocí difrakce pomalých elektronů sahá do roku 1959 [2], dnes uznávaný model rekonstrukce byl publikován v roce 1985 [3]. Vzhledem ke své složitosti, estetickým kvalitám a významu je často pochopení této struktury „iniciačním obřadem“ pro studenty fyziky povrchů. Rekonstrukce 7×7 rozděluje povrch na trojúhelníkové cely dvou typů daných orientací vrchních atomárních vrstev vůči objemové struktuře. Pro adsorbované atomy kovů tyto cely představují potenciálové jámy - adsorbovaný atom se snadno pohybuje uvnitř cely, pro přeskok mezi půlcelami však musí překonat potenciální bariéru. Rekonstrukce 7×7 proto představuje přirozenou šablonu pro růst uspořádaných klastrů.

Nárůst zájmu o studium interakce atomů kovů s povrchem 7×7 následoval po pozorování vysoce uspořádaných polí identických klastrů některých kovů (Al, Ga, In) [4, 5, 6, 7] na tomto povrchu. Uspořádané klastry byly nazvány magické (magic clusters), přičemž za „magické“ jsou označovány dvě vlastnosti: 1) dokonalá identičnost (velikost a tvar) těchto klastrů a 2) jejich periodické uspořádání na povrchu. V rámci klasické nukleační teorie [8] je pozorováno vždy spojité rozdělení velikosti klastrů, a to v rovnovážném i nerovnovážném stavu. Důvodem pro ostré rozdělení velikosti magických klastrů je vysoká stabilita klastru související s jeho strukturou - stabilita klastrů s jedním chybějícím nebo přebytečným atomem je značně nižší.

Zmíněné klastry vznikají za vyšších teplot a ve struktuře každého klastru jsou zahrnuty i atomy křemíku, dochází tedy k částečnému mísení povrchových a deponovaných atomů. Otázkou k vyřešení zůstávalo, jak dokonale lze využít vlastností 7×7 rekonstrukce k uspořádání čistě kovových klastrů.

1.2 Vliv rekonstrukce 7×7 na růst ostrůvků

Pro modelové studium je vhodnější systém, který zachovává ostré rozhraní mezi substrátem a deponovaným materiálem. Představitelem kovu splňujícího takové kritérium je např. stříbro [9]. Abychom pochopili (a byli schopni ovlivnit) proces samouspořádávání klastrů, bylo nutné studovat odděleně všechny dílčí procesy, postupně od hrubšího k nejjemnějšímu: mechanismus spojování malých klastrů ve větší ostrůvky (publikace P1), nukleaci klastrů (publikace P2), difuzi jednotlivých atomů po povrchu a jejich vzájemnou interakci (publikace P3). Navíc byl navržený model růstu použit pro nalezení optimálních růstových parametrů pro nejvyšší uspořádání Ag klastrů na povrchu (publikace P4).

V rámci studia interakce jednotlivých Ag atomů na povrchu byla vyvinuta a zdokonalena technika *in-vivo*, umožňující pozorování povrchu přímo během depozice. Svazek deponovaných atomů je v takovém experimentu směřován přímo na část povrchu snímanou hrotem STM. Technika byla dříve úspěšně použita v případě vysoce difundujícího adsorbátu, kdy deponovaný materiál difuzí dosáhl snímané oblasti [10, 11, 12, 13]. Ve studovaném případě s nízkou difuzivitou je předpokladem dostatečně malý poloměr křivosti použitého hrotu, v opačném případě by hrot stínil deponovaný svazek. Přímým *in-vivo* pozorováním Ag depozice byl potom zjištěn zajímavý fakt, že přeskoky atomů směrem k půlcelám již obsazeným adsorbátem jsou četnější - bariéra pro přeskok do částečně obsazené půlcely je nižší ve srovnání s bariérou pro přeskok do prázdné půlcely. Vzhledem k rozměrům půlcel (2,7 nm) byl jev interpretován jako dalekodosahová interakce [14].

1.3 Model růstu Ag klastrů na rekonstrukci 7×7

Na základě vložených publikací P1-P4 lze definovat model růstu Ag vrstev na povrchu Si(111), uspokojivě popisující všechna pozorování za pokojových a vyšších teplot. Model zde uvádím v úplnosti i s parametry (s vědomím, že bez začlenění do kontextu hodnoty těchto parametrů nemají velký význam,) abych demonstroval, jak detailně může být model určen na základě STM dat.

1. V počáteční fázi růstu je možné za elementární adsorpční pozici uvažovat půlcelu rekonstrukce 7×7.

2. Atomy dopadají do náhodně vybraných půlcel.

3. Deponovaný atom se rychle připojí k existujícímu klastru, pokud se nachází

v jedné z nejbližších sousedních půlcel.

4. Volný atom se pohybuje po povrchu rychlostí danou aktivační energií pro přeskok, $E_F = 0.70\,\mathrm{eV}$ a $E_U = 0.67\,\mathrm{eV}$ pro přeskok z F a U půlcel.

5. Atom se může odpojit od nukleovaného klastru o velikosti $n \leq n^*$ atomů ($n^* = 5$ je kritická velikost klastru), aktivační energie je $E_n = E_{F,U} + (n-1)E_a$, kde $E_a = 0.05\,\mathrm{eV}$ je efektivní vazebná energie mezi atomy v klastru.

6. Kapacita půlcely pro izolovaný klastr je omezena na přibližně 18 atomů.

7. Ostrůvky větší než jedna půlcela vznikají pouze zaplněním hranice mezi dvěma sousedícími půlcelami obsazenými saturovanými klastry.

8. Kapacita půlcely včetně hranic je přibližně 31 atomů. Další atomy se mohou přes obsazenou půlcelu volně pohybovat.

Tento model byl určen na základě statistických veličin získaných z STM dat měřených na vrstvách připravených za různých podmínek (práce P1 a P2). Po nafitování parametrů model úspěšně popsal všechny experimentální charakteristiky. V práci P4 byl tento model uplatněn v opačném módu - s jeho pomocí byly nalezeny podmínky pro nejlepší možné uspořádání klastrů, tyto podmínky byly experimentálně realizovány a výsledné uspořádání klastrů pozorováno pomocí STM.

1.4 Navazující práce

Obecně zájem o studium povrchu Si(111)7×7 a růst nanostruktur na tomto povrchu od svého nejvyššího vrcholu roku 1995 pomalu klesá. Je to z velké části proto, že struktura této rekonstrukce je pro mnoho účelů příliš komplikovaná - reaktivita je ovlivněna množstvím odlišných nenasycených vazeb a teoretické výpočty jsou komplikované velikostí základní cely. Nicméně ač složitý, je samotný povrch 7×7 dobře popsaný, proto zůstává oblíbeným substrátem pro studium interakce jednotlivých adsorbovaných atomů nebo molekul s vazbami křemíku s pestrostí elektronických vlastností na velmi lokální úrovni.

V této podkapitole budou shrnuty některé vybrané výsledky navazující nebo rozšiřující poznatky uvedené výše.

V rámci použitého modelu byla coby nejmenší jednotka postačující půlcela rekonstrukce 7×7. O stupeň realističtější je představa půlcely reprezentované množstvím adsorpčních pozic, oddělených relativně nízkou difuzní potenciálovou

bariérou. V práci [15] byla studována difuzivita jednotlivých Ag atomů uvnitř půlcely 7×7 pomocí STM v modu, ve kterém je hrot zastaven ve vybrané poloze a zaznamenává se fluktuace tunelového proudu, odrážející pohyb atomu pod hrotem. Výsledkem je četnost přeskoků atomů z jednotlivých adsorpčních pozic, ukazující m.j. neekvivalentnost F a U půlcel 7×7 rekonstrukce.

Jinou možností, jak zaznamenat přeskoky atomu uvnitř půlcely, je pozorovat systém za dostatečně nízkých teplot. Tento postup byl uplatněn v [16], za teploty tekutého dusíku byly identifikovány jednotlivé přeskoky, což umožnilo popsat difuzní cesty.

V publikaci P3 jsme identifikovali Ag monomer, dimer a klastr obsahující více než dva atomy na základě vývoje jednotlivých objektů. Tento postup byl dále uplatněn [17] a výsledkem je identifikace Ag trimeru, tetrameru a pentameru. Výsledné STM mapy půlcel obsazených těmito klastry jsou výsledkem kolektivního pohybu atomů vzájemně se ovlivňujících v rámci půlcely. Podobným způsobem byl detailně studován vznik Ag klastrů a pohyb dvou atomů v půlcele [18].

Hrot STM lze kromě zobrazování povrchu použít také jako nástroj pro řízenou úpravu atomární konfigurace povrchu - t.zv. atomární manipulace. Ming a spol. [19] našli jednoduchý způsob, jak lze přiblížením hrotu k povrchu při vhodném aplikovaném napětí vyzvednout Ag atom z půlcely. Podobně při jiném napětí naopak tento atom z hrotu umístili do vybrané půlcely. Touto cestou byly atom po atomu vytvořeny klastry o velikostech 2-25 atomů.

Literatura

[1] G. Binnig, H. Rohrer, C. Gerber, and E. Weibel, "7×7 reconstruction on Si(111) resolved in real space," *Phys. Rev. Lett.*, vol. 50, p. 120, 1983.

[2] R. E. Schlier and H. E. Farnsworth, "Structure and adsorption characteristics of clean surfaces of germanium and silicon," *J. Chem. Phys.*, vol. 30, p. 917, 1959.

[3] K. Takayanagi, Y. Tanishiro, M. Takahashi, and S. Takahashi, "Structural-analysis of Si(111)-7×7 by UHV-transmission electron-diffraction and microscopy," *J. Vac. Sci. Technol. A*, vol. 3, p. 1502, 1985.

[4] J.-L. Li, J.-F. Jia, X.-J. Liang, X. Liu, J.-Z. Wang, Q.-K. Xue, Z.-Q. Li, J. S. Tse, Z. Zhang, and S. B. Zhang, "Spontaneous Assembly of Perfectly Ordered Identical-Size Nanocluster Arrays," *Phys. Rev. Lett.*, vol. 88, p. 066101, 2002.

[5] J.-F. Jia, X. Liu, J.-Z. Wang, J.-L. Li, X. S. Wang, Q. K. X. nad Z.-Q. Li, Z. Zhang, and S. B. Zhang, "Fabrication and structural analysis of Al, Ga, and In nanocluster crystals," *Phys. Rev. B*, vol. 66, p. 165412, 2002.

[6] L. Vitali, M. G. Ramsey, and F. P. Netzet, "Nanodot formation on the Si(111)-(7×7) surface by adatom trapping," *Phys. Rev. Let.*, vol. 83, p. 316, 1999.

[7] M. Yoon, X. Lin, I. Chizhov, H. Mai, and R. F. Willis, "Self-assembled nanodot arrays on Si(111)-(7×7) surfaces," *Phys. Rev. B*, vol. 64, p. 085321, 2001.

[8] C. Ratsch and J. A. Venables, "Nucleation theory and the early stages of thin film growth," *J. Vac. Sci. Technol. A*, vol. 21, no. 5, pp. S96 – S109, 2003.

[9] S. Tosch and H. Neddermayer, "Initial Stage of Ag Condensation on Si(111)7×7 Ag/Si(111)," *Phys. Rev. Let.*, vol. 61, p. 349, 1988.

[10] T. Hasegawa, M. Kohno, S. Hosaka, and S. Hosoki, "Dynamic observation of si crystal-growth on a si(111)7x7 surface by high-temperature scanning-tunneling-microscopy," *Phys. Rev. B*, vol. 48, pp. 1943–1946, 1993.

[11] B. Voigtländer and T. Weber, "Growth processes in Si/Si(111) epitaxy observed by scanning tunneling microscopy during epitaxy," *Phys. Rev. Lett.*, vol. 77, pp. 3861–3864, 1996.

[12] B. Voigtländer, A. Zinner, and T. Weber, "High temperature scanning tunneling microscopy during molecular beam epitaxy," *Rev. Sci. Instrum.*, vol. 67, pp. 2568–2572, 1996.

[13] B. Voigtlander, M. Kastner, and P. Šmilauer, "Magic Islands in Si/Si(111) Homoepitaxy," *Phys. Rev. Lett.*, vol. 81, p. 858, 1998.

[14] I. Ošt'ádal, P. Kocán, P. Sobotík, and J. Pudl, "Direct observation of long-range assisted formation of ag clusters on Si(111)7 × 7," *Phys. Rev. Lett.*, vol. 95, p. 146101, Sep 2005.

[15] K. Wang, G. Chen, C. Zhang, M. Loy, and X. Xiao, "Intermixing of Intrabasin and Interbasin Diffusion of a Single Ag Atom on Si(111)-(7x7)," *Phys. Rev. Lett.*, vol. 101, p. 266107, Dec. 2008.

[16] M.-S. Ho, C.-C. Su, and T.-T. Tsong, "Dynamical Study of Single Silver Atoms on Si(111)-7x7 Surfaces," *Japanese Journal of Applied Physics*, vol. 45, pp. 2382–2385, Mar. 2006.

[17] J. R. Osiecki, K. Takusari, H. Kato, a. Kasuya, and S. Suto, "The atomistic growth of silver clusters on a Si(111)7 x 7 surface," *Journal of Physics: Conference Series*, vol. 61, pp. 1107–1111, Apr. 2007.

[18] J. Osiecki, H. Kato, A. Kasuya, and S. Suto, "Diffusion and Clustering of Ag Atoms on Si(111)7x7 Surface," *Jpn. J. Appl. Phys.*, vol. 45, pp. 2056–2058, Mar. 2006.

[19] F. Ming, K. Wang, S. Pan, J. Liu, X. Zhang, J. Yang, and X. Xiao, "Assembling and disassembling Ag clusters on Si(111)-(7x7) by vertical atomic manipulation.," *ACS Nano*, vol. 5, pp. 7608–16, Sept. 2011.

ELSEVIER

Surface Science 507–510 (2002) 389–393

SURFACE SCIENCE

www.elsevier.com/locate/susc

Reconstruction determined submonolayer growth of Ag on Si(1 1 1)-(7 × 7) surface

Pavel Sobotík *, Ivan Ošťádal, Pavel Kocán

Department of Electronics and Vacuum Physics, Faculty of Mathematics and Physics, Charles University of Prague, V Holešovičkách 2, 180 00 Praha 8, Czech Republic

Abstract

The submonolayer growth of Ag on Si(1 1 1)-(7 × 7) surface at temperatures from 420 to 540 K was studied. Island densities, size distributions and average number of Ag atoms per occupied half-unit cell (HUC) of 7 × 7 reconstruction were investigated. At higher coverage large 2D islands with jagged shapes were observed. A scenario of the growth was outlined, based on the assumptions of existence of saturated Ag islands on the surface which cannot overgrow HUC boundaries by adatom capture. Such a model explains morphology of the large islands as well as the presence of the large amount of small islands formed inside HUCs. The capacity of a single HUC was found to be ≈18 Ag atoms and the capacity of HUCs covered by the large islands was found to be ≈31 Ag atoms on average.

Keywords: Epitaxy; Growth; Surface structure, morphology, roughness, and topography; Silver; Silicon; Metal–semiconductor interfaces

1. Introduction

The control of the heteroepitaxial growth of metals on semiconductor surfaces is highly important for technological applications. The physical model of the heteroepitaxy requires knowledge of a number of processes accompanying adatom diffusion, nucleation, growth and coalescence of metal islands on oriented surfaces with a complex structure. Basic kinetic processes on atomic scale and their role in thin film growth have been widely studied especially by means of scanning tunneling microscopy (STM) [1].

Initial stages of metal growth on Si(1 1 1)-(7 × 7) surface are significantly influenced by the surface reconstruction. Large (2.7 nm) triangular half-unit cells (HUCs) of two different types (faulted—FHUCs—containing a stacking fault, and unfaulted—UHUCs) separated by dimer rows and corner holes [2] form a highly corrugated surface potential for diffusing metal adatoms. At temperatures when mixed surface reconstructions are not formed, HUCs act as potential traps and metal atoms cluster inside HUCs [3–5] with stronger or weaker preference for occupying FHUCs. Basic information on diffusion processes of non-reactive metals on Si(1 1 1)-(7 × 7) can be found in [6–8]. Using STM, they directly observed

* Corresponding author. Tel.: +420-2-2191-2336; fax: +420-2-8468-5095.

E-mail address: sobotik@mbox.troja.mff.cuni.cz (P. Sobotík).

0039-6028/02/$ - see front matter
PII: S0039-6028(02)01275-X

high mobility of Pb atoms inside HUCs but low hopping rate between HUCs.

Ag/Si(1 1 1)-(7 × 7) represents a suitable model system for the study of the mechanism of heteroepitaxy on the reconstructed surface. Ag is nonreactive at lower temperature (<500 K) and leaves the Si(1 1 1)-(7 × 7) reconstruction unchanged [3,4]. In addition, Ag/Si(1 1 1)-(7 × 7) is a heteroepitaxial system with a very abrupt interface and negligible interdiffusion of both elements.

In previous studies [3,9,10] growth at low coverages has been studied. STM images of a single Ag atom and of Ag dimer in a HUC of the reconstruction have been identified [11]. Preferential nucleation of Ag clusters in FHUCs was observed. An effective diffusion barrier for hops between HUCs was estimated to be $E_d = 0.75 \pm 0.1$ eV [12,13] and frequency prefactor $\nu_0 = 5 \times 10^{-9\pm1}$ s^{-1}. The cohesion of Ag cluster inside HUCs was found weak for smallest clusters but increasing substantially for clusters with five and more atoms. A limited capacity (≈18 Ag atoms) of a single HUC to accommodate adatoms was also reported [13]. The study of the growth at higher coverages (which is of the Stranski–Krastanov type) revealed a complex morphology of the first (wetting) metal layer [14]. The morphology reflects symmetry of the reconstructed substrate surface and shows a strong influence of the reconstruction on the growth. The formation of the wetting layer at higher temperatures (>400 K), when adatom diffusion between HUCs on the surface is not restricted but reconstruction 7 × 7 remains unchanged, is the main topic of this paper. Experimental data allowed us to outline a scenario of the submonolayer growth Ag on the Si(1 1 1)-(7 × 7) surface.

2. Experimental details

Samples were measured in situ using a home made UHV STM system with a base pressure of 3×10^{-9} Pa. We used Sb doped Si(1 1 1) substrates (resistivity 0.01–0.005 Ω cm, miscut angle ±0.25°). The substrates were resistively heated by passing DC current (see [12,13]). Ag was deposited from a tungsten evaporation filament and the deposition rate was monitored by a quartz balance calibrated in situ with absolute accuracy ±10% [12]. 1 ML corresponds to Si(1 1 1) surface (1 ML = 7.83×10^{14} atoms/cm^{-2}).

The pressure during the Ag deposition and sample manipulations did not exceed 2×10^{-8} Pa. Samples with a coverage up to 0.6 ML were prepared at the deposition rate of 0.01 ML/s and temperature 470 K. Samples with a coverage of 0.3 ML were also prepared at different temperatures from 420 to 540 K. The samples were quenched immediately after the deposition and measurements began at room temperature 2 h after preparation. We used W tips for STM imaging. Tip voltage was −2 V and tunneling current 0.7 nA.

3. Results and discussion

The thickness dependence of the island morphology of samples prepared at 470 K is shown in Fig. 1a–c. The corresponding distributions of island sizes are shown below each image. The basic size unit is an area of one HUC. A 1-HUC island denotes an Ag cluster formed inside a HUC, and an n-HUC island denotes an island covering n HUCs, where $n \geqslant 2$. At the coverage of 0.6 ML large jagged islands bordered by the dimer rows and corner holes of the 7 × 7 reconstruction are observed. Triangular shapes identifiable in the morphology of these islands follow the orientation of FHUCs. There is a considerable number of the smallest islands formed inside a HUC (1-HUC islands), as indicated in the size distributions for various coverages. The abundance of 1-HUC islands is also clearly visible in the temperature dependence of island morphology at the coverage of 0.3 ML shown in Fig. 2. The 1-HUC islands dominate the size distribution even at 540 K and are observed in the proximity of larger islands (see Fig. 2c). Thickness and temperature dependences of total island density are shown in Fig. 3a and b, respectively. The diagrams show the densities of islands of particular sizes. In both cases, the total island density is given mainly by the density of 1-HUC islands especially at lower coverage.

Comparing deposited amount of Ag (as measured by quartz balance) with number of HUCs

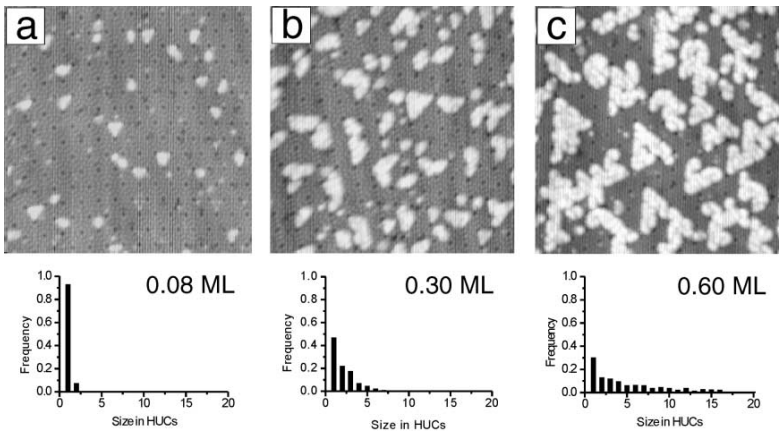

Fig. 1. Morphology of 2D Ag islands grown at 470 K and deposition rate 0.011 ML/s for different coverages: (a) 0.08 ML, (b) 0.3 ML and (c) 0.6 ML. Image sizes are 36×36 nm^2. Island size distributions (column plots) are shown below each image.

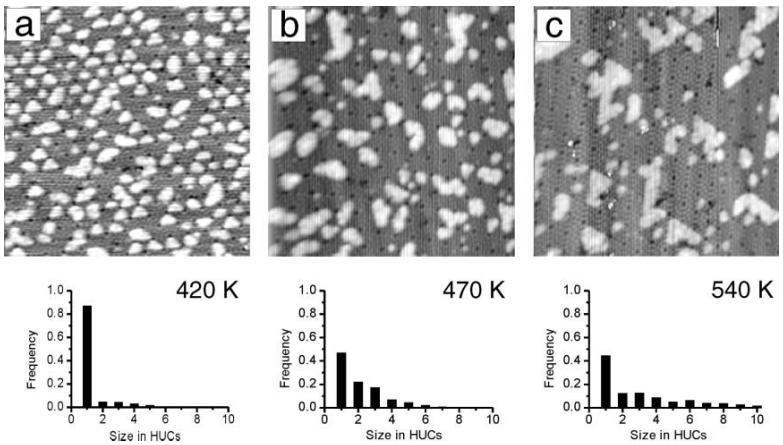

Fig. 2. Details of wetting layers grown at a deposition rate of 0.011 ML/s and different temperatures: (a) 420 K, (b) 470 K and (c) 540 K. Image sizes are 36×36 nm^2. Island size distributions (column plots) are shown below each image. 1-HUC islands dominate size distribution even at 540 K.

occupied by Ag, we obtained thickness dependence of an average number of Ag adatoms per occupied HUC (see Fig. 4). At higher coverages the majority of the deposited Ag is contained in saturated HUCs. Experimental data show (especially at higher coverages) that average density of Ag atoms per HUC area within 2-HUC and larger islands—N_{HUC} differs substantially from the capacity $C_{1\mathrm{HUC}}$ of the single occupied HUC. Using measured densities of islands of particular sizes, as shown in Fig. 3a, we can calculate the coverage dependence of an average number of Ag atoms per occupied HUC for any two values of N_{HUC} and $C_{1\mathrm{HUC}}$ and compare the dependence with the experimental curve in Fig. 4. By fitting the experimental dependence the best agreement was found for $C_{1\mathrm{HUC}} = 18 \pm 3$ and $N_{\mathrm{HUC}} = 31 \pm 3$ (Fig. 4, circles). The calculated dependences for $C_{1\mathrm{HUC}} =$

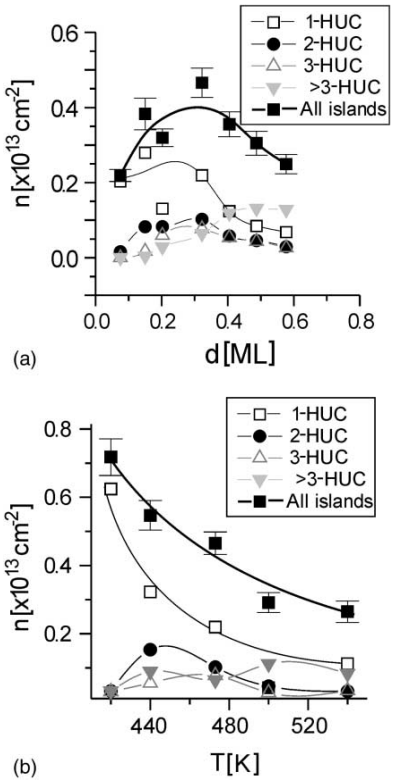

Fig. 3. The dependence of the island density on deposited amount (a) and the temperature dependence of island density (b) at the coverage of 0.3 ML. Deposition rate was 0.01 ML/s. Densities of islands of particular sizes are plotted as well.

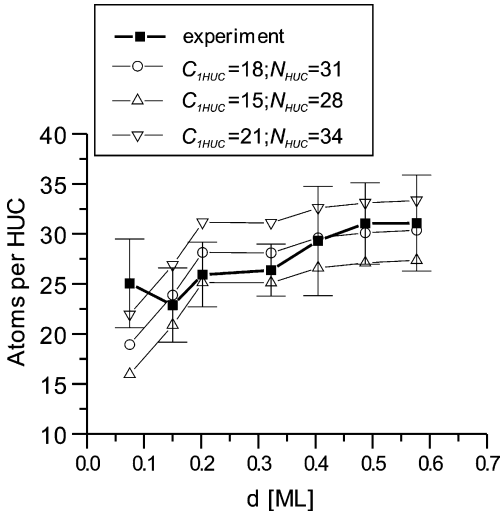

Fig. 4. The average number of atoms per HUC versus deposited amount obtained from the experiment (thick solid line). Fitting curves (thin solid lines) are obtained from measured densities of islands of particular sizes for three different combinations of numbers of Ag atoms per 1-HUC island (C_{1HUC}) and per HUC area within a larger islands (N_{HUC}): (○) $C_{1HUC} = 18$, $N_{HUC} = 31$ atoms; (▽) $C_{1HUC} = 21$, $N_{HUC} = 34$ atoms; (△) $C_{1HUC} = 15$, $N_{HUC} = 28$ atoms.

15 and $N_{HUC} = 28$ (△), and for $C_{1HUC} = 21$ and $N_{HUC} = 34$ (▽) are within the experimental error bars and we used them as an error estimate. The capacity of a single HUC can be explained by the theoretical predictions of Cho and Kaxiras [15]. In their model the existence of three diffusion paths (there referred to as basins of attraction) for an extra adatom around the rest atoms within HUC has been predicted. Along each diffusion path six stable lowest-energy adsorption positions were found (referred to as B_2, see [15]), which gives us 18 positions per HUC. For occupied HUCs covered by a large n-HUC Ag island one has to add some more Ag adatoms to cover dimer rows at the HUC boundaries.

The 1-HUC island is the basic building block of the first monolayer. Due to the existence of energetical barrier at dimer rows, HUC boundaries are less favourable for Ag adsorption than the area inside the HUC. An island in a HUC cannot overgrow the HUC boundary by simple adatom capture and a saturated 1-HUC island is formed. We suggest that an island covering two HUCs is created when two saturated 1-HUC islands appear in adjacent HUCs. Then the dimer row separating the HUCs can be covered by Ag adatoms—1-HUC islands coalesce into a larger one and the 2-HUC saturated island is formed. The growth of the first monolayer then proceeds as follows. At the very beginning of the growth a saturated density of nuclei is established. Islands in HUCs grow by adatom capture until they reach a maximum number of adatoms which can be accommodated in an 1-HUC island. The saturated islands do not capture diffusing adatoms any more, which results in an increase of adatom concentration around these islands and in subsequent nucleation

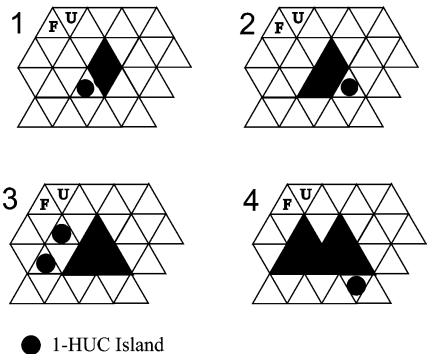

Fig. 5. The scenario of the island growth. Preference of the FHUCs determines an orientation of triangular contours of islands. This, together with a random nucleation of new 1-HUC islands, and following coalescence results in jagged island shapes.

of new islands in their proximity. Larger islands then grow by coalescence of smaller saturated islands. New 1-HUC islands nucleate all the time during the whole deposition process. Random nucleation of 1-HUC islands near the saturated islands and subsequent coalescence results in jagged island shapes (see Fig. 5). The observed orientation of triangular shapes can be explained by the preferential nucleation of silver in FHUCs.

4. Conclusions

The analysis of STM images shows that even when the diffusion of Ag adatoms on the Si(1 1 1)-(7 × 7) surface is well-released, the limited capacity of HUCs to accommodate adatoms substantially influences the mechanism of submonolayer growth. The model proposed explains the high number of isolated 1-HUC islands and the complex morphology of large islands on the reconstructed surface. The numbers of Ag adatoms in saturated 1-HUC islands and average density of Ag atoms per HUC area in the large islands were obtained as ≈18 and ≈31, respectively. The studied submonolayer growth characterized by jagged islands finally results in a discontinuous 2D interface wetting layer [14] on which further epitaxial growth is of the Stranski–Krastanov type.

Acknowledgements

This work was supported by the Grant Agency of Charles University—project GAUK 147/99 and by the Grant Agency of Czech Republic—project GAČR 202/01/0928.

References

[1] G. LeLay, Monolayer films of unreactive metals on semiconductors, in: D.A. King, D.P. Woodruff (Eds.), Growth and Properties of Ultrathin Epitaxial Layers, Elsevier, 1997.
[2] K. Takayanagi, Y. Tanishiro, S. Takahashi, M. Takahashi, J. Vac. Sci. Technol. A 3 (1985) 1502.
[3] St. Tosch, H. Neddermeyer, Phys. Rev. Lett. 61 (1988) 349.
[4] E. Ganz, I.-S. Hwang, F. Xiong, S.K. Theiss, J. Golovchenko, Surf. Sci. 275 (1991) 259.
[5] U.K. Köhler, J.E. Demuth, R.J. Hamers, Phys. Rev. Lett. 60 (1988) 2499;
St. Tosch, H. Neddermeyer, Surf. Sci. 211/212 (1989) 133;
M. Yoshimura, K. Takaoka, T. Yao, T. Sueyoshi, T. Sato, M. Iwatsuki, J. Vac. Sci. Technol. B 12 (1994) 2434;
I. Chizhov, G. Lee, R.F. Willis, Phys. Rev. B 56 (1997) 12316.
[6] J.M. Gómez-Rodríguez, J.J. Sáenz, A.M. Baró, J.Y. Veuillen, R.C. Cinti, Phys. Rev. Lett. 76 (1996) 799.
[7] J.M. Gómez-Rodríguez, J.-Y. Veuillen, R.C. Cinti, J. Vac. Sci. Technol. B 14 (1996) 1005.
[8] J.-Y. Veuillen, J.M. Gómez-Rodríguez, A.M. Baró, R.C. Cinti, Surf. Sci. 377–379 (1997) 847.
[9] St. Tosch, H. Neddermeyer, J. Microsc. 152 (1998) 415.
[10] A. Shibata, Y. Kimura, K. Takayanagi, Surf. Sci. 303 (1994) 161.
[11] I. Ošťádal, P. Sobotík, J. Mysliveček, T. Jarolímek, Czech. J. Phys. 49 (1999) 1613;
T. Jarolímek, P. Sobotík, I. Ošťádal, J. Mysliveček, Surf. Sci. 482–485 (2001) 386;
H. Hirayama, H. Okamoto, K. Takayanagi, Phys. Rev. B 60 (1999) 14260.
[12] P. Sobotík, I. Ošťádal, J. Mysliveček, T. Jarolímek, Surf. Sci. 454–456 (2000) 847.
[13] J. Mysliveček, P. Sobotík, I. Ošťádal, T. Jarolímek, P. Šmilauer, Phys. Rev. B 63 (2001) 045403.
[14] P. Sobotík, I. Ošťádal, J. Mysliveček, T. Jarolímek, F. Lavický, Surf. Sci. 482–485 (2001) 797.
[15] K. Cho, E. Kaxiras, Europhys. Lett. 39 (1997) 287.

PHYSICAL REVIEW B **69**, 165409 (2004)

Continuous and correlated nucleation during nonstandard island growth at Ag/Si(111)-7×7 heteroepitaxy

P. Kocán, P. Sobotík,* and I. Ošťádal
Department of Electronics and Vacuum Physics, Faculty of Mathematics and Physics, Charles University, V Holešovičkách 2, 180 00 Praha 8, Czech Republic

M. Kotrla
Institute of Physics, Academy of Sciences of the Czech Republic, Na Slovance 2, 182 21 Praha 8, Czech Republic
(Received 1 September 2003; revised manuscript received 23 December 2003; published 20 April 2004)

We present a combined experimental and theoretical study of submonolayer heteroepitaxial growth of Ag on Si(111)-7×7 at temperatures from 420 K to 550 K when Ag atoms can easily diffuse on the surface and the reconstruction 7×7 remains stable. Scanning tunneling microscopy measurements for coverages from 0.05 ML to 0.6 ML (ML—monolayer) show that there is an excess of smallest islands (each of them fills up just one half unit cell—HUC) in all stages of growth. Formation of a two-dimensional (2D) wetting layer proceeds by continuous nucleation of the smallest islands in the proximity of larger 2D islands (extended over several HUC's) and following coalescence with them. Such a growth scenario is verified by kinetic Monte Carlo simulation which uses a coarse-grained model based on a limited capacity of HUC and a mechanism which increases nucleation probability in a neighborhood of already saturated HUC's (correlated nucleation). The model provides a good fit for experimental dependences of the relative number of Ag-occupied HUC's and the preference in occupation of faulted HUC's on temperature and amount of deposited Ag. Parameters obtained for the hopping of Ag adatoms between HUC's agree with those reported earlier for initial stages of growth. The model provides two parameters—maximum number of Ag atoms inside HUC, and on HUC boundary.

DOI: 10.1103/PhysRevB.69.165409 PACS number(s): 68.55.Ac, 81.15.Kk, 81.15.Aa, 68.37.Ef

I. INTRODUCTION

Heteroepitaxial growth of metals on silicon surfaces has been studied for decades and morphologies of various grown structures were reported.[1–6] Reconstruction of oriented semiconductor surfaces determines the mobility of deposited adatoms and substantially influences growth mechanism. Recently reported experimental studies on self-organized growth of arrays of ordered metal islands—quantum dots—on the Si(111)-7×7 surface[4,7] stimulate need of detailed understanding of mechanisms controlling the growth. Heteroepitaxy of Ag on the Si(111)-7×7 surface represents one of frequently studied problems due to nonreactivity of Ag with the reconstructed surface, abrupt interface, and negligible interdiffusion of both elements. The growth mode is of the Stranski-Krastanov-type—three-dimensional (3D) islands are formed on a 2D Ag transition layer (wetting layer) grown on the 7×7 silicon surface.

Our initial scanning tunneling microscopy (STM) study of Ag/Si heteroepitaxy at low coverage[5] showed a growth mechanism affected by trapping Ag adatoms in triangular units of the 7×7 reconstruction—half unit cells (HUC's). The HUC's are of two types: ''faulted,'' FHUC (containing a structural fault according to the dimer-adatom-stacking fault model[8]) and ''unfaulted,'' UHUC. For deposited Ag atoms, the two types of HUC's represent potential wells with different depths $E_F > E_U$. This leads to preferential nucleation in the FHUC's (the preference P_F is defined as a ratio of FHUC's containing Ag adatoms to all occupied HUC's). In the successive work[9] we investigated processes of adatom diffusion, nucleation and island formation at the beginning of the Ag growth for a deposited amount <0.1 ML (ML—Monolayer) (1 ML$\approx 7.83\times 10^{14}$ atoms/cm^2), both experimentally and theoretically. We developed and used a simple coarse-grained model for the kinetic Monte Carlo (KMC) simulations. Fitting of experimental data provided values $E_F \approx E_U = (0.75 \pm 0.10)$ eV, $E_F - E_U < 0.05$ eV, and frequency prefactors $\nu_F^0 \approx \nu_U^0 = 5\times 10^{(9\pm 1)}$ s^{-1}.

Recently, we extended our STM measurements to coverages up to 0.6 ML.[6] In this regime a discontinuous 2D film, wetting layer,[10] is formed. We observed large 2D islands completely covering several HUC's. We did not observe any island to overgrow the HUC boundaries at its perimeter. This results in triangularly jagged island shapes. There was a considerable number of stable Ag clusters—each of them formed *inside* a HUC. We denoted such islands as 1-HUC islands. These islands were observed for coverages up to 0.6 ML and for high temperatures (540 K) as well. Statistical analysis of island population on the surface revealed a number of 1-HUC islands much higher than a value expected by the ''standard'' model of island film growth[11] in which island density saturates and then all adatoms are captured by existing islands.

We suggested a possible growth mechanism compatible with our observations: A single 1-HUC island grows by adatom capturing until a maximum number of adatoms which can be accommodated in a HUC is reached—a 1-HUC island is saturated. The saturated and isolated island does not capture diffusing adatoms anymore. It leads to an increase of Ag adatom concentration around such islands and results in enhanced nucleation of new islands in proximity of saturated HUC's (correlated nucleation). Larger islands grow by coa-

lescence of smaller saturated islands.

In this paper, we verify the above nonstandard growth scenario by a combined experimental and theoretical study. We performed STM experiments in a temperature range when Ag atoms can easily diffuse on the surface and the structure 7×7 remains stable. We measured dependences of several structure related quantities (object densities, preferences of occupation, island size distribution) on deposited amount, substrate temperature and deposition flux. We show that the results of measurements can be explained by KMC simulation using a modified coarse-grained model developed from the one we used for low coverage growth.[9] The new model, which takes into account limited capacity of HUC's and correlated nucleation, explains both morphological and statistical properties of island growth and coalescence on the reconstructed Si(111)-7×7 surface.

II. EXPERIMENTS

Series of samples with various amounts of deposited Ag from 0.05 ML to 0.6 ML were prepared at temperatures from 420 K to 550 K at deposition rate $F_1=0.011$ ML s^{-1}. Another series with Ag amounts from 0.05 ML to 0.3 ML were deposited at $T=(492\pm10)$ K and deposition rate $F_2=0.0005$ ML s^{-1}. Ag was evaporated from a tungsten filament in an ultrahigh vacuum chamber, the deposited amount was measured by a quartz thickness monitor with an absolute accuracy of $\pm10\%$. Sb doped Si(111) substrates with a miscut of $\pm0.1°$ and resistivity of 0.005–0.01Ω cm were heated by passing dc current (temperature calibrated with accuracy of ±10 K). Other experimental details (substrate treatment, thickness monitor, and temperature calibration, etc.) have been already reported elsewhere.[9,12] Before STM measurements, deposited films relaxed at least 1 h at room temperature (RT). Experimental procedures were performed at pressure $<2\times10^{-8}$ Pa. We used a STM of our design and construction with electrochemically polished tungsten tips.

III. EXPERIMENTAL RESULTS

Figure 1(a) shows an example of morphology of Ag islands grown at substrate temperature 490 K as observed in STM. Following morphological features have been found by analysis of a large number of images taken from various samples.

(i) Ag forms 2D islands of various sizes bordered always by dimer rows of the 7×7 reconstruction. The dimer rows at island boundary are not filled by Ag atoms, dimer rows inside larger islands are filled (overgrown) by Ag atoms—see detail A on Fig. 1(b).

(ii) We often observed islands covering adjacent HUC's but clearly separated by the dimer row—see detail B in Fig. 1(b).

(iii) Triangular shapes of larger islands follow the orientation of FHUC's [see Fig. 1(a) and Ref. 6].

(iv) An important feature is excess of 1-HUC islands in island size distribution even at very low deposition rates, higher temperatures, and coverages up to 0.6 ML.[13] This is illustrated in Fig. 2 which shows the island size distribution for different coverages (see also Fig. 1 and Fig. 2 in Ref. 6). The basic size unit is an area of one HUC. The 1-HUC islands clearly dominate in all distributions.

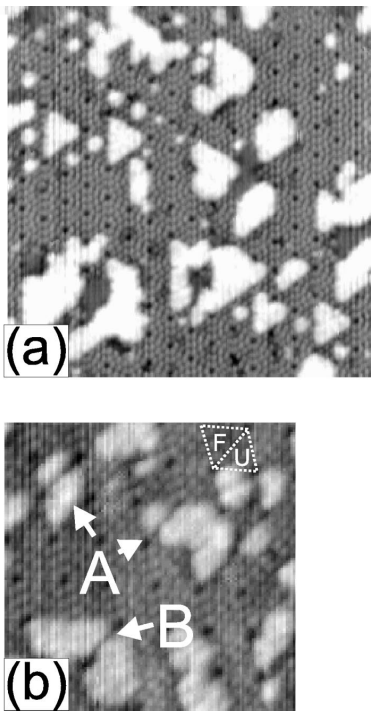

FIG. 1. (a) STM image of island morphology—white objects are Ag islands, with the exception of the smallest dots (impurities), 35×35 nm^2 area, evaporated amount $d=(0.5\pm0.1)$ ML at temperature $T=490$ K and flux $F=0.0005$ ML s^{-1}. (b) Detail of island morphology, 16×16 nm^2 area: A, the 1-HUC island grown in a HUC adjacent to a larger island; B, two larger separated islands.

The 1-HUC islands grow preferentialy in FHUC's and in proximity of larger islands rather than in vacant areas of the

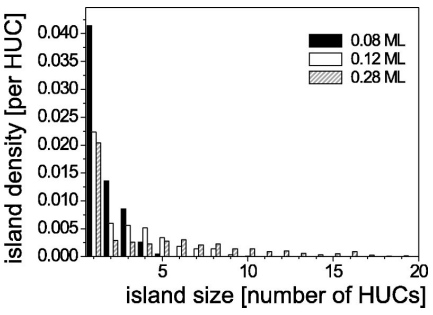

FIG. 2. Island size distribution for three different coverages. Samples were prepared at temperature 490 K and at deposition rate 0.011 ML s^{-1}.

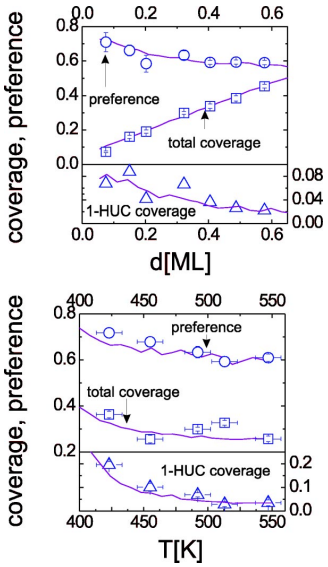

FIG. 3. Dependence of total coverage, 1-HUC coverage, and preference on amount of deposited Ag at $T=490$ K (upper panel) and on substrate temperature for $d=0.3$ ML (lower panel). Symbols—experimental data, lines—best fit using the model with center and boundary areas. All samples were prepared at deposition rate $F_1=0.011$ ML s^{-1}.

surface [Fig. 1(a)]. The formation of the wetting layer proceeds as continuous nucleation of new 1-HUC islands.

(v) STM imaging at room temperature does not allow to distinguish number of Ag atoms contained in the 2D Ag island[14] with exception of the smallest objects—HUC's containing one or two atoms.

The following quantities were obtained by statistical analysis of STM images: preference P_F, island size distribution (island size is measured in numbers of HUC's covered by the island), total coverage θ—the relative number of occupied HUC's (ratio of the occupied HUC's to the all HUC's on the surface), and 1-HUC coverage $\theta_{1\text{-HUC}}$—the relative number of 1-HUC islands (defined similarly). Ag objects are nonempty HUC's as well as islands larger than a HUC. When no Ag islands larger than a HUC are present $\theta=n_{\mathrm{Ag}}$, where n_{Ag} is density of Ag objects (number of objects normalized to the number of all HUC's on the surface). The preference P_F reflects existence of two different potential wells $E_F>E_U$ on the surface.

We measured dependences of P_F, θ and $\theta_{1\text{-HUC}}$ on deposited amount d (upper panel in Fig. 3) and substrate temperature (lower panel in Fig. 3). In the studied range of deposition parameters the total coverage θ is proportional to the deposited amount of Ag and decreases only slightly with the increasing substrate temperature. When islands larger than 1-HUC begin to grow, preference P_F decreases with both the deposited amount and the substrate temperature. However, it remains larger than 0.6 due to continuous nucleation of new 1-HUC islands preferably in FHUC's.

IV. SIMULATION MODELS

A. Original model

A coarse-grained KMC model with an algorithm derived from Ref. 15 was successfully applied for simulation of early stages of nucleation.[9] The model uses HUC's as basic units of the surface. Events included in the model correspond to the following growth scenario: Ag atoms arrive at the surface in random positions with a rate given by flux F. Diffusion of Ag adatoms on the Si substrate is modeled by thermally activated hops to neighboring HUC's. Depending on the HUC type, there are two different contributions to activation energy from interaction with the substrate. A frequency prefactor ν_0 is assumed (for simplicity) to be the same for FHUC's and UHUC's. The transient mobility of impinging Ag adatoms was included into the model to explain and simulate the short-range ordering of Ag objects and the low value of the total coverage at temperatures too low for sufficient adatom mobility between HUC's (Refs. 16 and 17) (however, in a temperature range, when Ag atoms can easily diffuse on the surface, this mechanism is not much important for the grown morphologies). Hopping adatoms can create nuclei inside HUC's. Let n be a number of Ag atoms in a HUC. The model assumes existence of a critical nucleus size n^*. Nuclei of more than n^* Ag atoms are stable. Nuclei with the size $n\leqslant n^*$ can decay with activation energy proportional to n. Hopping rate of an Ag atom out of a HUC is approximated as $\nu_n^{F,U}=n\,\nu_0\,\exp\{-[E_{F,U}+(n-1)E_a]/k_BT\}$, where E_a represents effective Ag-Ag interaction and k_B is Boltzmann's constant. The values $E_F\approx E_U=(0.75\pm0.10)$ eV, $E_F-E_U<0.05$ eV, $E_a\approx0.05$ eV, critical nucleus size $n^*=5$, and the frequency prefactor for hopping out of HUC's, $\nu_0=5\times10^{(9\pm1)}$ s^{-1}, were obtained in the Ref. 9. The original model has been used only for low coverages where real limits of capacity of HUC's cannot be reached. HUC's were treated like potential wells with unlimited capacity. When higher amount of Ag is deposited this simplification has to be replaced by a certain restriction.

B. Model with a simple constraint

The simplest way how to introduce a limitation of capacity is its direct implementation within a ''standard'' growth scenario[11] for growth simulations. At the beginning of growth the density of Ag nuclei reaches a saturated value and the islands grow simply by capturing hopping adatoms. Each HUC can accommodate n_H Ag atoms at the most and the next deposited or diffusing atom is forced to sit to the nearest HUC occupied by less than n_H Ag atoms. Hence, an island containing more than n_H adatoms overgrows HUC boundaries and extends over neighboring HUC's.

We tried to fit experimental data using the above simple modification. The same model and parameter values as in Ref. 9 were used, only limited capacity of a HUC, n_H, was included. The value n_H was determined by fitting the experimentally obtained dependence of the relative number of occupied HUC's, θ, on deposited amount d. The fit provided the value of $n_H=45\pm5$. However, the morphology obtained by using ''standard'' mechanism differs from the experimen-

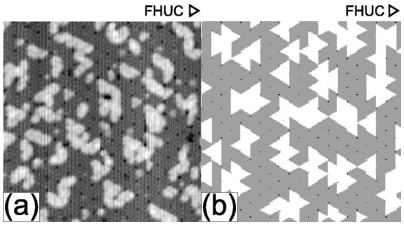

FIG. 4. (a) STM image of 35×35 nm^2 area, deposited amount $d=(0.50\pm0.05)$ ML at temperature $T=490$ K and flux $F=0.011$ ML s^{-1}; (b) layer simulated under the same conditions using "standard" 2D growth scenario (model with a simple constraint).

tal data, Fig. 4. Only a few 1-HUC islands are visible in the simulated layer. A statistical analysis of the experimental results reveals excess of 1-HUC islands in comparison with the simulated growth, Fig. 5. Therefore, the concept of limited capacity needs to be implemented in a more subtle way taking into account the role of 1-HUC islands in agreement with the scenario suggested in Ref. 6 and detailed experimental observations presented in Sec. III.

C. Model with center and boundary areas—final model

During the growth a 1-HUC island captures more and more diffusing adatoms until its size reaches a saturated value n_S given by the limited capacity of the HUC. The saturated 1-HUC Ag island cannot further grow by adatom capture. The value n_S is assumed to be the same for islands in both types of HUC's. When a diffusing adatom meets the saturated HUC, it hops fast out leaving dimer row unoccupied. This event is simulated by means of setting the energy barrier for hopping out of saturated HUC's close to zero value.

Larger islands grow by coalescence with 1-HUC islands only by the following mechanism: Boundaries between adjacent HUC's can be filled only if the cells are saturated. Such two HUC's can coalesce with assistance of a certain number of hopping adatoms, n_B, completing each HUC. In the simulation, the adjacent saturated HUC's can incorporate new adatoms until the boundary areas in HUC's (dimer rows separating adjacent HUC's) are filled by Ag atoms. The maximum number of atoms in a HUC with all the boundary areas filled is then $n_S+3\times n_B$. Therefore, in the computer model, each HUC is formally divided into one center and three boundary areas. The boundary area can accept Ag atoms if the center areas of both adjacent HUC's are saturated—each contains n_S Ag atoms (i.e., a saturated 1-HUC island).

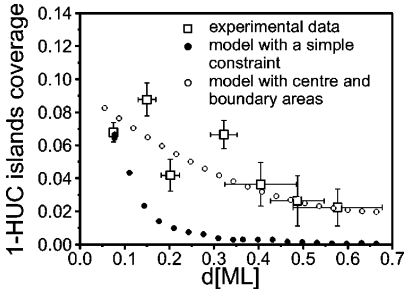

FIG. 5. Comparison of the dependence of 1-HUC island coverage on deposited amount at temperature $T=490$ K and flux $F=0.011$ ML s^{-1} in experiment and in two different models.

Each hopping event in the computer model is selected with probability determined by activation energy calculated with respect to a number of Ag atoms at a given position (HUC). We started with simulations in which the hopping probability was not affected by occupancy of a destination site (HUC). These simulations provided high population of 1-HUC islands but fitting of model parameters failed in achieving quantitative agreement with the experimentally measured dependences. The concentration of 1-HUC islands obtained by the simulations was much higher than the experimentally observed value. The experimentally observed increase of 1-HUC island density in proximity of larger islands was not reproduced by the model.

The enhanced nucleation of a new island in proximity of the saturated one (in an adjacent HUC) can be explained physically by an increase of time spent by a diffusing Ag adatom in the close neighborhood of saturated HUC. This might be caused by an interaction of Ag adatom with Ag atoms in saturated HUC. Another reason may be a change of the barrier for diffusion over the boundary of saturated HUC due to relaxation of Si atoms. The effect is modeled by decrease of the barrier for hopping into the saturated HUC by ΔE_S. It increases probability of nucleation near the saturated island. The correlated nucleation would also imply decrease of the concentration of 1-HUC islands because during further growth more 1-HUC islands will join larger islands. This modification implies the need to use a model with hopping rates depending on a final position. The introduction of anisotropy for hopping makes the code technically a bit more complicated (a hop-oriented code has to be employed).

V. SIMULATION RESULTS AND DISCUSSION

Simulations with the final model (the model with center and boundary areas) reproduce well growth morphologies observed in the experiment. Figures 6(a) and 6(b) show examples of real and simulated growth morphologies for two temperatures $T=490$ K, $T=550$ K and for the rate of deposition $F_1=0.011$ ML s^{-1}. Comparison of corresponding figures shows that an excess of 1-HUC islands is well reproduced for both temperatures.

We carefully fitted the experimental data presented in Fig. 3. To simplify the fitting, we assumed $n^*=5$ and $E_a=0.05$ eV as obtained in the previous work.[9] We varied three parameters n_S, n_B, and ΔE_S and at the same time we were changing values E_F and E_U within error bars of the previous work to find the best fit.

We found that the fitting of experimental data using the final model gives values $\nu_0=(5\times10^{9\pm1})$ s^{-1} and $E_F\approx E_U=(0.68\pm0.10)$ eV (at the fixed value $\nu_0=5\times10^9$ s^{-1} the values E_F,E_U can be determined with an accuracy of 0.02

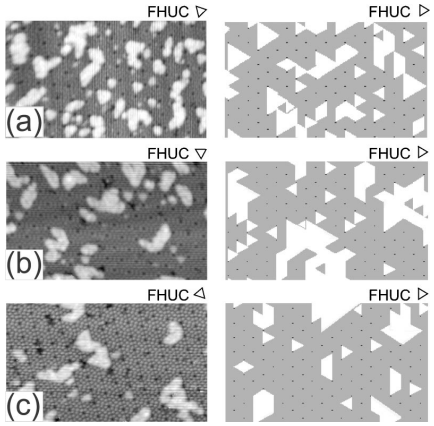

FIG. 6. Examples of experimental (left column) and simulated (right column) morphology of films with $d=(0.32\pm0.03)$ ML obtained by deposition at two temperatures and two deposition rates (a) $T=490$ K, $F_1=0.011$ ML s^{-1}; (b) $T=550$ K. $F_1=0.011$ ML s^{-1}; (c) $T=490$ K, $F_2=0.0005$ ML s^{-1}. Area 35 $\times 20$ nm^2. The model with center and boundary areas was used.

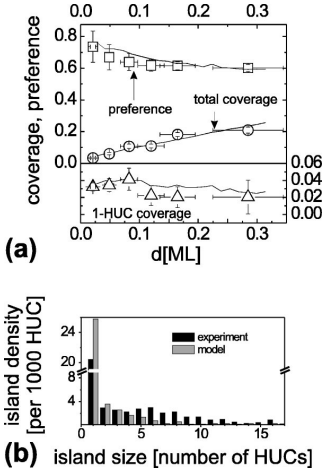

FIG. 7. Comparison of experimental (symbols) and simulated (lines—best fit using the model with center and boundary areas) data for films prepared at low deposition rate $F_2=0.0005$ ML s^{-1} at temperature $T=490$ K. (a) dependence of coverages and preference on deposited amount, (b) island size distribution.

eV) and the difference $E_F-E_U=(0.03\pm0.01)$ eV. The values are in a good agreement with our previous results.[9] In addition the model provided energy related to effective interaction with saturated HUC, $\Delta E_S=(0.10\pm0.05)$ eV, and numbers of Ag atoms $n_S=21\pm6$, and $n_B=5\pm2$. Maximum number of Ag atoms accommodated in a HUC with all three boundary areas filled is 36 ± 8. It is larger than a rough estimate reported in Ref. 6 (compare also with a value of 45 ±5 resulted from the "standard" growth model). The value of n_S is consistent with a number of potential minima in a HUC—18—proposed in Ref. 18.

The validity of the final model and the values of the parameters were further tested for quite different growth condition, very low deposition rate $F_2=0.0005$ ML s^{-1}. STM image in left part of Fig. 6(c) shows that there is excess of 1-HUC's even in this regime. Morphology obtained by simulation under the same growth conditions in right part of Fig. 6(c) has similar features. A series of samples provided dependences [see Fig. 7(a)] similar to those shown in Fig. 3. In the same figure, we show results obtained by calculation using the final model with the parameters given above. There was no additional fitting. We can see that the agreement is quite good. The model explains well excess of 1-HUC islands in the size distribution also for this much lower deposition rate—see a reasonable agreement between experimental data and simulation [Fig. 7(b)].

STM images of layers grown at various conditions show that a mean size of large irregular Ag islands is limited. During further growth the islands connect into a network—the wetting layer. The morphology of the irregular islands and wetting layer depend on growth temperature[6,10] and are driven by epitaxial strain. The current model does not take into account the strain which plays an important role in the formation of wetting layer. Therefore, the model cannot be used for simulation of growth above 0.6 ML of deposited metal but it allows to assess the structural properties of filling individual HUC's.

VI. CONCLUSIONS

Combined study of submonolayer growth of Ag on Si(111)-(7×7) by series of STM measurements and kinetic Monte Carlo simulations allowed to determine microscopic mechanism of growth in the regime of island coalescence. The surface reconstruction strongly affects nucleation and growth of islands. Islands do not extend laterally but by fast connection of preformed blocks—saturated HUC's—by filling dimer rows. Key feature of growth is slow and *continuous* nucleation of new small nuclei occupying the inner parts of HUC preferably in proximity of already saturated HUC's.

Both surface morphologies and quantitative measurements can be reproduced by KMC simulations using a model extending the coarse-grained model utilized for simulation of initial stages of growth. It turned out that it was necessary to resolve the inner part of HUC and its boundary. Comparison with experiment confirmed the applicability of this model for interpretation of growth for a large range of deposition parameters (temperature, deposition rate, time) and for deposited amount up to 0.6 ML. Correlated nucleation in proximity of saturated HUC's is obtained by introduction of effective interaction *decreasing* energy barrier for a hop into the saturated HUC by $\Delta E_S=(0.10\pm0.05)$ eV. The model can be used for simulations up to the coverage when epitaxial strain significantly influences growth of larger islands.

The model allowed to assess maximum numbers of Ag atoms per HUC in a 2D island: for an isolated 1-HUC island $n_S=21\pm6$; for a larger island (covering $\geqslant 2$ HUC's) the saturated number of Ag atoms filling one of the three boundary areas is $n_B=5\pm2$ and the maximum number of Ag at-

PRL 95, 146101 (2005) PHYSICAL REVIEW LETTERS week ending 30 SEPTEMBER 2005

Direct Observation of Long-Range Assisted Formation of Ag Clusters on Si(111)7 × 7

Ivan Ošt'ádal,* Pavel Kocán, Pavel Sobotík, and Jan Pudl

Charles University, Faculty of Mathematics and Physics, Department of Electronics and Vacuum Physics, V Holešovičkách 2, 180 00 Praha 8, Czech Republic

(Received 9 June 2005; published 27 September 2005)

Formation of Ag clusters on reconstructed surface Si(111)7 × 7 was for the first time observed in real time during deposition by means of scanning tunneling microscopy. The sequences of images taken at room temperature show mechanisms controlling the growth and behavior of individual Ag adatoms. Obtained data reveal new details of attractive interaction between adsorbates occupying adjacent half-unit cells of the 7 × 7 reconstruction. Time evolution of growth characteristics was simulated by means of a simple model. The growth scenario observed *in vivo* is discussed with respect to previously reported models based on data obtained after finishing the deposition—*post-mortem*.

DOI: 10.1103/PhysRevLett.95.146101 PACS numbers: 68.55.Ac, 68.37.Ef

Processes which control nucleation and thin film growth have been a subject of basic materials science research for decades. Preparation of ordered nanostructures using self-assembling of growing objects [1] is a promising alternative approach in nanotechnology. Growing laterally ordered metal structures on the silicon surfaces is of utmost practical importance due to ubiquitous use of silicon in microelectronic industry. The surface Si(111)7 × 7 consisting of large (2.7 nm) triangular half-unit cells (HUC's) of two different types [faulted (F-HUC's) and unfaulted (U-HUC's)] represents a natural template for growing arrays of identical ordered metal clusters [2,3]. Further development of techniques for manufacturing desirable structures deeply depends on detailed understanding of mechanisms controlling growth for particular combination of materials. Studying growth processes on atomic level is inevitable for such a purpose. The scanning tunneling microscopy (STM) provides unique, real space imaging of the surface with atomic resolution. It has been widely used for studying morphology of surfaces and grown structures for two decades.

Most of STM data on growth were obtained by *in situ* experiments in ultrahigh vacuum (UHV) in the following way: the growth was interrupted, a grown sample quenched and finally transferred to a position suitable for STM measurements [mostly at room temperature (RT)]. The obtained data—images of film structures at various stages of growth—were influenced by structure relaxation during the quenching and a time interval before the STM measurement. Information on growth kinetics can be obtained indirectly; general tendencies are estimated only. Another successful application of STM technique is direct observation of dynamics of thermally activated processes—surface diffusion [4–6] and phase transitions [7,8]. Such experiments require stability of an STM system in desired temperature range and sufficient scanning speed. Temperature is used to control rates of the observed processes. The other challenging step in STM utilization is direct observation of surface during deposition of material. In this case, a scanning STM tip represents a natural obstacle for the flux of the deposited material which results in a screening effect. First experiments on direct STM imaging of film growth (*in vivo*) were focused on epitaxial growth of semiconductor materials at higher temperatures [9,10]. The screening effect of an apex of a scanning STM tip [11] was partially eliminated by enlargement of scanned area (typically hundreds nm). Sufficiently high mobility of adatoms deposited at higher substrate temperature, when a mean free path of diffusing adatoms is comparable with a tip apex radius, further improves compensation of the tip screening. Island growth dynamics, attachment and detachment of adatoms at "stable" positions were observed excellently [12]. However, the mobile adatoms cannot be imaged by STM—its movement is too fast with respect to STM scanning speed.

Studies of growth at submonolayer coverage were reported for particular metals [2,3,5,13,14] and even for bimetallic combination [2]. Information on morphology of grown nanostructures and its evolution at various stages of the growth were obtained by *in situ* STM at RT after several hours delay and relaxation of grown structures. Different growth models, based on interpretation of *in situ* STM experiments, describe metal growth kinetics at very low coverages [13–15]. Diffusion parameters of metal adatoms have been obtained independently—from direct observation in STM [4,6].

Here we present STM experiments which—according to our knowledge—for the first time reveal individual behavior of adatoms during deposition of metal on the Si(111)7 × 7 surface, process of nucleation, and island growth at early stages of heteroepitaxial growth at RT. Direct STM observation of growth during metal deposition provided a movie showing dynamics of processes participating at growth.

Experimental.—STM measurements presented here were performed at RT when intercell mobility of diffusing Ag adatoms is sufficiently low [4]. A noncommercial UHV STM system developed by two of authors was used at

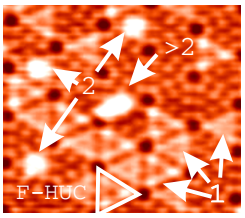

FIG. 1 (color online). Detail of STM image (13×11 nm^2) showing different objects on the surface: monomers (1), dimers (2), and larger clusters (> 2). Deposited amount of Ag ~0.6 atoms/HUC.

experiments. The surface was scanned with a rate of 1 image per minute. Si(111) substrates (Sb doped, n-type, resistivity 0.005–0.01 Ω cm) were used. The 7×7 reconstructed surface was obtained using a standard flashing procedure. Ag was deposited on the scanned surface from a miniature tungsten wire evaporator at a distance of 4 cm. A beam of the Ag atoms was defined by means of two apertures (1 mm diameter). Incidental angle of the deposited flux was 30°. The apex shape of a tungsten electrochemically etched tip allowed the deposition of the Ag atoms "under" the STM tip scanning an area of 40×40 nm^2.

The deposition rate was set to a relatively very low value of the order 10^{-5} ML/s (monolayer, 1 ML $= 7.54 \times 10^{14}$ atoms/cm^2). Temperature of the evaporator has been stabilized with negligible delay after switching on the heating current. The thermal drift due to radiation of the evaporator was eliminated by an STM control unit during the whole sequence of STM images covering 2–3 hours of the deposition ~0.1 ML of Ag. We used the tip voltage -2 V; the tunneling current <0.35 nA did not affect intercell hopping of Ag adatoms [see Ref. [4]].

Results.—The following Ag objects can be reliably distinguished on STM images (Fig. 1): monomers (single Ag adatoms) appearing as highlighted triangular HUC's due to fast motion of an Ag adatom inside the HUC [16]; dimers, with a pattern of a bright spot in the position of three Si adatoms central with respect to HUC [16] and clusters composed of more than two Ag atoms (a number of Ag atoms contained in larger clusters cannot be specified accurately on the images at RT [16]). Figure 2 shows evolution of Ag adsorbate on the surface during deposition from monomer population [Fig. 2(a)] to the population of larger clusters [Fig. 2(d)]. Sequences of hundreds of STM images were used for direct identification of atomic processes on the surface. After heating up the evaporator Ag atoms impinge on the sample surface [Fig. 2(a)]. Because of the screening effect of the STM tip the evaporation flux cannot be uniform along the whole scanned area. However, very low gradient of density of occupied HUC's indicates that the very end of the tip has a small diameter of about tens of nanometers (observation of similar tips in a transmission electron microscope showed the tip apex radius of 10–20 nm).

The most important atomic processes observed are hops of Ag adatoms between neighboring HUC's (Fig. 3). The hops to HUC's occupied by single Ag atoms are very rare at RT (< 5 events during several hours of observation of an area of ≈ 1000 nm^2) as well as the hops to unoccupied neighboring HUC's. The most frequent process is a hop from the HUC occupied by a single Ag atom to the neighboring HUC with a cluster of at least 2 Ag atoms. It indicates a kind of attractive intercell interaction of the Ag adsorbate. Surprisingly, we found several times a configuration corresponding to hops of a dimer to an adjacent occupied HUC. However, we cannot exclude such process being composed of two separated hops of single Ag atoms.

The attractive intercell interaction can be quantified in a simple way: when the total number of the Ag atoms in positions allowing hops to adjacent HUC's containing at least 2 Ag atoms is n_0, the number n of the atoms hopping within a time interval t is given by an equation $n = n_0[1 - \exp(-t/\tau)]$, where τ is the mean lifetime of an Ag atom in a HUC adjacent to the HUC occupied by an Ag cluster of 2 or more atoms. An analysis of image sequences showed that for $n_0 \approx 50$ suitable positions, 30% or 50% of Ag atoms hop within 3 or 5 min, respectively. It corresponds to a value $\tau = (8 \pm 4)$ min. Effective activation energy E of the process is given by the equation $\tau = \nu_0^{-1} \exp(E/kT)$, where k is the Boltzmann constant, T is the sample temperature, and ν_0 is the frequency prefactor. The value of the activation energy is $E = (0.78 \pm 0.02)$ eV when using the value $\nu_0 = 5 \times 10^{10}$ s^{-1} [an average of experimentally

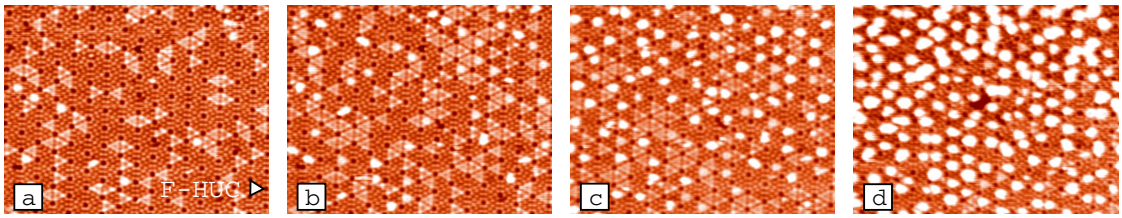

FIG. 2 (color online). Images of the same area taken during deposition after (a) 7 min, (b) 12 min, (c) 24 min, and (d) 92 min from the beginning of growth. Image size 40×30 nm^2. The complete sequence is available on the World Wide Web [20].

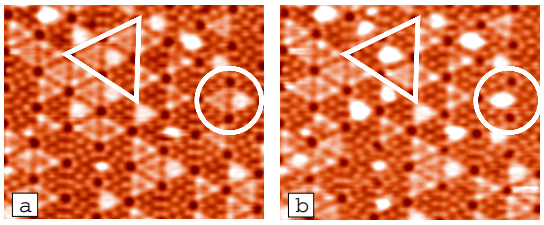

FIG. 3 (color online). Two consecutive images (20×16 nm^2, interval 1 min) showing details of hopping events. Inside the triangle two monomers jump to one of the neighboring larger clusters; inside the circle a dimer moved to a monomer.

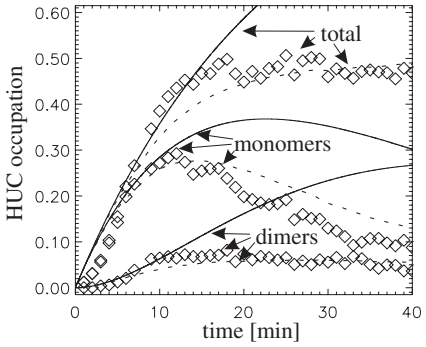

FIG. 4. Time evolution of HUC occupation with respect to monomers and dimers. Diamonds—experimental data, dashed lines—a simple kinetic Monte Carlo model, solid lines—*hit and stick* model, calculated from Eqs. (1)–(3).

obtained values of prefactors for jumps of monomers out of F-HUC's and U-HUC's to an empty HUC [4]].

Two qualitatively different growth regimes can be distinguished on sequences of STM images taken during the deposition at room temperature: (1) *hit and stick* (HS) mode—when a relative number of occupied HUC's is <0.5 no hops of Ag adatoms are observed and the atoms remain at positions of impingement. It is in agreement with long lifetimes τ_F, τ_U of monomers with no clusters in neighboring HUC's: $\tau_F = (6 \pm 2) \times 10^4$ s, $\tau_U = (3.5 \pm 2.0) \times 10^3$ s [reported in Ref. [4]]. The time evolution of HUC occupancies obtained from STM image sequences can be compared with a solution of the set of differential equations:

$$d\theta_1/dt = \gamma R(1 - \theta) - \gamma R\theta_1, \quad (1)$$

$$d\theta_2/dt = \gamma R\theta_1 - \gamma R\theta_2, \quad (2)$$

$$d\theta_{>2}/dt = \gamma R\theta_2, \quad (3)$$

where θ_i represents relative occupancy of HUC's containing i Ag atoms ($\theta_i = n_i/m$, n_i is number of HUC's occupied by i atoms, and m is the number of all HUC's), θ is relative occupancy of HUC's occupied by deposit, $\theta = \theta_1 + \theta_2 + \theta_{>2}$, R is a deposition flux in ML/s, and $\gamma = 23.64$ is a constant equal to number of atoms in ML of Ag per HUC area. The mean value of the flux was estimated from the best fit of the experimental data (Fig. 4) as $(3.0 \pm 0.5) \times 10^{-5}$ ML/s. (2) When clusters containing >2 Ag atoms begin to appear in HUC's adjacent to those with monomers (at relative number of occupied HUC's ≈ 0.5) intercell hops stimulated by Ag clusters start to influence the growth. In this regime the relative coverage increases rather slowly in comparison with the HS regime. Deposited atom impinges with high probability either on an occupied HUC or on adjacent HUC's and hops within several minutes to a HUC occupied by an Ag cluster. In this regime the preference in occupation of F-HUC's (ratio between the occupied F-HUC's and all occupied HUC's) increases up to the final value of ≈ 0.6 which reflects the difference between energy barriers for hops out of F-HUC's and U-HUC's, respectively.

The observed growth has been simulated by a simple kinetic Monte Carlo (KMC) model with HUC's as the smallest units. The only considered processes are deposition (random impingement) and thermally activated hops of monomers to clusters containing ≥ 2 Ag atoms. The hops to clusters of different size were not distinguished. When the fixed value of a frequency prefactor is used, $\nu_0 = 5 \times 10^{10}$ s^{-1}, the model contains only two parameters to be fitted: E_F, E_U—barriers for hops to a cluster from F-HUC and U-HUC, respectively. The corresponding hopping rates can be calculated as $\nu_{F,U} = \nu_0 \exp(-E_{F,U}/kT)$. Results of the KMC simulations are shown in Fig. 4. The best fit of experimental data has been obtained for the barrier energies $E_F = (0.71 \pm 0.02)$ eV and $E_U = (0.76 \pm 0.02)$ eV. The values are in a very good agreement with the effective value of the activation energy estimated from the simple analysis of the monomer mean lifetime τ in HUC's adjacent to a HUC occupied by the Ag cluster. The values are lower than barriers for hops to unoccupied HUC's obtained experimentally in Ref. [4]. The differences, which are 0.10 eV for hops out of F-HUC and 0.17 eV for U-HUC, respectively, quantitatively express influence of clusters in neighboring HUC's on the hopping rate of single Ag adatoms.

The observed behavior of Ag adatoms shows clearly interaction between metal adsorbates resulting in preferential hops of an adatom toward first-neighboring HUC's occupied by metal clusters. The clusters modifying surface mobility have to contain at least 2 Ag adatoms. Surprisingly, the interaction between Ag monomers in adjacent HUC's is negligible at RT. A kind of intercell interaction among metal adsorbates has been indicated by existence of capture zones observed in grown structures on the reconstructed 7×7 surface [Ag [13,17], Pb [5], Y [14], In [2], Tl [3]]. At RT, STM observation of mobile adsor-

bate showed that Pb adatoms hop faster into adjacent occupied HUC's than to empty ones [5]; in the case of Sn only jumps to occupied (monomer) neighboring HUC's were observed [18]. The data reported here agree with models for metal adatom surface mobility with hopping barrier reduced by the attractive nonlocal intercell interaction between adsorbates. The model of *cooperative* diffusion proposed in [14] and discussed in [15] explains well growth characteristics obtained from STM measurements on relaxed structures. The new data obtained here by STM during deposition show that the interaction among adsorbates, at least in case of Ag at RT, is more complex than situation described by the previous models.

The *in vivo* data show that the growth at RT and very low deposited amount (< 0.025 ML, HUC occupancy ≈ 0.5) can be approximated by the *hit and stick* regime. It could not be revealed by standard STM *in situ* measurements and has not been admitted by previous models. A problem of how to explain the preference in occupation of F-HUC's generally found for all studied metals at low coverage was solved in one of models by introducing a mechanism of transient mobility which allows hops of deposited adatoms immediately after arriving on surface [13]. The mechanism of *cooperative* diffusion based on interaction between adsorbates was successfully used in simulation as well [14]. Both models and modifications discussed elsewhere [15] supposed the preference in occupation of F-HUC's arising during the deposition. We have tested that the preference at very low coverage can be entirely explained by deposit relaxation during 2–3 hours before STM observation.

The growth models used previously for simulation of metal heteroepitaxial growth on the Si(111)7 $\times$ 7 surface were focused on intercell mobility of deposited adatoms [coarse grained models [13–15,19]] and were successful in simulation of integral growth characteristics obtained from STM measurements at various substrate temperature, deposition flux, and deposited amount. They provided microscopic parameters of intercell hopping, size of a stable cluster [13], and capacity of HUC's for accommodation of Ag adatoms [19]. The new experimental results presented here show all the models suffered by insufficient description of processes controlling growth at early stages.

Conclusions.—The metal adsorption, diffusion, and cluster nucleation were for the first time directly observed by STM during the deposition at room temperature on the reconstructed Si(111)7 $\times$ 7 surface. The *in vivo* observation revealed the *hit and stick* regime of growth up to a relative coverage ≈ 0.5 followed by formation of clusters via monomer mobility released and controlled by the arising clusters. The measured growth characteristics were interpreted by a simple model covering observed growth regimes. The KMC simulation of cluster formation provided values of hopping barriers between HUC's which reflect barrier height reduction expected due to the nature of an attractive interaction between metal adsorbates. The *in vivo* STM observation of growth during the deposition provides image sequences containing direct information on kinetics of surface processes and time evolution of deposit morphology. It allows us to specify details of growth model with incomparably higher accuracy than by using the standard STM *in situ* observation.

The work is a part of the research plan MSM 0021620834 that is financed by the Ministry of Education of Czech Republic and partly was supported by Projects No. GACR 202/03/0792 and No. GAUK 307/2004/B.

*Electronic address: ivan.ostadal@mff.cuni.cz

[1] C. Teichert, Phys. Rep. **365**, 335 (2002).
[2] J.-L. Li, J.-F. Jia, X.-J. Liang, X. Liu, J.-Z. Wang, Q.-K. Xue, Z.-Q. Li, J. S. Tse, Z. Zhang, and S. B. Zhang, Phys. Rev. Lett. **88**, 066101 (2002).
[3] L. Vitali, M. G. Ramsey, and F. P. Netzer, Phys. Rev. Lett. **83**, 316 (1999).
[4] P. Sobotík, P. Kocán, and I. Ošt'ádal, Surf. Sci. **537**, L442 (2003).
[5] J. M. Gómez-Rodríguez, J. J. Sáenz, A. M. Baró, J. Y. Veuillen, and R. C. Cinti, Phys. Rev. Lett. **76**, 799 (1996).
[6] E. Ganz, S. K. Theiss, I. S. Hwang, and J. Golovchenko, Phys. Rev. Lett. **68**, 1567 (1992).
[7] I. Brihuega, O. Custance, R. Pérez, and J. M. Gómez-Rodríguez, Phys. Rev. Lett. **94**, 046101 (2005).
[8] O. Custance, I. Brihuega, J. Y. Veuillen, J. M. Gómez-Rodríguez, and A. M. Baró, Surf. Sci. **482**, 878 (2001).
[9] T. Hasegawa, M. Kohno, S. Hosaka, and S. Hosoki, Phys. Rev. B **48**, 1943 (1993).
[10] B. Voigtländer and T. Weber, Phys. Rev. Lett. **77**, 3861 (1996).
[11] B. Voigtländer, A. Zinner, and T. Weber, Rev. Sci. Instrum. **67**, 2568 (1996).
[12] B. Voigtländer, M. Kästner, and P. Šmilauer, Phys. Rev. Lett. **81**, 858 (1998).
[13] J. Mysliveček, P. Sobotík, I. Ošt'ádal, T. Jarolímek, and P. Šmilauer, Phys. Rev. B **63**, 045403 (2001).
[14] C. Polop, E. Vasco, J. A. Martín-Gago, and J. L. Sacedón, Phys. Rev. B **66**, 085324 (2002).
[15] E. Vasco, C. Polop, and E. Rodríguez-Cañas, Phys. Rev. B **67**, 235412 (2003).
[16] T. Jarolímek, P. Sobotík, I. Ošt'ádal, and J. Mysliveček, Surf. Sci. **482**, 386 (2001).
[17] P. Sobotík, I. Ošt'ádal, J. Mysliveček, and T. Jarolímek, Surf. Sci. **454-456**, 847 (2000).
[18] O. Custance, I. Brihuega, J. M. Gómez-Rodríguez, and A. M. Baró, Surf. Sci. **482**, 1406 (2001).
[19] P. Kocán, P. Sobotík, I. Ošt'ádal, and M. Kotrla, Phys. Rev. B **69**, 165409 (2004).
[20] http://physics.mff.cuni.cz/kevf/vrstvy/index_eng.htm.

Available online at www.sciencedirect.com
SCIENCE DIRECT®
Surface Science 566–568 (2004) 216–220
SURFACE SCIENCE
www.elsevier.com/locate/susc

Self-organized growth of Ag islands on Si(1 1 1)-(7×7)-optimization of an STM experiment by means of KMC simulations

Pavel Kocán [a], Pavel Sobotík [a,*], Ivan Ošťádal [a], Miroslav Kotrla [b]

[a] Department of Electronics and Vacuum Physics, Charles University, V Holešovičkách 2, 180 00 Prague 8, Czech Republic
[b] Institute of Physics, Academy of Sciences of the Czech Republic, Na Slovance 2, 182 21 Prague 8, Czech Republic

Available online 17 June 2004

Abstract

A growth model and parameters obtained in our previous experimental (STM) and theoretical (Kinetic Monte Carlo simulations) studies of Ag/Si(1 1 1)-(7×7) heteroepitaxy were used to optimize growth conditions (temperature and deposition rate) for the most ordered self-organized growth of Ag island arrays on the (7×7) reconstructed surface. The conditions were evaluated by means of KMC simulations using the preference in occupation of half-unit cells (HUCs) of F-type as a criterion of island ordering. Morphology of experimentally prepared island structures was studied by STM. High degree of experimentally obtained island ordering is compared with the simulated data and results are discussed with respect to the model and parameters used at the KMC simulations.

Keywords: Epitaxy; Silver; Silicon; Monte Carlo simulations; Scanning tunneling microscopy; Self-assembly

1. Introduction

A lot of effort has been paid to prepare ordered arrays of metal nanoclusters because of interesting possible applications in the field of microelectronics. Reconstructed Si(1 1 1)-(7×7) surface was used as a template for spontaneous ordering. Recently ordered arrays of In, Al, Ga identical clusters have been prepared [1,2]. Highly ordered arrays of identical bimetal clusters of In/Ag and In/Mn were also reported in [2]. Growth of the identical clusters is mediated by the existence of particular magic sizes of atom clusters that are more stable than the others. In case of Tl [3], Sn [4] and Ag [5,6] more or less ordered island arrays were reported but magic clustering was not observed. Preparation of ordered structures requires a delicate control of deposition conditions. Kinetics of self-ordering of clusters on the reconstructed surface depends on many parameters and theoretical description of a role of deposition conditions is difficult and still not available. Kinetic Monte Carlo simulation (KMC) of the growth represents an effective approach for theoretical study of important processes involved. We used the KMC simulations together with growth experiments for studying nucleation and

* Corresponding author. Tel.: +420-2-21912336; fax: +420-2-84685095.
E-mail address: sobotik@mbox.troja.mff.cuni.cz (P. Sobotík).

0039-6028/$ - see front matter © 2004 Elsevier B.V. All rights reserved.
doi:10.1016/j.susc.2004.06.133

heteroepitaxial growth of Ag on the Si(1 1 1)-(7×7) surface [5–8].

The (7×7) reconstructed surface consists of triangular half-unit cells (HUCs), which represent potential wells for adsorbed atoms hopping on the surface [9,10]. Each HUC contains six Si adatoms of a top layer. The HUCs are of two types, one containing structural fault (FHUC), the other is unfaulted (UHUC) [11]. It results in different reactivities and consequently in preferential nucleation of Ag in FHUCs. The Ag adatom hopping between various adsorption positions within a HUC at room and higher temperatures is easy but the mobility of the Ag adatoms on the surface—important for growth processes—is determined by the hopping rate between HUCs (depends on barrier height). In a coarse grained model, we used for the simulations, the surface is represented by adsorption sites of two types (FHUCs, UHUCs) with different barrier heights. The preference in FHUC occupancy, P_F (ratio of number of FHUCs occupied by Ag clusters to number of all occupied HUCs) is determined by the barrier difference.

Metal clusters on Si(1 1 1)-(7×7) surface can be ordered in two ways—they can occupy either HUCs of both types (honey comb symmetry) or HUCs of one type only (triangular symmetry). The second case reflects the preferential adsorption of metal adatoms in one type of HUCs and the preference P_F is a measure of cluster ordering.

In this paper we focus on finding optimum deposition conditions for the most ordered arrays of Ag clusters on the Si(1 1 1)-(7×7) surface. We use the growth model developed in our previous studies and parameters obtained from KMC simulations [6,8,12]. We performed computer simulations to study the influence of deposition parameters (temperature and deposition rate) on island ordering and visualize it. The series of samples was prepared at various temperatures to verify simulated dependencies. The film morphology was studied by STM.

2. KMC model

The coarse grained KMC model implements the following growth scenario:

(i) Random surface positions (HUCs) are selected for atoms impinging with rate F. To mimic the short-range ordering of Ag-object and the low value of coverage (see [5,6] for details) at RT, when thermally activated hopping is negligible, the transient mobility is implemented according to [6] as follows:
Atoms deposited into a HUC are immediately moved to adjacent occupied HUC, if it is presented, otherwise they stay with 100% probability in FHUC and 94% probability in UHUC (to reproduce preference at RT). [1]

(ii) Single adsorbed Ag atoms (Ag adatoms) jump between adjacent HUCs and create nuclei (clusters).

(iii) When number of atoms in a cluster $n \leqslant n^*$ (n^*—critical size, the same for F and UHUCs) the cluster can decay. The activation energy for hop out of HUC containing n atoms is given by $E_n = E_{F,U} + (n-1)E_a$ for $n \leqslant n^*$ ($E_{F,U}$ is the barrier for single Ag atom hop out of FHUC or UHUC respectively, E_a is the effective binding energy between adatoms inside a HUC). Rate of the corresponding process is $v_n^{F,U} = nv_0^{F,U}\exp(-E_n/kT)$ ($v_0^{F,U}$ is the frequency prefactor, k Boltzmann constant and T sample temperature).

(iv) The capacity of a HUC to accommodate atoms is limited; clusters containing n_S atoms do not capture further adatoms—isolated cluster cannot overgrow HUC boundaries (see [7,8]).

(v) Further model features, which involve processes at formation of larger islands (during the growth up to 0.6 ML), are described in details in [7,8], but they are not important for the structures studied in this paper.

The model parameters used for simulations: $v_0^F = v_0^U = 5 \times 10^9\ \mathrm{s}^{-1}$, $E_F = 0.70$ eV, $E_U = 0.67$

[1] Due to the unclear origin of the transient mobility mechanism an alternative mechanism of correlated diffusion [13] or biased diffusion was offered [5,6]. But this mechanism is still not able to explain observed morphological features of Ag growth [5,6] (especially ordered F and U domains) along with observed dynamical behaviour of single Ag adatoms [14]. Only further experimental data together with the theoretical effort can contribute to the current discussion.

eV, $E_a = 0.05$ eV, $n^* = 5$, $n_S = 21$. Details of the model implementation were described in [6], simulations of larger islands growth will be presented elsewhere [8].

3. Experimental details

We used an UHV STM of our design and construction (base pressure $<5\times10^{-9}$ Pa) for in situ measurements. Samples with thickness (0.11 ± 0.03) ML ($\sim$2.5 atoms per HUC, 1 ML = 7.83×10^{14} atoms/cm^2) were prepared at substrate temperatures from 340 to 390 K (absolute calibration error ±10 K) and at deposition rate $R = 0.0006$ ML/s. Ag was evaporated from the tungsten wire. The deposition rate was measured by a quartz thickness monitor (absolute accuracy $\pm10\%$). Clean Si(1 1 1)-(7×7) surface was obtained using standard flashing procedure. Substrates (Sb doped, resistivity $0.005\div0.01$ Ω cm) were heated by passing DC current. Samples relaxed before STM measurements at least 1 h at room temperature (RT).

4. Results and discussion

The Ag adatoms preferentially occupy FHUCs, which are energetically the most favourable (for low amounts of deposited material). The preference P_F is kinetically determined and depends on a ratio between hopping rate and deposition flux. Maximum value of P_F can be achieved when Ag adatoms have enough time for rearranging on the surface during the growth. Such conditions are considerably supported by presence of unstable Ag clusters—i.e. when amount of deposited Ag corresponds to n^* Ag atoms per a couple of HUCs ($\approx$0.1 ML) at the most.

The simulated dependences of the preference P_F and the coverage (ratio of occupied to the total number of HUCs on the surface) on substrate temperature for various deposition rates are in Fig. 1. For every deposition rate a temperature T_M corresponding to a maximum of the preference P_{FM} can be found. At temperatures $T < T_M$ lower mobility of Ag adatoms results in lowering of opportunity to occupy FHUCs. Increasing mobility at temperatures $T > T_M$ at given deposition rate results in growth of larger islands covering two or more HUCs, which decreases the preference. Lowering the maxima P_{FM} with higher values of T_M in Fig. 1 corresponds to decreasing role of the barrier difference between FHUCs and UHUCs with increasing temperature [14].

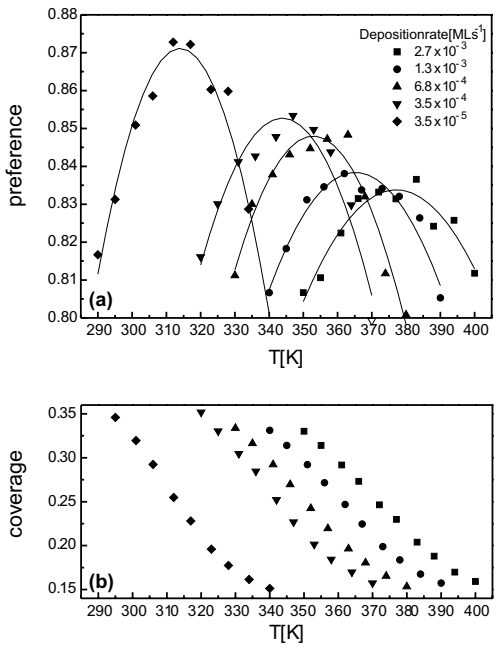

Fig. 1. Simulated dependences of preference in FHUC occupation (a) and HUC coverage (b) on deposition temperature T for films prepared at various deposition rates. Polynomial fitting (lines) was used to highlight maxima in the preference at the panel (a). Deposited amount $d = (0.11\pm0.03)$ ML corresponds to 2.5 atoms per HUC.

The temperature T_M increases with the deposition rate—Fig. 2a. The almost linear dependence in a semi-logarithmic scale shows that the ratio between the deposition and hopping rates is constant for the best ordering conditions. Decreasing of P_{FM} with the rate (Fig. 2b) means that the deposition should be as slow as possible at an experiment—the temperature corresponding to the deposition rate is given by the plot in Fig. 2a.

STM images of films prepared at the theoretically obtained conditions show high degree of

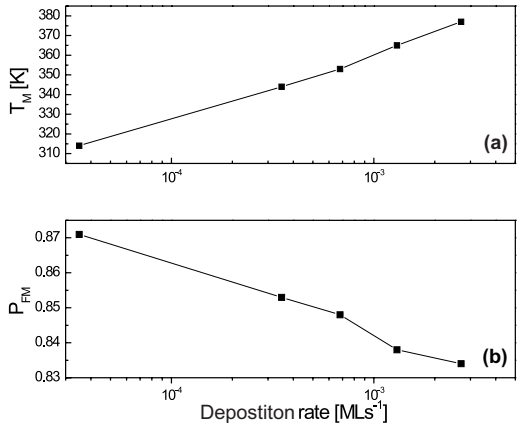

Fig. 2. Temperature T_M (a) and preference P_{FM} (b) corresponding to the most ordered films as functions of deposition rate. Conditions are the same as in Fig. 1.

cluster ordering—Fig. 3a and b. Morphology of samples prepared at temperatures higher than T_M is in Fig. 3c and d. Experimental dependences of the preference and coverage on the substrate temperature are compared with the simulated data in Fig. 4a and b. An agreement between the coverage dependences is very good. The temperature T_M obtained from the experiment differs from the simulated value within a range of error estimated for temperature measurement. The experimental value of P_{FM} is lower than the theoretical one. The dependences on temperature quantitatively differ also. We can understand the difference as a measure of proximity of the model and real processes under conditions when the sensitivity of the growth on conditions is extreme. The simulations indicated considerable dependence of the preference on a number of atoms in unstable cluster—n^*.

STM images cannot provide numbers of Ag atoms in clusters, only monomers and dimers can be distinguished [9]. Cluster size distributions can be obtained from simulations. The simulations showed that the investigated structures are unstable even after several hours of relaxation at RT (there are still monomers and dimers present on the surface). It was confirmed experimentally from STM images as well. Stability of the ordered structures can be increased by annealing (few minutes at 500 K [6]) which results in decay of

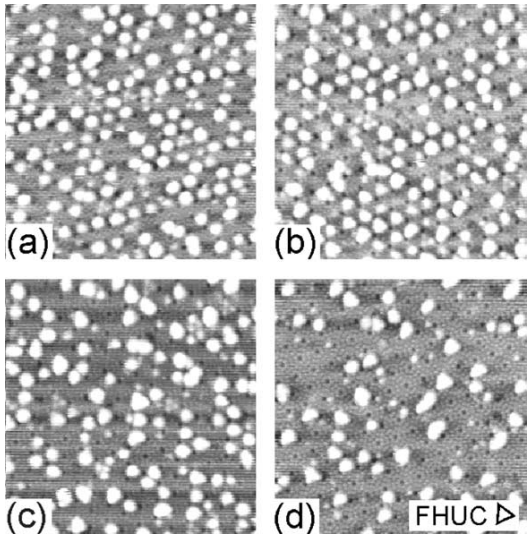

Fig. 3. STM images (35×35 nm^2, tip voltage ≈ -2 V, tunneling current ≈ 0.4 nA) of films deposited at the rate $F = 0.0006$ ML s^{-1}. Deposited amount $d = 0.11$ ML, substrate temperatures: (a) $T = 346$ K, (b) $T = 354$ K, (c) $T = 372$ K, (d) $T = 384$ K. Orientation of FHUCs (the same for all frames) is marked in the frame (d). Morphologies (a) and (b) show high degree of cluster ordering.

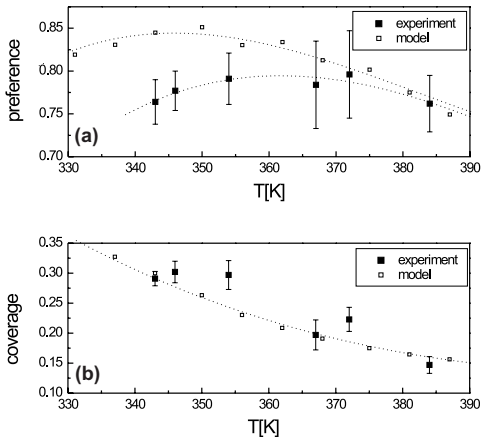

Fig. 4. Comparison of experimental and simulated data for films ($d = 0.11$ ML) deposited at the rate $F = 0.0006$ ML s^{-1}. (a) Preference in FHUC occupation, (b) HUC coverage as functions of the substrate temperature.

unstable clusters and attachment of hopping adatoms to the stable ones. Further deposition stabilizes the structure as well—existing clusters capture deposited Ag adatoms until the saturated value n_S is reached.

5. Conclusions

The growth conditions for the most ordered films were found by means of the KMC model and verified by the STM measurements. The ability of the model to show the influence of deposition conditions on the film morphology was demonstrated.

The model can be used for other non-reactive metals after adequate adjustment of the model parameters and, if necessary, definition of more complex dependence of the activation energy E_n on number of atoms in a HUC. Though we did not find any experimental support for magic clustering at Ag/Si(1 1 1)-(7×7) heteroepitaxy at room and higher temperatures, such mechanism can be implemented into the model via $E_n(n)$.

Acknowledgements

The presented work was supported by the Grant Agency of Czech Republic—projects 202/01/0928 and 202/03/0792, and by the Ministry of Education, Youth and Sports of Czech Republic—project FRVŠ 2735/2003.

References

[1] J.-F. Jia, Xi Liu, J.-Z. Wang, J.-L. Li, X.S. Wang, Q.K. Xue, Z.-Q. Li, Z. Zhang, S.B. Zhang, Phys. Rev. B 66 (2002) 165412.
[2] J.-L. Li, J.-F. Jia, X.-J. Liang, X. Liu, J.-Z. Wang, Q.-K. Xue, Z.-Q. Li, J.S. Tse, Z. Zhang, S.B. Zhang, Phys. Rev. Lett. 88 (2002) 066101.
[3] L. Vitali, M.G. Ramsey, F.P. Netzet, Phys. Rev. Lett. 83 (1999) 316.
[4] M. Yoon, X.F. Lin, I. Chizhov, H. Mai, R.F. Willis, Phys. Rev. B 64 (2001) 085321.
[5] P. Sobotík, I. Ošt'ádal, J. Mysliveček, T. Jarolímek, Surf. Sci. 454–456 (2000) 847.
[6] J. Mysliveček, P. Sobotík, I. Ošt'ádal, T. Jarolímek, P. Šmilauer, Phys. Rev. B 63 (2001) 45403.
[7] P. Sobotík, I. Ošt'ádal, P. Kocán, Surf. Sci. 507 (2002) 389.
[8] P. Kocán, P. Sobotík, I. Ošt'ádal, M. Kotrla, Continuous and correlated nucleation during nonstandard island growth at Ag/Si(1 1 1)-7×7 heteroepitaxy, Phys. Rev. B, in press.
[9] T. Jarolímek, P. Sobotík, I. Ošt'ádal, J. Mysliveček, Surf. Sci. 482–485 (2001) 386.
[10] O. Custance, I. Brihuega, J.-Y. Veuillen, J.M. Gomez-Rodriguez, A.M. Baro, Surf. Sci. 482–485 (2001) 878.
[11] K. Takayanagi, Y. Tanishiro, S. Takahashi, J. Vac. Sci. Technol. A 3 (1985) 1502.
[12] I. Ošt'ádal, P. Kocán, J. Mysliveček, P. Sobotík, Czech. J. Phys. 53 (2003) 41.
[13] E. Vasco, C. Polop, E. Rodríguez-Cañas, Phys. Rev. B 67 (2003) 235412.
[14] P. Sobotík, P. Kocán, I. Ošt'ádal, Surf. Sci. 537 (2003) L442.

2. Růst lineárních řetízků na povrchu Si(100)

2.1 Specifika povrchu Si(100)

Oproti rekonstrukci 7×7 vzniká na povrchu Si(100) relativně jednoduchá struktura - sousední atomy vytvoří dimery, které jsou uspořádány v řadách. V základním stavu jsou dimery asymetrické (vždy jeden atom výš) s periodicitou c(4×2) [1]. Při teplotách okolo 200 K (přesná teplota závisí na mnoha parametrech povrchu) dochází k fázovému přechodu [2] mezi uspořádanou rekonstrukcí c(4×2) a neuspořádaným stavem, kdy naklopení jednotlivých dimerů rychle fluktuuje. Za pokojové teploty je tak pozorována rekonstrukce 2×1, která ve skutečnosti vzniká rychlým překlápěním dimerů. Lineární uspořádání dimerů má za následek charakteristický rys povrchu Si(100) - jeho anizotropii.

Pro pohyb atomů adsorbovaných na Si(100)2×1 lze rozlišit dva význačné směry - rovnoběžný resp. kolmý s řádky dimerů. Difuzní bariéra se pro pohyb v obou směrech obecně liší a míra této anizotropie zásadně ovlivňuje kinetiku růstu.

Při nízkém pokrytí mají atomy mnoha deponovaných kovů tendenci pro uspořádání do řetízků kolmých na dimerové řádky. Mechanismus růstu řetízků složených opět z dimerů byl popsán jako povrchová polymerizační reakce [3]: Každý adsorbovaný dimer přeruší π vazby sousedních křemíkových dimerů, na vzdálenějších koncích Si dimerů pak vznikne nenasycená vazba, tvořící preferovanou adsorpční pozici pro další dimer. Atomární řetízky na povrchu Si(100) představují ideální jedno-dimenzionální (1D) nanostrukturní objekty, a proto je jejich růst studován jako modelový případ 1D uspořádávání.

2.2 Vliv přítomnosti reaktivních defektů

Pro modelový popis je velmi často uvažován povrch bez defektů. Nicméně ve skutečnosti se žádný povrch neobejde bez poruch - atomárních schodů, adsorbovaných atomů či molekul zbytkové atmosféry, nebo poruch atomární struktury rekonstrukce. Důležitou otázkou je, nakolik přítomnost defektů ve studovaném případě ovlivňuje chování a růst adsorbátu.

Vliv reaktivních defektů pochopitelně závisí na povrchové difuzivitě adsorbátu. Na povrchu Si(100) je za pokojové teploty růst vrstev většiny kovů doprovázen

vysokou mobilitou atomů po povrchu a vliv defektů proto nelze zanedbat. Na tomto povrchu byly běžně pozorovány tři typy defektů [4], z nichž reaktivní je defekt typu „C“ (C-defekty), který byl vysvětlen jako disociovaná molekula vody ze zbytkové atmosféry, kdy -OH a -H skupiny jsou adsorbovány na sousedící Si dimery [5, 6].

V Publikacích P5, P6 a P7 je pomocí techniky *in-vivo* - díky možnosti zobrazit stejnou oblast povrchu před, během a po depozici - demonstrováno, že množství kovů preferovaně nukleuje na C-defektech, což zcela mění představy o modelu růstu v tomto systému. V Publikaci P7 je studován „kotvící“ efekt C-defektů na atomární řetízky pomocí pro tento účel upravené techniky STM, kdy jedna souřadnice řádkování je zafixována a v obrazu lze pozorovat vývoj 1D struktury s frekvencí v řádu 10 Hz. Na rozdíl od neukotvených konců řetízků jsou konce ukotvené defekty stabilní a zásadně tak ovlivňují kinetiku řetízků. Tento stabilizační efekt je dále studován v Publikaci P8 pomocí *ab-initio* techniky a je ukázáno, že vazba k defektu je o 0.5 eV silnější oproti bezdefektní pozici. Mechanismus zesílení vazby je popsán následovně: Adsorbovaná disociovaná molekula vody saturuje dvě ze čtyř vazeb dvou Si dimerů a způsobí vznik stavů těsně pod Fermiho mezí, adsorbované atomy kovů jsou na tento stav citlivé a tudíž je reaktivita dané pozice vyšší.

Pro úplnost podotkněme, že ostatní nereaktivní defekty běžně pozorované na povrchu Si(100) nemají při malých pokrytích na růst velký vliv, pouze limitují růst dlouhých řetízků.

2.3 Růstové charakteristiky

Zajímavou diskusi vzbudilo zjištění publikované v práci [7], ukazující monotónně klesající rozdělovací funkci (RF) délky Ga řetízků na povrchu Si(100). Z hlediska kinetiky nukleace a růstu ostrůvků na površích je takový tvar rozdělovací funkce nezvyklý - ať už se jedná o homogenní nukleaci (všechny adsorpční pozice povrchu rovnocenné), nebo o nukleaci heterogenní (zpravidla nukleace na defektech povrchů). Rozdělovací funkce totiž bývá obvykle monomodální, kde maximum odpovídá střední délce řetízků [8, 9]. Ve své práci Albao a spol. interpretovali pozorování jako výsledek souhry silně anizotropní difuze po povrchu a 1D charakteru růstu, kdy pouze konce řetízků jsou reaktivní, zatímco boky řetízků naopak adsorbát odpuzují – tedy fakt, že okraje 1D řetízků mají 0D charakter, navíc jsou z jedné strany blokovány řetízkem. Tato omezení mají za následek omezené připojování adsorbátu k řetízkům, a tím zvýšenou nukleaci nových řetízků, tedy monotónnost

RF. Pomocí Monte Carlo simulací našli parametry, které vyhovovaly momotónně klesající rozdělovací funkci délky řetízků [7]. Proti platnosti uvedeného modelu ale stojí jednoduché argumenty. Při dané difuzivitě (difuzní bariéra ve směru rovnoběžném s růstem řetízků = 0.4 eV) je za studovaných podmínek difuzní délka taková, že adsorbovaný atom s vysokou pravděpodobností dříve interaguje s defektem, než se připojí k existujícímu řetízku či jinému difundujícímu atomu.

Později Tokar a Dreyssé [10] pomcí MC simulací a analytického řešení navrhli jiný model, dávající vždy monotónně klesající RF. Klíčovým předpokladem byla vratnost procesů během růstu a rovnováha rozpadu řetízků a nukleace. Za takových podmínek po zavedení čistě párové interakce atomů v řetízků, odvodili exponenciálně klesající RF. STM experimenty ale ukazují, že tento model není aplikovatelný na systém Ga/Si(100) vzhledem k pozorované stabilitě řetízků, které se během pozorování za pokojové teploty nerozpadají (na rozdíl od např. In, Tl, Ag...). Podmínka rovnováhy tudíž nemůže být splněna.

Důslednou analýzou STM dat publikovaných v práci [7] jsme zjistili, že předpoklad zanedbatelného vlivu defektů není splněn - více než polovina řetízků má jedno zakončení, které jme identifikovali jako zakončení reaktivním C-defektem. V publikaci P6 na tento fakt poukazujeme s tím, že přítomnost reaktivních defektů může výrazně ovlivnit růstové charakteristiky, což se později potvrdilo. V publikaci P9 jsme podrobně studovali vliv defektů na kinetiku růstu řetízků v různých případech, a demonstrovali jsme, že již při koncentraci defektů běžně experimentálně pozorované (okolo 0,3% pozic obsazených C-defektem), je jejich vliv na RF dominantní. Vliv defektů má za následek potlačení jiných významných parametrů, např. rovnovážnosti vs. nevratnosti růstu, a výsledná RF je vždy monotónně klesající.

2.4 Model chování adsorbovaných atomů na povrchu Si(100)

Vzhledem ke své relativní jednoduchosti je možné pro jednotlivé adsorbované prvky definovat atomární model růstu s počtem parametrů dostatečně nízkým pro KMC simulace. Model musí v principu zahrnovat pouze následující události:

- Anizotropní difuze - rozdílná energetická bariéra pro přeskok ve směru kolmém a rovnoběžném na směr růstu řetízků, $E^0_{\perp,\parallel}$.
- Atraktivní interakce mezi sousedními atomy ve směru růstu řetízků, E_{attr}.

- Interakce mezi sousedními atomy ve směru kolmém na růst řetízků, v případě 1D růstu odpudivá, E_{rep}. V mezním případě je možné tuto interakci modelovat zakázáním adsorpce v pozicích sousedících s řetízky [7, 11], toto nefyzikální zjednodušení je ovšem přípustné jen pro velmi malá pokrytí.

- Atraktivní interakce mezi adsorbátem a reaktivními bodovými defekty (C-defekty), E_{attrD}.

- Depozice atomů na náhodnou pozici povrchu.

Bariéra pro přeskok z pozice s $N_{\perp,\parallel}$ sousedy ve směru kolmém a rovnoběžném na růst řetízků a s $N_{D\parallel}$ reaktivními defekty ve směru rovnoběžném je možno vyjádřit jako

$$E_{\perp,\parallel} = E^0_{\perp,\parallel} + N_{\parallel}E_{attr} - N_{\perp}E_{rep} + N_{D\parallel}E_{attrD}. \tag{2.1}$$

Variacemi pěti parametrů pro výpočet aktivační energie lze docílit mnoha odlišných charakteristik růstu.

Energie vazby v řetízku má rozhodující vliv na četnost rozpadání řetízků, které je nezbytné pro vratnost procesů - tento parametr proto rozhoduje, za jakých podmínek systém dosáhne rovnovážného stavu. Silná vazba má za následek nevratný růst určený pouze difuzivitou a depoziční rychlostí, pro malé hodnoty vazby řetízky relaxují směrem ke stavu dynamické rovnováhy.

Rozdíl bariéry pro přeskok ve směru kolmém a rovnoběžném na směr řetízků určuje míru anizotropie růstu. V krajním případě silně anizotropního růstu (Publikace P9) lze pohyb atomů aproximovat na omezený v jedné dimenzi. V tom případě se při stejné četnosti přeskoků mění charakter růstu, např. atom odpojený z řetízku se s velkou pravděpodobností vrátí zpět, „volný“ atom je často uvězněn mezi blokovanými pozicemi, apod.

Nakonec parametr E_{repp} ovlivňuje míru 1D charakteru ostrůvků. Pro simulaci 1D řetízků stačí splnit požadavek $E_{repp} << E_{attr}$. Experimentálně pozorovaného potlačení nukleace v okolí řetízků lze dosáhnout nastavením dostatečně velké hodnoty repulzivní interakce. Naopak záporná hodnota parametru E_{repp} (tedy přitažlivá interakce ve směru kolmém na směr růstu řetízků) má za následek růst 2D ostrůvků, který je pozorován (Publikace P5) např. v případě Ag/Si(100).

2.5 Navazující práce

V této kapitole bude nastíněn další vývoj studia souvisejícího s publikacemi P5-P9 uvedením vybraných citací, které na tyto práce navazují. Lze konstatovat,

že především vliv přítomnosti defektů je významný i pro řadu jiných materiálů, navíc je možno tohoto vlivu využít. Na druhou stranu při detailním zkoumání morfologií řetízků atomů různých kovů (nebo jejich kombinací) je třeba vyjít z abstrahovaného modelu popsaného v předchozí části a upravit jej pro potřeby konkrétního prvku. V některých případech je klíčová (v uvedeném modelu nezahrnutá) dimerizace adatomů. Jindy se ukazuje, že i jiné než výše uvedené pozice představují pro adatomy stabilní konfigurace.

Vliv C-defektů na adsorpci dalších, chemicky odlišných kovových atomů, byl studován pomocí DFT výpočtů [12]. Bylo ukázáno, že stabilizující vliv mají defekty i na hliník (III. skupina), olovo (IV. skupina) a stříbro (přechodový kov). Kromě C-defektů (disociovaná molekula vody) byla studována možnost využití jiných defektů pro kontrolovanou změnu růstových charakteristik. Vliv defektů tvořených adsorbovanými atomy vodíku byl studován kombinací DFT a KMC [13]. V práci [14] byly jako stabilizující defekty použity molekuly benzonitrilu, které mají tu výhodu, že mohou být snadno manipulovány hrotem STM. Autoři prezentují strategii, při které STM hrotem cíleně umístí molekuly představující kotvy pro další růst řetízků.

Navazujícímu studiu byl podroben růst In řetízků - jejich růstové charakteristiky byly dále detailně studovány kombinací STM a KMC [15], stabilita těchto řetízku v závislosti na jejich délce byla analyzována pomocí DFT [16]. Difuzivita jednotlivých In atomů byla měřena pomocí STM za nízkých teplot [17], které umožnily rozlišit teplotně aktivovanou difuzi od vlivu hrotu. Vliv hrotu na stabilitu In řetízků byl dále simulován pomocí KMC [18].

Růst řetízků dalších kovů IIIA skupiny byl studován pomocí DFT [19] a kombinace DFT a KMC [20], výsledkem jsou odhady difuzních bariér a velikostí interakce kovových atomů pro jednotlivé prvky. Podobné principy 1D růstu byly pozorovány i u jiných kovů, např. u růstu řetízků z atomů manganu [21], včetně vlivu defektů na jejich růst [22].

Kromě růstu řetízků z atomu vybraného kovu byla značná pozornost věnována i růstu smíšených dimerů. Důvodem je nekovový charakter atomárních řetízků tvořených pouze jedním prvkem. Mají-li být řetízky prototypem atomárních vodičů, je samozřejmě kovový charakter základním předpokladem. Motivací pro studium dimerů smíšených z atomů s různým počtem valenčních elektronů spočívá tedy v očekávání nespárování některých elektronů s následným kovovým charakterem řetízku. Jednou studovanou kombinací jsou InSn řetízky, u kterých byl pozorován kovový stav u některých konfigurací [23]. Růst smíšených InSn dimerů během současné depozice byl studován pomocí KMC [24] a experimentálně po-

mocí nekontaktního AFM (mikroskopie atomárních sil) [25], které umožnilo chemické rozlišení jednotlivých atomů ve smíšeném dimeru. Další studovanou kombinací prvků ve smíšených dimerech byly PbAl. DFT výpočty ukázaly, že krátké řetízky (dimery, trimery) mají sice kovový charakter, ale delší řetízky už jsou polovodivé [26].

Literatura

[1] D. J. Chadi, "Atomic and Electronic Structures of Reconstructed Si(100) Surfaces," *Phys. Rev. Lett.*, vol. 43, pp. 43–47, July 1979.

[2] T. Tabata, T. Aruga, and Y. Murata, "Order-disorder transition on Si(001): c(4x2) to (2x1)," *Surf. Sci.*, vol. 179, no. 1, pp. L63–L70, 1987.

[3] G. Brocks, P. Kelly, and R. Car, "Adsorption of al on si(100) - a surface polymerization reaction," *Phys. Rev. Lett.*, vol. 70, no. 18, pp. 2786 – 2789, 1993.

[4] R. J. Hamers, "Effects of coverage on the geometry and electronic-structure of al overlayers on Si(111)," *Phys. Rev. B*, vol. 40, pp. 1657–1671, 1989.

[5] S. Okano and A. Oshiyama, "A new alternative model of type-C defects on Si(100) surfaces," *Surf. Sci.*, vol. 554, no. 2-3, pp. 272–279, 2004.

[6] M. Z. Hossain, Y. Yamashita, K. Mukai, and J. Yoshinobu, "Model for C defect on Si(100): The dissociative adsorption of a single water molecule on two adjacent dimers," *Phys. Rev. B*, vol. 67, no. 15, p. 153307, 2003.

[7] M. A. Albao, M. M. R. Evans, J. Nogami, D. Zorn, M. S. Gordon, and J. W. Evans, "Monotonically decreasing size distributions for one-dimensional Ga rows on Si(100)," *Phys. Rev. B*, vol. 72, no. 3, p. 35426, 2005.

[8] M. Bartelt and J. Evans, "Scaling analysis of diffusion-mediated island growth in surface adsorption processes," *Phys. Rev. B*, vol. 46, p. 12675, 1992.

[9] C. Ratsch and J. A. Venables, "Nucleation theory and the early stages of thin film growth," *J. Vac. Sci. Technol. A*, vol. 21, no. 5, pp. S96 – S109, 2003.

[10] V. Tokar and H. Dreyssé, "Scaling in the equilibrium size distribution of one-dimensional surface clusters," *Phys. Rev. B*, vol. 74, p. 115414, Sept. 2006.

[11] M. Albao, M. Evans, J. Nogami, D. Zorn, M. Gordon, and J. Evans, "Reply to Comment on Monotonically decreasing size distributions for one-dimensional Ga rows on Si(100)," *Phys. Rev. B*, vol. 74, p. 037402, July 2006.

[12] B. Pieczyrak and L. Jurczyszyn, "Influence of C-defect at Si(001) surface on the adsorption of Al, Ag and Pb atoms," *Appl. Surf. Sci.*, vol. 304, pp. 91–95, June 2014.

[13] M. a. Albao, D. B. Putungan, C.-H. Hsu, and F.-C. Chuang, "Enhanced nucleation of Al islands on H-dosed Si(100)-2x1 surface: A combined density functional theory and kinetic Monte Carlo study," *Surf. Sci.*, vol. 617, pp. 73–80, Nov. 2013.

[14] D. R. Belcher, M. W. Radny, S. R. Schofield, P. V. Smith, and O. Warschkow, "Guided self-assembly of metal atoms on silicon using organic-molecule templating.," *J. Am. Chem. Soc.*, vol. 134, pp. 15312–7, Sept. 2012.

[15] J. Javorský, M. Setvín, I. Ošt'ádal, P. Sobotík, and M. Kotrla, "Heterogeneous nucleation and adatom detachment at one-dimensional growth of In on Si(100)-2x1," *Phys. Rev. B*, vol. 79, p. 165424, Apr. 2009.

[16] M. W. Radny, P. V. Smith, and L. Jurczyszyn, "Adsorption-enhanced reactivity of the In/Si(001) system," *Phys. Rev. B*, vol. 81, p. 085424, Feb. 2010.

[17] M. Setvín, J. Javorský, Z. Majzik, P. Sobotík, P. Kocán, and I. Ošt'ádal, "Competition between thermally activated and tip-induced hopping of indium atoms on Si(100)," *Phys. Rev. B*, vol. 85, p. 081403, Feb. 2012.

[18] M. a. Albao, "Impact of STM tip on coarsening of In atomic chains on Si(100): A kinetic Monte Carlo study," *Surf. Sci.*, vol. 625, pp. 90–96, July 2014.

[19] E.-Z. Liu, J.-T. Wang, C.-Y. Wang, and J.-Z. Jiang, "Formation of Ga dimer linear chains on Si(001): a first-principles study," *J. Phys. Condens. Matter*, vol. 20, p. 445002, Nov. 2008.

[20] M. a. Albao, C.-H. Hsu, D. B. Putungan, and F.-C. Chuang, "Room-temperature deposition of group III metals on Si(100): A comparative study of nucleation behavior," *Surf. Sci.*, vol. 604, pp. 396–403, Feb. 2010.

[21] C. Nolph, H. Liu, and P. Reinke, "Bonding geometry of Mn-wires on the Si(100)(2x1) surface," *Surf. Sci.*, vol. 605, pp. L29–L32, July 2011.

[22] K. Simov, C. Nolph, and P. Reinke, "Guided self-assembly of Mn wires on the Si (100)(2x1) surface," *J. Phys. Chem.*, no. 100, pp. 1670–1678, 2012.

[23] P. Sobotík, M. Setvín, P. Zimmermann, P. Kocán, I. Ošt'ádal, P. Mutombo, M. Ondráček, and P. Jelínek, "Emergence of state at Fermi level due to the formation of In-Sn heterodimers on Si(100)-2x1," *Phys. Rev. B*, vol. 88, p. 205406, Nov. 2013.

[24] D. B. Putungan, H. J. Ramos, F.-C. Chuang, and M. a. Albao, "Modeling of Co-Deposition of Indium and Tin on Silicon(100): a Kinetic Monte Carlo Study," *Int. J. Mod. Phys. B*, vol. 25, pp. 1889–1898, June 2011.

[25] M. Setvín, P. Mutombo, and M. Ondráček, "Chemical identification of single atoms in heterogeneous III–IV chains on Si (100) surface by means of nc-AFM and DFT calculations," *ACS Nano*, no. 8, pp. 6969–6976, 2012.

[26] A. Puchalska, A. Racis, L. Jurczyszyn, and M. Radny, "Structural and electronic properties of chain-like structures formed by mixed PbAl dimers on Si(001) — Computational DFT study," *Surf. Sci.*, vol. 608, pp. 188–198, Feb. 2013.

Available online at www.sciencedirect.com
ScienceDirect
Surface Science 600 (2006) 3928–3931
SURFACE SCIENCE
www.elsevier.com/locate/susc

Growth of silver structures on silicon surfaces observed in vivo by scanning tunneling microscopy

P. Kocán *, I. Ošťádal, P. Sobotík

Charles University in Prague, Faculty of Mathematics and Physics, Department of Electronics and Vacuum Physics, V Holešovičkách 2, 180 00 Praha 8, Czech Republic

Available online 8 May 2006

Abstract

Early stages of growth of silver thin films on oriented silicon surfaces Si(1 0 0)2 × 1 and Si(1 1 1)7 × 7 were studied directly during deposition at room temperature by the scanning tunneling microscopy. Single Ag atoms deposited on the Si(1 0 0)2 × 1 surface diffuse too fast on the surface to be imaged by the microscope. Nucleation on C-type defects of the Si(1 0 0)2 × 1 reconstruction has been observed. During further growth, the defects represent stable terminations of silver chains. Ag nanoclusters growing on the Si(1 1 1)7 × 7 surface have been studied as a system with low diffusivity at room temperature. On this surface, presence of effective interaction between Ag clusters and individual Ag atoms in neighboring cells of the reconstruction has been identified. The interaction results in lowering the barrier for Ag atom hopping to an adjacent unit cell occupied by an Ag cluster. Unique possibilities arising from scanning the surface directly during growth are demonstrated.

Keywords: Scanning tunneling microscopy; Si(1 0 0); Si(1 1 1); Silver

1. Introduction

Growth processes have been intensively studied by modern surface physics and chemistry with a prospect of controlling growth of novel nanostructures. In order to prepare technologically and scientifically well-defined structures with desired properties, detailed information on surface processes is necessary. For this purpose, new methods for investigation of surface dynamics are valuable.

Scanning tunneling microscopy (STM) is widely used in a ''post-mortem'' regime to observe morphology of stable structures prepared in situ. Dynamics of deposit can be studied by repetitive imaging of unstable configurations. In this way, surface diffusion [1–3] and phase transitions [4,5] have been successfully investigated. Next innovative step in STM utilization is observation of growth processes, directly during deposition [6]. Benefits of such ''in vivo'' experiment are non-contentious. The method enables to image directly evolution of surface structures during growth. Besides, it enables to obtain local information on usually imperfect surface before deposition, so that influence of surface defects on growth can be studied. Moreover, the method allows to observe relaxation of structures immediately after finishing deposition.

When scanning surface during deposition, the STM tip naturally represents obstacle for the flux of deposited material (Fig. 1). This screening effect is not critical when adsorbed atoms diffuse fast on the surface and migrate to the scanned area [6]. In the case of low diffusivity, the screening effect can be eliminated by using extremely sharp tips.

Silver deposited on silicon surfaces at room temperature (RT) is a model example of metal–semiconductor system with sharp interface between substrate and deposit. On the Si(1 0 0)2 × 1 surface, Ag atoms (or dimers [7]) migrate freely. During growth, the atoms form islands composed of parallel chains of Ag dimers. A tendency to assembly in the chains of dimers perpendicular to the dimer rows of the

* Corresponding author.
E-mail address: pavel.kocan@mff.cuni.cz (P. Kocán).

0039-6028/$ - see front matter © 2006 Elsevier B.V. All rights reserved.
doi:10.1016/j.susc.2006.01.103

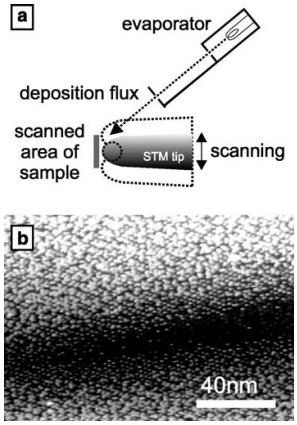

Fig. 1. (a) Experimental setup of the in vivo experiment – deposited atoms impinge the sample directly during scanning. (b) Si(1 1 1)7 × 7 surface after deposition of ~0.75 ML of Ag during scanning – surface area screened by a sharp STM tip is clearly visible.

2 × 1 reconstruction has been observed in the case of various metals (e.g. Pb [8], Al [9,10], In and Ga [11]). Growth of the dimer chains has been described as a surface polymerization reaction [10]. However, detailed explanation of the chain nucleation and stability is still missing.

Growth of silver structures on the Si(1 1 1)7 × 7 surface represents another often studied problem. The Si(1 1 1)7 × 7 surface consists of large (2.7 nm) triangular half unit cells (HUC's) of two different types [faulted (F-HUC's) and unfaulted (U-HUC's)]. The HUC's represent traps for adsorbed metal atoms with fast diffusion inside HUC [12,13] and slow hopping between HUC's (mean lifetimes of atoms in F- and U-HUC's were evaluated as $\tau_F = (6 \pm 2) \times 10^4$ s, $\tau_U = (3.5 \pm 2.0) \times 10^3$ s, respectively [1]). In such a system with low surface diffusivity, a hit and stick regime of growth would be expected. However, observed morphologies of the structures grown at RT show a certain degree of cluster ordering and could not be explained by the hit and stick model [1,14]. Despite of many studies on early stages of Ag/Si(1 1 1)7 × 7 growth, the mechanism of cluster formation is still a subject of discussion [14–16].

In this paper, we demonstrate the power of the STM during deposition (in vivo). This method allows to obtain new data on RT growth of silver structures on the Si(1 0 0)2 × 1 (fast surface diffusion) and the Si(1 1 1)7 × 7 (slow surface diffusion). Such information could not be obtained using standard in situ STM.

2. Experimental setup

STM experiments were performed using a non-commercial microscope operating in ultra-high vacuum (base pressure $<3 \times 10^{-9}$ Pa). Si(1 1 1) substrates were Sb doped, n-type, with resistivity 0.005–0.01 Ω cm; the 7 × 7 reconstructed surface was obtained using a standard flashing procedure. Si(1 0 0) samples were cut from the n-type, Sb doped silicon wafer with resistivity ⩽0.014 Ω cm. To obtain the 2 × 1 reconstruction, samples were flashed several times for ~20 s to 1200 °C. For STM experiments, tungsten electrochemically etched tips were used. We adopted an etching circuit according to Ref. [17]. The shape of the tip apex allowed deposition "under" the STM tip during scanning an area of 40×40 nm^2 (Fig. 1b). A miniature tungsten wire evaporator distanced 4 cm from the sample was used to deposit silver on the scanned surface. Incidental angle of deposited flux was 30 °C. All presented images were obtained using constant current mode, scanned with a frequency of 1 image per ~60 s.

3. Results

3.1. Deposition on the Si(1 0 0)2 × 1 surface

Fig. 2a and b show unoccupied and occupied surface states images of the Si(1 0 0)2 × 1 surface before deposition. At unoccupied states, defects appearing as bright spots next to depressions can be recognized (Fig. 2a). These features are commonly observed on clean Si(1 0 0)2 × 1 surfaces and have been assigned as C-type defects. Recently, two groups proposed independently a similar structural model for these defects [18,19], explaining satisfactorily the C-type defect as a dissociated molecule of H_2O with OH and H adsorbed on two adjacent Si atoms of neighboring dimers.

Fig. 2c–e shows evolution of the surface during deposition. On STM images, no diffusing species can be observed, due to diffusion much faster than data acquisition. At very early stages, Ag atoms are trapped by the C-type defects (Fig. 2c), in the positions adjacent to the bright parts of the defects observed at unoccupied state imaging. During continuous deposition, the C-type defects act as stable terminations of Ag dimer chains. The opposite termination is unstable, attaching and detaching Ag atoms – both growth and decay of chains can be observed. Another possible nucleation sites for the Ag deposit are step edges (Fig. 2e), as could be expected due to increased adsorption energy of these sites. Fig. 2f shows the situation after 20 min of relaxation without further deposition. Most of unstable Ag chains and islands decayed to zero-dimensional (0D) objects in the positions of the C-type defects, while the rest of Ag atoms were captured by steps. Therefore, these 0D objects can be interpreted as single Ag monomers or dimers trapped by the C-type defects.

Finally, we propose a following growth scenario: Atoms deposited on the surface diffuse rapidly and nucleate at first available site with increased adsorption energy. Such sites are C-type defects, step edges and already nucleated Ag islands. During relaxation, the islands nucleated at the C-type defects decay, while the detached atoms form more stable islands at step edges.

During deposition, islands with stable terminations occurred in positions, where C-type defects were originally not observed. Appearance and behavior of these

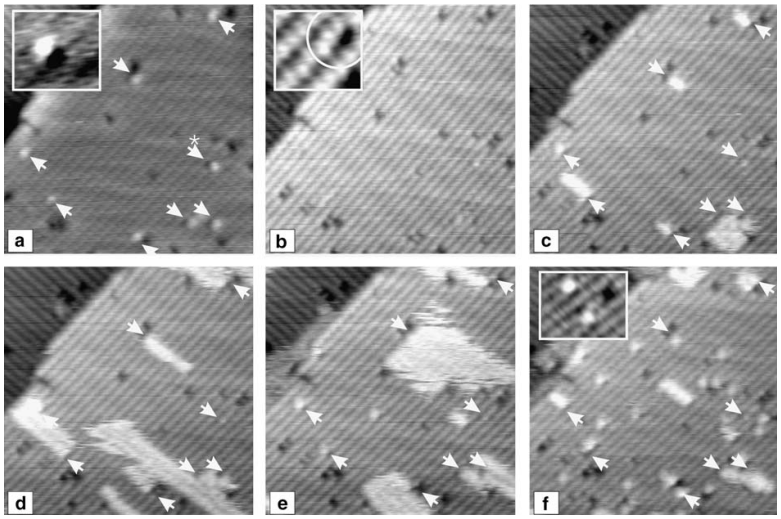

Fig. 2. (a) Unoccupied states (+2.0 V) image of the Si(1 0 0)2 × 1 surface before deposition. (b) Occupied states (−2.0 V) image of the same area. Insets in (a) and (b) show details of a C-type defect. (c–e) Evolution of the surface during Ag deposition after 3, 11 and 28 min, respectively. (f) Situation 20 min. after end of the deposition, the inset shows C-type defects with trapped Ag atoms. Arrows mark positions of C-type defects appearing as bright spots next to depressions in (a) and representing stable chain terminations in (c–f). Image size 20×20 nm^2.

terminations and original C-type defect terminations are the same. We assume that the origin of the new terminations is also the same – new C-type defects occur on the surface as contaminants from residual gas in the system.

3.2. Deposition on the Si(1 1 1)7 × 7 surface

Evolution of the Si(1 1 1)7 × 7 surface during Ag deposition at RT is shown in Fig. 3. After heating the evaporator, atoms impinge on the surface and are trapped by triangular HUC's of the reconstruction. A HUC occupied by a single Ag atom appears as a bright triangle due to fast hopping of the Ag atom inside the HUC [20,13,12]. No hops between HUC's are observed in the early stages, when relative HUC occupancy $\theta < 0.5$ ($\theta = n_{Ag}/N_{HUC}$, where n_{Ag} is the number of HUC's occupied by a silver object and N_{HUC} is the number of all HUC's). Evolution of θ during this growth stage was fitted by theoretical curve corresponding to hit and stick HUC filling with the only parameter – deposition rate R (Fig. 4). The best agreement was obtained for the value $R = (7 \pm 2) \times 10^{-5}$ ML/s (ML $= 7.83 \times 10^{14}$ atoms/cm^2).

During further deposition, dimers and larger clusters are formed by random impingement to already occupied HUC's. A dimer appears as bright spots at the positions of three Si center adatoms in a HUC; number of atoms in larger clusters cannot be specified at RT [20]. When the relative occupancy approaches ~0.5, inter-cell hopping processes begin to influence the growth (Fig. 4). In this stage, the relative HUC occupancy slightly decreases. The most often observed process is a jump of monomer to a HUC occupied by a dimer or a larger cluster. Jumps of monomer to a HUC occupied by the other monomer are very rare. Surprisingly, situation corresponding to a jump of a dimer to a HUC occupied by a monomer has been observed several times. However, this process could be explained by two subsequent jumps of individual Ag atoms. The nature of inter-cell hopping suggests a kind of inter-cell attractive interaction between metal adsorbates in neighboring HUC's, reported in different forms for various materials (Pb [2], Y [15], In [21], Tl [22]). During further deposition, a limited capacity of a HUC to accommodate Ag atoms [23,14] results in nucleation of new clusters.

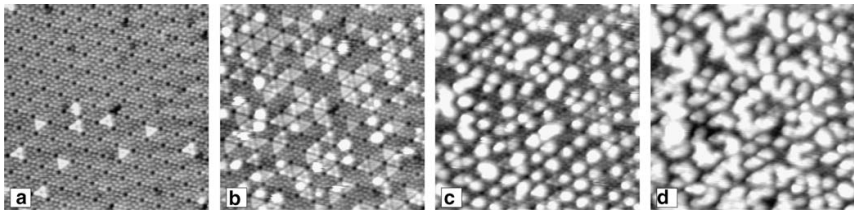

Fig. 3. Images of the same area of the Si(1 1 1)7 × 7 surface taken during Ag deposition after (a) 1 min, (b) 5 min, (c) 25 min, (d) 55 min from the beginning of growth. Image size 30×30 nm^2.

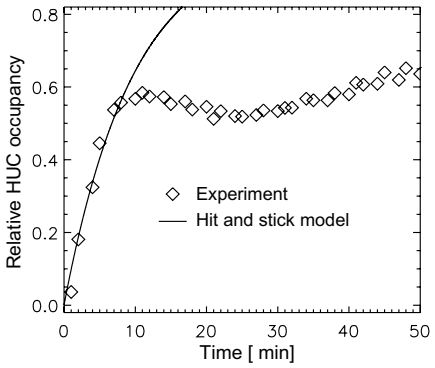

Fig. 4. Evolution of relative HUC occupancy during Ag deposition on the Si(1 1 1)7 × 7 surface.

Islands covering more than one HUC grow mostly by filling boundaries of adjacent HUC's occupied by clusters [14].

4. Conclusion

In vivo STM allowed to study surface processes directly during silver film growth and revealed directly growth scenario. On the Si(1 0 0)2 × 1, diffusing atoms nucleate on C-type defects. During growth, these defects represent the only stable terminations of dimer chains on terraces. After relaxation, small 0D objects remain on the terraces – atoms or dimers trapped by the C-type defects. The remaining Ag atoms form larger islands, mostly attached to the step edges. On the Si(1 1 1)7 × 7 surface, effective inter-cell attractive interaction between clusters containing at least two Ag atoms and monomers in adjacent HUC's has been observed. The interaction results in correlated hops, breaking hit and stick regime observed at the earlier stages of the growth.

Acknowledgement

The work is a part of the research plan MSM 0021620834 that is financed by the Ministry of Education of Czech Republic and partly was supported by projects GAUK 307/2004/B and GACR 202/03/0792.

References

[1] P. Sobotík, P. Kocán, I. Ošt'ádal, Surf. Sci. 537 (2003) L442.
[2] J.M. Gómez-Rodríguez, J.J. Sáenz, A.M. Baró, J.Y. Veuillen, R.C. Cinti, Phys. Rev. Lett. 76 (1996) 799.
[3] E. Ganz, S.K. Theiss, I.S. Hwang, J. Golovchenko, Phys. Rev. Lett. 68 (1992) 1567.
[4] I. Brihuega, O. Custance, R. Pérez, J.M. Gómez-Rodríguez, Phys. Rev. Lett. 94 (2005) 046101.
[5] O. Custance, I. Brihuega, J.Y. Veuillen, J.M. Gómez-Rodríguez, A.M. Baró, Surf. Sci. 482 (2001) 878.
[6] B. Voigtländer, A. Zinner, T. Weber, Rev. Sci. Instrum. 67 (1996) 2568.
[7] K. Kong, H. Yeom, D. Ahn, H. Yi, B. Yu, Phys. Rev. B 67 (2003).
[8] Z. Dong, T. Yakabe, D. Fujita, Q. Jiang, H. Nejo, Surf. Sci. 380 (1997) 23.
[9] J. Nogami, A. Baski, C. Quate, Phys. Rev. B 44 (1991) 1415.
[10] G. Brocks, P. Kelly, R. Car, Phys. Rev. Lett. 70 (1993) 2786.
[11] M. Evans, J. Nogami, Phys. Rev. B 59 (1999) 7644.
[12] C. Zhang et al., Phys. Rev. Lett. 94 (2005).
[13] K. Wang, C. Zhang, M. Loy, X. Xiao, Phys. Rev. Lett. 94 (2005).
[14] P. Kocán, P. Sobotík, I. Ošt'ádal, M. Kotrla, Phys. Rev. B 69 (2004) 165409.
[15] C. Polop, E. Vasco, J.A. Martín-Gago, J.L. Sacedón, Phys. Rev. B 66 (2002) 085324.
[16] E. Vasco, Surf. Sci. 575 (2005) 247.
[17] Y. Nakamura, Y. Mera, K. Maeda, Rev. Sci. Instrum. 70 (1999) 3373.
[18] M. Hossain, Y. Yamashita, K. Mukai, J. Yoshinobu, Phys. Rev. B 67 (2003).
[19] S. Okano, A. Oshiyama, Surf. Sci. 554 (2004) 272.
[20] T. Jarolímek, P. Sobotík, I. Ošt'ádal, J. Mysliveček, Surf. Sci. 482 (2001) 386.
[21] J.-L. Li et al., Phys. Rev. Lett. 88 (2002) 066101.
[22] L. Vitali, M.G. Ramsey, F.P. Netzer, Phys. Rev. Lett. 83 (1999) 316.
[23] P. Sobotík, I. Ošt'ádal, P. Kocán, Surf. Sci. 507–510 (2002) 389.

PHYSICAL REVIEW B **74**, 037401 (2006)

Comment on "Monotonically decreasing size distributions for one-dimensional Ga rows on Si(100)"

Pavel Kocán,* Pavel Sobotík, and Ivan Ošťádal
Charles University, Faculty of Mathematics and Physics, Department of Electronics and Vacuum Physics, V Holešovičkách 2, 180 00 Praha 8, Czech Republic

(Received 7 October 2005; revised manuscript received 23 January 2006; published 21 July 2006)

Albao *et al.* [Phys. Rev. B **72**, 035426 (2005)] recently reported on a study on room temperature growth of Ga on Si(100). Monotonically decreasing island size distribution observed by means of scanning tunneling microscopy was explained using kinetic Monte Carlo simulations with a complex mechanism of atom capture. In the simulation, influence of the *C*-type defects on the growth process is not considered. These defects are commonly observed on the Si(100) surfaces and act as initial adsorption sites for deposited metal atoms.

DOI: 10.1103/PhysRevB.74.037401 PACS number(s): 68.37.Ef, 68.55.Ac, 81.15.Aa

In their paper,[1] authors present a detailed kinetic Monte Carlo (KMC) study of one-dimensional growth of Ga dimer rows on the Si(100)2×1 surface. The key assumption of the authors is, that the growth is not influenced by the presence of surface defects. The condition of the low influence is well satisfied in the case of the defects assigned as *A* and *B* type[2] interpreted as missing Si dimers. On the other side, the defects assigned as *C* type[2] have a strong influence on a nucleation process, as will be demonstrated here.

Two independent groups interpreted the *C*-type defects as dissociated water molecules.[3,4] The defects are commonly observed on the Si(100)2×1 surface even at pressures $<10^{-8}$ Pa, the number of defects increases with time.[5] On the empty state scanning tunneling microscopy (STM) image of the surface, *C*-type defects are clearly visible as bright protrusions [Fig. 1(a)], while at filled states the defects appear as almost undetectable depressions [Fig. 1(b)].

Figure 2 in the commented paper[1] shows Ga rows with several types of terminations. On the filled state STM image, most of the rows have at least one end terminated by depression. Evans and Nogami assigned such terminations as "dark ends" in Ref. 6. In the case of Pb deposited on the Si(100)2×1 surface, Juré *et al.* observed the same type of terminations.[7] From the analysis of row relaxations, the terminations were interpreted as Pb atoms pinned to the *C*-type defects.[7] In the same study, the authors offered a model of early growth stages based on the nucleation of diffusing atoms on the *C*-type defects. This model has been confirmed by means of a low temperature experiment.[8]

Our *in vivo* experiments, performed under pressure $<3\times10^{-9}$ Pa during a whole process, revealed terrace nucleation of Ag and In exclusively on the *C*-type defects. The experiments were based on real-time observation directly during deposition (rate $\sim5\times10^{-5}$ ML/s) with the experimental setup the same as in Ref. 9. Figures 1(a) and 1(b) show empty and filled state STM images of the Si(100)2×1 surface directly before deposition. The *C*-type defects are well visible on the image in Fig. 1(a). Figure 1(c) shows a filled state STM image of In rows grown on the same area. Original positions of the *C*-type defects are marked by arrows—all of the rows in Fig. 1(c) are pinned to these defects. Analysis of STM images showed that most of all of the In rows were pinned to the defects. A line profile across one of the rows [Fig. 1(d)] reveals a depression in the position of the *C*-type defect marked C1, corresponding to the dark end, similarly to the Ga (Ref. 6) and Pb (Ref. 7) rows.

In order to clarify the origin of the observed row terminations, the STM line scans at occupied states over an In row during its evolution are presented in Fig. 2. The termination by depression, i.e., the termination by the *C*-type defect, remains stable. This is valid even for long periods of observation (~h). The opposite row end evolves during observation. At used scanning conditions, imaging of this termination switches between two types. (i) Bright termination, appearing as a protrusion $\sim4\times$ higher than the height of the middle part of the row; (ii) normal termination with apparent height similar to the height of the middle row part. After two changes of the row termination, the row became $2a$ shorter (a being the surface lattice constant). Therefore, each change could be considered as a process of one atom detachment,

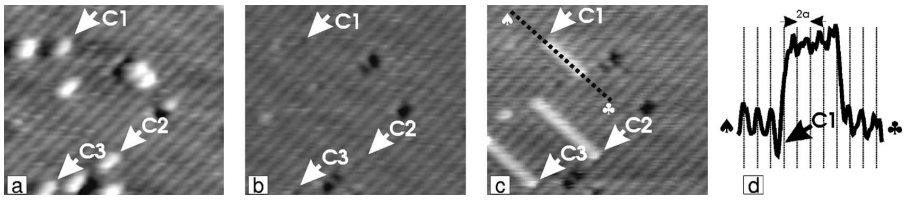

FIG. 1. STM images of the same area before (a), (b), and after (c) the deposition of In. Arrows mark positions of *C*-type defects well visible in the empty states image (a), almost hidden in the filled states image (b), and acting as terminations of one-dimensional islands (c). Tip voltage (a) −1.8 V, (b), (c) 2.5 V; image size 14×12 nm^2. The images were obtained directly during deposition. (d) A line profile over the island in frame (c) with a depression in the position of the *C*-type defect marked C1.

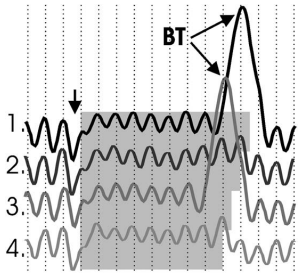

FIG. 2. Line scans over evolving In row obtained with interval of ≈10 s. Tip voltage +2 V, current 0.3 nA. *C* marks the position of termination by *C*-type defect, BT—bright terminations. Background shade schematically denotes length of the row.

resulting in termination either by monomer or dimer.

In Ref. 1, the authors state that "Detailed analysis of high-resolution images in fact shows that rows are equally likely to be terminated by a metal dimer or monomer." This statement is based on proposals of Ref. 6, where the dark ends are interpreted as the monomer terminations. This is in evident disagreement with our observation. Analogously to Pb, Ag, and In we interpret the dark ends of the rows in Fig. 2 of Ref. 1 as the terminations by the *C*-type defects. Therefore, observation of rows equally terminated by dark ends and normal terminations shows that most of the rows were terminated by the *C*-type defects.

In the case of In rows growing on Si(100)2×1 the observed influence of the *C*-type defects can be summarized as follows: (a) Deposited atoms nucleate merely on the defect sites. (b) Row terminations by the *C*-type defects are stable during observation. (c) No deposited atoms are attached to a row on the end terminated by the *C*-type defect.

For a proper simulation, introducing the *C*-type defects into the physical model is necessary. At present, we are not able to decide, if introduction of the defects into the simulation would preserve monotonically decreasing the size distribution presented in Ref. 1. However, values of the parameters evaluated from the model would be different.

In conclusion, the authors of the commented paper[1] presented the model fitting well with the observed monotonous size distribution of Ga islands in the case of negligible influence of defects on growth. Comparing the presented image (Fig. 2 in Ref. 1) to the images of Pb, Ag, and In rows, we point out that the assumption of negligible defect influence is not acceptable either in the case of Ga on Si(100)2×1. Experiments show that deposited metal atoms nucleate with high preference on the *C*-type defects. Due to high reactivity of the defects, their influence on growth must be considered in the case of any fast diffusing deposit on the Si(100)2×1 surface.

This work is a part of the research plan MSM 0021620834 that is financed by the Ministry of Education of the Czech Republic and partly was supported by Projects Nos. GACR 202/06/0049 and GAUK 307/2004/B.

*Electronic address: pavel.kocan@mff.cuni.cz

[1] M. A. Albao, M. M. R. Evans, J. Nogami, D. Zorn, M. S. Gordon, and J. W. Evans, Phys. Rev. B **72**, 035426 (2005).
[2] R. J. Hamers and U. K. Köhler, J. Vac. Sci. Technol. A **7**, 2854 (1989).
[3] M. Z. Hossain, Y. Yamashita, K. Mukai, and J. Yoshinobu, Phys. Rev. B **67**, 153307 (2003).
[4] S. Okano and A. Oshiyama, Surf. Sci. **554**, 272 (2004).
[5] M. Nishizawa, T. Yasuda, S. Yamasaki, K. Miki, M. Shinohara, N. Kamakura, Y. Kimura, and M. Niwano, Phys. Rev. B **65**, 161302(R) (2002).
[6] M. M. R. Evans and J. Nogami, Phys. Rev. B **59**, 7644 (1999).
[7] L. Juré, L. Magaud, J.-M. Gómez-Rodríguez, P. Mallet, and J.-Y. Veuillen, Phys. Rev. B **61**, 16902 (2000).
[8] H. S. Yoon, M.-A. Ryu, K.-H. Han, and I.-W. Lyo, Surf. Sci. **547**, 210 (2003).
[9] I. Ošt'ádal, P. Kocán, P. Sobotík, and J. Pudl, Phys. Rev. Lett. **95**, 146101 (2005).

Available online at www.sciencedirect.com
ScienceDirect
Surface Science 601 (2007) 4506–4509
SURFACE SCIENCE
www.elsevier.com/locate/susc

Stability of In rows on Si(100) during STM observation

P. Kocán *, P. Sobotík, I. Ošťádal, J. Javorský, M. Setvín

Charles University in Prague, Faculty of Mathematics and Physics, Department of Electronics and Vacuum Physics, V Holešovičkách 2, 180 00 Praha 8, Czech Republic

Available online 24 April 2007

Abstract

Structural and dynamical properties of In rows grown on the Si(100)2 × 1 surface were studied in detail by the scanning tunneling microscopy at room temperature. The rows on terraces are preferably pinned to C-type defects, the unpinned ends detach and attach In atoms during observation. Evolution of the rows was recorded with single atom precision. Time constants for detachment of atoms from the rows were measured as a function of row length; a stabilizing effect of the C-type defects was quantified. Dynamics of the In rows was found to depend on tunneling voltage. An effect of electric field is proposed to be responsible for the influence.

Keywords: Scanning tunneling microscopy; 1-D organization; Silicon; Indium; Nanostructures

1. Introduction

Group III metals (Al, Ga, In, Tl) deposited on the Si(100) surface are often studied as an example of a model system forming well defined 1-dimensional rows of metal atoms. During decades, the scanning tunneling microscopy (STM) has proven as a powerful tool for examining structural and electronic properties of such rows. During examining the structures, an STM tip was found not only imaging surface, but also influencing dynamics of a deposit [1–4]. Especially, Tl layers on Si(100) were shown [2,4] as extremely unstable under an STM tip at room temperature (RT) even under tunneling conditions common for imaging silicon surfaces (voltage $\approx \pm 2$ V, tunneling current $\approx$ 0.1 nA). On the other hand, Al and Ga rows are believed to be stable even during RT STM observation [5,6]. In the case of In, manipulation with addimers was presented [3] when extreme tunneling conditions (tip voltage ≈ -4 V, tunneling current ≈ 10 nA) were applied. However, no detailed study on stability of In rows at RT using moderate tunneling voltage and current ($\approx \pm 2$ V, ≈ 0.1 nA) is available.

Indium rows on the Si(100)2 × 1 surface are composed of dimers parallel to surface Si dimers, similarly to the other group III metals [5,7,8]. The growth has been explained as the surface polymerization reaction [5]. Ends of the rows represent preferred adsorption sites for rapidly diffusing atoms. The rows nucleate preferentially at the S_B type steps [7,9]. On terraces, almost exclusive nucleation on C-type defects has been observed [10].

In this study, we report on dynamics of the In rows at RT imaged by STM using common tunneling conditions. We present both qualitative and quantitative description of instability of the rows and discuss a possible mechanism of a tip influence.

2. Experimental

A non-commercial STM system operating in ultra-high vacuum (base pressure $< 3 \times 10^{-9}$ Pa) has been used for experiments. Si(100) samples were cut from the n-type, Sb doped silicon wafer with resistivity $\leqslant 0.014\ \Omega$ cm. To obtain 2 × 1 reconstruction, samples were several times flashed for ≈ 20 s to 1200 °C. Tungsten electrochemically etched tips were used. Indium was deposited from a miniature tungsten wire evaporator during imaging the surface by STM. Deposition rate was $\approx 10^{-4}$ ML s^{-1},

* Corresponding author.
E-mail address: pavel.kochan@mff.cuni.cz (P. Kocán).

0039-6028/$ - see front matter
doi:10.1016/j.susc.2007.04.132

ML = 6.87×10^{14} atoms/cm^2. The rate was estimated from STM images. Deposition and STM experiments were performed at RT. All presented images are constant current topographs obtained after deposition; a typical scanning speed was 300 nm/s.

Without exceptional experimental setup [11], scanning rate of STM is ≈1 image/min. In order to increase data acquisition speed, the x-axes of an imaged area was oriented parallel with respect to In rows and the y-coordinate was fixed at a position of a chosen row. This "line-scanning mode" allowed to image dynamics of the rows ≈10^3 times faster than when using a basic area-scanning mode.

3. Results and discussion

3.1. Structural features

A series of occupied states images of the Si(1 0 0)2 × 1 surface with low coverage of In is shown in Fig. 1. Fig. 1a shows C-type defects (CD's) on the surface before deposition of In. The CD's, commonly observed on Si(1 0 0) surfaces, have been interpreted as dissociated water molecule adsorbed to two adjacent Si dimers [12,13]. During the deposition, In rows grow from the positions of the CD's [10] – see Fig. 1b and c. In occupied states images, the termination by a CD is imaged as a depression (dark end). No In atoms are attached to the row from the side of the dark end. The opposite row end switches between two states: (i) a termination with a height similar as in the middle of the row ("normal termination") and (ii) a termination by a bright protrusion ("bright termination"). Normally terminated rows are shown in Fig. 1b and c; a detail of the end switching between the bright and normal terminations is shown in Fig. 1d. In empty states STM images, In rows are imaged with higher contrast in comparison to occupied states images. No significant difference between ends corresponding to the bright and normal terminations was observed at the empty states.

From evolution of In rows we extracted numbers of In atoms composing rows of different lengths. Fig. 2a shows the empty states image of an In row pinned to a CD obtained in the line-scanning mode. The observation reveals clearly single atom changes in length of the row; detachment or diffusion of dimers is not probable. Line profiles extracted from the image (Fig. 2a) are shown in Fig. 2b. The situation marked '0' corresponds to a CD without In row. The labels '1'–'6' give numbers of In atoms composing corresponding rows. In agreement with the concept of the surface polymerization reaction, the rows could be classified as rows with even and odd number of In atoms (CD + $n \times$ dimer and CD + $n \times$ dimer + monomer, $n = 1, 2, 3 \ldots$). Undimerized odd atoms are imaged as peaks slightly narrower than the peaks corresponding to dimers. In the occupied states images, numbers of atoms composing rows of different lengths were evaluated analogously (Fig. 2c). According to the analysis, bright and normal terminations correspond to terminations by a monomer and a dimer respectively.

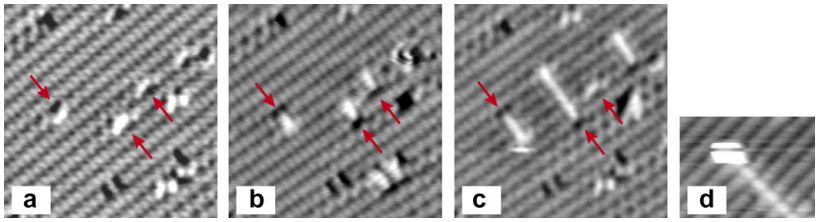

Fig. 1. STM images ($U_{tip} = 2$ V) of the Si(1 0 0)2 × 1 surface before (a) and during (b–d) growth of In rows. Arrows mark C-type defects, acting as nucleation centers for the rows shown in (b) and (c). (d) Detail of a row end switching between normal and bright termination during scanning.

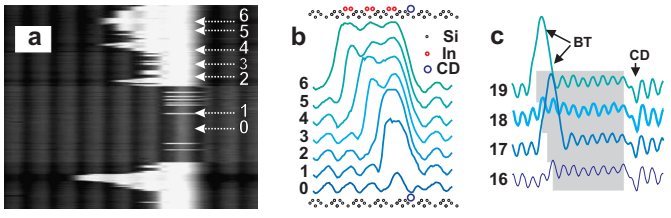

Fig. 2. (a) Unoccupied STM image ($U_{tip} = -2$ V, total time 19 s) obtained in the line-scanning mode over C-type defect and a row containing fluctuating number of In atoms, length of scanned line is 7.4 nm. (b) Selected lines extracted from (a), labels mark numbers of In atoms contained in the row. Atomic structures are illustrated for bottom (pure C-type defect) and top profiles (three dimers attached to the C-type defect). (c) Line profiles extracted from occupied states STM image ($U_{tip} = 2$ V, length of lines is 12 nm); BT marks bright terminations, CD a termination by a C-type defect. A shadow is used to mark length of the row.

A high contrast between imaging occupied and unoccupied states of In dimers on Si(1 0 0)2 × 1 was explained in the following way [14]: The highest occupied (lowest unoccupied) states on the surface are σ-bonded $p_x + p_y$ (π-bonded $s + p_z$) hybridized orbitals of In atoms respectively. In-plane orientation of the σ-type bond results in the low contrast of In rows at occupied states, while the standing-up direction of the π-type bond is responsible for high contrast observed in unoccupied states images [15]. In the case of an undimerized In atom, we explain the STM appearence as follows. The $s + p_z$ orbital of the undimerized atom is half-filled, and therefore imaged at both polarities. Due to a stand-up character of this orbital, the undimerized atom is imaged with high contrast when compared to the clean Si(1 0 0) surface at both occupied and unoccupied states.

3.2. Stability of In rows

In order to compare stability of rows with different lengths, time constants for detachment of terminating atoms from rows containing different numbers of atoms were estimated, using STM measurements at a tip voltage of −2 V. We note that the estimates have only comparative character, because the values depend on tunneling conditions, as will be shown later. The following objects were examined: CD + monomer, CD + dimer, CD + n × dimer and CD + n × dimer + monomer ($n = 1, 2, 3, \ldots$). The corresponding time constants are listed in the Table 1.

As expected, the rows terminated by dimers are more stable than the rows with odd number of In atoms. The parallel dimer structure saturates all three valence electrons of each In atom without causing significant stress [5,7], and thus represents the most stable structure on low coverage In/Si(1 0 0)2 × 1 surfaces. Indium dimer adsorbed next to a CD was found to be the most stable In object. The CD rearranges charge distribution of two Si dimers to which it is bonded. The rearrangement causes an increase of reactivity of the remaining dangling bonds of the dimers. Surprisingly, a single atom next to a CD is less stable than undimerized atom at the end of a longer row – the stabilizing effect of the CD is much weaker in the case of a single atom when compared to its stabilizing effect on a dimer.

3.3. Tip influence

Rates of detachment processes depend on tunneling conditions, as clearly demonstrated in Fig. 3, where tip voltage was switched from +2.0 V to −2.0 V during scanning over an In row. Significantly faster detachment and attachment processes are observed when imaging empty states. Large variations in rates of detachment processes were also found when comparing data obtained with different STM tips using similar tunneling conditions. Therefore, the rates of the processes depend both on tunneling conditions and on an STM tip shape.

Table 1
Estimated time constants τ for detachment of In atom from rows of different lengths

Row	τ [s]
CD + monomer	<0.06
CD + dimer	≈100
CD + n × dimer	≈5
CD + n × dimer + monomer	0.27 ± 0.03

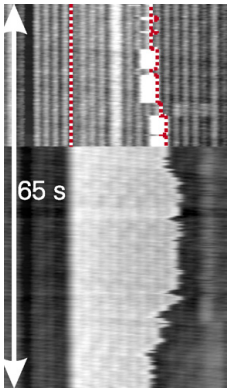

Fig. 3. A line-scanning mode STM image shows different activity of an In row at tip voltage of +2 V (top part) and −2 V (bottom part). Evolution of the row imaged at occupied states is outlined.

In general, small distance of an STM tip from a sample together with a narrow channel of tunneling electrons may influence dynamics of observed deposit in several ways: (1) when tip-sample separation is 0.5–1.0 nm and voltage ≈1 V, the electric field is $\approx 10^7$ V cm^{-1}. The field may result in forces on charged adsorbate, as well as on static or induced dipoles [16]; (2) localized current of high density may cause local heating; (3) injection of electrons or holes into a gap region may result in breaking of chemical bonds; (4) due to a limited response of STM feedback, the tip can occasionally approach the sample to a distance, when atomic forces between atoms of the surface and the tip are not negligible.

In order to propose a possible mechanism of the tip influence, sets of line scans over In rows were recorded at various tunneling conditions – current, voltage and scanning speed. To eliminate a dependence of dynamics on row length, the well-defined and resolved feature – CD + dimer + monomer was selected for a statistical analysis of a time constant of atom detachment. The time constants τ were obtained from exponential decay fit of a histogram of measured lifetimes. If the tip influenced the dynamics by means of localized current, i.e. by local heating or by injection of electrons or holes, rates of the atom detachment, $\nu = 1/\tau$, would depend clearly on the tunneling current. As shown in Fig. 4a, this is not the case. The data were obtained using negative tip voltage, when the detachment rates were the highest observed. An atomic force between the tip and adsorbate would result in

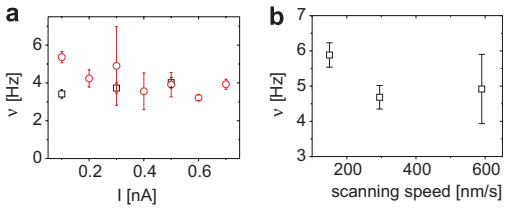

Fig. 4. Detachment rates of In atom from a row composed of three In atoms as function of tunneling current (a) and scanning speed (b). The data in (a) were obtained using tip voltage −2.1 V (squares) and −1.5 V (circles), scanning speed 300 nm s^{-1}; data in (b) were obtained with tip voltage −1.8 V, tunneling current 0.3 nA.

detachment rate ν increasing with the frequency of the tip scanning over an In row. Data obtained with different scanning rates, at other tunneling conditions and scanned size unchanged, are shown in Fig. 4b. Evidently, the dependence shows no significant increase of the rate with frequency, so the mechanical influence could be ruled out.

The remaining probable mechanism is the influence of a strong electric field. The dependence on tip polarity (see Fig. 3) shows that both attachment and detachment rates are influenced by presence of the field. In the case of Tl on the Si(1 0 0)2×1 surface, even stronger influence on tip polarity was observed [4,2]. Depending on polarity of scanning tip, Tl adsorbate disappears and reappears on the scanned area during few seconds. This feature was explained by presence of a static dipole caused by adsorption-induced charge transfer. The field with gradient caused by a shape of the tip apex results in forces on the static dipole. The forces are attractive and repulsive with respect to the tip position, according to the tip polarity. The tip induced diffusion was also observed for In atoms deposited on the Si(1 1 1)$\sqrt{3}\times\sqrt{3}$ surface [1]. The tip influence was explained by charging of In adatoms and subsequent field-induced diffusion based on direction-dependent lowering of diffusion barriers [16].

A quantitative analysis of the field influence is complicated for two reasons: First, direction and strength of induced forces change during scanning over the studied line. Second, shape of a tip, determining gradient of the field, is usually unknown. However, a simplified physical image could be proposed: Influence of a tip on In rows on Si(1 0 0) can be explained by positive charging of In adsorbate or formation of a static dipole, similarly to Tl on Si(1 0 0) [4,2] and In on Si(1 1 1) [1]. Low attachment rate observed at positive tip voltage can be explained by repulsion of freely migrating In atoms from scanned line. An attractive force in direction to the position of a negatively biased tip results in sequence of detachment and attachment of atoms from and to the studied row, respectively. This "trapping" of atoms close to the tip region causes increased "liveness" of row terminations when imaged at unoccupied states.

4. Conclusion

The line-scanning STM mode allowed to observe a fast evolution of In rows. From the observation of the single atom attachment and detachment we derived structural models of the rows pinned to C-type defects. We used a simplified electronic configuration of adsorbed atoms to interpret STM images of different terminations. Analysis of evolution of row lengths provided comparison of stability of rows with different number of atoms. Dimer terminated rows were found to be more stable than those terminated by undimerized atom, in agreement with predictions based on a parallel dimer model. Strong stabilizing effect of a C-type defect on single dimer was observed, explaining the preferable nucleation of In rows on the C-type defects. A strong influence of tunneling voltage and STM tip shape on the rate of detachment of atoms from ends of the rows was found. From the considered mechanisms of the tip influence, the effect of a high electric field was proposed as the most probable.

Acknowledgements

The work is a part of the research plan MSM 0021620834 that is financed by the Ministry of Education of Czech Republic and partly was supported by projects GACR 202/06/0049, GAUK 227/2006/B and GAUK 225/2006/B.

References

[1] A.A. Saranin, T. Numata, O. Kubo, H. Tani, M. Katayama, V.G. Lifshits, K. Oura, Phys. Rev. B 56 (1997) 7449.
[2] A.A. Saranin, A.V. Zotov, V.G. Kotlyar, I.A. Kuyanov, T.V. Kasyanova, A. Nishida, M. Kishida, Y. Murata, H. Okado, M. Katayama, K. Oura, Phys. Rev. B 71 (2005) 035312.
[3] Z.C. Dong, T. Yakabe, D. Fujita, H. Nejoh, Ultramicroscopy 73 (1998) 169.
[4] M. Kishida, A.A. Saranin, A. Zotov, V.G. Kotlyar, A. Nishida, Y. Murata, H. Okado, M. Katayama, K. Oura, Appl. Surf. Sci. 237 (2004) 110.
[5] G. Brocks, P. Kelly, R. Car, Phys. Rev. Lett. 70 (18) (1993) 2786.
[6] M.A. Albao, M.M.R. Evans, J. Nogami, D. Zorn, M.S. Gordon, J.W. Evans, Phys. Rev. B 74 (3) (2006) 037402.
[7] Z. Dong, T. Yakabe, D. Fujita, Q. Jiang, H. Nejo, Surf. Sci. 380 (1) (1997) 23.
[8] X.Q. Dai, W.W. Ju, G.T. Wang, M.H. Xie, Surf. Sci. 572 (2004) 77.
[9] A.A. Baski, J. Nogami, C.F. Quate, J. Vac. Sci. Tech. A 9 (1991) 1946.
[10] P. Kocán, P. Sobotík, I. Ošťádal, Phys. Rev. B 74 (2006) 037401.
[11] M.J. Rost, L. Crama, P. Schakel, E. van Tol, G.B.E.M. van Velzen-Williams, C.F. Overgauw, H. ter Horst, H. Dekker, B. Okhuijsen, M. Seynen, A. Vijftigschild, P. Han, A.J. Katan, K. Schoots, R. Schumm, W. van Loo, T.H. Oosterkamp, J.W.M. Frenken, Rev. Sci. Instrum. 76 (2005) 053710.
[12] M. Hossain, Y. Yamashita, K. Mukai, J. Yoshinobu, Phys. Rev. B 67 (2003) 153307.
[13] S. Okano, A. Oshiyama, Surf. Sci. 554 (2–3) (2004) 272.
[14] L. Magaud, A. Pasturel, L. Jure, P. Mallet, J.Y. Veuillen, Surf. Sci. 454 (2000) 489.
[15] Z.C. Dong, D. Fujita, H. Nejoh, Phys. Rev. B 63 (2001) 115402.
[16] T. Nakayama, D.H. Huang, M. Aono, Microelectronic Engineering 32 (1996) 191.

PHYSICAL REVIEW B **77**, 113301 (2008)

Defects on the Si(100)-(2×1) surface: Anchoring sites of the surface polymerization reaction of In atoms

Pavel Kocán,[1,2,*] Leszek Jurczyszyn,[3] Pavel Sobotík,[1] and Ivan Ošt'ádal[1]

[1]*Charles University in Prague, Faculty of Mathematics and Physics, Department of Surface and Plasma Science, V Holešovičkách 2, 180 00 Praha 8, Czech Republic*

[2]*Department of Molecular and Material Sciences, Kyushu University, Kasuga, Fukuoka 816-8580, Japan*

[3]*Institute of Experimental Physics, University of Wrocl'aw, Plac Maksa Borna 9, 50-204 Wrocl'aw, Poland*

(Received 10 December 2007; revised manuscript received 3 February 2008; published 3 March 2008)

Indium atoms are found to interact strongly with the so-called C defects, commonly present on the Si(100)-2×1 surface. As a consequence, In rows growing on the surface are pinned to these defects. The reaction of adsorbate with the C defects is studied in detail by *ab initio* calculations in combination with the scanning tunneling microscopy and spectroscopy. For calculations, we successfully adopted a model of the C defect as a dissociated water molecule. The presence of the defect induces a surface state just below the Fermi level, resulting in a surface-mediated reaction forming a row of indium atoms. The end of the row not pinned to a C defect is unstable at room temperature. Transition between metallic and nonmetallic characters of the unpinned termination, given by parity of atoms in the row, was observed and explained by *ab initio* calculations.

DOI: 10.1103/PhysRevB.77.113301 PACS number(s): 68.55.ag, 68.37.Ef, 68.43.Bc

Studying physics of low-dimensional structures and utilization of their new and unique features is a challenge of recent material research. Technique of scanning tunneling microscopy (STM) and spectroscopy (STS) can provide data important for deeper understanding of relation between atomic arrangement and electronic structure on solid state surfaces. Room temperature (RT) growth of metal rows on the Si(100)-2×1 surface is generally studied as a model system showing spontaneous one-dimensional organization. The Si(100) surface reconstructs by forming dimers aligned in rows perpendicular to dimer bonds. These dimers are buckled at low temperature, forming the $c(4\times2)$ reconstruction, while at RT, fast flip-flop motion of the dimers results in the 2×1 symmetry. Anisotropic character of the surface is responsible for one-dimensional growth of many materials, such as group III-IV metals (Al, Ga, In, Pb, Sn).[1–5] Atomic rows of group III metals are composed of dimers [Fig. 1(b)], structure of which saturates all valence electrons of the atoms involved (one electron per silicon atom and three electrons of group III atom), without causing significant stress. Mechanism of formation of the rows has been explained in the case of Al by an *ab initio* study—an increased local density of states (LDOS) in a position neighboring to a dimerized end of the row results in preferred adsorption at this site.[6] Attachment of another metal atom results in formation of a dimer again. Repetition of these two steps leads to growth of one-dimensional rows.[6] Because of its analogy in organic chemistry, Brocks *et al.* assigned this mechanism as a surface polymerization reaction.[6]

Three types of defects are commonly observed on the Si(100)-2×1 surface: A- and B-type, believed to be one and two missing dimers, respectively, and particularly interesting C-type defects.[7] Hossain *et al.* and Okano and Oshiyama independently interpreted the C defect as a dissociated H_2O molecule, with the H and hydroxyl group bonded to neighboring Si atoms of two adjacent surface dimers.[8,9] It should be noted that all experimentally observed features have not been yet satisfactorily explained. For growth of metal rows on the Si(100)-2×1 surface, the C defects play a significant role.[10,11] In contrast to previous assumptions, we found that In rows are pinned almost exclusively to the C defects. Unlike A- and B-type defects, inert to diffusing atoms, the C defects are reactive and act as nucleation centers on terraces.[10,11] An impact of neglecting the influence of the C defects is a subject of recent discussion.[10,12,13] We study in detail a mechanism of stabilization of In rows by the C de-

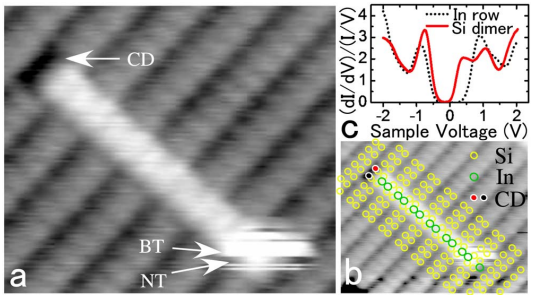

FIG. 1. (Color online) (a) STM image of the indium row anchored by the C defect (marked CD). The opposite end fluctuates between the bright and normal termination (marked BT and NT), the change corresponds to the process of single atom detachment and attachment. Scanning in horizontal direction with rate of 180 ms per line, with sample voltage of −2 V. (b) STM image shown in (a), with a proposed structural model overlaid. (c) STS spectrum proportional to a local density of states, measured at a position of In dimer within a row. A nonmetallic character is clearly revealed. As a reference, STS spectrum taken with the same tip on the clean Si(100)-2×1 surface is shown as well. The spectra are averaged from approximately ten measured characteristics. Recording time of a single spectrum was 11 s and set-point sample voltage and tunneling current where 2 V and 0.6 nA, respectively.

fects using *ab initio* calculations in combination with STM and STS.

For experiments, we used a noncommercial ultrahigh vacuum STM with a base pressure of below 2×10^{-9} Pa. Indium was deposited on Si samples (Sb doped, resistivity of $<0.014\ \Omega\,\mathrm{cm}$) at RT directly during scanning the surface using STM. This method allows examining the surface before, during, and after deposition (*in vivo* STM). Details are described elsewhere.[14] The 2000-point $dI/dV-V$ characteristics were measured at an open control loop using lock-in detection (EG&G 5209) of the ac driven by 963 Hz, 70 mV signal added to tunneling bias.

The *ab initio* structural calculations presented in this Brief Report are based on the density functional theory and the use of the local orbital basis[15,16] (code FIREBALL). In this approach, the wave functions of valence electrons were constructed using the pseudoatomic, slightly excited orbitals,[17,18] which were confined to the regions limited by optimized radii. The ion cores were simulated by norm-conserving pseudopotentials,[19] while the exchange-correlation contributions were introduced by local-density approximation. Our total energy calculations presented here have been performed for the system where the silicon substrate was described by an asymmetric slab built up of four atomic layers: the positions of atoms in the bottom were fixed and the dangling bonds at this layer were saturated by hydrogen atoms. However, we have also performed the checking structural calculations with the silicon substrate represented by six atomic layers. The relaxation of atomic positions has been performed using the combination of conjugate gradient and dynamical quenching algorithms. Results presented in this Brief Report have been obtained for a 8×6 unit cell (if not stated else) with the use of two k points. Error of the calculated adsorption energies is estimated as <0.01 eV. Energy scale of shown LDOS spectra is related to the Fermi level.

STM simulations presented in this Brief Report were based on the nonequilibrium Green-function formalism developed by Keldysh[20] and described in detail in Ref. 21. The matrices of the Green functions and density of states which are necessary for the calculations of the tunneling current have been obtained from the local orbital Hamiltonian (sample) and the cluster-Bethe-lattice method (tip).[22] Hopping interactions between the tip and the sample were calculated using the Bardeen expression for the tunneling current between orbitals of particular atoms of the tip and the sample.[23]

In order to determine the atomic structure of In rows, the *in vivo* experimental setup allowing observation of growth directly during deposition was used. The experiment clearly showed that most of In rows are pinned to C defects. An example of the In row pinned to a C defect is shown in Fig. 1(a). From dynamical study of time evolution of the indium rows,[11] we proposed a structural model shown in Fig. 1(b). The row termination at the C defect is very stable during growth and relaxation and appears as a depression in STM images. The opposite termination fluctuates at RT due to attachment and detachment of metal atoms. At occupied states, two different terminations of the fluctuating end are observed. The bright termination (BT) or normal termination (NT) corresponds to a single indium atom or dimer, respectively.

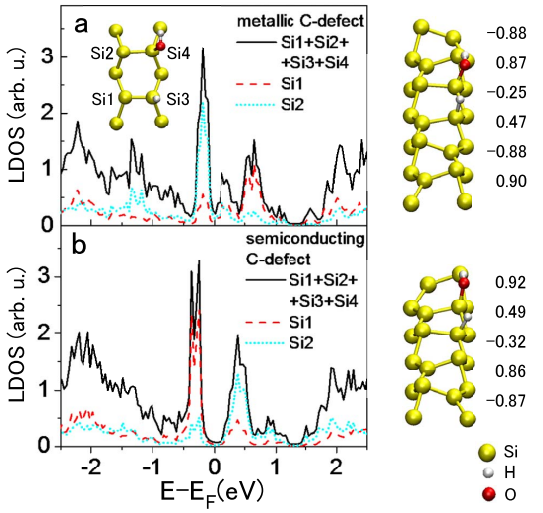

FIG. 2. (Color online) Calculated local density of states of C defects on Si(100)-2×1: (a) metallic and (b) semiconducting C defect. Atoms in Si dimers are labeled accordingly to inset in (a). Corresponding relaxed structures in top-side view are shown on right-hand side. Indicated numbers—differences in z coordinate (in Å) of atoms forming topmost Si dimers—demonstrate different bucklings.

For *ab initio* calculations, we adopted the structural model of a C defect as a dissociated water molecule.[8,9] At low temperature, Hata *et al.* observed two types of the C defects—buckling angels of the nearest unperturbed Si dimers have the same sign in one case (showing semiconducting STS spectra, therefore called semiconducting C defect) and the opposite sign in the other one (called metallic C defect).[24] These two types could not be distinguished at RT. Therefore, we tested both metallic and semiconducting case in our calculations. For calculation of the metallic and semiconducting C defect, 2×6 and 2×5 supercells were used, respectively. Stabilized structures of the both types are shown in Fig. 2 together with corresponding LDOS spectra. The density of electronic states is in a very good agreement with the low-temperature STS data measured by Hata *et al.*[24] The surface state present just below the Fermi level, localized mostly in the position of a Si atom marked Si2 in Fig. 2(a) in the case of metallic C defect) or Si1 (in the case of semiconducting C defect) is of special importance. In analogy to the surface polymerization reaction,[6] deposited metal atoms are supposed to be sensitive to this state, which results in preferred adsorption in the position next to the C defect.

The structural model of an In row as a chain of dimerized atoms pinned to a C defect [see Fig. 1(b)] was used in our calculations, starting with the C defect and one adsorbed metal atom, followed by forming a row of increasing length. To evaluate the stabilizing effect of the defects, calculations for corresponding structures on clean surface were performed. According to the calculations, the adsorption energies of an In adatom pinned to the metallic and semiconduct-

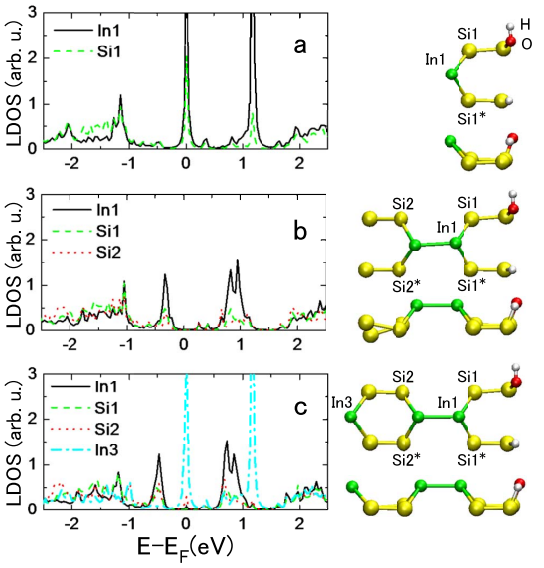

FIG. 3. (Color online) Calculated local density of states for In row growing from the position of the C defect: (a) monomer, (b) dimer, and (c) three atoms. Corresponding relaxed atomic structures (top and side views) are shown on the right-hand side panels. Locations of the spectra in (a)–(c) are marked accordingly in the structural models. The LDOSs at positions of atoms labeled Si1* and Si2* (not shown) are almost the same as the LDOS of its counterparts, Si1 and Si2, respectively.

ing C defects are 3.12 and 3.01 eV, respectively. The adsorption energy of the In atom in a corresponding position on the clean surface is much lower—2.56 eV. Therefore, both metallic and semiconducting C defects create preferred adsorption positions. From here on, we show only results obtained using the metallic C defect. However, very similar results were obtained for the case of the semiconducting defect as well. The LDOS calculated for representative positions in the case of a single In adatom pinned to the C defect is shown in Fig. 3(a). Evidently, the presence of the In adsorbate changes significantly the electronic structure of the considered system [compare to LDOS of the C defect shown in Fig. 2(a)]. Now, LDOSs at the position of an In and two nearest Si atoms exhibit a sharp maximum located at the Fermi level—the system is strongly metallic.

We continue by calculation of two In atoms on the surface. A metal dimer pinned to the C defect represents the most stable structure examined—the adsorption energy of the second In atom is 3.74 eV. The relaxed structure is shown in Fig. 3(b). The pinned indium dimer is more stable than a dimer adsorbed on the clean surface—the corresponding energy difference is 0.17 eV. The presence of the second atom changes again the electronic structure of the system significantly, as shown in Fig. 3(b). The LDOS maximum present at the Fermi level in the case of a monomer now disappears and the electronic structure of the whole system becomes nonmetallic.

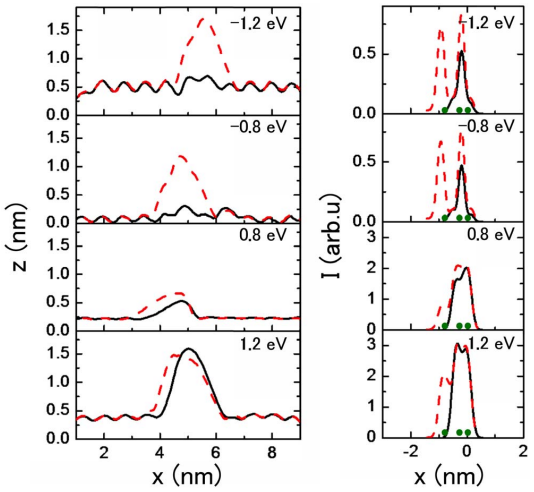

FIG. 4. (Color online) STM profiles along the row formed by two (solid line) and three (dashed line) indium atoms obtained at various sample voltages, as indicated in each frame. Left panel—measured profiles (constant current mode); right panel—calculated profiles (constant height mode). The circles show lateral positions of the In atoms in the case of calculated profiles.

Adding further In atoms to the row gives results similar to those obtained for the monomer and dimer pinned to a C defect. The electronic structure of the row termination shows repeatedly the metallic or nonmetallic character according to the termination by a single atom or dimer, respectively. The adsorption energies of third to sixth atoms terminating the row are 2.86, 3.74, 2.87, and 3.73 eV, respectively.

The *ab initio* calculations show that electronic structure and stability of the last atom in a row strongly depend on parity of number of indium atoms in the row (Fig. 3). In the case of an odd number, the last atom is not dimerized and one of the three valence electrons of the In atom is not paired. This half-filled surface state results in metallic character of LDOS in the positions of the last In atom and two nearest Si atoms. The difference in electronic structure can be resolved by STM. Figure 4 shows both measured and calculated STM profiles along the rows formed by two and three atoms. A direct comparison of profiles is difficult, due to many factors, such as different imaging modes and different shapes of STM tips. Nevertheless, the relevant features agree: The row composed of three atoms appears much brighter than a dimer; the effect is stronger especially at occupied states. This big difference in contrast explains well the switching between bright and normal terminations, as shown in Fig. 1(a). Hence, the bright and normal terminations correspond to termination by the monomer and dimer, respectively.

Nonmetallicity of dimerized In atoms was proofed by means of scanning tunneling spectroscopy [Fig. 1(c)]. The absence of states at the Fermi level is clearly consistent with the calculated LDOS spectra. Unfortunately, the terminations by single indium atoms are too unstable at RT for reliable STS measurement.

With respect to the calculated stabilizing effect of the C defects, we propose the following scenario for growth of metal rows on the Si(100)-2×1 surface. Deposited atoms migrate on the surface, until they attach to C defects or another metal atoms. The atoms tend to align to one-dimensional rows due to their anisotropic surface-mediated interaction. Rows unpinned to C defects are unstable; with time, the most stable terminations—at C defects—dominate. Therefore, in a dynamic equilibrium, all In rows on the surface are anchored at the C defects. The time necessary to reach the dynamic equilibrium depends on strength of bonding within metal rows and can vary for different metals.

In conclusion, interaction between the C defects and metal adsorbate on silicon surface was studied by *ab initio* calculations. We show the anchoring effect of the C defects, commonly observed on the Si(100)-2×1 surface, for growth of the In rows. The model of the C defect as a dissociated water molecule satisfies well the experimentally observed features. The presence of the C defect results in the surface state just under the Fermi level. Indium adatoms are sensitive to this surface state; bonding at this position is stronger by 0.5 eV in comparison with the equivalent position on the clean silicon surface. Adsorption of the second In atom—formation of a dimer—results in the even more stabilized structure. Adding or removing of a single atom results in changing electronic character of the row end; structures terminated by the monomer or dimer have strongly metallic or nonmetallic character, respectively. This feature was revealed by STM observations as well. A similar behavior can be expected in the case of other group III metals deposited on the Si(100)-2×1 surface.

The work is a part of the research plan MSM 002160834 that is financed by the Ministry of Education of Czech Republic and was supported by Projects No. GACR 202/06/0049, No. GAUK 225/2006/B, and No. GAUK 227/2006/B.

*pavel.kocan@mff.cuni.cz

[1] Z. Dong, T. Yakabe, D. Fujita, Q. Jiang, and H. Nejo, Surf. Sci. **380**, 23 (1997).
[2] J. Nogami, A. A. Baski, and C. F. Quate, Phys. Rev. B **44**, 1415 (1991).
[3] J. Nogami, S. I. Park, and C. F. Quate, Appl. Phys. Lett. **53**, 2086 (1988).
[4] J. Y. Veuillen, J. M. Gómez-Rodríguez, and R. C. Cinti, J. Vac. Sci. Technol. B **14**, 1010 (1996).
[5] A. A. Baski, C. F. Quate, and J. Nogami, Phys. Rev. B **44**, 11167 (1991).
[6] G. Brocks, P. J. Kelly, and R. Car, Phys. Rev. Lett. **70**, 2786 (1993).
[7] R. Hamers and U. Kohler, J. Vac. Sci. Technol. A **7**, 2854 (1989).
[8] M. Z. Hossain, Y. Yamashita, K. Mukai, and J. Yoshinobu, Phys. Rev. B **67**, 153307 (2003).
[9] S. Okano and A. Oshiyama, Surf. Sci. **554**, 272 (2004).
[10] P. Kocán, P. Sobotík, and I. Ošt'ádal, Phys. Rev. B **74**, 037401 (2006).
[11] P. Kocán, P. Sobotík, I. Ošt'ádal, J. Javorský, and M. Setvín, Surf. Sci. **601**, 4506 (2007).
[12] M. A. Albao, M. M. R. Evans, J. Nogami, D. Zorn, M. S. Gordon, and J. W. Evans, Phys. Rev. B **72**, 035426 (2005).
[13] M. A. Albao, M. M. R. Evans, J. Nogami, D. Zorn, M. S. Gordon, and J. W. Evans, Phys. Rev. B **74**, 037402 (2006).
[14] I. Ošt'ádal, P. Kocán, P. Sobotík, and J. Pudl, Phys. Rev. Lett. **95**, 146101 (2005).
[15] J. P. Lewis, K. R. Glaesemann, G. A. Voth, J. Fritsch, A. A. Demkov, J. Ortega, and O. F. Sankey, Phys. Rev. B **64**, 195103 (2001).
[16] P. Jelínek, H. Wang, J. P. Lewis, O. F. Sankey, and J. Ortega, Phys. Rev. B **71**, 235101 (2005).
[17] A. A. Demkov, J. Ortega, O. F. Sankey, and M. P. Grumbach, Phys. Rev. B **52**, 1618 (1995).
[18] O. F. Sankey and D. J. Niklewski, Phys. Rev. B **40**, 3979 (1989).
[19] G. B. Bachelet, D. R. Hamann, and M. Schlüter, Phys. Rev. B **26**, 4199 (1982).
[20] L. Keldysh, Zh. Eksp. Teor. Fiz. **47**, 1515 (1964).
[21] N. Mingo, L. Jurczyszyn, F. J. Garcia-Vidal, R. Saiz-Pardo, P. L. de Andres, F. Flores, S. Y. Wu, and W. More, Phys. Rev. B **54**, 2225 (1996).
[22] L. Martin-Moreno and J. A. Vergés, Phys. Rev. B **42**, 7193 (1990).
[23] E. C. Goldberg, A. Martín-Rodero, R. Monreal, and F. Flores, Phys. Rev. B **39**, 5684 (1989).
[24] K. Hata, S. Ozawa, Y. Sainoo, K. Miyake, and H. Shigekawa, Surf. Sci. **447**, 156 (2000).

PHYSICAL REVIEW E **80**, 061603 (2009)

Modeling growth of one-dimensional islands: Influence of reactive defects

Pavel Kocán,* Pavel Sobotík, Ivan Ošt'ádal, Martin Setvín, and Stanislav Haviar
Charles University in Prague, Faculty of Mathematics and Physics, Department of Surface and Plasma Science, V Holešovičkách 2, 180 00 Prague 8, Czech Republic
(Received 29 July 2009; published 22 December 2009)

Influence of reactive defects on size distribution of one-dimensional islands is studied by means of kinetic Monte Carlo simulations in combination with an analytical approach. Two different models are examined: a model with anisotropically diffusing atoms irreversibly aggregating to islands, and a reversible model close to thermal equilibrium which allows atom detachment from islands during the growth. The models can be used to simulate island growth of group III metals deposited on the Si(100)2×1 surface at room temperature: Al, Ga (irreversible model), and In (equilibrium model). We demonstrate that concentration of the reactive defects 0.0025 per site may change the island size distribution from monomodal to monotonically decreasing in the case of the irreversible model. At concentration $\geq$0.005 defects per site, a difference between results of the studied models is suppressed by the influence of the defects and similar island size distributions are obtained.

DOI: 10.1103/PhysRevE.80.061603 PACS number(s): 81.15.Aa, 87.10.Rt, 68.55.ag

I. INTRODUCTION

Anisotropy of crystal surfaces often results in growth of one-dimensional (1D) nanostructures upon deposition of mobile adatoms. Formation of such single-atom-wide islands is a subject of both experimental [1–7] and theoretical [3,7–12] research as a model of 1D self-organization. Experimentally, the scanning tunneling microscopy (STM) provided island size distributions for several systems of 1D islands [3,7,8]. Various theoretical approaches were used to explain the experimentally quantified morphologies: kinetic Monte Carlo (kMC) simulation [3,8,10,13], rate equations [11], and analytical derivation from thermodynamic consideration [10].

Besides other systems of 1D assembling, group III metal atoms deposited on the Si(100)2×1 surface attracted attention. In this case, formation of 1D chains of dimerized atoms was explained by a surface mediated reaction [14]. Experiments showed that islands composed of group III atoms with larger atomic radii (In, Tl) are unstable at room temperature [1,2,4,15], while those with smaller atomic radii (Al, Ga) form stable islands [3,14]. Based on STM observation, Albao *et al.* reported monotonically decreasing size distribution (MDSD) of Ga islands grown on the Si(100)2×1 surface [3]. Such a form of the distribution is rather surprising, because in the case of low-coverage irreversible island growth, generally monomodal distribution is expected, independently on island geometry [16,17]. Albao *et al.* interpreted the MDSD by means of kMC simulations using an irreversible model with strong anisotropy in combination with presence of so-called prohibited zones along islands (Fig. 1). Later, their experimental data [3] were interpreted by Tokar and Dreyssé [10] by using a qualitatively different model. In the latter case, the MDSD was obtained as a result of reversible growth under thermal equilibrium. This model contains one parameter only—metal atom pair interaction energy between the nearest neighbors in a metal chain. By fitting this single parameter Tokar and Dreyssé [10] obtained the same statistics as measured by Albao *et al.*

Even though perfect periodic surface of a crystal is commonly used in theoretical studies, defects are always present on real surfaces. The defects can be classified as line (e.g., step edges, domain boundaries) or point defects (e.g., molecules of adsorbate, step kinks, missing atoms); reactive (acting as nucleation centers) or inert with respect to adsorbed atoms. Especially in the case of highly mobile adsorbate, all stages of growth may be governed by presence of defects, as demonstrated for growth of two-dimensional islands [18]. Therefore, it is important to understand how various defects influence surface adsorption, nucleation and growth of nanostructures.

In the case of the Si(100)2×1 surface, *C*-type defects, interpreted as dissociated water molecules [19–21], are commonly observed on the substrate. It was demonstrated both by experiments and *ab initio* calculations [4,15,22,23] that the *C*-type defects represent preferred nucleation sites for deposited atoms. For the first time, the *C* defects were accounted for in simulations in Ref. [13] in the case of irreversible model applied to Ga growth on Si(100)2×1. A reversible model taking into account nucleation on defects was recently used to simulate growth of In islands on the Si(100)2×1 surface [8]. However, role and impact of the defects remained under discussion [8,13,22]. Another example of point defects pinning 1D islands can be found at

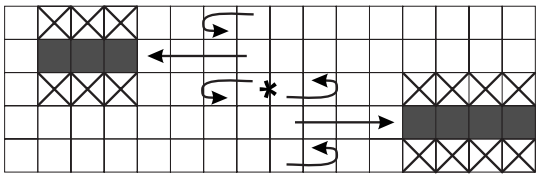

FIG. 1. A schematic illustration of a model with prohibited zones (crosses) along islands (shaded). Mobility of metal adatoms is much higher in direction parallel with 1D islands than in perpendicular direction. The arrows indicate tendency of adatoms either to be attached to island ends or repelled from the prohibited zones. The asterisk marks the position where a single adatom is trapped between two prohibited zones.

*pavel.kocan@mff.cuni.cz

adsorption of metal atoms on vicinal Pt surface [5–7]. On Pt surface, step edges are decorated by diffusing adatoms, assembling to 1D islands along step edges. Step kinks, representing the most stable sites for deposited atoms, play a role of the reactive defects.

Here, we analyze an influence of reactive defects on low coverage growth (<0.1 monolayer, ML) of 1D atomic islands. Two different models are studied, irreversible and close-to-equilibrium one, respectively. The goal was to diminish number of parameters without loosing accuracy. As a result, important processes are identified and risk of "correct" results obtained by an "incorrect" simulation with too many parameters is reduced. From the irreversible model, we extracted important processes and defined a simple model utilizing capture zones. A model with diffusion restricted to one dimension, which reflects the surface anisotropy, is tested. For the close-to-equilibrium model we solved equilibrium conditions taking into account nucleation on defects and neglecting diffusion pathways. The approximative methods are compared to "exact" results of kMC simulations.

We use growth of the group III metals deposited on the Si(100)2×1 surface with *C*-type defects as an example of growth of 1D islands strongly influenced by reactive defects. However, such an approach can be easily adopted to other systems with growth of 1D objects.

II. MONTE CARLO IMPLEMENTATION

A kMC implementation of the standard activation dynamics [17] was used for simulations. A lattice was orthogonal with occupancy of each cell equal to zero or one. In the model, anisotropy is included by means of distinguished directions perpendicular ($\perp$) and parallel ($\parallel$) with respect to orientation of 1D islands, respectively. Rates $\nu_{\perp,\parallel}$ of hopping processes were calculated using equation

$$\nu_{\perp,\parallel} = \nu_0 \exp\left(\frac{-E_{\perp,\parallel}}{kT}\right), \tag{1}$$

where ν_0 is the frequency prefactor, k is the Boltzmann constant, and T is the temperature. Activation energies for jumps in both directions are calculated at each position occupied by an adatom with respect to the nearest neighbors (NN),

$$E_{\perp,\parallel} = E^0_{\perp,\parallel} + N_{\parallel}E_{attr} - N_{\perp}E_{rep} + N_{D\parallel}E_{attrD}, \tag{2}$$

where $E^0_{\perp,\parallel}$ is the energy barrier for a jump of an isolated atom in the direction perpendicular or parallel to island orientation, respectively; $N_{\perp,\parallel}$ is number of NN in perpendicular and parallel direction, respectively; E_{attr} is the attractive energy of a bond within a 1D island; E_{rep} is the repulsion energy in positions along islands; $N_{D\parallel}$ is a number of NN reactive defects in the parallel direction and finally E_{attrD} is the bonding energy between a defect and adatom. A similar model [except for the last term in Eq. (2)] was previously used for simulations on the defect-free lattice [10].

One-dimensional islands composed of group III metals are not formed in the nearest neighborhood in $\perp$ direction, but are separated at least by a distance of $2a$, where a =0.384 nm is surface unit cell spacing. This can be explained by lack of dangling bonds on the sites neighboring to the positions occupied by an island. There are two possible ways how to include this feature easily into a model. First, by means of prohibited zones, which exclude $NN_{\perp}$ positions along 1D islands from diffusion pathways. Diffusion restricted by the prohibited zones and by strong anisotropy is schematically illustrated in Fig. 1. Second possibility is to decrease dramatically adatom lifetime at the $NN_{\perp}$ sites, which practically excludes nucleation of islands with spacing $1a$. Observation of adsorbate dynamics on In deposited Si(100)2×1 surface at regime close to saturation coverage (0.5 ML) indicates that mobile adatoms can overcome occupied and prohibited zones [15]. So far there is no experimental evidence of a real mechanism at low coverage available. Therefore, we tested both suggested possibilities.

In all presented kMC results, we used deposition parameters close to the values typically used in experiments: 0.08 ML of atoms were deposited with rate 0.002 ML s^{-1}. Temperature was set to 300 K. A frequency prefactor value of 10^{13} s^{-1} was used. Array of 512×512 positions with periodic boundary conditions was used for calculation. If necessary (small volume of statistical data in case of large island growth), averaging over several runs was performed.

III. RESULTS AND DISCUSSION

A. Irreversible growth with anisotropic diffusion

1. Model without prohibited zones

Figure 2(a) (squares) shows the island size distribution simulated by the kMC model with highly anisotropic diffusion parameters ($E_{\parallel}$=0.4 eV and $E_{\perp}$=0.81 eV for comparison to Ref. [3]) and without reactive defects. Irreversibility is assured by setting E_{attr} to a high value, so that no decay of islands takes place during simulation. Repulsion energy was set E_{rep}=0.8 eV. The distribution is monomodal as usual in a standard irreversible growth by aggregation of diffusing adatoms [16,17]. The corresponding concentration of islands is $N=\Sigma N(s)$=0.0024 ML where $N(s)$ is concentration of islands with a size of s. A change in the distribution when reactive defects are placed on the surface prior to deposition of adatoms is shown in Fig. 2(b) and 2(c). In Fig. 2(b), defect concentration (defined as ratio of number of defects and number of available sites) is 0.0025 ML, which is comparable to the island concentration N after deposition of the same coverage on the surface without defects; in Fig. 2(c) the defect concentration is doubled, 0.005 ML. The defect concentration of 0.0025 ML [Fig. 2(b)] results in a significant change in the island size distribution—number of small islands increases and the distribution is monotonically decreasing. With increasing concentration of defects the distribution decreases more steeply with s and at a value of 0.005 ML becomes exponential [dashed line in Fig. 2(c)]. The Fig. 2 shows that monotonicity of the size distribution can be reached as result of presence of reactive defects without introducing prohibited zones to the model.

This finding is opposite to the result of Ref. [13], in which it is argued that defects could not be responsible for monotonicity of size distribution. The main reasons mentioned in

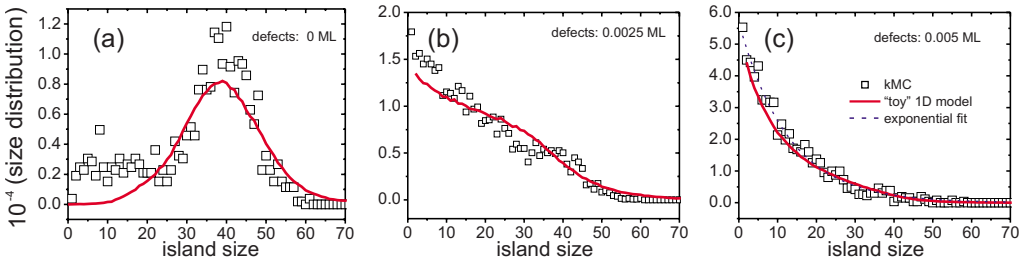

FIG. 2. (Color online) Island size distributions obtained by kMC simulation using the anisotropic irreversible model without prohibited zones (squares) and by a simple 1D "toy" model (solid lines). Concentration of reactive defects on the surface is 0 (a), 0.0025 (b), and 0.005 ML (c). With increasing defect concentration, the distribution changes from monomodal to exponentially decreasing. The exponential fit is shown in (c) by dashed line.

[13] are: (i) at observed concentration of the defects (0.003 ML) just about half of islands nucleated on the defects, which makes the effect significant but not dominant; (ii) a strong influence of defects is limited to islands with weak bonding between adatoms; (iii) if the defects represent nucleation sites, island size distribution would reflect the size distribution of corresponding capture zones, which is monomodal. Next we discuss all points listed above in the view of our results. (i) At defect coverage of 0.0025 ML (see Fig. 3), island density is 0.0044 ML, of which 0.0024 ML (0.0020 ML) are terminated (not terminated) by defects. It means that ~55% of islands are nucleated on defects, the rest is "self-nucleation," which is comparable to [13]. Yet, the distribution is monotonically decreasing, as shown in Fig. 2(b). A model explaining the calculated distribution is discussed below. (ii) Even in the case of irreversible growth (Fig. 2) the distribution becomes monotonically decreasing upon introducing defects. Fast diffusion (in one direction) compared to deposition rate allows adatoms to find reactive defects in amount sufficient for qualitative change in the distribution function. (iii) The size (area) distribution of capture zones of randomly deposited defects on the surface is monomodal in the two-dimensional case. However, in a strongly anisotropical system (as the studied one) the capture zones are rather one-dimensional. Then, the size (length) distribution of the capture zones is exponentially decreasing, as we further discuss in this section.

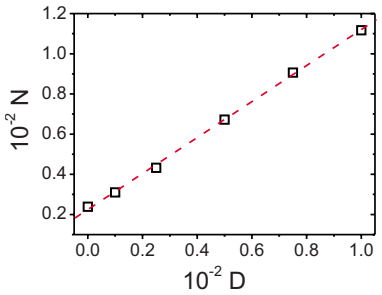

FIG. 3. (Color online) Dependence of concentration of islands on concentration of reactive defects (squares). Dashed line is a linear fit. Data obtained from kMC simulations using an anisotropic irreversible model without prohibited zones.

Growth with nucleation on defects is in a way analogical to growth with nuclei created by irreversible reaction with atoms of the substrate [24]. In that case, defect concentration (probability of finding a defect) is replaced by probability of the reaction with a substrate atom. The important difference is that number of defects available is decreasing during the growth, while number of sites available to the reaction with substrate atoms [24] is almost constant in the low coverage regime. In both cases, the size distribution is monotonically decreasing.

The concentration of islands N depends linearly on concentration of defects D, as shown in Fig. 3 (squares). A slope of the linear fit (dashed line) is 0.9 and in the studied regime about 90% of defects are occupied by islands independently on defect concentration.

Furthermore, we discuss in detail a reason of a change in the island size distribution in case of surface with defects [Figs. 2(a)–2(c)]. The activation energies used in the above simulation correspond to strongly anisotropic diffusion. A degree of the anisotropy can be defined as a ratio of the relative jump rates in parallel and perpendicular directions, respectively, $R_{\parallel}/R_{\perp}=\exp[(E_{\perp}-E_{\parallel})/\mathrm{kT}]\approx 8\times 10^{6}$ at room temperature. Considering a free isolated adatom, the corresponding average diffusion distance (parallel with islands) between two consecutive jumps in the perpendicular direction would be $\sqrt{R_{\parallel}/R_{\perp}}\approx 3000$ positions, which is comparable to a common width of a terrace on real surfaces experimentally observed. We assume that due to the high anisotropy, the two-dimensional surface can be reduced to a one-dimensional representation: 1D array of sites which can be empty or occupied either by an adatom or by a defect. To mimic the C-type defects on Si(100) surface, one side of each defect is randomly selected as reactive and the opposite one as inert [23]. Random deposition of the defects divides the 1D array into "boxes" separated by the defects. From the basic probability theory, distribution of the box length b is $\lambda \exp(-\lambda b)$, where λ is the number of boxes per unit length. Adatoms impinging to such a box cannot escape. Assume that all atoms deposited to a particular box aggregate and form an island (we call such case the limit of fast diffusion). Then, a size of the island formed in the box is proportional to the length of the box, because on average $F\times b$ atoms impinge into the box of length b, where F is the deposition flux. Finally, the island size distribution is proportional to the ini-

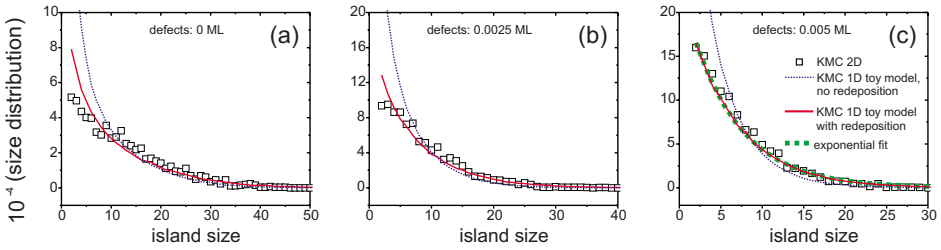

FIG. 4. (Color online) Island size distributions obtained by kMC simulation using anisotropic irreversible model with prohibited zones (squares), compared to results of 1D "toy model" (dotted lines) and to 1D "toy" model using redeposition of adatoms (solid lines). Concentration of reactive defects on the surface is 0 (a), 0.0025 (b), and 0.005 ML (c). Slope of the distribution increases with concentration of the defects. Exponential fit is shown in (c) by dashed line.

tial distribution of box length, i.e., exponentially decaying.

In order to test a validity of the used simplification—restriction to 1D model and the limit of fast diffusion—we used a simple "toy" Monte Carlo model. Initially, the surface is represented by a 1D array of sites onto which defects are randomly distributed. During growth, the only parameter representing diffusion is a length of 1D capture zone l_C—all atoms deposited into the zone (within the distance l_C from a reactive defect or island) are trapped by this reactive site. In more detail, the following steps are repeated: (i) an adatom is randomly deposited, (ii) if there is a reactive defect or island in a distance $l<l_C$ from the deposited adatom, the adatom attaches to the nearest of such positions, otherwise, a new island of size 1 is established. The simulation terminates when desired coverage θ is reached. The results of the "toy" simulations (obtained with fitted value of $l_C=460$) are compared to kMC "exact" simulations in Figs. 2(a)–2(c) (solid lines). A very good agreement demonstrates that the simplifications used in the "toy" model are justified for the studied case. Figure 2(b) represents a critical situation when l_C is comparable to average spacing between neighboring defects D^{-1}, where D is the concentration of defects. If $l_C \gg D^{-1}$ [Fig. 2(c)], all adatoms deposited into a box surrounded by two defects belong to the same capture zone and create a single island. Thus, the limit of infinite diffusion is reached by the defect concentration even if ratio of hopping rate and deposition flux is finite.

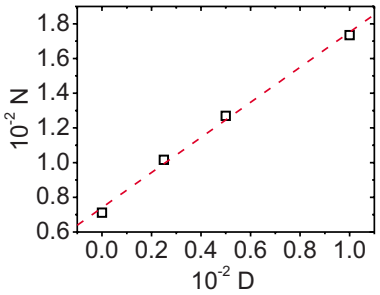

FIG. 5. (Color online) Dependence of concentration of island on concentration of reactive defects (squares). Dashed line is a linear fit. Results of kMC simulation using anisotropic irreversible model with prohibited zones.

2. Model with prohibited zones

The monotonically decreasing size distribution of Ga islands was previously obtained as a result of a model with strongly anisotropic diffusion in combination with prohibited zones [3]. Albao *et al.* obtained a good agreement with their experimental data for diffusion barriers $E_{\parallel}=0.4$ eV and $E_{\perp}=0.81$ eV (for parallel and perpendicular diffusion, respectively). Concentration of diffusing (free) atoms in such a case is high and nucleation of new islands is enhanced.

Figure 4 (squares) shows the influence of increasing defect concentration, as calculated by the kMC model, after introducing prohibited zones [3]. All parameters are set the same as used to calculate data shown in Fig. 2. Compared to the model without prohibited zones (Fig. 2), a higher amount of smaller islands is formed. Due to the adatom repulsion from the prohibited zones (marked by arrows in Fig. 1) attachment of adatoms is limited. Considering the anisotropic diffusion, deposited adatoms can be trapped in a gap between two prohibited zones (marked by asterisk in Fig. 1). The trapped atom cannot attach to any of the existing islands until it jumps in perpendicular direction (which is a rare event due to the large diffusion barrier in this direction) or another atom is randomly deposited to the gap. The resultant island concentration N is shown in Fig. 5 (squares) as a function of defect concentration. The dependence is linear (dashed line) with slope close to 1.0.

In the kMC model described above, there are two zones prohibited for diffusing atoms along each 1D island (the prohibited zones are marked by the crosses in Fig. 1). The zones can be effectively introduced to the "toy" 1D model by generating two zones per a new nucleated island at random positions within the 1D array (see the process marked "A" in Fig. 6 for illustration). Results of such simulations are shown

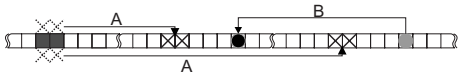

FIG. 6. Schematic illustration of processes used in the "toy" 1D model. Arrow marked "A"—formation of prohibited zones (crosses) at random positions when new island nucleates. Dotted crosses show positions where the prohibited zones would appear in a 2D model. Arrow marked "B"—random redeposition of adatom (ball) simulating jumps between adjacent rows.

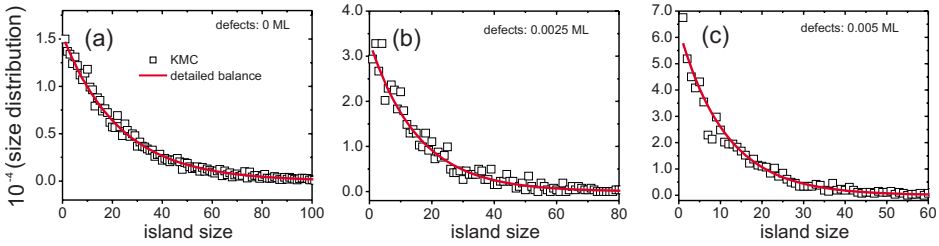

FIG. 7. (Color online) Island size distributions obtained by kMC simulation using the close-to-equilibrium model (squares), compared to analytical solution (solid lines). Concentration of reactive defects on the surface is 0 (a), 0.0025 (b), and 0.005 ML (c).

in Fig. 4 (dotted line), the agreement is not very good. An explanation is that the 1D simplification fails when prohibited zones are introduced—jumps of adatoms trapped between two prohibited zones take place even if time constant of such a process is high (≈ 4 s when $E_{\perp}=0.81$ eV). Such escape jumps can be effectively modeled by random redeposition (removing and depositing again) of an adatom, as schematically illustrated in Fig. 6 by the arrow "B." Indeed, after introducing the random escape with a time constant of 4 s to the "toy" model, a better agreement with kMC is obtained (Fig. 4, solid lines). The agreement confirms that low rate processes can be introduced to the toy model without need of "exact" hopping event-based kMC simulation, which usually requires significant computational time, especially in the case of highly diffusive atoms.

B. Close-to-equilibrium model

In this section, we consider systems with decaying islands growing on the substrate by means of reversible processes. If allowed to relax sufficiently long time, a morphology does not depend on preparation condition (deposition rate). For atoms of group III elements deposited on Si(100) decay of islands at room temperature was reported in the case of In [4,23] and Tl [1,2]. On a perfect substrate, monotonically decreasing size distribution was reported as a result of thermal equilibrium reached by reversible processes [8,10]. In case of the equilibrium, all competing processes are in balance and the island size distribution can be derived analytically with a good approximation for low coverages (≤ 0.1 ML). A detailed balance condition gives

$$N(s+1)\nu_{DET} = N(1)N(s)\nu_{ATT}, \tag{3}$$

where $N(s)$ is the number of islands of size s, ν_{DET} is the detachment rate and ν_{ATT} is the attachment rate, i.e., the rate of jumps to a position where atom is bonded to an island. The left side of Eq. (3) represents decay rate of islands of size $s+1$ and the right side represents growth rate of islands of size $s+1$ by means of attachment of diffusing adatom to islands of size s. The condition of detailed balance results in expression for the distribution $N(s)$

$$N(s) = N(1)\left[N(1)\frac{\nu_{ATT}}{\nu_{DET}}\right]^{(s-1)} = \frac{\nu_{DET}}{\nu_{ATT}}\exp\left[s \times \ln\left(N(1)\frac{\nu_{ATT}}{\nu_{DET}}\right)\right]. \tag{4}$$

From a normalization condition $\Sigma sN(s)=\theta$, where θ is the coverage, $N(1)$ can be calculated,

$$N(1) = [\alpha + 1 - \sqrt{2\alpha+1}]/(\alpha\nu_{ATT}/\nu_{DET}), \tag{5}$$

where $\alpha = 2\theta\nu_{ATT}/\nu_{DET}$. Evidently, the distribution $N(s)$ is always monotonically decreasing in the case of thermal equilibrium.

It should be noted that the distribution $N(s)$ depends for given θ only on the ratio ν_{ATT}/ν_{DET}. The rates ν_{ATT} and ν_{DET} can be calculated using Eq. (1) with activation energies for diffusion (E_{dif}) and atom detachment ($E_{det}=E_{dif}+E_{attr}$), respectively. For the identical frequency prefactors of both thermally activated processes, we obtain $\nu_{ATT}/\nu_{DET} = \exp[(E_{det}-E_{dif})/kT] = \exp[E_{attr}/kT]$. In the other words, the distribution $N(s)$ depends only on bonding energy between the nearest neighbors in the 1D island. Thus, diffusion parameters of free adatoms (hopping rates) do not influence the distribution of island size, once equilibrium is reached (but the time of establishing the equilibrium depends of course on the diffusion parameters). This is in agreement with results derived from thermodynamical consideration of the relaxing system previously [10].

In Fig. 7(a), kMC results are compared to an analytical solution of Eq. (4). In the kMC simulation, the activation energies were calculated using Eq. (2). Energy of NN atom interaction within an island was set to $E_{attr}=E_{det}-E_{dif} = 0.22$ eV in both cases, the same as the value used in Refs. [8,10]. Values of diffusion parameters $E_{\parallel}=0.64$ eV and $E_{\perp} = 0.62$ eV were taken from Ref. [8] and deposited islands were allowed to relax 3 h after deposition at room temperature. A good agreement of kMC and analytical distributions confirms that the simulated morphologies are close to the thermal equilibrium.

Next, we focus on influence of reactive defects on the distribution in the thermal equilibrium. Figures 7(b) and 7(c) show kMC results for different concentrations of defects, 0.0025 (b) and 0.005 ML (c). The monotonically decreasing character is preserved, slope of the distribution is steeper in the case of higher defect concentration. Resulting dependence of island density N on defect concentration is linear with slope 0.65, as shown in Fig. 8.

The balance condition [Eq. (3)] can be modified for a system with the defects. The distribution is divided into two parts corresponding to a population of islands pinned by defects, $N_d(s)$, and nonpinned islands, $N_n(s)$, respectively. The detailed balance condition is expressed by equations

$$N_n(s+1)\nu_{DET} = N_n(1)N_n(s)\nu_{ATT}, \tag{6}$$

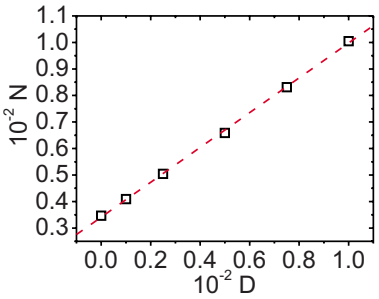

FIG. 8. (Color online) Island concentration as function of concentration of reactive defects simulated by kMC simulation using the close-to-equilibrium model (squares). Dashed line is a linear fit.

$$N_d(1)\nu_{2DET} = N_n(1)N_{\text{free}D}\nu_{ATT}, \tag{7}$$

$$N_d(s+1)\nu_{DET} = N_n(1)N_d(s)\nu_{ATT}, \tag{8}$$

where ν_{2DET} is the detachment rate of an adatom from a defect, and N_{freeD} is the concentration of defects not occupied by islands. Normalization conditions are $\Sigma sN_n(s) + \Sigma sN_d(s) = \theta$, and $D = \Sigma N_d(s) + N_{freeD}$, where D is the defect concentration. Resulting distributions for both N_n and N_d are again exponentially decaying for $N_d \geq 2$. The distributions $N_n(s) + N_d(s)$ calculated for different defect concentrations are compared to kMC simulations in Figs. 7(b) and 7(c).

In our kMC simulations, we use a high value of interaction energy between a defect and an island, in agreement with experiment and ab-initio calculation [23]. In such case, $\nu_{2DET} \to 0$ and all defects become occupied by islands in equilibrium, $N_{freeD} = 0$. We note that for higher defect concentrations ($\sim$0.01 ML), some of the defects ($\sim$10%) randomly placed on 2D lattice are so close to each other that some of pinned islands would grow in unfavored proximity with spacing of a in the $\perp$ direction. Therefore, number of "active" defects is then lower than D.

It is interesting to mention that distributions obtained for surface with $\geq$0.005 ML of reactive defects are in fact the same in the case of irreversible anisotropic aggregation [Fig. 2(c)] and in the case of the equilibrium system [Fig. 7(c)]. The presence of the reactive defects may suppress differences between results of the different models. It demonstrates a need of a careful interpretation of experimental data obtained for growth at presence of surface defects. For the correct interpretation, experimental data additional to island size distribution are required, e.g., size fluctuation of selected islands.

IV. CONCLUSION

Two different models of 1D island growth were used to study an influence of reactive defects on size distribution of islands—the irreversible model with anisotropic diffusion and the equilibrium model with balance between attachment and detachment of atoms. In the case of the irreversible model, a nontrivial single-parameter simplification to 1D model with capture zones was applied, sufficiently reproducing "exact" results of kMC simulation. If average defect spacing is smaller than size of the capture zone ($\sim 5 \times 10^2$ in the studied case), the growth becomes controlled by the defect concentration only. The distribution of island size changed from monomodal to monotonically decreasing at concentration of defects comparable to density of islands on the surface without defects (0.0025 ML of defects for deposited amount 0.08 ML). In the case of the equilibrium model, we derived an analytical solution of island size distribution taking into account preferred nucleation on defects. Independently on defect concentration, the distribution is exponential. At a defect concentration of 0.005 ML, irreversible and equilibrium models give a similar island size distributions, depending only on amount of atoms and defects deposited on the surface.

ACKNOWLEDGMENTS

This work is a part of the research plan Grant No. MSM 0021620834 that is financed by the Ministry of Education of the Czech Republic and was partly supported by Project No. 100907 of GAUK.

[1] M. Kishida, A. Saranin, A. Zotov, V. Kotlyar, A. Nishida, Y. Murata, H. Okado, M. Katayama, and K. Oura, Appl. Surf. Sci. **237**, 110 (2004).
[2] A. A. Saranin *et al.*, Phys. Rev. B **71**, 035312 (2005).
[3] M. A. Albao, M. M. R. Evans, J. Nogami, D. Zorn, M. S. Gordon, and J. W. Evans, Phys. Rev. B **72**, 035426 (2005).
[4] P. Kocán, P. Sobotík, I. Ošt'ádal, J. Javorský, and M. Setvín, Surf. Sci. **601**, 4506 (2007).
[5] P. Gambardella, M. Blanc, H. Brune, K. Kuhnke, and K. Kern, Phys. Rev. B **61**, 2254 (2000).
[6] P. Gambardella, M. Blanc, L. Bürgi, K. Kuhnke, and K. Kern, Surf. Sci. **449**, 93 (2000).
[7] P. Gambardella, H. Brune, K. Kern, and V. I. Marchenko, Phys. Rev. B **73**, 245425 (2006).
[8] J. Javorský, M. Setvín, I. Ošt'ádal, P. Sobotík, and M. Kotrla, Phys. Rev. B **79**, 165424 (2009).
[9] V. I. Tokar and H. Dreyssé, Phys. Rev. E **68**, 011601 (2003).
[10] V. I. Tokar and H. Dreyssé, Phys. Rev. B **74**, 115414 (2006).
[11] R. B. Stinchcombe and F. D. A. Aarão Reis, Phys. Rev. B **77**, 035406 (2008).
[12] S. Jun, H. Zhang, and J. Bechhoefer, Phys. Rev. E **71**, 011908 (2005).
[13] M. A. Albao, M. M. R. Evans, J. Nogami, D. Zorn, M. S. Gordon, and J. W. Evans, Phys. Rev. B **74**, 037402 (2006).
[14] G. Brocks, P. J. Kelly, and R. Car, Phys. Rev. Lett. **70**, 2786 (1993).
[15] I. Ošt'ádal, J. Javorský, P. Kocán, P. Sobotík, and M. Setvín, J. Phys.: Conf. Ser. **100**, 072006 (2008).

[16] M. C. Bartelt and J. W. Evans, Phys. Rev. B **46**, 12675 (1992).
[17] C. Ratsch and J. A. Venables, J. Vac. Sci. Technol. A **21**, S96 (2003).
[18] F. Slanina and M. Kotrla, Physica A **256**, 1 (1998).
[19] M. Z. Hossain, Y. Yamashita, K. Mukai, and J. Yoshinobu, Phys. Rev. B **67**, 153307 (2003).
[20] S. Okano and A. Oshiyama, Surf. Sci. **554**, 272 (2004).
[21] S.-Y. Yu, H. Kim, and J.-Y. Koo, Phys. Rev. Lett. **100**, 036107 (2008).
[22] P. Kocán, P. Sobotík, and I. Ošt'ádal, Phys. Rev. B **74**, 037401 (2006).
[23] P. Kocán, L. Jurczyszyn, P. Sobotík, and I. Ošt'ádal, Phys. Rev. B **77**, 113301 (2008).
[24] D. D. Chambliss and K. E. Johnson, Phys. Rev. B **50**, 5012 (1994).

3. Růst silicidu manganu na povrchu Si(111)

3.1 MnSi - bulk vs. epitaxní růst Si(111)

Naší motivací pro studium růstu tenkých vrstev MnSi na povrchu Si(111) byl především jejich zajímavý aplikační potenciál. Na základě teoretických výpočtů bylo totiž předpovězeno [1] feromagnetické uspořádání spinů v tenké vrstvě MnSi na povrchu Si(111). Dále byla předpovězena polarizace spinů na Fermiho hladině, což by v principu umožnilo využití této vrstvy jako spin injektující materiál, navíc konzistentní s technologiemi na bázi křemíku.

Objemový monosilicid manganu (MnSi) je feromagnetická látka se strukturou B20, což je i struktura silicidů jiných přechodových kovů (FeSi, CoSi, CrSi). Struktura B20 je odvozena od struktury kamenné soli, v každé elementární buňce jsou čtyři Mn a čtyři Si atomy, posunuté podél směru [111]. Posunutí se projeví ztrátou inverzní symetrie, což má za následek spirální magnetickou strukturu pod teplotou $T_C = 29\,\mathrm{K}$ [2, 3].

Růst silnějších vrstev byl studován množstvím technik (např. transmisní elektronovou mikroskopií [4, 5, 6, 7], difrakcí pomalých elektronů [8], nebo elektronovými spektroskopiemi [8, 9]. Na povrchu Si(111) roste MnSi epitaxně, díky podobné velikosti $\sqrt{3}\times\sqrt{3}$ buňky na Si(111) a 1×1 buňky roviny MnSi(111) v B20 krystalické struktuře – rozdíl činí pouze 3.2%. Až při větším množství deponovaného Mn je preferován růst $MnSi_{1.7}$ [6].

Z hlediska porozumění růstových mechanismů je systém Si/MnSi příklad reaktivního systému, kdy se materiál substrátu podílí na růstu tenké vrstvy. Výsledná morfologie tudíž odráží i nutnost odleptání části podložky.

3.2 Hledání podmínek růstu optimální vrstvy MnSi

Pro případné využití vysokého stupně polarizace spinů v MnSi vrstvě je mimo jiné nezbytné zamezit rozptylu spinů na defektech rozhraní. V publikaci [10] je studována účinnost průniku spinově polarizovaných elektronů do povrchu GaAs. Detekcí fotonů vzniklých při rekombinaci elektronů bylo změřeno, že v blízkosti atomárních schodů je účinnost snížena $6\times$ a doba života spinu $12\times$. MnSi při

malých deponovaných množstvích má obecně tendenci růst na povrchu Si(111) ve formě oddělených krystalických ostrůvků s množstvím atomárních schodů, spíše než ve formě homogenní tenké vrstvy. Proto bylo třeba najít podmínky, kdy je tato tendence co nejvíce kineticky potlačena a výsledná vrstva a její rozhraní se substrátem obsahují minimum schodů a jiných defektů.

Prvním krokem bylo na základě intenzity LEED difraktogramů najít podmínky (depozice a teplota podložky) pro co nejvyšší pokrytí povrchu silicidem manganu při zachování co nejnižší tloušťky vrstvy (publikace P10). Důležitým údajem je teplota, kdy se výrazně začíná tvořit epitaxní silicid. Na základě experimentů jsme tuto teplotu určili jako $\sim 200°C$. Pomocí Augerovy elektronové spektroskopie (AES) jsme potvrdili, že při teplotách 200-250°C dochází k reakci Mn a Si. Při teplotách vyšších než 250°C intenzita difrakce klesá, protože vznikají termodynamicky výhodnější 3D ostrůvky MnSi. Tato teplota byla tudíž označena jako optimální ve smyslu uspořádání silicidu. Za teploty 250°C bylo nalezeno optimální množství deponovaného Mn, první maximum intenzity difraktogramu odpovídá depozici 3 ML. STM měření potvrdilo, že při těchto podmínkách je již povrch zcela pokryt vrstvou MnSi a při vyšších deponovaných množstvích roste hrubost povrchu. Na základě analýzy STM jsme ukázali, že MnSi roste na Si(111) epitaxně s nejmenší vertikální jednotkou odpovídající čtyř-vrstvě (quadruple layer, QL) struktury B20. Vrstvy s tloušťkou pouze jedné QL však na povrchu pozorovány nebyly, nejtenčí vrstvy odpovídaly dvěma a více QL. I při plném pokrytí povrchu Si(111) epitaxním MnSi po depozici 3 ML a 30 min ohřevu na 250 °C je však na povrchu množství oblastí lišících se výškou, oddělených schody o výšce odpovídající násobkům QL. Důvodem je narušení rozhraní Si-MnSi způsobené nutností dodat atomy Si pro růst silicidu. STM morfologie naznačují, že pro růst silicidu je zcela použita vrchní dvojvrstva Si(111). Křemík zakrytý vrstvou silicidu je ochráněn před reakcí, proto je zbylá ~ 1 ML materiálu ze substrátu poskytnuta za cenu tvorby hlubokých kráterů.

3.3 Monte Carlo model růstu

Pro lepší pochopení vlivu úbytku Si z podložky na tvar MnSi vrstvy jsme použili – v souladu se strategií obhajovanou napříč touto prací – Monte Carlo simulace. Proces růstu silicidu manganu je poměrně komplexní - atomy křemíku jsou odpojovány z různých vazebných pozic, k odpojení navíc může docházet interakcí s atomy Mn, atomy obou prvků migrují po nehomogenním povrchu, složitým způsobem krystalizují ve formě silicidu s B20 strukturou. Pro potřeby simulací by-

lo proto nezbytné výrazně zjednodušit problém se zachováním pouze důležitých vlastností. Následující model je popsán v Publikaci P11. Tři typy přítomných struktur jsou rozlišeny na základě koncentrace Mn a Si:

1. Si(111) - koncentrace 2 ML Si,
2. Si(111)7×7 - koncentrace 2.08 ML Si,
3. MnSi - koncentrace 4/3 ML Mn a 4/3 ML Si.

Nejmenší uvažovaná jednotka povrchu má velikost půlky $\sqrt{3}\times\sqrt{3}$ cely a výšku jedné QL v případě MnSi a jedné dvojvrstvy v případě Si krystalu. Difuze jednotlivých atomů není zahrnuta, uvažujeme případ limitně rychlé difuze. Během simulace je neustále zachováváno deponované množství obou prvků - přebytečný materiál přebývající po vybraném procesu tvoří na povrchu „rezervoár“, dále použitelný v jiných reakcích. V první růstové fázi jsou uvažovány tři procesy:

1. růst MnSi cely místo Si,
2. růst MnSi na povrchu již vytvořeného MnSi,
3. rozpuštění cely Si do rezervoáru.

V druhé, rekrystalizační fázi, je uvažována relaxace systému opakováním kroků:

1. rozpuštění MnSi cely,
2. vytvoření nové MnSi cely na náhodně zvolené pozici.

Pravděpodobnost rozpuštění konkrétní jednotky Si nebo MnSi je definována množstvím sousedů.

I přes zásadní zjednodušení oproti reálnému modelu byla získána velmi dobrá shoda simulovaných morfologií s experimentálními daty (Publikace P10), a to s použitím minimálního množství parametrů. Nejvýznamnějším závěrem simulací byl fakt, že je-li model správný, nelze docílit homogenní vrstvy MnSi bez dodání Si z vnějšího zdroje.

3.4 Růst MnSi při současné depozici Mn a Si

Z výsledků předchozí kapitoly je zřejmé, že s využitím pouze materiálu podložky coby zdroje atomů Si nelze dosáhnout ideálně homogenní vrstvy MnSi na povrchu Si(111). I po depozici 8/3 ML Mn, odpovídajícím ideální vrstvě dvou QL MnSi, je potřeba stejné množství atomů Si ze substrátu. Vrchní dvojvrstva s rekonstrukcí

7×7 poskytne 2.08 ML, zbylých 0.59 ML je poskytnuto za cenu vzniku kráterů. V literatuře lze nalézt zmínky o zlepšení kvality LEED difraktogramů současnou depozicí Mn a Si [11], příp. Fe a Si [12].

V Publikaci P12 je ukázáno, že při vhodném množství obou materiálů lze připravit vrstvu s minimem defektů. Ideálním se ukázal být následují postup: nejdříve deponovat 1.5 ML Si, poté 3 ML Mn a nakonec opět 1.5 ML Si, s následným ohřevem na 250 °C. Morfologie výsledné vrstvy pozorovaná pomocí STM vykazuje homogenní koherentní strukturu na škále stovek nm s malým množstvím děr, které jsou pravděpodobně pouze důsledkem malé odchylky od optimálního deponovaného množství. Na základě uvedených faktů lze předpokládat, že využití tenkých MnSi vrstev coby materiálu injektujícího spinově polarizované elektrony je možné.

3.5 Navazující práce

Jak je patrné z předchozího textu, možnost aplikace systému Si-MnSi je zásadně spojena s morfologií těchto vrstev. Proto byla tato morfologie dále studována v širším rozsahu pokrytí a teplot [13, 14, 15, 16, 17] s ohledem na strukturu rozhraní MnSi-vakuum [13, 14, 15], hrubnutí povrchu s teplotou [16] a fraktální charakter MnSi ostrůvků [17]. V rámci těchto prací byly potvrzeny a dále doplněny výsledky publikací P10-P12.

Důležitou podmínkou pro další uplatnění MnSi je však experimentální ověření magnetických vlastností předpovězených teoreticky [1]. Pomocí magneto-optického Kerrova jevu (MOKE) byly měřeny magnetické vlastnosti systému Si-MnSi-Si [18]. Práce ukázala, že magnetické vlastnosti souvisí s vyrovnáváním pnutí během růstu silicidu. Shodný závěr má i teoreticky zaměřená práce [19] studující závislost magnetických vlastností silicidů přechodových kovů na pnutí, a tedy na tloušťce vrstvy. V ideálním případě byl pozorován trend zvýšení Curieovy teploty T_C oproti objemovému MnSi z 29 K na 40 K. Mnohem vyšší $T_C \sim 300$ K změřili Magnano a spol. pomocí supravodivé kvantové interference (SQUID) na vrstvách MnSi chráněných před oxidací vrstvou stříbra [20]. Je možné, že vysoká hodnota T_C je způsobena právě rozhraním MnSi-Ag.

Je třeba poznamenat, že experimenty zaměřené na magnetické vlastnosti Mn-Si vrstev na Si(111) povrchu byly dosud omezeny na vrstvy silnější, než jaké byly na základě našich pozorování určeny jako ideální pro potenciální spintronické využití. Důvodem je především komplikovanost experimentů v případě velmi tenkých vrstev.

Literatura

[1] M. Hortamani, P. Kratzer, and M. Scheffler, "Density-functional study of Mn monosilicide on the Si(111) surface: Film formation versus island nucleation," *Phys. Rev. B*, vol. 76, p. 235426, Dec. 2007.

[2] Y. Ishikawa, K. Tajima, D. Bloch, and M. Roth, "Helical spin structure in manganese silicide," *Solid State Commun.*, vol. 19, no. 6, pp. 525 – 528, 1976.

[3] T. Moriya, "Temperature-induced local magnetic moment in narrow band electron systems," *Solid State Commun.*, vol. 26, no. 8, pp. 483 – 486, 1978.

[4] Q. Zhang, M. Takeguchi, M. Tanaka, and K. Furuya, "Structural observation of Mn silicide islands on Si (111)7x7 surface with UHV-TEM," *J. of Cryst. Growth*, vol. 239, pp. 1956–1960, 2002.

[5] Q. Zhang, M. Tanaka, M. Takeguchi, and K. Furuya, "Analytical UHV transmission electron microscopy studies of electronic structure changes between as-deposited Mn and Mn silicide on Si(111) surface," *Surf. Sci.*, vol. 507-510, pp. 453–457, June 2002.

[6] M. Tanaka, Q. Zhang, M. Takeguchi, and K. Furuya, "In situ characterization of Mn and Fe silicide islands on silicon," *Surf. Sci.*, vol. 532-535, pp. 946–951, June 2003.

[7] K. Schwinge, C. Müller, a. Mogilatenko, J. J. Paggel, and P. Fumagalli, "Structure and magneto-optic Kerr measurements of epitaxial MnSi films on Si(111)," *J. of Appl. Phys.*, vol. 97, no. 10, p. 103913, 2005.

[8] S. Shivaprasad, C. Anandan, and S. Azatyan, "The formation of MnSi (111) interface at room and high temperatures," *Surf. Sci.*, vol. 382, pp. 258–265, 1997.

[9] E. Carleschi, E. Magnano, M. Zangrando, F. Bondino, a. Nicolaou, F. Carbone, D. Van der Marel, and F. Parmigiani, "Manganese silicide single crystal and films deposited on Si(111): A comparative spectroscopic study," *Surf. Sci.*, vol. 601, pp. 4066–4073, Sept. 2007.

[10] V. P. LaBella, D. W. Bullock, Z. Ding, C. Emery, A. Venkatesan, W. F. Oliver, G. J. Salamo, P. M. Thibado, and M. Mortazavi, "Spatially resolved spin-injection probability for gallium arsenide.," *Science*, vol. 292, pp. 1518–21, May 2001.

[11] E. Magnano, E. Carleschi, a. Nicolaou, T. Pardini, M. Zangrando, and F. Parmigiani, "Growth of manganese silicide films by co-deposition of Mn and Si on Si(111): A spectroscopic and morphological investigation," *Surf. Sci.*, vol. 600, pp. 3932–3937, Sept. 2006.

[12] U. Starke, W. Weiss, M. Kutschera, R. Bandorf, and K. Heinz, "High quality iron silicide films by simultaneous deposition of iron and silicon on Si(111)," *J. of Appl. Phys.*, vol. 91, no. 9, p. 6154, 2002.

[13] J. Hirvonen Grytzelius, H. M. Zhang, and L. S. O. Johansson, "Coverage dependence and surface atomic structure of Mn/Si(111)-v3xv3 studied by scanning tunneling microscopy and spectroscopy," *Phys. Rev. B*, vol. 80, p. 235324, Dec. 2009.

[14] S. Azatyan, O. Utas, N. Denisov, a.V. Zotov, and a.a. Saranin, "Variable termination of MnSi/Si(111) films and its effect on surface properties," *Surf. Sci.*, vol. 605, pp. 289–295, Feb. 2011.

[15] B. Geisler, P. Kratzer, T. Suzuki, T. Lutz, G. Costantini, and K. Kern, "Growth mode and atomic structure of MnSi thin films on Si(111)," *Phys. Rev. B*, vol. 86, p. 115428, Sept. 2012.

[16] Z.-Q. Zou, D. Wang, J.-J. Sun, and J.-M. Liang, "Scanning tunneling microscopy studies of the formation and coarsening of manganese silicides on Si(111)," *J. Appl. Phys.*, vol. 107, no. 1, p. 014302, 2010.

[17] Z.-q. Zou and W.-c. Li, "Two-dimensional fractal-like growth on semiconductors : The formation of continuous manganese monosilicide ultrathin films on Si (111)," *Phys. Lett. A*, vol. 375, no. 4, pp. 849–854, 2011.

[18] E. Karhu, S. Kahwaji, T. L. Monchesky, C. Parsons, M. D. Robertson, and C. Maunders, "Structure and magnetic properties of MnSi epitaxial thin films," *Phys. Rev. B*, vol. 82, p. 184417, Nov. 2010.

[19] B. Geisler and P. Kratzer, "Strain stabilization and thickness dependence of magnetism in epitaxial transition metal monosilicide thin films on Si(111)," *Phys. Rev. B*, vol. 88, p. 115433, Sept. 2013.

[20] E. Magnano, F. Bondino, C. Cepek, F. Parmigiani, and M. C. Mozzati, "Ferromagnetic and ordered MnSi(111) epitaxial layers," *Appl. Phys. Lett.*, vol. 96, no. 15, p. 152503, 2010.

APPLIED PHYSICS LETTERS **93**, 013104 (2008)

Epitaxially grown flat MnSi ultrathin film on Si(111)

Shougo Higashi,[1] Yuichi Ikedo,[1] Pavel Kocán,[1,2] and Hiroshi Tochihara[1,a)]
[1]*Department of Molecular and Material Sciences, Kyushu University, Kasuga, Fukuoka 816-8580, Japan*
[2]*Faculty of Mathematics and Physics, Department of Surface and Plasma Science, Charles University in Prague, V Holešovičkách 2, 180 00 Praha 8, Czech Republic*

(Received 28 March 2008; accepted 8 June 2008; published online 8 July 2008)

Flat MnSi ultrathin films are epitaxially grown on the Si(111)-(7×7) surface by Mn deposition and subsequent annealing. Low-energy electron diffraction exhbits the brightest $(\sqrt{3}\times\sqrt{3})$R30° patterns when Mn atoms are deposited at ~3 ML with subsequent annealing at 250 °C. Scanning tunneling microscopy shows that atomically flat MnSi(111) surfaces with the $(\sqrt{3}\times\sqrt{3})$R30° periodicity are formed under above condition, and that the thickness of the flat MnSi films is ~7 Å. The results support a recent theoretical prediction of flat-film formation of the *B*20-type MnSi on the Si(111) surface. © *2008 American Institute of Physics*. [DOI: 10.1063/1.2952495]

Recent density-functional-theory studies of Mn silicides formed on Si(001) and Si(111) have provided fruitful information on their structural and magnetic properties.[1–3] Especially, Mn silicides on Si(111) seem to have a great potential for future spintronics applications because of the tendency to flat-film formation. Hortamani *et al.*[3] showed that the *B*20 structure (bulk crystal structure, see Fig. 1 for a schematic structural model) of the Mn monosilicide, whose (111) plane coincides with the $(\sqrt{3}\times\sqrt{3})$R30° lattice of the Si(111) plane (hereafter $\sqrt{3}$-MnSi for simplicity) with a mismatch of 3.2%, is more stable than the pseudomorphic *B*2 (CsCl-type structure), and that ferromagnetic ordering is slightly more favorable than other magnetic structures at least for ultrathin films. It was also demonstrated that Mn atoms at the surface and interface possess large magnetic moments, and that they exhibit large spin polarization at the Fermi level.

Therefore, the flat $\sqrt{3}$-MnSi ultrathin film is a promising material for semiconductor-based spintronics. Experimental studies of the formation of the flat $\sqrt{3}$-MnSi thin film are required, but most studies reported so far on the formation of three dimensional islands[4–7] or on very initial processes[8–11] of Mn deposition on the Si(111)-(7×7) surface. At 1 ML; (1 ML=7.83×10^{14} atoms/cm^2) by using scanning tunneling microscopy (STM), Evans *et al.*[4] observed tabular islands with the $(\sqrt{3}\times\sqrt{3})$R30° termination interrupted by bare Si surface at annealing temperatures between 325 and 450 °C. Nagao *et al.* found such islands ranging up to several hundreds of angstroms with various heights depending on the annealing temperature.[5] Kumar *et al.* observed that with increasing coverage to 5 ML such islands almost close the bare Si surface at 400 °C, leading to patched films with various heights.[6]

In this letter, we demonstrate a recipe for the formation of an atomically flat $\sqrt{3}$-MnSi ultrathin film on the Si(111)-(7×7) surface by Mn deposition and subsequent annealing. We have studied the quality and features of the epitaxially grown films by means of STM and low-energy electron diffraction (LEED). As for the structure of the $\sqrt{3}$-MnSi, the *B*20 has been suggested by the theoretical work mentioned above[3] and several experimental studies.[6,12,13] We support that the epitaxially grown ultrathin films in the present study are the *B*20.

Experiments were carried out in two ultrahigh vacuum chambers. In both chambers base pressures are in a range of 10^{-11} Torr. Samples used in this experiment were Sb-doped Si(111) wafers of resistivity 0.005–0.01 Ω cm, and cleaned by flashing to 1200 °C by passing dc. Mn atoms were deposited from a Ta tube including pure Mn grains by resistive heating,[14] and the pressures during deposition were less than 3×10^{-10} Torr. In a LEED chamber, Mn deposition rate was calibrated by using a well-known structure of Cu(001)-*c*(2×2)-Mn.[14–16] In a STM chamber, LEED and STM are installed with a quartz thickness monitor. STM observation was carried out at room temperature (RT). In the LEED chamber Auger electron spectroscopy (AES) can be measured using four-grid LEED optics. LEED spot intensity was recorded with a computer-controlled intensified charge coupled device camera.[14] Sample temperatures were monitored by infrared pyrometers.

Mn deposition followed by annealing leads to the formation of the $\sqrt{3}$-MnSi on Si(111).[4–7] We have studied the change of LEED patterns as a function of the annealing temperature for 3 ML Mn deposited surfaces in the LEED chamber. The coverage of 3 ML was obtained from the calibration mentioned above. The intensity of (1/3 1/3) LEED spots is plotted against the annealing temperature 185–400 °C in Fig. 2(a). Annealing time was 5 min otherwise noted. In each measurement the sample was flashed to obtain fresh (7×7) clean surfaces, and then 3 ML Mn atoms were deposited under the same condition. In Fig. 2(a) the largest intensity was obtained after annealing at 250 °C, suggesting that the $\sqrt{3}$-MnSi structure is formed most extensively on the surface. It is interesting to note that the AES intensity of Mn (40 eV)

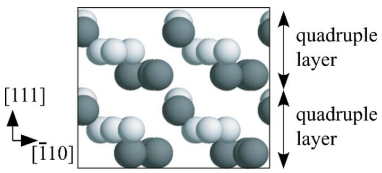

FIG. 1. (Color online) A schematic ball model of *B*20-type structure of MnSi. Small white balls represent Si atoms and large dark balls Mn atoms.

a)Electronic mail: tochihar@mm.kyushu-u.ac.jp.

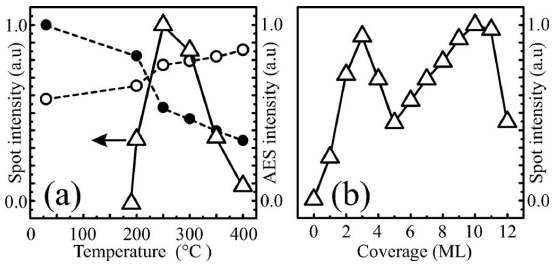

FIG. 2. (a) Intensity change of (1/3 1/3) spots as a function of annealing temperature (triangles). In addition, the AES intensity of Mn (40 eV, filled circles) and Si (92 eV, open circles) are plotted against annealing temperature. 3 ML Mn was deposited at RT. Incident electron energies for LEED and AES are 115 eV and 1 keV, respectively. (b) Intensity change of (1/3 1/3) spots at 115 eV as a function of Mn coverage. Samples were annealed at 250 °C for 5 min.

decreased steeply at temperatures between 200 and 250 °C, while that of Si (92 eV) considerably increased, as also shown in Fig. 2(a). The AES results suggest that vertical mass transfer between the substrate and Mn overlayers to create the $\sqrt{3}$-MnSi is accelerated considerably at 200–250 °C. In Fig. 2(b), the intensity of (1/3 1/3) spots is plotted against Mn coverage at the annealing temperature of 250 °C. At the coverage of 3 ML, the intensity exhibits a sharp maximum. It was confirmed in the STM chamber, and the thickness monitor gave a value of 2.8 ML at the maximum, being consistent with the calibration mentioned above. Therefore, it is sure that the $\sqrt{3}$-MnSi thin film grows most extensively at ~3 ML.

Thus, it is found that the deposition of ~3 ML and subsequent annealing at 250 °C is the most appropriate condition for the formation of the $\sqrt{3}$-MnSi thin film. Then, constant-height STM images of the films prepared under the above condition were taken, as shown in Fig. 3. Annealing time was 30 min to assure complete formation of the $\sqrt{3}$-MnSi thin film. The surface consists mostly of a flat layer. The main flat area (~80% of the surface) in Fig. 3 was assigned to the second layer (labeled 2) of the growing

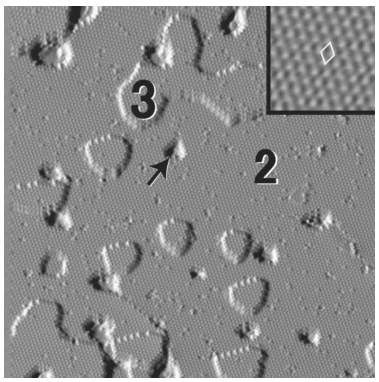

FIG. 3. Constant-height STM image of ~3 ML Mn deposited Si(111) surface after annealing at 250 °C for 30 min. Sample bias is −1.6 V and the size is 60×60 nm^2. Numbers 2 and 3 mark second and third level of MnSi film, respectively. An arrow points to a hole which is down to Si surface. The inset shows magnified STM image of 5×5 nm^2. Unit cell of the ($\sqrt{3}$ × $\sqrt{3}$)R30° is outlined.

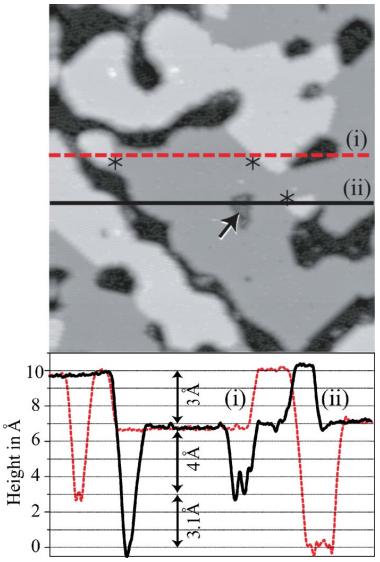

FIG. 4. (Color online) Constant-current STM image of ~2 ML Mn deposited Si(111) surface after annealing at 250 °C for 30 min. Sample bias is −1.6 V and the size is 56×60 nm^2. An arrow points to a region of bare Si surface, boundaries between two levels of MnSi along lines (i) and (ii) are marked by asterisks. Profiles along lines (i) and (ii) in the STM image are extracted as shown at bottom panel.

$\sqrt{3}$-MnSi film. The reason for this assignment is described below. The inset at top right is an enlarged image in the second layer and exhibits the $\sqrt{3}$ arrangement of protrusions as observed previously.[4–7] Two dimensional islands are the third layer (labeled 3 in Fig. 3), exhibiting the same STM image as the second layer. Most of small holes in Fig. 3 (typical one is shown by arrow) go down to the bare Si surface.

Layer thickness was measured in constant-current STM images, such as shown in Fig. 4 for the surface prepared by ~2 ML Mn deposition with subsequent annealing at 250 °C. Two line profiles are shown at the bottom panel. Along line (ii), there are regions of the bare Si surface with a bilayer-height difference (3.1 Å), which can be used as the calibration for the height (higher bare Si region is indicated by arrow). Then we can estimate the height difference between the second and the third MnSi layer (gray and white layers in Fig. 4, respectively), and the same heights of ~3 Å are obtained along lines (i) and (ii) at three points marked by asterisk. This is in agreement with the stacking-unit distance of the *B*20-type MnSi crystal along the [111] direction (Fig. 1). That is, the stacking unit is a quadruple layer (QL) with 2.7 Å thickness consisting of the so-called Si-sparse, Mn-sparse, Si-dense, and Mn-dense layers.[3] Thus, our prepared flat $\sqrt{3}$-MnSi thin films are in agreement with the *B*20-type structure as calculated by Hortamani *et al.*[3] The reason that we assigned the gray layer in Fig. 4 as the second QL of the $\sqrt{3}$-MnSi is that the height difference between the gray layer and the dark bare Si area is ~7 Å as measured in profiles (i) and (ii) in Fig. 4. This assignment seems to be plausible, because there might be an additional Si layer at the interface with the substrate, as suggested by Hortamani *et al.*[3]

Thus, it is demonstrated that the $\sqrt{3}$-MnSi films grow vertically with a unit of single QL at least in the ultrathin film stage. Two QLs seem to be favored on the Si(111) surface, as seen in Figs. 3 and 4. Since the Mn coverage in one QL is 4/3 ML,[3] the required coverage for the completion of two QLs is 8/3 ML. This value almost coincides with ~3 ML where the flat film is most extensively formed in Fig. 3. Hortamani *et al.* calculated the stability of the *B*20 structure of two QLs on Si(111) and found it is more stable than the *B*2 as mentioned above.[3] Further studies are required to understand the reason and mechanism for the extensive formation of flat two QLs of the $\sqrt{3}$-MnSi on Si(111).

In summary, we have formed flat epitaxial ultrathin films of the *B*20-type MnSi with a $(\sqrt{3}\times\sqrt{3})$R30° termination by deposition of Mn atoms on the Si(111)-(7×7) surface and subsequent annealing, and offered a proper recipe to make it. We have demonstrated that the MnSi films grow with a thickness unit of the QL, which is inherent of the *B*20 MnSi crystal. By using the present recipe, the fabrication of Si-based spintronics devices can be highly expected.

S. H. and P. K. gratefully acknowledge the support by the Japan Society for the Promotion of Science. H. T. appreciates partial financial supports from Nippon Sheet Glass foundation and Grants-in-Aid from the Ministry of Education, Science, Culture, and Sports of Japan.

[1]H. Wu, M. Hortamani, P. Kratzer, and M. Scheffler, Phys. Rev. Lett. **92**, 237202 (2004).
[2]M. Hortamani, H. Wu, P. Kratzer, and M. Scheffler, Phys. Rev. B **74**, 205305 (2006).
[3]M. Hortamani, P. Kratzer, and M. Scheffler, Phys. Rev. B **76**, 235426 (2007).
[4]M. M. R. Evans, J. C. Glueckstein, and J. Nogami, Phys. Rev. B **53**, 4000 (1996).
[5]T. Nagao, S. Ohuchi, Y. Matsuoka, and S. Hasegawa, Surf. Sci. **419**, 134 (1999).
[6]A. Kumar, M. Tallarida, M. Hansmann, U. Starke, and K. Horn, J. Phys. D: Appl. Phys. **37**, 1083 (2004).
[7]M. Tanaka, Q. Zhang, M. Takeguchi, and K. Furuya, Surf. Sci. **532**, 946 (2003).
[8]S. Azatyan, M. Hirai, M. Kusaka, and M. Iwami, Appl. Surf. Sci. **237**, 105 (2004).
[9]S. G. Azatyan, M. Iwami, and V. G. Lifshits, Surf. Sci. **589**, 106 (2005).
[10]H. Wang and Z.-Q. Zou, Appl. Phys. Lett. **88**, 103115 (2006).
[11]D.-Y. Wang, H.-Y. Wu, L.-J. Chen, W. He, Q.-F. Zhan, and Z.-H. Cheng, J. Phys.: Condens. Matter **18**, 6357 (2006).
[12]Q. Zhang, M. Takeguchi, M. Tanaka, and K. Furuya, J. Cryst. Growth **237**, 1956 (2002).
[13]E. Carleschi, E. Magnano, M. Zangrando, F. Bondino, A. Nicolaou, F. Carbone, D. Van der Marel, and F. Parmigiani, Surf. Sci. **601**, 4066 (2007).
[14]S. Higashi, T. Ohshima, S. Mizuno, and H. Tochihara, Surf. Sci. **600**, 591 (2006).
[15]M. Wuttig, Y. Gauthier, and S. Blügel, Phys. Rev. Lett. **70**, 3619 (1993).
[16]M. Wuttig, C. C. Knight, T. Flores, and Y. Gauthier, Surf. Sci. **292**, 189 (1993).

publikace P11

e-Journal of Surface Science and Nanotechnology 18 December 2008

e-J. Surf. Sci. Nanotech. Vol. 6 (2008) 276-280 **Regular Paper**

Growth of Ultra-Thin MnSi Films on Si(111) Surface: Monte Carlo Simulation

Pavel Kocán*

Department of Molecular and Material Sciences, Kyushu University, Kasuga, Fukuoka 816-8580, Japan and Charles University in Prague, Faculty of Mathematics and Physics, Department of Surface and Plasma Science, V Holešovičkách 2, 180 00 Praha 8, Czech Republic

Shougo Higashi and Hiroshi Tochihara

Department of Molecular and Material Sciences, Kyushu University, Kasuga, Fukuoka 816-8580, Japan

(Received 23 October 2008; Accepted 8 December 2008; Published 18 December 2008)

Thin MnSi films growing by units of a quadruple layer of a B20-type structure are observed on the Si(111) surface by scanning tunneling microscopy. Based on the observation, a model of growth controlled by an interplay between MnSi crystal growth and supply of Si atoms from substrate is proposed. A simple Monte Carlo model efficiently simulating significant experimentally observed features is presented. [DOI: 10.1380/ejssnt.2008.276]

Keywords: Monte Carlo simulations; Scanning Tunneling Microscopy; Silicides; MnSi; Si(111)

I. INTRODUCTION

MnSi flat films fabricated on the Si(111) surface have recently attracted attention as a promising material for spin-based electronic devices. According to ab-initio calculations [1], MnSi can exist in a form of a flat film with a B20-like structure. Importantly, these films exhibit 50% of spin polarization according to the calculation. In our preceding publication [2] we presented conditions leading to almost atomically flat MnSi films on the Si(111) surface. We have shown that room temperature (RT) deposition of ~ 3 monolayers (ML; 1 ML=7.83×10^{14} atoms/cm^2) and annealing to 250°C resulted in surface covered mostly by flat MnSi films with $(\sqrt{3}\times\sqrt{3})$R30° reconstruction (hereafter called $\sqrt{3}\times\sqrt{3}$ for simplicity). We also demonstrated that the film grows by units of quadruple layers (QL) of the B20 MnSi (see Fig. 1) and that 2 QLs are preferred against 1 QL during initial growth.

Understanding a rather complicated process of the MnSi film formation is crucial for further improvement of the film quality, which is essential in its utilization for spin-based devices. In the MnSi B20 structure, silicon and manganese atoms are equally included. Therefore, after deposition of some amount of Mn, the same amount of Si must be provided by the surface. A resulting morphology is thus by necessity influenced by MnSi crystal growth and by decomposition of Si layers.

For growth of thin films on oriented surfaces of crystals, kinetic Monte Carlo simulations are widely used [3] in order to test proposed models and provide a quantitative evaluation of physical parameters. However, simulations of such complicated systems as silicides are rather challenging, mainly because of too many processes involved during silicide formation and high number of related parameters.

Here we present a minimal model of MnSi growth based on our experimental results. The model is tested by a Monte Carlo simulation. We show that even with highly simplified model with just few parameters it is possible to explain all important experimentally observed features.

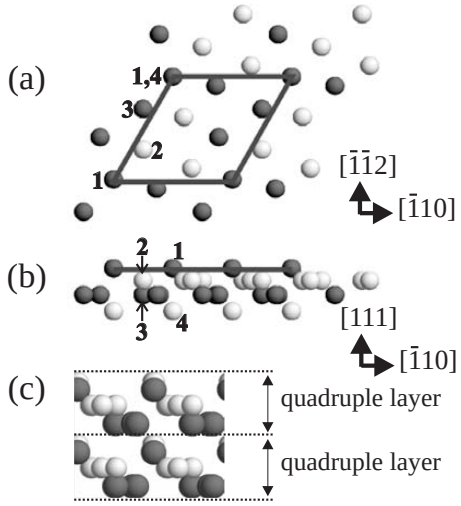

FIG. 1: A schematic model of the B20-type structure of MnSi. White balls represent Si atoms and dark balls Mn atoms. (a) top view and (b) side view of a single quadruple layer. Selected corresponding atoms in four layers are labeled by numbers. (c) side view of two quadruple layers showing their respective stacking. A unit cell corresponding to $\sqrt{3}\times\sqrt{3}$ on Si(111) is outlined.

II. EXPERIMENTAL

MnSi films were grown on Si(111)7×7 surfaces by depositing Mn from a home-made Ta tube and subsequent annealing. Deposited amount was estimated by a quartz crystal thickness monitor. The Si(111)7×7 reconstruction was prepared by a standard flashing procedure and confirmed by the low-energy electron diffraction. Samples were annealed to 250°C for several minutes. Temperature was measured by infra-red pyrometers. Morphologies of the samples were observed by a UNISOKU scanning tunneling microscope (STM) at RT few hours after

*Corresponding author: pavel.kocan@mff.cuni.cz,tochihar@mm.kyushu-u.ac.jp

preparation. The base pressure of apparatus was about 1.0×10^{-10} Torr.

III. RESULTS AND DISCUSSION

A. STM observation of film morphology

In this section we summarize experimental results of STM observation. For further details, see Ref. 2.

Fig. 2(a) shows a constant-current STM image of 1.5 ML Mn deposited sample. On the figure, MnSi islands (white and light gray) coexist with bare Si surface (dark gray). On closer inspection two levels of bare Si can be seen, e.g. in the area outlined by a rectangle. Magnified image of this area is shown in Fig. 2(d). Lower level of the Si surface (bottom part of the figure) shows a disordered structure, mostly with 2×2 periodicity, while the higher level (marked by an arrow) exhibits a partly broken 7×7 structure. Thus it can be deduced that the higher Si level is the original, partly survived 7×7 surface, while the lower level is area, where one bi-layer of Si was removed during growth of MnSi. A line profile extracted along the line indicated in Fig. 2(a) is plotted in Fig. 2(f). The profile crosses area of survived 7×7 (left part), areas of removed Si bi-layer (marked by "x") and MnSi islands of two different heights (indicated by hatching). A level of the original surface is marked by a dashed line. Difference of height of higher and lower MnSi island is ∼ 3 Å, which is consistent with a growth by units of quadruple layers of B20-type structure (Fig. 1), as we previously reported [2]. From STM images, we measured area of two levels of MnSi, obtaining ∼20% occupation of the higher and ∼30% of the lower level. Recalling the density of Mn in a QL of B20 is 4/3 ML we can calculate approximate amount of Mn in the islands. Using the thickness of the lower and higher level as 2 and 3 QLs we obtain amount of 1.6 ML, which is in a good agreement with the value measured by a crystal monitor. Therefore we propose that the lower level of MnSi is 2 QL thick and the higher one is 3 QLs. Levels in the Fig. 2(f) are marked correspondingly. Using a bulk lattice-plane distance between QLs in B20 structure (2.7 Å), a thickness of 2 Qls and 3 QLs is 5.4 Å and 8.1 Å, respectively. This suggests that the MnSi growth *under* the original level of 7×7, i.e. one bi-layer of Si is removed on the site of MnSi growth and replaced by MnSi, as indicated by hatching in the Fig. 2(f). We note that a level of MnSi corresponding to a single QL is not observed on our STM figures.

Fig. 2(b) shows the sample after deposition of ∼3 ML of Mn. The surface is almost completely covered by MnSi with $\sqrt{3}\times\sqrt{3}$ termination [unit of the $\sqrt{3}\times\sqrt{3}$ is outlined in a magnified image in Fig. 2(e)]. Next to the main flat area, few islands and tiny holes can be found on the surface. By considering deposited amount and occupation by the present levels of MnSi we obtained that the main level of MnSi is 2 QLs thick and the islands are 3 QLs. Plot profile along the line marked in the Fig. 2(b) is plotted in Fig. 2(g), demonstrating the flat area (marked "2"), island (marked "3") and a hole.

The surface after deposition of 5 ML of Mn is shown in Fig. 2(c). At this coverage the surface became rather corrugated with many levels of MnSi. Similar results were obtained previously [4]. A selected line profile extracted from the Fig. 2(c) is shown in the Fig. 2(h) with approximate thickness of the MnSi levels.

The observation can be summarized in few points: (1) MnSi grows by means of units consistent with quadruple layers of the B20 structure. (2) A minimum thickness of observed MnSi is 2 QLs. (3) Silicon necessary for formation of the MnSi film is provided by canceling bi-layers of Si both on site of MnSi and from surrounding area. (4) At about 3 ML of Mn the surface is almost completely covered by 2 QLs of MnSi. (5) At higher coverages the surface becomes corrugated.

B. Minimal model and Monte Carlo implementation

Based on the observation described in the previous section we propose a physical model of growth of MnSi. At elevated temperature, Mn atoms react with Si surface, partially destroying originally flat 7×7 surface. If a concentration of Mn is locally sufficient, MnSi is formed, 2 QLs are preferred to a single QL. When the surface becomes covered by a silicide film, another layers of MnSi film are formed on top of the film, while Si atoms are supplied from holes in the film. Thus with increasing coverage over ∼3 ML the surface becomes corrugated as many levels are formed and deep holes are created to supply Si atoms. Upon longer annealing, the less stable (isolated or edge) areas of MnSi decay and re-crystallize to a more stable formation.

Next we proceed to describe a minimal model sufficient for simulation of MnSi film formation and its Monte Carlo implementation. In our model, the surface is represented by separated matrices for MnSi and Si, the smallest (coarse-grained) unit is a triangular half of $\sqrt{3}\times\sqrt{3}$ unit cell (UC) with height of 1 QL in the case of MnSi and 1 bi-layer in the case of Si. Diffusion by single hopping of atoms between adjacent positions, as is common in a conventional kinetic Monte Carlo simulation of thin film growth, is not implemented in our simulation in order to keep the model the simplest possible and with minimum of parameters. Structures of MnSi and Si(111)7×7 surface are implemented only by means of concentration of Mn and Si atoms, i.e. one quadruple layer of MnSi consists of 4/3 ML of Mn and 4/3 ML of Si, one bi-layer with 7×7 reconstruction (original surface) consists of 2.08 ML and a bi-layer of Si of lower levels consists of 2.0 ML. In terms of unit cells, one MnSi UC contains 2 Si and 2 Mn atoms, one original-surface-silicon UC contains 3.12 Si atoms and one lower-level-silicon UC contains 3 Si atoms.

The simulation is divided to two stages. During the first stage, MnSi film is formed with supply of Si atoms by means of formation of holes. This stage is irreversible and corresponds to very initial reaction of Mn with Si surface upon annealing. Three general processes are considered in this stage.

1a) Formation of 2 MnSi UCs on bare Si surface implemented to mimic preferred growth of 2 QLs thick film. In this process, one Si UC is removed and two UCs of MnSi are formed on the site. For formation of 2 MnSi UCs, 4 atoms of Si are necessary. 3.12 Si atoms or 3 atoms are supplied by removing surface or lower UC of Si. Remain-

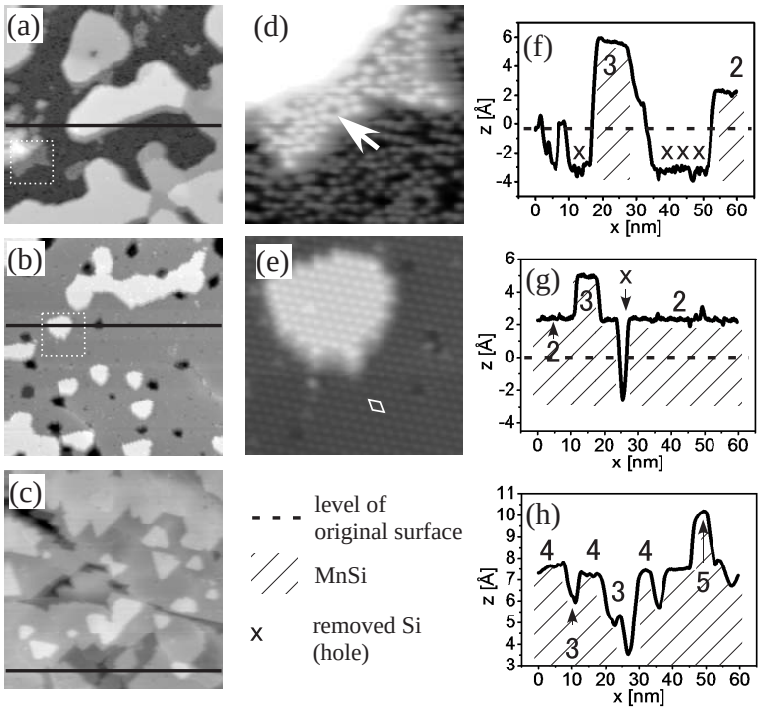

FIG. 2: STM images of MnSi thin films on Si(111) surface prepared by annealing to 250°C . (a) 1.5 ML Mn deposited sample. Brighter islands are MnSi films, darker gray is bare Si surface. (b) 3 ML Mn deposited sample. Most of area is covered by flat MnSi film, several islands and holes are observed. (c) 5 ML Mn deposited sample. Surface shows high corrugation, many levels of MnSi are observed together with deeper holes. (d,e) magnified image of area marked by rectangles in (a,b). Arrow in (d) points to a survived corner hole of the 7×7 reconstruction. In (e) a unit of $(\sqrt{3}\times\sqrt{3}\ )$R30° is outlined. (f-h) line profiles along lines marked in (a-c). Numbers denote a probable local thickness of the MnSi film. Size of images (a-c) is 60×60 nm^2, (d,e) are 10×10 nm^2.

ing 0.89 or 1 Si atom is supplied from a reservoir of "free" Si atoms, which is used to control mass balance during the simulation, as we describe later.

1b) Formation of 1 MnSi UC on top of existing MnSi. The process is consuming 2 Si atoms from the reservoir of "free" Si atoms.

1c) Formation of hole in bare Si surface. 3.12 or 3 Si atoms are supplied to the reservoir of "free" Si atoms if the hole is formed on the original surface or on a lower level, respectively.

Each type of process is divided to four possibilities with respect to a number of the nearest neighbors. A simple linear bond-cutting model is used, so the relative probability of formation of hole (process 1c) on a site with n nearest neighbors is $\exp(-n\times E_{\rm Si}/kT)$, where $E_{\rm Si}$ is effective energy of bond between neighboring units of Si, k is the Boltzmann constant and T is the temperature. On the other hand, formation of MnSi (processes 1a and 1b) on highly coordinated sites is preferred and the relative probability is $\exp(n\times E_{\rm MnSi}/kT)$, where $E_{\rm MnSi}$ is an effective energy of bond between neighboring MnSi units. Here we note that attempt frequencies for all processes are considered equal in our simulation for simplicity. Different values of the frequencies can in fact effectively influence values of the activation energies.

Formation of MnSi during the first stage proceeds as follows: Initially, there are no "free" (not incorporated in UCs of MnSi or Si) Si atoms in the reservoir, number of the "free" Si atoms is $\rho_{\rm Si}=0$. In each step, hole formation event (process 1c) or MnSi formation event (process 1a or 1b) is realized if the $\rho_{\rm Si}\le 0$ or $\rho_{\rm Si}>0$, respectively. After each realization, value of $\rho_{\rm Si}$ is updated with respect to local silicon supply and consumption. In this way, a balance of mass is controlled throughout the MnSi formation. Each specific realization of event is selected with respect to its relative probability, as common in kinetic Monte Carlo simulations [3]. The first stage is finished when amount of incorporated Mn in MnSi reaches a certain value. During the first stage, three parameters are to be fitted: $E_{\rm Si}$, $E_{\rm MnSi}$ and the relative probability of processes 1a and 1b $P_{1a/1b}$.

The second stage corresponds to a recrystallization of MnSi during annealing. During this stage, amount of Mn on the surface is constant and matrix of Si surface is not changed. Two processes are repeated:

2a) Removing one MnSi UC.

2b) Random formation of a new UC of MnSi.

Realization of the event 2a is again selected randomly with weight of $\exp[(-n\times E_{\rm MnSi'}+E^v)/kT]$ where n is number of the nearest horizontal neighbors, $E_{\rm MnSi'}$ is the effective energy of bonding to the nearest neighbors and E^v is effective energy of bonding to an underlaying

layer, different for Si to MnSi ($E^v_{\mathrm{MnSi-Si}}$) and MnSi to MnSi ($E^v_{\mathrm{MnSi-MnSi}}$) bonding. A position of re-appearing of new MnSi unit (event 2b) is selected randomly in order to effectively simulate diffusion of freed Mn and Si atoms. During the recrystallization stage, the MnSi film evolves in direction to minimum of total energy by means of preferring highly coordinated positions. Two parameters are to be fitted during this stage: $E_{\mathrm{MnSi'}}$ and $\Delta E^v = E^v_{\mathrm{MnSi-MnSi}} - E^v_{\mathrm{MnSi-Si}}$.

Results of simulation for 1.5 ML, 3 ML and 5 ML of Mn are shown in Fig. 3(a-c). The following values of the model parameters were used: $E_{\mathrm{Si}} = 0.31$ eV, $E_{\mathrm{MnSi}} = 0.07$ eV, $P_{1a/1b}$=5, $E_{\mathrm{MnSi'}} = 0.4$ eV and $\Delta E^v = 0.20$ eV. Line profiles extracted along lines marked in (a-c) are shown in Fig. 3(d-f). All scales are set to be same as in Fig. 2(a-c), so that STM and Monte Carlo results can be directly compared. In the 1.5 ML case, the same levels of MnSi and Si can be observed on the simulated and STM images - 2 and 3 QLs of MnSi, an original Si surface and a lower Si surface. Compared to the experiment, occupation by level of 2 QLs (3 QLs) is higher (lower) in case of simulation. Possible reasons will be discussed later. In the 3 ML case, the agreement between experiment and theory is reasonable [Fig. 2(b) and Fig. 3(b)]. In both cases, the surface is mostly covered by 2 QLs of MnSi, the rest are islands of 3 QLs and small holes. Corrugation of the surface after 5 ML deposition is reproduced well by the simulation [Fig. 3(c)] as well. Same levels of 3, 4 and 5 QLs are observed as in Fig. 2(c) together with very deep holes.

On the line profiles in Fig. 3(d-f), small steps up and down with height of 0.4 Å can be seen [see e.g. position marked by an asterisk in Fig. 3(d)]. Such a step is a result of a similar thickness of Si bi-layer (3.1 Å) and MnSi quadruple layer (2.7 Å). For example, two QLs and one QL plus extra Si bi-layer have a thickness of 5.4 Å and 5.8 Å, respectively. On our STM images (not shown here), we have observed such slight and smooth corrugation suggesting that steps at Si-MnSi interface can be crystalically overgrown and the small difference in height (0.4 Å) can be overcome by means of MnSi crystal relaxation.

Finally we discuss impact of simplifications of the model and limits of its application. First simplification to be mentioned is excluding of atom-by-atom diffusion. On a real surface, free Si and Mn atoms diffuse on the surface, interacting together as well as with steps of Si and edges of MnSi. In our simulation, the diffusion is simplified to annihilation of MnSi UC and random reappearance of the whole unit with no correlation to a position of the original MnSi UC. Such effects like diffusion barriers along step edges may of course influence values of model parameters. Thus we emphasize that the model parameters are indeed just of effective values.

Another simplification is recrystallization restricted only to MnSi, while the Si crystal is not allowed to restructure during the second stage described above. Experimentally, evolution of Si step edges was studied by high-temperature STM [5–7]. For example, an Si island of ∼100 nm size almost decayed after 60 min at 560°C. Possibly, the decomposition of a step edge may be faster in the case of Mn deposited surface, because of a reaction with free Mn atoms. However, we suppose that our simplification is acceptable in the case of temperatures bellow

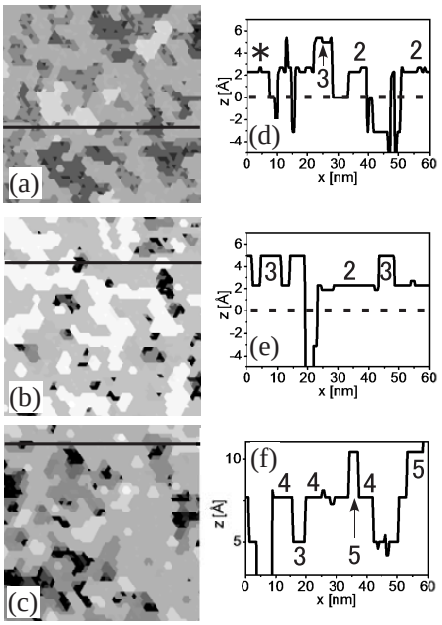

FIG. 3: Results of Monte Carlo simulations. (a) 1.5 ML, (b) 3 ML, (c) 5 ML of Mn. Size of images corresponds to 60×60 nm^2. (d-f) - profiles extracted over lines marked in (a-c). Numbers denote a local thickness of the MnSi film. The structures were allowed to relax for 20 events per site.

∼500°C.

The last simplification to be discussed is neglecting of a possible inhomogeneity of Mn atom density before crystallization starts. It has been proposed that to form the MnSi, Mn atoms need to cluster together and form clusters with a sufficient size to react with Si substrate [8, 9]. This effect is stronger in the case of low coverage and can result in a formation of higher islands. This may be the reason why the occupation by the level of 3 QLs is higher on STM images (Fig. 2a), compared to the simulation (Fig. 3a).

IV. CONCLUSION

Based on STM observation of morphology of MnSi thin films grown at 250°C we proposed a model of the film formation. The film grows by units with thickness of a quadruple layer of B20 type structure. 2 QLs are preferred during initial MnSi formation. Silicon atoms necessary for MnSi growth are provided both on site of the formation and from bare Si surface. We have tested the proposed model by a simple coarse-grained Monte Carlo simulation. Obtained results are in a good qualitative agreement with experimentally observed morphology.

Acknowledgments

This work was supported by the following KAKENHIs: Grant-in-Aid for Scientific Research (B) (19340083); Grant-in-Aid for JSPS fellows (18.06750); Grant-in-Aid

for JSPS fellows (18.9776). One of the authors (P. K.) appreciates support of the JSPS Postdoctoral Fellowship for Foreign Researchers.

[1] M. Hortamani, P. Kratzer, and M. Scheffler, Phys. Rev. B **76**, 235426 (2007).
[2] S. Higashi, Y. Ikedo, P. Kocán, and H. Tochihara, Appl. Phys. Lett. **93**, 013104 (2008).
[3] M. Kotrla, Comput. Phys. Commun. **97**, 82 (1996).
[4] A. Kumar, M. Tallarida, M. Hausmann, U. Starke, and K. Horn, J. Phys. D **37**, 1083 (2004).
[5] I.-S. Hwang, M.-S. Ho, and T. T. Tsong, Surf. Sci. **514**, 309 (2002).
[6] I.-S. Hwang, M.-S. Ho, and T. T. Tsong, Phys. Rev. Lett. **83**, 120 (1999).
[7] M.-S. Ho, I.-S. Hwang, and T. T. Tsong, Phys. Rev. Lett. **84**, 5792 (2000).
[8] T. Nagao, S. Ohuchi, Y. Matsuoka, and S. Hasegawa, Surf. Sci. **419**, 134 (1999).
[9] M. M. R. Evans, J. C. Glueckstein, and J. Nogami, Phys. Rev. B **53**, 4000 (1996).

PHYSICAL REVIEW B **79**, 205312 (2009)

Reactive epitaxial growth of MnSi ultrathin films on Si(111) by Mn deposition

Shougo Higashi,[1] Pavel Kocán,[1,2] and Hiroshi Tochihara[1,*]
[1]*Department of Molecular and Material Sciences, Kyushu University, Kasuga, Fukuoka 816-8580, Japan*
[2]*Department of Surface and Plasma Science, Faculty of Mathematics and Physics, Charles University in Prague, V Holešovičkách 2, 180 00 Praha 8, Czech Republic*

(Received 8 December 2008; revised manuscript received 10 April 2009; published 13 May 2009)

Manganese (Mn) adsorption on the Si(111)-(7×7) surface followed by annealing at a relatively low temperature of 250 °C has been studied by using scanning tunneling microscopy as well as low-energy electron diffraction and Auger-electron spectroscopy. The B20-type structure of a Mn monosilicide (MnSi) of epitaxial ultrathin films is formed with a $(\sqrt{3}\times\sqrt{3})$R30° periodicity. Morphologies of the crystalline MnSi ultrathin films have been investigated for Mn coverage of 1.5, 3, and 5 monolayers (ML). We found a characteristic mode of crystal growth for compound formation in the solid-on-solid system. At each amount of the Mn deposition, structural features, morphology, and formation processes of the MnSi films can be explained by the mass balance between deposited Mn and usable Si atoms. We found that the epitaxial MnSi ultrathin films can be grown coherently on Si(111) at 3 ML of Mn deposition. At 5 ML, the supply of Si atoms from bulk to surface becomes significant, then many deep holes are formed and the surface morphology becomes rough. It is found that the codeposition of Mn and Si leads to the formation of anomalously smooth MnSi surfaces.

DOI: 10.1103/PhysRevB.79.205312 PACS number(s): 68.55.−a, 68.37.−d

I. INTRODUCTION

Fabrication of ferromagnetic (FM) layer onto semiconductor surfaces has received a considerable attention because of its potential application to information processing devices utilizing the spin of electron,[1] categorized as spintronics.[2] Accomplishment of an efficient injection of spin polarized current from FM layers into semiconductors is one of major challenges to realize practical devices. So far, several investigations have been conducted on the growth of FM transition metals or metal silicide films on semiconductors.[3–6] However, studies concerned with FM films on silicon surfaces, which are widely used in semiconductor industry, are few and the film required as the efficient spin injector has not been reported yet. Among systems of transition-metal silicides on Si surfaces, MnSi is considered to be a good candidate as a spin injector since it exhibits the ferromagnetism in the bulk. In addition, it was reported that ultrathin MnSi films formed on the Si(111) surface have a spin polarization of 50% at the Fermi level by calculations using density-functional theory (DFT).[7] It was also demonstrated that Mn atoms at the surface and interface possess large magnetic moments. Therefore, the MnSi ultrathin film on Si(111) would be a promising material for Si-based spintronics.

Experimentally, Mn deposition on the Si(111)-(7×7) surface has been studied by several groups but most studies reported so far are on the formation of three-dimensional (3D) islands or on very initial processes of Mn deposition on the surface.[8–10] At 1 monolayer (ML; 1 ML=7.83×10^{14} atoms/cm^2) deposition, Evans *et al.*[11] observed by using scanning tunneling microscopy (STM) tabular islands with a $(\sqrt{3}\times\sqrt{3})$R30° termination interrupted by bare Si surface at annealing temperatures between 325 °C and 450 °C. Nagao *et al.*[13] found such islands ranging up to several hundreds of angstroms with various heights depending on the annealing temperature. Kumar *et al.*[12] observed that with increasing coverage to 5 ML such islands almost close the bare Si surface at 400 °C, leading to patched films with various heights as well as deep holes. So far, the annealing was done under relatively high temperatures in most studies.[11–13] Recently, Hortamani *et al.*[7] showed by using DFT calculations that the B20-type structure (bulk crystal structure) of the MnSi, whose (111) plane coincides with the $(\sqrt{3}\times\sqrt{3})$R30° lattice of the Si(111) plane with a mismatch of 3.2%, is more stable than the pseudomorphic B2 (CsCl-type structure). Ball model of the B20-type structure is depicted in Fig. 1. The validity of the assignment of the B20-type MnSi structure formed on Si(111) is recently confirmed by means of surface x-ray diffraction analysis using synchrotron radiation.[14]

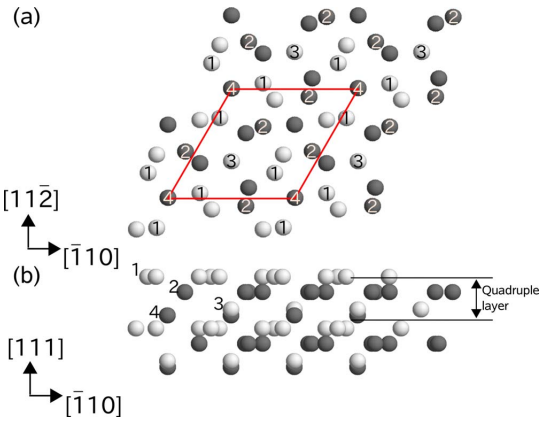

FIG. 1. (Color online) Ball model of the B20-type structure of MnSi for (a) top view and (b) side view. White balls represent Si atoms and dark balls Mn atoms. In (a), a unit mesh of $(\sqrt{3}\times\sqrt{3})$R30° with respect to the Si(111) is outlined. In (b), it is shown that 1 QL consists of four different layers (numbered 1–4). In (a), all atoms located in the four different layers are numbered from 1 to 4 only for the top QL according to the numbers in (b).

Very recently, we have reported a recipe for the epitaxial growth of flat MnSi ultrathin films on Si(111).[15] As the spin injector, atomic flatness of an interface between Si substrate and FM films is crucial to minimize scattering from defects and/or impurity states. We can expect the formation of flat interfaces between the MnSi and the Si(111) substrate if the surfaces of the MnSi films are atomically smooth. The recipe is simple: after deposition of Mn atoms of 3 ML on the Si(111)-(7×7) surface at room temperature (RT) the sample is annealed at a relatively low temperature of 250 °C for more than 5 min.

In this paper, in order to know the reason why the 3 ML-Mn deposition is the appropriate condition to form the flat MnSi ultrathin films at 250 °C annealing, we have investigated STM images of surfaces where Mn atoms are deposited by 1.5, 3, and 5 ML. In addition we have studied the effect of annealing time. Detailed investigation led to proposal of another mode of crystal growth and to understanding of the formation processes of the MnSi ultrathin films. We have tried another procedure for producing flat MnSi ultrathin films. That is, not only Mn but Si atoms are deposited on the Si(111)-(7×7) surface (denoted codeposition) then the surface is annealed at 250 °C. This procedure produces anomalously flat surfaces of the MnSi films.

After the description of experimental part in Sec. II, results of low-energy electron-diffraction (LEED) intensity measurement and Auger-electron spectroscopy (AES) are briefly mentioned in Sec. III. Then, STM images taken at 1.5, 3, and 5 ML are separately presented with detailed discussion in Sec. IV. In Sec. V, the formation processes of the MnSi ultrathin films are discussed based on the results obtained mainly by STM measurements. We show the STM images of surfaces prepared by codeposition of Mn and Si in Sec. VI. Finally, we summarize our experimental results and the essence of the formation processes of the MnSi films.

II. EXPERIMENT

Experiments were carried out in an ultrahigh-vacuum system consisting of a sample preparation chamber with LEED and a chamber for STM measurement. The base pressures of both chambers were about 1×10^{-10} Torr. Clean surfaces were accomplished by flashing samples at 1200 °C for a few seconds several times, with subsequent annealing at 700 °C for 5 min and cooling down to RT with a rate of 10 °C/s in order to prepare large terraces of (7×7). The surface quality was checked by observing clear and sharp (7×7) LEED patterns. Mn was evaporated from a homemade Knudsen cell by resistive heating[16] and Si deposition was carried out by passing dc directly to a piece of Si wafer (10×2 mm^2). The calibration of deposited amounts was performed using a crystal thickness monitor and the deposition rates of Mn and Si were estimated to be ~0.3 and ~0.6 ML/min, respectively. Sample temperature was kept at RT and pressures during deposition were less than 3×10^{-10} Torr. After the deposition, the sample was annealed at 250 °C for several minutes. The temperature was measured with an infrared pyrometer. The AES was measured by using a four-grid LEED optics. Intensities of LEED spots were measured with a high sensitive charge-coupled device (CCD) camera at RT. After annealing, the samples were transferred to the STM chamber and the structure and morphology were investigated by STM (Unisoku, USM-901) at RT.

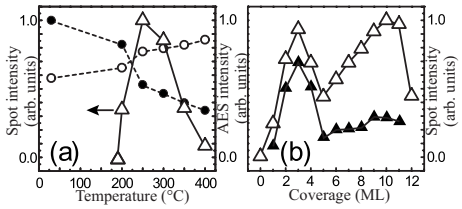

FIG. 2. (a) Intensity change of (1/3 1/3) LEED spots as a function of annealing temperature (triangles). AES intensities of Mn (40 eV, filled circles) and Si (92 eV, open circles) are plotted against annealing temperature. 3 ML Mn was deposited at RT. Incident electron energies for LEED and AES are 115 eV and 1 keV, respectively. (b) Intensity change of (1/3 1/3) LEED spots at incident energy of 115 (open triangle) and 173 (filled triangle) eV as a function of Mn coverage. Samples were annealed at 250 °C for 5 min.

III. LEED SPOT INTENSITY AND AES MEASUREMENTS

LEED intensities of (1/3 1/3) spots reflecting the area of ordered MnSi domains with the $(\sqrt{3}\times\sqrt{3})$R30° periodicity are shown in Fig. 2(a) as a function of annealing temperature between 185 °C and 400 °C (annealing time is 5 min). The amount of deposited Mn was ~3 ML. AES intensities of Mn (40 eV, filled circle) and Si (92 eV, open circle) are also plotted in Fig. 2(a). AES intensity of Mn decreased steeply between 200 °C and 250 °C, while that of Si considerably increased. The changes in the AES intensities suggest that vertical mass transfer of Si atoms takes place efficiently around 250 °C. In accordance with the AES changes, the LEED intensity steeply increases between 200 °C and 250 °C and reaches a maximum at 250 °C. Then, it decreases rapidly above 300 °C. The decrease reflects a change in morphology from the MnSi two-dimensional (2D) islands to 3D islands.[11] Thus, at 250 °C the MnSi films are most extensively formed on the surfaces. In Fig. 2(b), LEED intensities of the (1/3 1/3) spots at incident energies of 115 (open triangle) and 173 (filled triangle) eV are plotted as a function of Mn coverage. Mn deposited surfaces were annealed at 250 °C for 5 min for each measurement. At both energies, the intensities exhibit sharp maxima at 3 ML, where the area of the ordered MnSi is the widest. More deposition of Mn than 3 ML leads to a decrease in the ordered area of the MnSi. Thus, the MnSi thin film grows most extensively at 3 ML of Mn deposition and subsequent annealing at 250 °C. In the next section, we see how the surface morphology changes with increase in Mn coverage and in annealing time by observing STM images.

IV. INDIVIDUAL DEPOSITION OF Mn ON Si(111)

A. 1.5 ML-Mn deposition followed by annealing

Figures 3(a) and 3(b) show STM images of 1.5-ML-Mn-deposited surfaces followed by annealing at 250 °C for 5

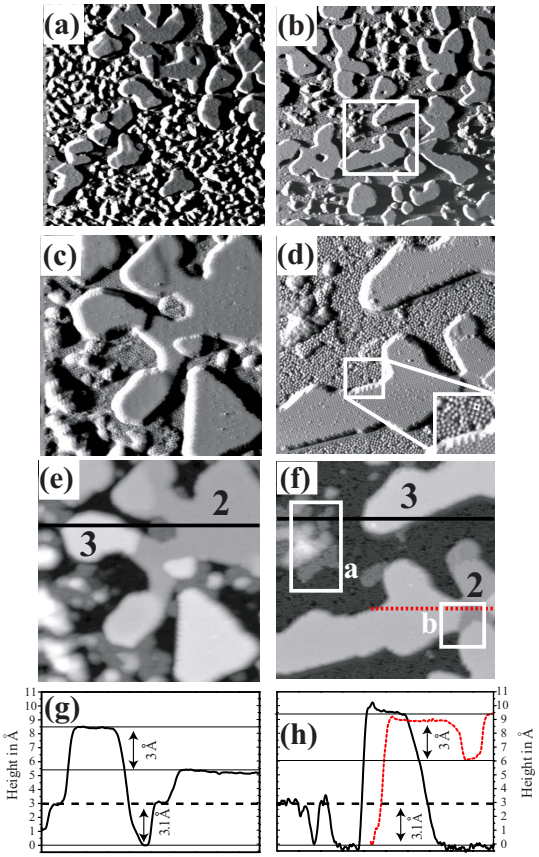

FIG. 3. (Color online) STM images of 1.5-ML-Mn-deposited surfaces followed by annealing at 250 °C. Annealing times for (a) and (b) are 5 and 30 min, respectively, and both imaging areas are 150×150 nm^2. (a)–(d) are CH mode images with sample bias (V_S) of 1.5 V. (c)–(f) are magnified images of 60×60 nm^2. (d) is a magnified image of the outlined region in (b). (e) and (f) are CC mode images of (c) and (d), respectively. The numbers in (e) and (f) indicate height of the grown MnSi 2D islands in unit of QL. Regions a and b in (f) are magnified in Figs. 4(a) and 4(b), respectively. (g) and (h) show profiles along lines in (e) and (f), respectively. The original level of the Si(111)-(7×7) is shown by dashed line.

and 30 min, respectively. Both areas are 150×150 nm^2 but probing sites are not identical. Figures 3(a) and 3(b) are constant-height (CH) mode images. In the present study we used a sample bias (V_S) of 1.5 V otherwise noted. In Fig. 3(a) there are many irregular clusters in addition to small 2D islands and the former almost disappears after 30 min annealing in Fig. 3(b). It is noted that Mn deposition of 1.5 ML at RT led to the appearance of a range of "hillock" in STM images (not shown here).[11] Therefore, we conclude that the irregular clusters in Fig. 3(a) consist of Mn atoms. In Fig. 3(b), in addition to the grown 2D islands, relatively large areas of bare Si(111) surfaces can be seen (denoted "craters" hereafter).

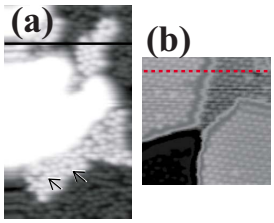

FIG. 4. (Color online) (a) and (b) are magnified CC mode images from regions a and b in Fig. 3(f), respectively. In (a) arrows indicate corner holes on the (7×7) reconstruction in survived area. White area is an unknown structure, probably unreacted Mn cluster. Contrast in (b) is nonlinearly enhanced to show the structure of different levels of the MnSi.

A clear image of the crater is shown in a magnified image of Fig. 3(d) from an outlined region in Fig. 3(b). The inset in Fig. 3(d) clearly shows that the surface of the craters is decorated by Si adatoms[11] which are arranged to be a rather disordered (2×2) [denoted "2×2" hereafter]. Figure 3(c) is a similarly magnified image from the surface after 5 min annealing but its location is not within Fig. 3(a). Figures 3(e) and 3(f) correspond to constant-current (CC) mode images of Figs. 3(c) and 3(d), respectively. A further enlarged STM image of region *a* outlined in Fig. 3(f) is shown in Fig. 4(a). We can recognize narrow areas of survivals of the original Si(111) surface: corner holes being specific to the (7×7) reconstruction can be seen as shown by arrows. Thus, we assign that the height difference between the survived narrow areas and the craters is the thickness of 1 bilayer (BL) of the Si(111) plane, 3.1 Å. This value is used as a height standard in line profiles in Figs. 3(g) and 3(h). The height of the original Si(111)-(7×7) surface is depicted by a dashed line in Figs. 3(g) and 3(h).

Along a dotted line in Fig. 3(f) the tip scans a higher and a lower level of a 2D island. Its profile is shown in Fig. 3(h) as a dotted line. The height difference between the higher and lower levels is derived to be ~3 Å, which is practically in good agreement with a stacking-unit distance of the B20-type MnSi crystal along the [111] direction. We call the unit 1 quadruple layer (QL) (see Fig. 1, strictly its thickness is 2.7 Å in the bulk structure). One QL consists of the so-called Si sparse, Mn sparse, Si dense, and Mn dense layers[7] and atoms in each layer are marked with numbers 1–4, respectively, as shown in Fig. 1. The interlayer distance of ~3 Å has been also confirmed in Fig. 3(g) as well as on several 2D islands. Therefore, we suggest that the grown 2D islands are the B20-type MnSi and that the MnSi islands grow with the thickness unit of 1 QL. Figure 4(b), being magnified from outlined square *b* in Fig. 3(f), shows that both higher and lower levels of the 2D island exhibit the $(\sqrt{3}\times\sqrt{3})$R30° arrangement of protrusions. In order to know clearly the relation of the arrangement of the protrusions between the two layers with the height difference of 1 QL, we show another CC mode image around the two-level structure in Fig. 5(a). A hexagonal grid of the $(\sqrt{3}\times\sqrt{3})$R30° order is partially overlaid on the image. It is found that on the lower level the protrusions are located at centers of triangles in the

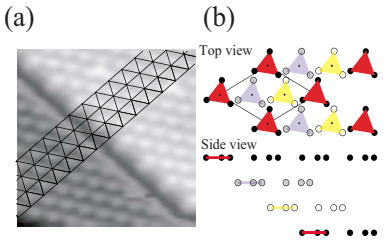

FIG. 5. (Color online) CC mode image (60×60 nm^2) around two-level structure (height difference corresponds to 1 QL). A single triangular mesh of the $(\sqrt{3}\times\sqrt{3})$R30° is overlaid partially. (b) Schematic top and side views of consecutive 3 QLs, in which a Si-dense layer represents each QL for simplicity: filled, gray, and open circles represent Si atoms in the top, second, and third QLs, respectively, as seen in a side view. Three nearby Si atoms (hatched triangle in top view) is assumed to exhibit one protrusion in STM image in (a). A parallelogram is a unit mesh of $(\sqrt{3}\times\sqrt{3})$R30° with respect to the Si(111). Contrast in (a) is nonlinearly enhanced to show the structure of different levels of the MnSi.

grid while they are at corners of the triangles on the higher level. This is consistent with the B20-type MnSi structure schematically shown in Fig. 5(b). We do not know which layer appears on the top of each QL among the four different layers at this moment, but we assume here it is the dense Si layer. (Even if we choose other layers, the discussion below is the same.) So only atoms in the Si-dense layer of three consecutive QLs are depicted in Fig. 5(b) for simplicity: filled, gray, and open circles represent Si atoms in the top, second, and third QLs, respectively, as seen in a side view. Three nearby Si atoms [a hatched triangle in top view of Fig. 5(b)] is assumed to exhibit one protrusion in STM images in Fig. 5(a). Atoms in the lower QL are shifted by 4 Å along a long diagonal of a parallelogram. This is in agreement with the observed shift of the protrusions in Fig. 5(a). Thus it is supported again that the grown MnSi is the B20-type structure and that the MnSi films grow with a unit of 1 QL.

In several CC mode images after 30 min annealing we measured fractions of area of the higher and lower levels of the MnSi, obtaining 20% and 30%, respectively on average. Recalling the density of Mn in 1 QL is 4/3 ML, we can calculate approximate amount of Mn in the islands. Assuming the thickness of the lower level in Fig. 3(f) as 2 QLs, we obtain a total amount of 1.6 ML of Mn, which practically agrees with the value measured by the crystal monitor, 1.5 ML. If we assume that the lower level is 1 or 3 QLs, then the amount of Mn in the MnSi islands is 0.9 or 2.7 ML. Therefore, we exclude the two possible thicknesses. Thus, we assign the levels marked 2 and 3 in Figs. 3(e) and 3(f) as the second and the third QLs of the MnSi 2D islands, respectively. 2D islands with a thickness of 1 QL have never been found in the present studies.

B. 3 ML-Mn deposition followed by annealing

3 ML-Mn deposition with subsequent annealing at 250 °C results in transformation of almost entire surface into the flat MnSi films as shown in Figs. 6(a) and 6(b), which are

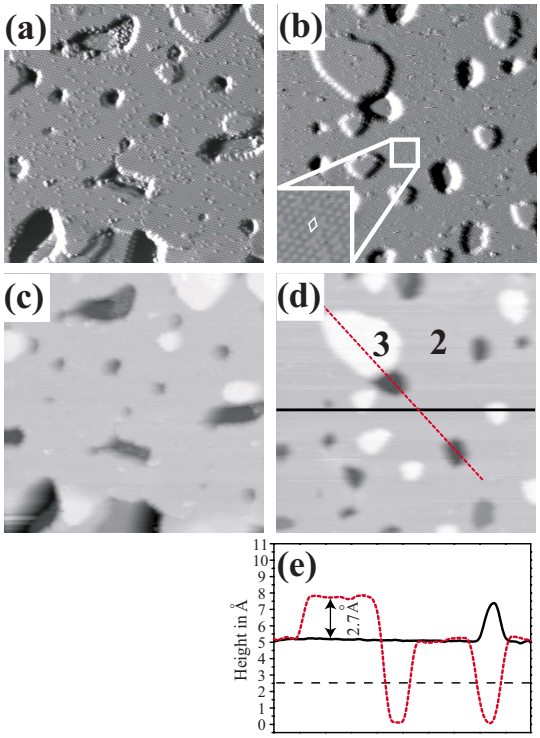

FIG. 6. (Color online) STM images of samples prepared by deposition of 3 ML of Mn followed by annealing at 250 °C. (a) and (b) constant-height mode images at annealing time of 5 and 30 min, respectively. (c) and (d) constant-current mode images of (a) and (b), respectively. All images are taken at V_S=−1.0 V with 50×50 nm^2. In (d), numbers 2 and 3 mark second and third QLs of MnSi film, respectively. (e) Profiles along lines in (d). Dashed line indicates the original surface level.

CH mode images after 5 and 30 min annealing, respectively. Corresponding CC mode images are presented in Figs. 6(c) and 6(d), respectively. There occur no significant morphological changes caused by annealing time, but we note that larger holes observed at 5 min annealing change to small ones at 30 min. About 80% of the surface is covered by the atomically flat MnSi films. A magnified image is shown at the bottom left of Fig. 6(b), indicating the $(\sqrt{3}\times\sqrt{3})$R30° arrangement of the protrusions. In CC mode images there exist some small white 2D islands on the flat surface (~15% of the whole surface). According to the conclusion in the case of 1.5 ML-Mn, the white islands are higher by 1 QL than the flat area. Thus, we assigned that the height difference between the lower and higher levels is 2.7 Å and it is used as a height standard in Fig. 6. We suggest that the flat area is the second QL: the total amount of Mn atoms in the films can be estimated to be $(0.8\times2\times\frac{4}{3}+0.15\times3\times\frac{4}{3})$ =2.7 ML from the area percentages and Mn coverage mentioned above. This is in good agreement with the value measured by the crystal monitor, ~3 ML. Thus, we conclude that almost complete MnSi films of 2 QLs are formed by 3

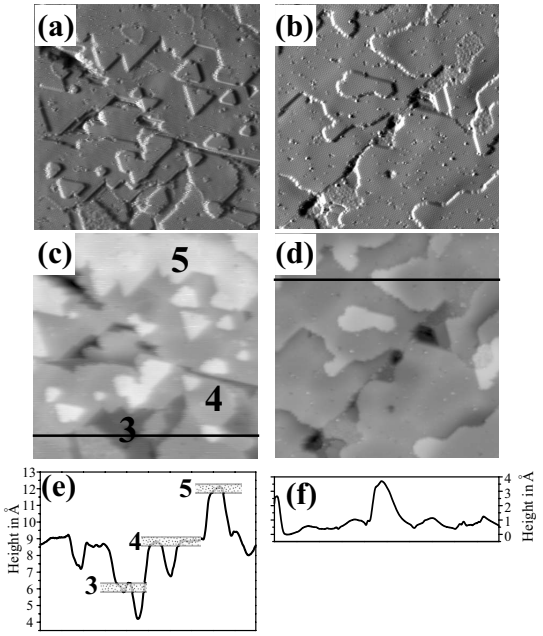

FIG. 7. STM images of samples prepared by depositing 5 ML of Mn followed by annealing at 250 °C. (a) and (b) constant-height mode images at annealing time of 5 and 30 min, respectively. V_S=1.0 V. (c) and (d) constant-current mode images of (a) and (b), respectively. All images are 60×60 nm^2. (e) and (f) are profiles along lines in (c) and (d), respectively. In (c) and (e), numbers 3, 4, and 5 mark third, fourth, and fifth QLs of MnSi film, respectively.

ML-Mn deposition and subsequent annealing at 250 °C. It is noted that such atomically flat MnSi surfaces can be formed only at ~3 ML deposition under the condition of postannealing at 250 °C. In accordance with STM observations, LEED spot intensity of the third order against the amount of deposited Mn in Fig. 2(b) indicates that the MnSi films grow most extensively at 3 ML. If we raise the annealing temperature higher than 300 °C, the flat MnSi films convert to 3D islands as indicated in the decrease in the spot intensity in Fig. 2(a). As another feature in Fig. 6, there exist small holes with diameters of 1.5–6 nm in Fig. 6(d). These holes reach deeper levels than the original surface as seen along a dotted-line profile in Fig. 6(e). Later we discuss the relationship between the holes and the grown MnSi.

C. 5 ML-Mn deposition followed by annealing

Deposition of 5 ML-Mn and subsequent annealing at 250 °C for 5 min led to the formation of uneven surfaces as shown in Fig. 7(a), contrary to the case of 3 ML deposition. The corresponding CC mode image is shown in Fig. 7(c). As in the case of 3 ML-Mn deposition, holes are observed. Referring a line profile in Fig. 7(e) taken along a solid line in Fig. 7(c), we can distinguish three layers with a height difference of 1 QL thickness (hatched three bars). We assign that the highest layer [white area in Fig. 7(c)] is the fifth QL.

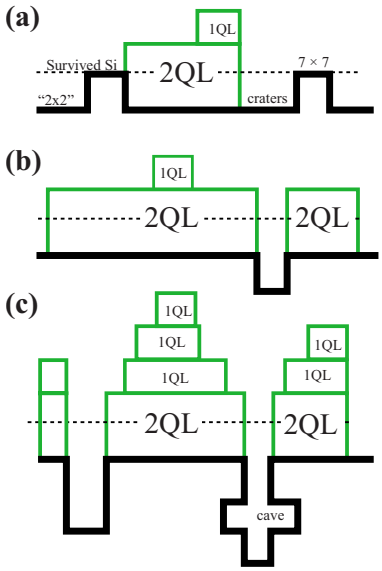

FIG. 8. (Color online) Schematic cross sectional views of (a) 1.5, (b) 3, and (c) 5-ML-Mn deposited surfaces followed by annealing at 250 °C. 2 QLs of the MnSi film appearing at the initial growth are shown. Thick lines indicate the bare Si surface and interface. Dotted lines show the level of original surface of the (7×7) reconstruction.

The fourth and the third QLs are numbered as well. The assignment of the layer number is not evidenced by experimental results, but here we simply assign the middle layer in Fig. 7(c) as the fourth QL because the deposited amount of Mn is 5 ML. Upon further annealing of 30 min, the surface morphology exhibited a significant change. That is, the layered structure with discrete heights changed to rather even surfaces in Figs. 7(b) and 7(d). Along a solid line in Fig. 7(d), a profile in Fig. 7(f) does not exhibit the discrete layered structure as seen in Fig. 7(e). In Fig. 7(f), near the center along the profile a rather steep peak appears and gradually goes down by about 3 Å toward right-hand side, despite the region should show a flat profile because of the same layer. The line profile in Fig. 7(f) leads us to denote the morphology of Fig. 7(d) as a wavy surface structure. We discuss the morphology change upon annealing below.

V. FORMATION PROCESSES OF MnSi

In this section, we discuss formation processes of the MnSi ultrathin films based on the findings in the preceding section. Figure 8 represents schematic illustrations of the grown MnSi ultrathin films on Si(111) at 1.5, 3, and 5 ML of Mn deposition followed by annealing at 250 °C. At 1.5 ML deposition followed by subsequent annealing for 30 min, two levels of Si surfaces are observed as seen in Fig. 3(b): the survived original (7×7) surface regions (nonreacted regions) and the lower "2×2" regions where 1 BL of the original surface has been removed [see Fig. 8(a)]. As noted

above, we denote the removed regions craters. Here, it is emphasized that the MnSi 2D islands of 1 QL have never been observed and that the MnSi thin films grow with a thickness unit of 1 QL after 2 QL formation. We suggest that the first QL formed on Si(111) is so active that the second QL covers simultaneously the first one. 2 QLs are the minimum thickness for the initial epitaxial growth of the MnSi films. Therefore, the 2 QL MnSi 2D islands are formed (together with 3 QLs) in the case of 1.5 ML Mn as shown in Fig. 8(a). For the formation of 2 QLs, Mn atoms with $2\times\frac{4}{3}=2.67$ ML gather locally upon annealing, and the same coverage of Si atoms has to exist there in order to form a 2 QL MnSi 2D island. The top BL provides 2.08 ML of Si atoms in the on-site reaction with Mn atoms and the rest of Si atoms are supplied from the surrounding nonreacted top BL leaving craters.

In the case of 3 ML Mn, sufficient amount of Mn atoms is deposited for covering an entire surface with the 2 QL MnSi films. Since whole top BL is used in the on-site reaction, deep holes down to the second and the third BLs are created. Necessary amount of Si to form the 2 QL MnSi films $[(2.67-2.08)=0.59$ ML] is supplied efficiently through the holes. Most surfaces of the MnSi films of 2 QLs are atomically flat as typically shown in Fig. 6. Thus, it is understood why the flat MnSi ultrathin films are formed on the entire surface at ~3 ML-Mn deposition. The interface between the MnSi and Si substrate would be rather smooth as shown in Fig. 8(b) except for holes.

At 5 ML-Mn deposition followed by annealing at 250 °C for 5 min, Si atoms of 5 ML are used for the reactive growth of the MnSi. Besides Si atoms of 2.08 ML in the top BL, about 3 ML (rather large amount) should be supplied from deeper BLs of the substrate. For this supply, many large holes are created as seen in Fig. 7(c) and a schematic illustration is depicted in Fig. 8(c). The surface is not so flat as the case of 3 ML-Mn deposition (cf. Fig. 6) and exhibits a layered structure with discrete heights as seen in Fig. 7(c). The wavy surface structure in Fig. 7(d) appears after prolonged annealing as mentioned above. Its origin is not clear at this stage. One possible reason is a collapse of "caves" which are formed by mining of deep Si layers. As mentioned above, necessary amount of Si atoms are supplied through the holes. Because the amount is significant, the mining toward lateral directions might be necessary and caves are formed around the holes as illustrated in Fig. 8(c). These caves having 1 BL height would collapse upon prolonged annealing. Then, the surface exhibits the wavy structure in Fig. 7(f). The decrease in the height seen in Fig. 7(f), ~3 Å might support the above possibility.

VI. CODEPOSITION OF Mn AND Si

It has become clear in the present experiments that the surface morphology including the holes and the craters is strongly affected by the processes of the supply of Si atoms. Even if 8/3 ML of Mn is deposited (corresponding to the exact amount for 2 QLs), the top BL can supply only 2.08 ML of Si. Then, 0.59 ML of Si should be supplied through the holes. Suppose that 2.08 ML Mn is deposited, whole Si

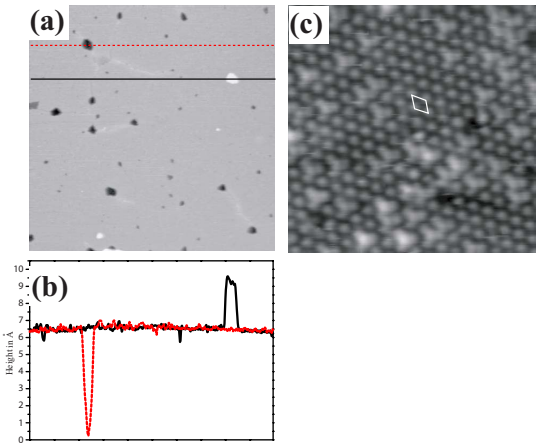

FIG. 9. (Color online) CC mode image of the MnSi surface formed by codeposition followed by annealing at 250 °C (150×150 nm^2). (b) Profiles along solid and dotted lines in (a). (c) A magnified image (10×10 nm^2) of the smooth surface, where the $(\sqrt{3}\times\sqrt{3})$R30° arrangement of protrusions is seen as outlined.

atoms in the top BL can react to form the 2 QL MnSi. However, the craters are formed on the surfaces according to a balance of masses of Mn and Si (see Fig. 4 of Ref. 15). Therefore, it seems impossible to form completely flat surfaces of the MnSi films by the process of Mn deposition and subsequent annealing.

By using LEED, Magnano *et al.*[17] reported previously an improvement of the surface quality of films by means of simultaneous deposition of Mn and Si. Starke *et al.*[18] also found that the quality of LEED patterns of iron silicides was improved by simultaneous deposition of Fe and Si on the Si(111) surface followed by annealing. However, there is no STM report on the improvement of surface morphology by the codeposition. Here, we have successfully prepared highly smooth surfaces of the crystalline MnSi thin films by dosing Si atoms in addition to Mn atoms as shown in STM images (CC mode) of Fig. 9(a). A small number of tiny holes are found but almost entire surface (98%) exhibits an atomically flat MnSi film. Profiles along lines in Fig. 9(a) are depicted in Fig. 9(b). An enlarged image of Fig. 9(c) exhibits the $(\sqrt{3}\times\sqrt{3})$R30° arrangement of protrusions, where some unknown adatoms exist.[12] This smooth surface is prepared as follows: 1.5 ML Si was deposited first; then the deposition of Mn of 3 ML was carried out; finally 1.5 ML Si was deposited again. Then, the sample was annealed at 250 °C for 5 min. In Fig. 9(a), the smooth surface is the second QL of the MnSi because both deposited amounts of Si and Mn are 3 ML, which is close to 8/3 ML required for 2 QLs. Since Si atoms are supplied from outside of the sample, Mn atoms on the surface can react with adsorbed Si atoms to form the MnSi without making holes. Thus, it is confirmed that the formation of the holes on the epitaxially grown MnSi thin films formed by Mn deposition (3 and 5 ML) and subsequent annealing is caused by the necessity of supply of Si atoms to saturate Mn atoms to form the MnSi.

VII. SUMMARY

Mn adsorption followed by annealing at a relatively low temperature of 250 °C on the Si(111)-(7×7) has been studied by STM as well as by LEED and AES. The B20-type structure of the MnSi is formed in processes of the reactive epitaxial growth. Morphological changes in the crystalline MnSi ultrathin films have been investigated by mainly STM for Mn coverage of 1.5, 3, and 5 ML. We summarize important features of the MnSi growth obtained in the present experiments: (1) the minimum thickness of the grown MnSi 2D films is 2 QLs as observed at 1.5 ML-Mn deposition; (2) the MnSi grows with the thickness unit of 1 QL of the B20 structure after the initial 2 QLs formation; (3) Si atoms in the top BL of the original Si(111)-(7×7) surface are used to produce the MnSi 2D islands leaving craters as evidenced at 1.5 ML-Mn deposition; (4) at 3 ML-Mn deposition, the surface is almost flat in atomic scale and mostly covered by 2 QLs of the MnSi; (5) holes going down to the bare Si are created at 3 and 5 ML-Mn depositions; (6) and at 5 ML-Mn deposition, the surface exhibiting discrete layered structures changes to a wavy structure upon prolonged annealing.

Based on the above features, it is noted first that a characteristic mode of crystal growth for compound formation is found in the solid-on-solid system. That is, the crystalline MnSi ultrathin films grow epitaxially as 2 QLs at the initial growth, and the films further grow in a mode of 1-QL-by-1-QL after the initial 2 QLs formation. The reason for the occurrence of this specific growth mode in the epitaxial MnSi ultrathin films is not clear. Theoretical studies are required to solve the problems. Next, we summarize formation processes at each deposition amount of Mn. At 1.5 ML of Mn, the top BL with Si adatoms of the Si(111)-(7×7) reconstruction (2.08 ML) is provided on site for the MnSi formation, while the rest of Si is supplied from nonreacted Si surface leaving craters. At 3 ML, the MnSi covers the entire surface since an appropriate amount of Mn is deposited for the almost complete formation of the 2 QLs MnSi. Additionally necessary amount of Si atoms is supplied by making holes. Thus, most surfaces are atomically flat, although small holes and 2D islands of 3 QLs coexist. At 5 ML, uneven surfaces of the MnSi are formed with holes at short annealing time. After prolonged annealing, the layered structure with discrete heights drastically changes to rather even surfaces. Thus, we found that surface morphology is strongly dependent on the Si supply processes. In order to get more smooth MnSi layers on Si(111), we adopted the procedure of the codeposition of Si and Mn. Anomalously smooth surfaces of ultrathin films of the MnSi are coherently grown, where very low density of holes and 2D islands (only 2% of the surface) is demonstrated by STM. Thus prepared MnSi ultrathin films are expected to have smooth interface structures and therefore their application to the Si-based spintronics is highly hopeful.

ACKNOWLEDGMENTS

This work was supported by the Grants-in-Aid for Scientific Research under Grants No. 19340083, No. 18.06750, and No. 18.9776. P.K. appreciates support from the JSPS.

*tochihar@mm.kyushu-u.ac.jp

[1] G. A. Prinz, Science **282**, 1660 (1998).
[2] S. A. Wolf, D. D. Awschalom, R. A. Buhrman, J. M. Daughton, S. von Molnár, M. L. Roukes, A. Y. Chtchelkanova, and D. M. Treger, Science **294**, 1488 (2001).
[3] H. J. Zhu, M. Ramsteiner, H. Kostial, M. Wassermeier, H.-P. Schönherr, and K. H. Ploog, Phys. Rev. Lett. **87**, 016601 (2001).
[4] M. Ramsteiner, H. Y. Hao, A. Kawaharazuka, H. J. Zhu, M. Kästner, R. Hey, L. Däweritz, H. T. Grahn, and K. H. Ploog, Phys. Rev. B **66**, 081304(R) (2002).
[5] M. Zwierzycki, K. Xia, P. J. Kelly, G. E. W. Bauer, and I. Turek, Phys. Rev. B **67**, 092401 (2003).
[6] A. Kawaharazuka, M. Ramsteiner, J. Herfort, H.-P. Schönherr, H. Kostial, and K. H. Ploog, Appl. Phys. Lett. **85**, 3492 (2004).
[7] M. Hortamani, P. Kratzer, and M. Scheffler, Phys. Rev. B **76**, 235426 (2007).
[8] S. Azatyan, M. Hirai, M. Kusaka, and M. Iwami, Appl. Surf. Sci. **237**, 105 (2004).
[9] S. G. Azatyan, M. Iwami, and V. G. Lifshits, Surf. Sci. **589**, 106 (2005).
[10] D. Y. Wang, H. Y. Wu, L. J. Chen, W. He, Q. F. Zhan, and Z. H. Cheng, J. Phys.: Condens. Matter **18**, 6357 (2006).
[11] M. M. R. Evans, J. C. Glueckstein, and J. Nogami, Phys. Rev. B **53**, 4000 (1996).
[12] A. Kumar, M. Tallarida, M. Hausmann, U. Starke, and K. Horn, J. Phys. D **37**, 1083 (2004).
[13] T. Nagao, S. Ohuchi, Y. Matsuoka, and S. Hasegawa, Surf. Sci. **419**, 134 (1999).
[14] T. Shirasawa, S. Higashi, H. Tochihara, W. Voegeli, and T. Takahashi, 64th Annual Meeting Abstracts of the Physical Society of Japan, 2009, Vol. 64, 4–871.
[15] S. Higashi, Y. Ikedo, P. Kocán, and H. Tochihara, Appl. Phys. Lett. **93**, 013104 (2008).
[16] S. Higashi, T. Ohshima, S. Mizuno, and H. Tochihara, Surf. Sci. **600**, 591 (2006).
[17] E. Magnano, E. Carleschi, A. Nicolaou, T. Pardini, M. Zangrando, and F. Parmigiani, Surf. Sci. **600**, 3932 (2006).
[18] U. Starke, W. Weiss, M. Kutschera, R. Bandorf, and K. Heinz, J. Appl. Phys. **91**, 6154 (2002).

4. Desorpce kovů z povrchu Si(111)

4.1 Interakce thallia s povrchem Si(111)

Zájem o systém Tl/Si(111) vzbudilo nedávno pozorované rozštěpení spinu (Rashba efekt [1]) vlivem spin-orbitální interakce. Elektron pohybující se v elektrickém poli vznikajícím v důsledku gradientu elektrostatického potenciálu u povrchu vnímá díky relativistickým transformacím toto pole jako magnetické, ve kterém následně dochází k Zeemanovu jevu, tedy rozštěpení spinů. V tomto případě se jednalo o první pozorování Rashba efektu na povrchu polovodiče.

Thallium (Tl) je nejtěžším prvkem IIIA skupiny periodické tabulky. Oproti ostatním kovům této skupiny se díky efektu inertního páru elektronů vyskytuje i v mocnosti 1^+. To se projevuje i v interakci Tl s povrchem Si(111). Zatímco ostatní kovy IIIA skupiny jsou v povrchových rekonstrukcích nejčastěji zastoupené v trojmocném stavu (nejtypičtější rekonstrukcí je $\sqrt{3}\times\sqrt{3}$), Tl po depozici jedné monovrstvy a ohřevu $\sim 300°$C vytvoří rekonstrukci 1×1. V této struktuře je ideálně zakončený Si(111) povrch pokryt atomy Tl v pozicích T_4 [2, 3, 4]. Charakter vazby je převážně iontový, trčící vazby povrchových Si atomů jsou saturovány přesunem náboje z Tl vrstvy [4]. Důsledkem tohoto přesunu náboje je polovodivý charakter vrstvy se zakázaným pásem ~ 0.34 eV [4].

Další významnou vlastností tohoto systému je nízká desorpční teplota Tl z povrchu - desorpce začíná už při 350°C [5]. Jelikož je v rekonstrukci 1×1 povrch Si(111) ideálně zakončen, vzniká po jeho obnažení během desorpce situace podobná štípání krystalu ve vakuu. Poměrně jednoduše lze tak studovat metastabilní struktury na povrchu Si a jejich vývoj. Díky nízké desorpční teplotě je možné využít vrstvu Tl jako surfaktant při reakci povrchu s jinými kovy (M). V takovém případě Tl usnadní reakci s povrchem tím, že zruší 7×7 rekonstrukci, což obecně představuje značnou kinetickou bariéru, a při ohřevu nad 350°C Tl desorbuje dříve než kov M. Tl tedy vstoupí do reakce a usnadní ji, a zároveň ve výsledné vrstvě není zastoupeno.

4.2 Kovový charakter Tl monovrstvy

Podobně jako systém MnSi/Si(111) (viz kap. 3), je i Tl vrstva na povrchu Si(111) slibným kandidátem coby spin injektující materiál, z důvodu rozštěpení spinu vlivem Rasha efektu, jak je zmíněno výše. Nehomogenita povrchu zde nepředstavuje problém, na druhou stranu komplikací je nekovový charakter vrstvy,

znemožňující pochopitelně přenos polarizovaných nábojů. Povrchový stav protínající Fermiho mez byl doposud pozorován v případě monovrstvy Pb na povrchu Ge(111) [6], ale ne na technologicky zajímavějším povrchu Si(111). V Publikaci P13 referujeme o překvapivě kovovém charakteru Tl monovrstvy pozorovaném pomocí STM a STS, v rozporu s DFT výpočty, předpovídajícími zakázaný pás. Na STM obrázcích měřených v těsné blízkosti Fermiho meze je patrná lokalizace „kovového“ stavu v okolí defektů vznikajících spolu s 1×1-Tl rekonstrukcí. Na základě STM dat byl navržen strukturní model těchto defektů, sestávající z jednoho Si adatomu v T_4 pozici, který saturuje tři trčící vazby povrchu, a tím blokuje šest sousedních pozic pro adsorpci Tl. V důsledku zůstávají některé Si vazby na okraji šestiúhelníkového defektu nedokonale nasycené, a mohou tak způsobit dopování 2D vrstvy. Tunelová spektra ale neukazují jenom posuv Fermiho meze, očekávaný v případě dopované vrstvy, ale úplné vymizení zakázaného pásu. Vliv defektů na elektronickou strukturu 1×1-Tl vrstvy je proto patrně složitější - přítomnost defektu pravděpodobně indukuje strukturní relaxaci vrstvy, která je spojená s delokalizací povrchových elektronů. Detailní informaci o změnách vrstvy způsobených přítomností defektů mohou poskytnout pouze DFT simulace.

4.3 Strukturní změny během desorpce

Jak již bylo řečeno, jednou ze zajímavých vlastností rekonstrukcí Tl-Si(111) je jednomocný charakter struktury 1×1 odpovídající pokrytí jednou monovrstvou. Při snížení pokrytí Tl byla pozorována rekonstrukce Si(111)$\sqrt{3}\times\sqrt{3}$ -Tl, z analogie s jinými trojmocnými kovy tvořícími tuto rekonstrukci bylo předpokládáno, že Tl atomy jsou v této struktuře v trojmocném stavu [4]. Nicméně, na základě fotoemisních experimentů, ukazujících odlišný typ vazby ve srovnání s jinými kovy IIIA skupiny [7] a monovalentní charakter, vznikla kontroverze ohledně valenčního stavu Tl v této struktuře [8]. I přes množství studií zabývajících se povrchem Si(111)$\sqrt{3}\times\sqrt{3}$ -Tl a jeho souvislostí se strukturou Si(111)1×1-Tl nebyla atomární struktura nikdy spolehlivě určena.

V práci P14 jsme využili techniky STM k zobrazení morfologie povrchu Si(111)-Tl v jednotlivých stadiích během desorpce Tl. Prvním významným zjištěním bylo pozorování, že už během počátečního stádia vzniku $\sqrt{3}\times\sqrt{3}$ struktury ve formě malých ostrůvků, je značná část atomů této struktury substituovaná atomy Si. Při úplném pokrytí rekonstrukcí $\sqrt{3}\times\sqrt{3}$ je pozorována mozaika Si a Tl atomů, poměr Tl:Si je zhruba 1:1. Jinými slovy, oproti původním očekáváním, $\sqrt{3}\times\sqrt{3}$ struktura s $\frac{1}{3}$ ML Tl není na povrchu přítomna v žádném stadiu desorpce, čímž

se opět liší od ostatních kovů IIIA skupiny. Podotkněme, že depozice $\frac{1}{3}$ ML Tl na povrch Si(111)7×7 a následný ohřev mají za následek vznik oblastí nestejnoměrně pokrytých Tl: 1×1 (1 ML) a 7×7 s klastry Tl (méně než $\frac{1}{3}$ ML). Zdá se, že přítomnost substitučních Si atomů je nutným stabilizačním prvkem této struktury. V průběhu pokračující desorpce Tl vznikají na povrchu metastabilní rekonstrukce Si, především c(2×8), c(2×4), (9×9), (5×5).

STM data popsaná v práci P14 umožnila určit desorpční závislot Tl pokrytí Θ na teplotě T při konstantním intervalu ohřevu. Křivku lze proložit jednoduchou závislostí

$$\Theta = \Theta_0 \exp(-Rt), \quad R = \nu \exp(-E_{des}/k_B T), \tag{4.1}$$

kde Θ_0 je výchozí pokrytí, t doba ohřevu, ν frekvenční prefaktor, R je rychlost desorpce daná desorpční energií E_{des} a k_B je Boltzmannova konstanta. Tato jednoduchá křivka vyhovuje rozsahu pokrytí, která odpovídají jak struktuře 1×1, tak $\sqrt{3}\times\sqrt{3}$. Jinými slovy, desorpční rychlost R zde není překvapivě závislá na struktuře, v jaké se Tl nachází, energetická bariera pro desorpci Tl z 1×1 je v rámci chyby stejná jako z $\sqrt{3}\times\sqrt{3}$. Z toho lze vyvodit, že vazebný stav Tl v obou strukturách je stejný - tedy i v rekonstrukci $\sqrt{3}\times\sqrt{3}$ jsou atomy Tl jednomocné a charakter vazby je silně iontový. Nedostatek elektronů pro saturaci volných Si vazeb je potom kompenzován množstvím substitučních Si atomů.

4.4 KMC simulace

Problematikou vzniku rekonstrukce $\sqrt{3}\times\sqrt{3}$ z fází odpovídajících jedné monovrstvě kovů na povrchu Si(111) se hlouběji zabývá práce P15. Zavedení kinetického modelu strukturní změny během desorpce kovu z povrchu umožnilo porovnat dva vybrané kvalitativně odlišné systémy - Si(111)-Pb a Si(111)-Tl. V případě Tl byla tato transformace experimentálně pozorována v práci P14 a popsána v části 4.3. Na rozdíl od Tl, vznikají během desorpce Pb dvě odlišné fáze, historicky nazvané β a γ (těsně uspořádaná 1×1 byla označena jako α), v prvním případě se jedná o povrch pokrytý $\frac{1}{3}$ ML atomů Pb v T_4 pozicích, v případě druhém o mozaiku Pb a Si atomů v poměru 1:1. Během transformací $\alpha \rightarrow \beta \rightarrow \gamma$ byl překvapivě pozorován nultý řád desorpce [9, 10, 11, 12].

Nultý řád indikuje neobvyklé chování, při kterém rychlost desorpce $d\Theta/dt$ nezávisí na množství materiálu Θ. V literatuře [13] je navržen mechanismus desorpce nultého řádu, spočívající v dynamické rovnováze mezi dvěma fázemi, z nichž jedna (desorbující fáze) má charakter 2D plynu. Takové vysvětlení však u systémů kov/Si selhává vzhledem k nedostatečné difuzivitě po tomto povrchu.

V práci P15 je ukázáno, že s využitím jednoduchých kinetických procesů lze získat desorpčí spektra odpovídající nultému řádu. Postačující podmínkou je rozlišit pravděpodobnost desorpce pro atomy s různě obsazeným nejbližším okolím (konfigurace) a zavedení fyzikálně opodstatněné pravděpodobnější desorpce z neuspořádaných konfigurací. Rostoucí množství atomů v neuspořádaných konfiguracích během strukturních změn má za následek charakter desorpčních spekter konzistentní s nultým řádem desorpce.

Dalším kinetickým problémem vhodným pro Monte Carlo simulaci je mechanismus uspořádávání mozaikové struktury složené z Si a M adatomů, kde M je kov, typicky Sn, Pb nebo Tl. Rozmístění jednotlivých atomů v mozaikové struktuře není náhodné, ale reflektuje repulzivní interakci mezi atomy stejného typu. Díky tomu tento systém představuje 2D realizaci Isingova spinového modelu [14, 15, 16]. V práci P15 ukazujeme, že experimentálně pozorovaných rozdělení počtů nejbližších sousedů v mozaikové struktuře lze přirozeně docílit selektivní desorpcí - kdy desorpční energie je funkcí počtu nejbližších sousedů stejného typu. Naopak doposud navrhovaný model difúzně řízeného uspořádání mozaiky se ukázal nevyhovujícím.

4.5 Navazující práce

Přestože byly práce P13-P15 publikovány až v posledních letech, lze najít několik zajímavých výsledků týkajících se zmíněné problematiky. Díky výjimečným vlastnostem povrchu Si(111)-1×1-Tl lze očekávat, že zájem o studium tohoto povrchu dále poroste. V současnosti je například studována možnost využití tohoto povrchu coby podložky pro růst dalších nanostruktur, s výhodami povrchu křemíku (snadná příprava a dobrá definovanost), ale díky saturaci všech povrchových vazeb nesoucí některé parametry kovových povrchů, především vysokou difuzivitu adsorbovaných atomů nebo molekul. Díky nízké desorpční teplotě lze navíc Tl vrstvu využít jako surfaktantu, který usnadní uspořádání na povrchu, aniž by byl ve výsledném produktu přítomen.

Značné pozornosti se pochopitelně těší elektronová struktura povrchu Si(111)-1×1-Tl v souvislosti s přítomností defektů. V práci [17] jsou pomocí spinově i úhlově rozlišené inverzní fotoelektronové spektroskopie v kombinaci s ab-initio výpočty studovány neobsazené stavy tohoto povrchu. Tyto neobsazené stavy mají charakter Diracových kuželů a jsou stoprocentně spinově polarizované. V zásadní práci [18] je dále studován vliv defektů na elektronovou strukturu vrstvy Si(111)-1×1-Tl pomocí spinově rozlišené fotoelektronové spektroskopie. Je diskutováno,

že defekty, v tomto případě pocházející od nadbytečných atomů Tl, posouvají původně neobsazené stavy pod Fermiho mez. Vzhledem k C3 symetrii povrchu je polarizace opačná v $\overline{\mathrm{K}}$ a $\overline{\mathrm{K}}$' bodech reciprokého prostoru. Autoři diskutují, že díky této opačné polarizaci je potlačen nežádoucí rozptyl elektronů, což otevírá cestu k spintronickému využití povrchu Si.

Jiná strategie získání vodivého spinově polarizovaného stavu je navržena a studována v [19]. Strategie spočívá ve vytvoření povrchové slitiny atomů se silnou spin-orbitální interakcí (např. Tl) s jiným kovem, který umožní hustější uspořádání atomů ve 2D vrstvě. Toto těsnější uspořádání má za následek „propojení" elektronových stavů a tudíž i vodivý charakter vrstvy. Tento postup autoři aplikují v rámci dvou systémů - Si(111)-1×1-Tl s extra atomy Pb, tvořící Si(111)$\sqrt{3}\times\sqrt{3}$ -Tl,Pb s povrchovou hustotou kovových atomů $\frac{4}{3}$ ML, a v případě Si(111)-$\sqrt{3}\times\sqrt{3}$ -B s extra Na atomy.

Literatura

[1] Y. Bychkov and E. Rashba, "Properties of a 2D electron gas with lifted spectral degeneracy," *JETP lett*, vol. 39, no. 2, p. 78, 1984.

[2] T. Noda, S. Mizuno, J. Chung, and H. Tochihara, "T 4 Site Adsorption of Tl Atoms in a Si(111)-(1x1)-Tl Structure, Determined by Low-Energy Electron Diffraction Analysis," *Jpn. J. Appl. Phys.*, vol. 42, pp. L319–L321, Mar. 2003.

[3] N. Kim, C. Hwang, J. Chung, T. Kim, H. Kim, and D. Noh, "Structural properties of a thallium-induced Si(111)-1x1 surface," *Phys. Rev. B*, vol. 69, p. 195311, May 2004.

[4] S. Lee, H. Song, N. Kim, J. Chung, K. Kong, D. Ahn, H. Yi, B. Yu, and H. Tochihara, "Structural and electronic properties of thallium overlayers on the Si(111)-7x7 surface," *Phys. Rev. B*, vol. 66, p. 233312, Dec. 2002.

[5] V. Kotlyar, A. Saranin, A. Zotov, and T. Kasyanova, "Thallium overlayers on si(111) studied by scanning tunneling microscopy," *Surf. Sci.*, vol. 543, p. L663, 2003.

[6] Y. Ohtsubo, S. Hatta, H. Okuyama, and T. Aruga, "A metallic surface state with uniaxial spin polarization on Tl/Ge(111)-(1x1).," *J. Phys. Condens. Matter*, vol. 24, p. 092001, Mar. 2012.

[7] K. Sakamoto, P. Eriksson, N. Ueno, and R. Uhrberg, "Photoemission study of a thallium induced surface," *Surf. Sci.*, vol. 601, pp. 5258–5261, Nov. 2007.

[8] K. Sakamoto, P. E. J. Eriksson, S. Mizuno, N. Ueno, H. Tochihara, and R. I. G. Uhrberg, "Core-level photoemission study of thallium adsorbed on a Si(111)-(7x7) surface: Valence state of thallium and the charge state of surface Si atoms," *Phys. Rev. B*, vol. 74, p. 075335, Aug. 2006.

[9] E. Ganz, F. Xiong, I.-S. Hwang, and J. Golovchenko, "Submonolayer phases of Pb on Si(111)," *Phys. Rev. B*, vol. 43, p. 7316, 1991.

[10] M. Saitoh, K. Oura, K. Asano, F. Shoji, and T. Hanawa, "Low energy ion scattering study of adsorption and desorption processes of Pb on Si (111) surfaces," *Surf. Sci.*, vol. 154, pp. 394–416, 1985.

[11] J. Carlisle, T. Miller, and T. Chiang, "Photoemission study of the growth, desorption, Schottky-barrier formation, and atomic structure of Pb on Si (111)," *Phys. Rev. B*, vol. 45, no. 7, pp. 3400–3409, 1992.

[12] E. Ganz, H. Ing-Shouh, X. Fulin, S. K. Theiss, and J. Golovchenko, "Growth and morphology of Pb on Si(111)," *Surf. Sci.*, vol. 257, pp. 259–273, Nov. 1991.

[13] H. Kreuzer and S. Payne, "Desorption from a two-phase adsorbate: Zero or fractional order," *Surf. Sci.*, vol. 200, pp. 433–440, 1988.

[14] M. Švec, P. Jelínek, P. Shukrynau, C. González, V. Cháb, and V. Drchal, "Local atomic and electronic structure of the PbSi(111) mosaic phase: STM and ab initio study," *Phys. Rev. B*, vol. 77, p. 125104, Mar. 2008.

[15] L. Ottaviano, B. Ressel, C. Di Teodoro, G. Profeta, S. Santucci, V. Cháb, and K. Prince, "Short-range order in two-dimensional binary alloys," *Phys. Rev. B*, vol. 67, p. 045401, Jan. 2003.

[16] J. M. Carpinelli, H. H. Weitering, and E. W. Plummer, "Charge rearrangement in the GexPb1-x/Ge (111) interface," *Surf. Sci.*, vol. 401, pp. L457–L463, 1998.

[17] S. D. Stolwijk, A. B. Schmidt, M. Donath, K. Sakamoto, and P. Krüger, "Rotating Spin and Giant Splitting: Unoccupied Surface Electronic Structure of Tl/Si(111)," *Phys. Rev. Lett.*, vol. 111, p. 176402, Oct. 2013.

[18] K. Sakamoto, T.-H. Kim, T. Kuzumaki, B. Müller, Y. Yamamoto, M. Ohtaka, J. R. Osiecki, K. Miyamoto, Y. Takeichi, A. Harasawa, S. D. Stolwijk, A. B. Schmidt, J. Fujii, R. I. G. Uhrberg, M. Donath, H. W. Yeom, and

T. Oda, "Valley spin polarization by using the extraordinary Rashba effect on silicon.," *Nat. Commun.*, vol. 4, p. 2073, Jan. 2013.

[19] D. V. Gruznev, L. V. Bondarenko, A. V. Matetskiy, A. a. Yakovlev, A. Y. Tupchaya, S. V. Eremeev, E. V. Chulkov, J.-P. Chou, C.-M. Wei, M.-Y. Lai, Y.-L. Wang, A. V. Zotov, and A. a. Saranin, "A strategy to create spin-split metallic bands on silicon using a dense alloy layer.," *Sci. Rep.*, vol. 4, p. 4742, Jan. 2014.

PHYSICAL REVIEW B **84**, 233304 (2011)

Metallic-like thallium overlayer on a Si(111) surface

Pavel Kocán,* Pavel Sobotík, and Ivan Ošt'ádal
Charles University in Prague, Faculty of Mathematics and Physics, Department of Surface and Plasma Science, V Holešovičkách 2, 180 00 Praha 8, Czech Republic

(Received 21 April 2011; revised manuscript received 7 June 2011; published 14 December 2011)

A (1×1) ordered monolayer of thallium atoms on a Si(111) surface has promising potential as a material generating spin-polarized electrons [Sakamoto *et al.*, Phys. Rev. Lett. **102**, 096805 (2009)]. In an ideal form the surface is nonmetallic [Lee *et al.*, Phys. Rev. B **66**, 233312 (2002)]. Our scanning-tunneling microscopy and spectroscopy study of the (1×1)-Tl surface shows clearly its metallic-like character. On the surface, intrinsic regularly shaped defects with increased density of states near the Fermi level are observed. The relationship between the presence of the defects, which we interpret as Tl multivacancies induced by Si adatoms, and metallicity of the layer is briefly discussed.

DOI: 10.1103/PhysRevB.84.233304 PACS number(s): 68.37.Ef, 68.55.Ln, 73.20.Hb

A great challenge nowadays is to provide background for utilizing the spin of electrons in new devices. Recently, Rashba spin splitting was reported for the Pb/Ge(111) system[1] with the split band crossing the Fermi level. In applications, compatibility of spintronic elements with silicon technology would be a significant advantage. On a silicon substrate, Rashba spin splitting was observed in the case of a Tl/Si(111)-(1×1) surface.[2] However, this surface is not metallic-like, and transfer of spin-polarized electrons is difficult. Thus, motivation is high for studying possibilities of doping the surface on an atomic level.

With miniaturization of semiconductor electronic elements trending downward to sizes of hundreds of interatomic lengths, each individual dopant becomes crucial to a component's functioning.[3] The possibility of mapping dopants on an atomic scale is therefore of great value.[4]

Deposition of one monolayer (ML, 7.83×10^{14} atoms cm^{-2}) of Tl on a Si(111) surface and annealing to 300–350 °C results in formation of a (1×1) Tl reconstruction. Its structure has been studied by various techniques: low-energy electron diffraction,[5] synchrotron x-ray scattering,[6] and *ab initio* calculations.[7] It is agreed that Tl atoms occupy T_4 sites of a bulk-terminated Si(111) surface. The structure is stabilized by a charge transfer from the Tl adlayer to the topmost silicon atoms, Tl $6p$ electrons are partially donated to dangling bonds of the Si atoms, which become fully saturated.[7] According to angle-resolved photo-emission spectroscopy and calculations using density-functional theory (DFT), the Tl/Si(111)-(1×1) surface is semiconducting with a band gap of 0.34 eV.[7] Scanning tunneling spectroscopy (STS) on the Tl/Si(111)-(1×1) surface reported by Vitali *et al.*[8] supported the semiconducting character with a surface state band gap of ∼0.5 eV.

If surface concentration of Tl atoms is decreased by desorption from the (1×1) layer, a Tl/Si(111)-($\sqrt{3}\times\sqrt{3}$) reconstruction forms.[7] A band gap of 0.3 eV was calculated for this structure,[9] in agreement with results of a photoemission study.[10]

In both (1×1) and ($\sqrt{3}\times\sqrt{3}$) phases, Tl $6s^2$ electrons are chemically inactive[11] due to a so called inert pair effect, making the Tl behavior different from the other—strictly trivalent—group III metals.

In the case of the Tl/Ge(111)-(1×1) surface, which is isoelectronic to Tl/Si(111)-(1×1), a band crossing the Fermi level was observed by angle-resolved photo-emission spectroscopy (ARPES).[12] Because *ab initio* calculations did not confirm the metallic character, the authors proposed that the band crossing the Fermi level is caused by intrinsic Tl vacancies acting as acceptor dopants.[12]

In this Brief Report we present observations of the metallic-like Tl/Si(111)-(1×1) surface, as revealed by scanning-tunneling microscopy (STM) and spectroscopy. On the surface, we recognize ring-shaped objects, the structure of which is discussed. Following the proposals for the Tl/Ge(111)-(1×1) surface we discuss possible doping behavior of these objects.

For experiments, Si(111) samples (Sb doped, with a resistivity of 0.005–0.01 Ω cm) were cleaned by flashing to 1200 °C. Thallium (purity 99.999%) was evaporated onto the silicon surface at room temperature, with the amount controlled by a quartz thickness monitor. The Tl/Si(111)-(1×1) surface was prepared by heating the sample with one predeposited monolayer of Tl to 300 °C for 2 min. The STM and STS measurements were performed by using a non-commercial scanning tunneling microscope in an ultrahigh-vacuum chamber with base pressure $< 3\times10^{-9}$ Pa. The pressure during the Tl deposition was in the 10^{-8} Pa order. STS curves were obtained using a lock-in technique (∼10 s per spectrum), and the reported data were averaged over several equivalent spectra normalized by I/V. Noise in the data near the Fermi level was suppressed by a procedure noted in Ref. 13. In addition, fast $I(V)$ curves (∼50 ms per curve) were measured separately. All presented data were acquired at room temperature.

First we focus on STM imaging of the Tl/Si(111)-(1×1) surface. An STM image of the Si(111) surface after deposition of 1 ML of Tl and subsequent annealing to ∼300 °C is shown in Fig. 1(a). On the terraces, many craterlike objects are observed. Most of the objects are regularly ring shaped, and others are formed by several ring-shaped objects merging together. Typically, concentration of the objects (hereafter called defects) is in the range of 0.5–1 × 10^{13} cm^{-2}.

To study the influence of preparation conditions on formation of the defects, different preparation procedures were tested as well: deposition of 1 ML of Tl on a surface held at 300 °C,

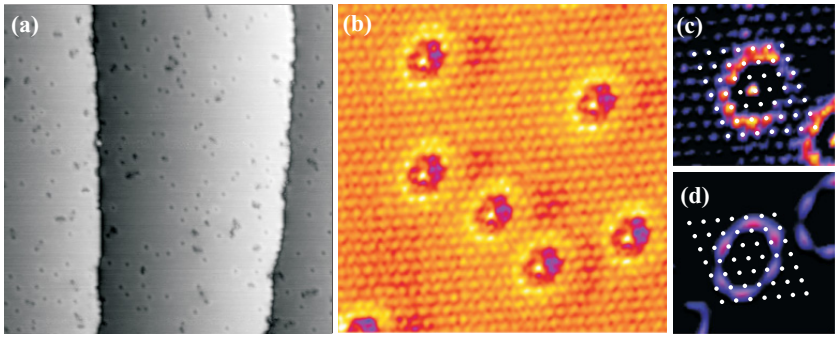

FIG. 1. (Color online) (a) Empty-state STM image of the (1 × 1) surface with defects (area 50 × 50 nm^2, sample voltage $U_s = 0.2$ V, and $I = 0.7$ nA). (b) Detail of the (1 × 1) structure with ring-shaped defects (area 7 × 7 nm^2, $U_s = 9$ mV, and $I = 2.2$ nA). (c) Detail of the defect, zoomed out from (b) (area 2.7 × 2.7 nm^2). (d) The same scale as in (c) but recorded at $U_s = 0.44$ V. The color contrast is adjusted to highlight a ring surrounding the defect. Dots in (c) and (d) mark equivalent positions in the 1×1 grid.

varying the temperature to a lower limit of (1×1) formation, and deposition of slightly more or less than 1 ML. All the procedures resulted in the presence of the defects once the (1×1) structure was formed, and the concentration of the defects was not observed to depend strongly on the preparation procedure.

A detail (7×7 nm^2) of the surface obtained at a significantly low sample-tip bias of 8 mV is shown in Fig. 1(b). The (1×1) reconstruction is clearly visible together with the ring-shaped defects. A magnified detail (2.7×2.7 nm^2) of a defect taken from Fig. 1(b) is shown in Fig. 1(c). On the image, the defect is dominated by 12 spots of the 1×1 pattern forming a ring brighter than the 1×1 protrusions far from the defects. We note that the bright ring is not a result of STM feedback, since the same images are observed in both scanning directions (not shown). The most probable explanation of the bright ring lies in the surface states originating from the presence of the defects. In the middle of the ring, another bright protrusion is observed. This central protrusion is visible only at low sample voltage, disappears at ∼±200 mV, and is not reproduced at all tip apex conditions. The area between the central protrusion and the surrounding ring appears darker than the 1×1 surface far from the defects. A detail of the defect obtained with the same tip as in Fig. 1(c) but at higher sample voltage (0.44 V) is shown in Fig. 1(d). The size and orientation of the defect is the same as in Fig. 1(c). At this voltage, the 1×1 corrugation and the central protrusion disappear, and the apparent shape of the ring is different, now being composed of six prolonged protrusions. When imaging occupied states close to the Fermi level (sample voltage ∼−40 mV), the STM pattern of the defect (not shown) is similar to that at low positive voltages: a highlighted ring surrounding a crater. The 1×1 pattern is less corrugated at the negative biases. At higher negative sample voltages (∼−0.2 V), the bright ring disappears and the defect looks like a hole on the surface.

Over the STM details of defects in Figs. 1(c) and 1(d), the 1×1 grid of white dots is superimposed as a guide. For discussion of a structural model, we suppose that these dots and the corresponding protrusions in Fig. 1(c) are located in the T_4 sites occupied by the Tl atoms.[14]

STM imaging at a bias of a few millivolts is the first indication that the surface is metallic, in contradiction with the reported ARPES and STM results and with *ab initio* calculations.[7,8] In order to show the surface metallicity, we measured dI/dV tunneling spectra near the Fermi level. STS taken at a (1×1) area is shown in Fig. 2(a) by the solid line. For comparison, a spectrum taken at a Tl-($\sqrt{3} \times \sqrt{3}$) area by the same tip and under the same conditions is shown by the broken line in Fig. 2(a). The ($\sqrt{3} \times \sqrt{3}$) area was locally formed on the otherwise (1×1) surface with defects, as shown in Fig. 2(b). The STS spectra from Tl-($\sqrt{3} \times \sqrt{3}$) exhibit a band gap of ∼0.4 eV, which is in a good agreement with a value of 0.3 eV measured[10] and calculated[9] previously. In contrast, the surface local density of states of the (1×1) area is nonzero at the Fermi level. The increase of density of states at negative and positive sample voltages is possibly related to the surface states S_1 and S_2 from Ref. 7, respectively.[15] In addition to the spectra measured by the lock-in technique that are in principle sensitive to a phase shift between the reference and measured signals, we recorded a fast (50 ms per curve) I-V

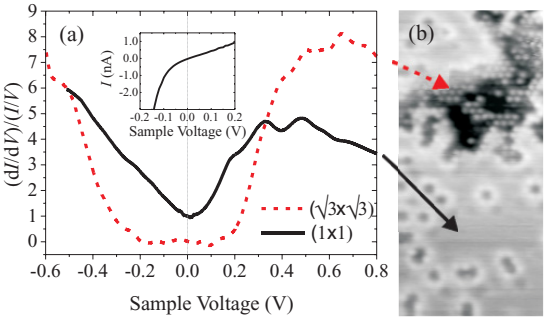

FIG. 2. (Color online) (a) Normalized tunneling spectra $(dI/dV)/(I/V)$ on the (1×1) (solid line) and ($\sqrt{3} \times \sqrt{3}$) (broken line) surfaces, showing nonzero density of states of the (1×1) surface at the Fermi level. Inset: fast I-V characteristic measured separately on the (1×1) surface. (b) STM image of the surface with coexisting (1×1) (solid arrow) and ($\sqrt{3} \times \sqrt{3}$) (broken arrow) areas, used for measuring $(dI/dV)/(I/V)$ data in (a). Image size 9×18 nm^2, $U_s = 1.0$ V.

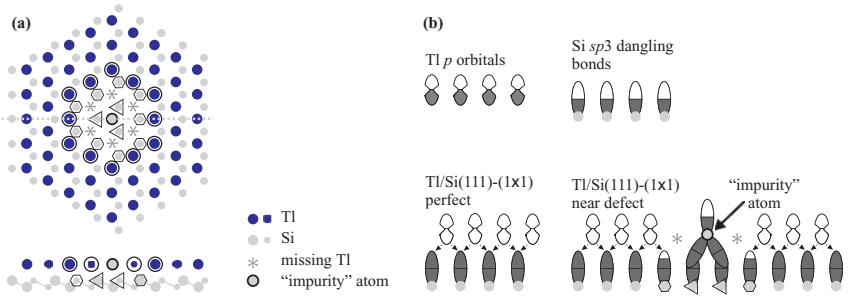

FIG. 3. (Color online) (a) Top and side schematic views of a possible model of Tl multivacancy observed on the (1×1) surface. Dark and light circles denote Tl and Si atoms, respectively. Selected positions are marked. Triangles: Si atoms to which central "impurity" atom is bonded. Asterisks: Tl vacancies. Hexagons: Si atoms with less than three Tl neighbors. Large circles: Tl atoms forming a ring shape on the STM images. (b) A simple electron bond filling scheme of surface orbitals (depicted by ovals) near the vacancy. Occupation of orbitals is represented by gray shading.

characteristic on the (1×1) surface. The result is shown in the inset of Fig. 2(a). Obviously, slope of the $I(V)$ curve at zero bias (Fermi level) is nonzero, showing the metallicity of the surface.

We continue by discussing the possible origin of the defects. First we exclude simple Tl vacancies because the defects were observed even at deposited amounts exceeding one monolayer. Another possible origin of the defect could be a relic of the 7×7 reconstruction containing a structural fault.[16] However, concentration of such defects would depend on annealing temperature, in contrast to our experimental findings. Thus, impurity atoms are likely to be responsible for the defects. The first possible impurity would be Sb, because we used highly Sb-doped samples for experiments. However, volume dopant concentration in the samples was ∼0.01%, which is not sufficient for the observed surface concentration (∼1%) of the defects. A significant segregation of Sb at surface could be excluded, because Sb desorbs from the Si(111) surface at ∼750 °C[17] and the sample was annealed to 1200 °C prior to every experiment. The most probable "impurities" in the Tl layer remain Si atoms residual of the Si-rich (7×7) reconstruction. We note that Si adatoms tend to substitute for Tl atoms during Tl desorption, which results in formation of a mosaic $(\sqrt{3}\times\sqrt{3})$ surface.[18] Moreover, isolated Si adatoms from the $(\sqrt{3}\times\sqrt{3})$ mosaic[18] resemble the defects shown in Fig. 1(b). Even though we cannot completely exclude other impurities causing defects (e.g., from residual atmosphere), Si adatoms seem to be the most probable.

A possible structural model of the ring-shaped defects is schematically depicted in Fig. 3(a). In the figure, the light and dark circles denote Si and Tl atoms, respectively. Assume an "impurity" Si adatom is adsorbed instead of Tl in the central T_4 position, marked by the light-filled dark-outlined circle in Fig. 3(a). The adatom saturates dangling bonds of three nearest surface Si atoms (marked by triangles). As the dangling bonds are saturated, six T_4 positions neighboring the saturated Si atoms are not occupied by Tl atoms (the vacancies are marked by asterisks). Nine Si atoms marked by hexagons neighbor only two or one Tl atoms, while in the perfect (1×1) structure there are three neighbors. We note that a similar model with the central impurity adatom adsorbed in the H_3 position can be constructed as well. In that case, the protrusions forming the ring [with the same size as the ring in Fig. 3(a)] and the 1×1 protrusions would appear in the H_3 positions. To confirm one of the two models, *ab initio* calculations would be needed.

Next we discuss a possible influence of the multivacancy defect on the surface properties. A simplified charge-transfer consideration of the atomic arrangement is schematically depicted in Fig. 3(b). Before the interaction, Tl p orbitals and dangling bonds of an ideal Si(111)-(1×1) termination are half filled [top of Fig. 3(b)]. During formation of the perfect Tl/Si(111)-(1×1) reconstruction, every Si dangling bond is saturated by a charge transferred from the Tl orbitals [effectively one third of electrons from each of the three neighboring Tl atoms; bottom left of Fig. 3(b)].[7] According to DFT calculations of an isoelectronic Tl/Ge(111)-(1×1) surface,[12] the Tl 6p state is not emptied completely; the highest occupied surface state has partial $p_x + p_y$ character and is separated by a band gap from the lowest unoccupied band. If a Tl vacancy is created, the neighboring Si atoms (marked by hexagons in Fig. 3) lack the charge from the missing Tl atoms, as indicated in the right-hand-side bottom part of Fig. 3(b). This charge deficit can possibly be partially balanced by redistribution of charge from the next nearest neighboring Si dangling bonds, from the partially occupied Tl $6p_x + p_y$, orbitals, or by charge transfer from the "impurity" atom orbitals. Such charge transfer may be accompanied by relaxation of atomic positions and by relief of strain in the epitaxial layer. The structural relaxation and charge redistribution may result in significant modification of the density of states at the Fermi level.

In Ref. 12, a hole-doping behavior of Tl vacancies was proposed to explain photoemission results. In such cases, the position of the Fermi level would be shifted to the valence band. From our STS observation, we cannot confirm this simple picture, since the band gap is not shifted but is completely reduced. Our results suggest that the metallic-like character of the surface is a consequence of more complex surface structural relaxation and charge redistribution.

In conclusion, observation of the metallic character of the Tl/Si(111)-(1×1) surface is reported in contrast with the previous experimental and theoretical work. The regularly shaped vacancies observed on the surface are proposed to be

responsible for metallicity of the 2D adlayer. The Tl vacancies give arise to an increase of the density of states near the Fermi level as measured by STS. Consequently, the dopants can be mapped by STM at very low biases.

This work was supported by The Grant Agency of the Czech Republic, Project No. 202/09/P033 of GACR and by research plan No. MSM 0021620834 financed by the Ministry of Education of Czech Republic.

*pavel.kocan@mff.cuni.cz

[1]K. Yaji, Y. Ohtsubo, S. Hatta, H. Okuyama, K. Miyamoto, T. Okuda, A. Kimura, H. Namatame, M. Taniguchi, and T. Aruga, Nature Commun. **1**, 17 (2010).

[2]K. Sakamoto, T. Oda, A. Kimura, K. Miyamoto, M. Tsujikawa, A. Imai, N. Ueno, H. Namatame, M. Taniguchi, P. E. J. Eriksson, and R. I. G. Uhrberg, Phys. Rev. Lett. **102**, 096805 (2009).

[3]S. Roy and A. Asenov, Science **309**, 388 (2005).

[4]M. R. Castell, D. A. Muller, and P. M. Voyles, Nature Mater. **2**, 129 (2003).

[5]T. Noda, S. Mizuno, J. W. Chung, and H. Tochihara, Jpn. J. Appl. Phys. **42**, L319 (2003).

[6]N. D. Kim, C. G. Hwang, J. W. Chung, T. C. Kim, H. J. Kim, and D. Y. Noh, Phys. Rev. B **69**, 195311 (2004).

[7]S. S. Lee, H. J. Song, N. D. Kim, J. W. Chung, K. Kong, D. Ahn, H. Yi, B. D. Yu, and H. Tochihara, Phys. Rev. B **66**, 233312 (2002).

[8]L. Vitali, M. G. Ramsey, and F. P. Netzer, Surface Sci. **452**, L281 (2000).

[9]S. Özkaya, M. Çakmak, and B. Alkan, Surface Sci. **602**, 1376 (2008).

[10]K. Sakamoto, P. E. J. Eriksson, N. Ueno, and R. I. G. Uhrberg, Surface Sci. **601**, 5258 (2007).

[11]K. Sakamoto, P. E. J. Eriksson, S. Mizuno, N. Ueno, H. Tochihara, and R. I. G. Uhrberg, Phys. Rev. B **74**, 075335 (2006).

[12]S. Hatta, C. Kato, N. Tsuboi, S. Takahashi, H. Okuyama, T. Aruga, A. Harasawa, T. Okuda, and T. Kinoshita, Phys. Rev. B **76**, 075427 (2007).

[13]M. Prietsch, A. Samsavar, and R. Ludeke, Phys. Rev. B **43**, 11850 (1991).

[14]From our STM images we cannot strictly decide which site corresponds to the protrusions in Fig. 1(c). According to *ab initio* calculations, the lowest unocupied orbitals should be Tl $6p_x + 6p_y$.[12] However, the exact location of the protrusions with respect to Tl atoms is not known.

[15]Note the unusual notation in Ref. 7: S_1 for the highest occupied state and S_2 for the lowest unoccupied state.

[16]A. Zotov, A. Saranin, V. Kotlyar, O. Utas, and Y. Wang, Surface Sci. **600**, 1936 (2006).

[17]H. Guesmi, L. Lapena, G. Tréglia, and P. Müller, Phys. Rev. B **77**, 085402 (2008).

[18]V. G. Kotlyar, A. A. Saranin, A. V. Zotov, and T. V. Kasyanova, Surface Sci. **543**, L663 (2003).

Surface Science 606 (2012) 991–995

Contents lists available at SciVerse ScienceDirect

Surface Science

journal homepage: www.elsevier.com/locate/susc

An STM study of desorption-induced thallium structures on the Si(111) surface

Pavel Kocán *, Pavel Sobotík, Peter Matvija, Martin Setvín, Ivan Ošťádal

Charles University in Prague, Faculty of Mathematics and Physics, Department of Surface and Plasma Science, V Holešovičkách 2, 180 00 Praha 8, Czech Republic

ARTICLE INFO

Article history:
Received 11 October 2011
Accepted 26 December 2011
Available online 1 March 2012

Keywords:
Scanning tunneling microscopy
Si(111)
Thallium
Desorption

ABSTRACT

The scanning tunneling microscopy is used to study morphology of a Tl adlayer in various stages of Tl desorption from the Si(111) surface. Transition from the Si(111)/(1×1)-Tl structure through the (√3×√3)R30° mosaic phase to domains of metastable Si reconstructions is observed. Silicon substitutional atoms are found to be intrinsic to the (√3×√3)R30° structure. The temperature dependence of the amount of residual Tl atoms on the surface is successfully fitted by a model using the first order desorption. The same desorption energy of (2.1±0.3) eV and frequency prefactor $5\times10^{14\pm2}$ s^{-1} during all stages of the desorption are sufficient for the fitting. It is concluded that bonding of Tl in both (1×1) and (√3×√3) configurations is of the same nature.

1. Introduction

Recently, the Si(111) surface with one deposited monolayer of thallium has attracted a significant attention due to the observation of an unusual Rashba spin splitting [1]. The spin splitting, lifted by a spin–orbit interaction in combination with a broken symmetry [2], represents a promising mechanism for generation of spin-polarized electrons for spintronic applications [3].

Deposition of Tl on the Si(111) surface and annealing to 250–300 °C results in formation of the Si(111)/(1×1)-Tl reconstruction [4]. Upon annealing to a higher temperature (~350 °C) a Si(111)/$\left(\sqrt{3}\times\sqrt{3}\right)$ R30°-Tl reconstruction [hereafter called $\left(\sqrt{3}\times\sqrt{3}\right)$ for simplicity] is formed via desorption of Tl [4,5]. Structure of the (1×1) reconstruction was determined as a monolayer of Tl atoms in T_4 site positions (see Fig. 1a) using low energy electron diffraction [6], synchrotron X-ray scattering [7], and ab-initio calculations [4]. On the other hand, structure of the $\left(\sqrt{3}\times\sqrt{3}\right)$ reconstruction is not settled yet. Ab-initio calculations [8] denoted 1/3 of monolayer of Tl atoms at T_4 sites (Fig. 1b) as the stable structure. Such structure is similar to the $\left(\sqrt{3}\times\sqrt{3}\right)$ reconstruction formed by other group III metals with trivalent metal atoms. However, photo-emission results show a different bonding nature [9] and a monovalent state [10] of the Tl atoms in the $\left(\sqrt{3}\times\sqrt{3}\right)$ structure. By means of the scanning tunneling microscopy (STM), only a mosaic $\left(\sqrt{3}\times\sqrt{3}\right)$ structure with some Tl adatoms replaced by Si adatoms (Fig. 1c) was observed [5].

We use STM to study the desorption-mediated transitions (1×1) → $\left(\sqrt{3}\times\sqrt{3}\right)$ → Si metastable structures. Morphology of Tl ad-layer in different stages of desorption is observed as a function of annealing temperature *T*. The atomic resolution allows us to analyze the amount Θ of residual Tl on the surface. By fitting the dependence Θ(*T*) we obtain the desorption energy, which reflects character of bonding of Tl atoms to the substrate.

2. Experimental

One ML (monolayer, 7.83×10^{14} atoms cm^{-2}) of thallium (purity 99.999%) was evaporated from a resistively heated Ta tube onto the Si(111)/(7×7) substrate (Sb doped with resistivity of 0.005–0.01 Ω cm) cleaned by flashing to ~1200 °C. Deposited amount was controlled by a quartz thickness monitor and calibrated by STM. The (1×1)-Tl surface was prepared as the initial point of each experiment by annealing the surface to 280 °C. The samples were annealed by passing DC current for 2 min, absolute (relative) temperature accuracy was ±30 °C (±10 °C). The STM measurements were performed by means of a non-commercial STM in an ultra-high vacuum chamber with the base pressure better than 3×10^{-9} Pa. Pressure during Tl deposition was within the 10^{-8} Pa order. Electrochemically etched tungsten tips cleaned in-situ by electron bombardment were used for measurements.

3. Results and discussion

Fig. 2a shows an STM image of the surface prepared by annealing of the Si(111) surface with one Tl monolayer at 280 °C for 2 min. The surface is almost uniformly covered by the (1×1)-Tl layer. On the main flat area, several hexagonally shaped 2D islands are observed. We propose that these islands contain an extra bi-layer of Si atoms

* Corresponding author. Tel.: +420 2191 2349.
E-mail address: pavel.kocan@mff.cuni.cz (P. Kocán).

0039-6028/$ – see front matter © 2012 Elsevier B.V. All rights reserved.
doi:10.1016/j.susc.2011.12.016

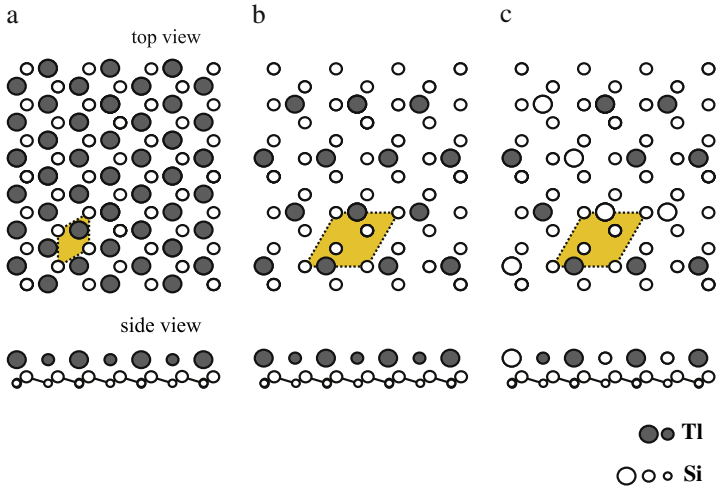

Fig. 1. Schematic structural models of the Si(111) surface with (a) (1×1)-Tl [4], (b) $\left(\sqrt{3}\times\sqrt{3}\right)$-Tl [8] and (c) mosaic $\left(\sqrt{3}\times\sqrt{3}\right)$-Tl [5] reconstructions. Filled and empty circles represent Tl and Si atoms. Unit cells of (1×1) and $\left(\sqrt{3}\times\sqrt{3}\right)$ are outlined by the rhombuses.

covered by the (1×1) monolayer of Tl. The surface concentration of Si atoms in the (7×7) reconstruction [prior to (1×1)-Tl formation] is 0.08 ML higher than that of the bulk-terminated surface. These extra Si atoms would form bilayers with total area of 4%, which well agrees with 5% obtained from our STM data. The surface of these islands (not shown) appears on STM images the same as the surface of the main area, shown in the inset of Fig. 2a. Their apparent height corresponds to one Si bi-layer high step on the Si(111) surface — see the line profile along the dashed line crossing three bright islands in Fig. 2a. The inset in Fig. 2a shows a detail of the (1×1)-Tl surface with resolved 1×1 periodicity and several regularly shaped defects, interpreted as Tl multi-vacancies [11].

The structures observed after annealing of the (1×1) surface at different temperatures are shown in Fig. 2b–f. After annealing at 300 °C (Fig. 2b) the (1×1) ad-layer, appearing as a bright surface without corrugation, became broken by areas with desorbed Tl. In

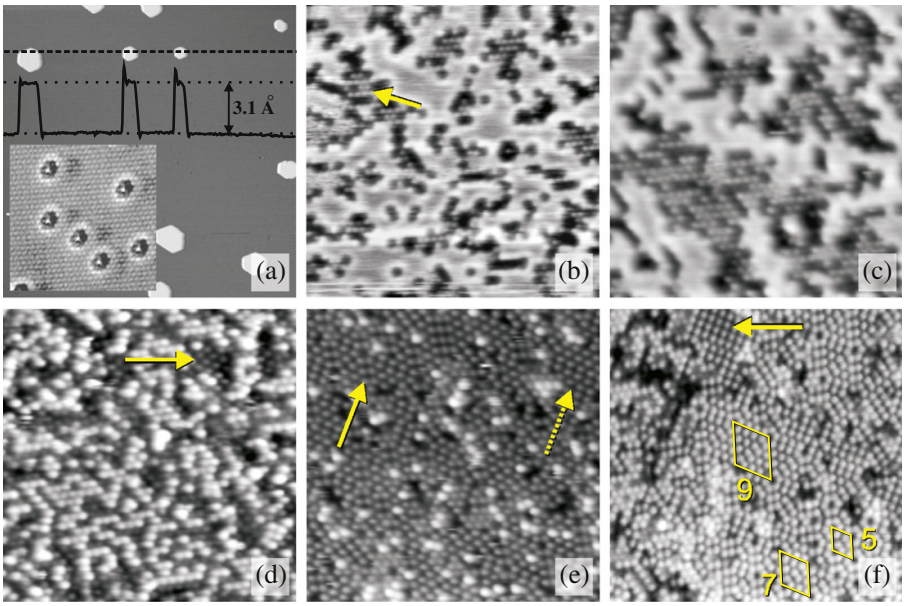

Fig. 2. STM images of the Si(111) surface with one monolayer of Tl after annealing at different temperatures. (a) $T=280$ °C: surface covered entirely by the (1×1)-Tl structure. The inset shows detail of the (1×1) surface. The plot shows a line profile along the dashed line crossing 2D islands. (b) $T=300$ °C and (c) $T=330$ °C: coexisting (1×1) and $\left(\sqrt{3}\times\sqrt{3}\right)$ structures. (d) Surface covered mostly by $\left(\sqrt{3}\times\sqrt{3}\right)$ mosaic after two cycles of annealing at 300 °C and 330 °C. (e) $T=360$ °C: the surface, from which Tl almost completely desorbed. (f) $T=450$ °C: surface covered mostly by $(2n+1)(2n+1)$ reconstructions. Dimensions of images: (a) 200×200 nm^2, inset 7×7 nm^2, (b–f) 20×20 nm^2. Sample voltage: (a) -3.0 V, inset: 9 mV, (b) 1.1 V, (c) 0.3 V, (d) 0.5 V, (e) 1.0 V, (f) 1.6 V. Other details are in text.

these areas (see e.g. the area marked by the arrow in Fig. 2b) the $\left(\sqrt{3}\times\sqrt{3}\right)$ reconstruction forms up locally. If the annealing temperature is increased to 330 °C, the total area of the $\left(\sqrt{3}\times\sqrt{3}\right)$ reconstruction is larger, as shown in Fig. 2c. In both Fig. 2b and c the $\left(\sqrt{3}\times\sqrt{3}\right)$ reconstruction is not perfect, some spots in the lattice are darker than the others. The darker spots on empty states STM images were previously interpreted as Si substitutional atoms in the $\left(\sqrt{3}\times\sqrt{3}\right)$ domain (see Fig. 1c) [5]. Fig. 2d shows the surface prepared by annealing at 300 °C followed by annealing at 330 °C. The (1×1) areas are completely replaced by a mosaic of Tl and Si adatoms with the $\left(\sqrt{3}\times\sqrt{3}\right)$ periodicity depicted in Fig. 1c. A small fraction of the surface appears darker (see e.g. the area marked by the arrow in Fig. 2d) and a local structure is different in these areas. The darker regions can be assigned to Si metastable local structures [12] with Tl completely desorbed.

The area of the Si metastable structures increases rapidly after annealing at 360 °C, as shown in Fig. 2e. On the surface, only few mostly isolated Tl atoms remain, appearing as bright protrusions. The rest of the surface is covered with a mixture of locally ordered Si adatom structures. Specifically, origins of $c(2\times8)/c(2\times4)$ reconstruction can be found (see the dotted arrow in Fig. 2e pointing to a $c(2\times8)$ region) as well as origins of dimer-adatom-stacking fault (DAS) structures $(2n+1)(2n+1)$ (see the solid arrow in Fig. 2e). After annealing at higher temperatures Tl atoms desorb completely. An example after annealing at 450 °C is shown in Fig. 2f. Compared to Fig. 2e, domains containing several unit cells of DAS reconstructions can be recognized, see selected unit cells of (9×9), (7×7) and (5×5) reconstructions outlined by the rhombuses labeled by 9, 7 and 5, respectively. The arrow in Fig. 2f points to an area of the $c(2\times8)$ local structure coexisting with $(2n+1)(2n+1)$ areas.

An amount of non-desorbed Tl atoms Θ (hereafter called coverage) was extracted from STM images using different contrast of Si and Tl atoms. The amount of Tl atoms in the (1×1) structure was obtained by measuring its area with known concentration of Tl atoms, while the amount of Tl atoms in the $\left(\sqrt{3}\times\sqrt{3}\right)$ structure was counted 'atom-by-atom'. In order to estimate the accuracy of measuring the Tl coverage from STM images, test experiments were performed as follows. The surface with 0.7 ML of deposited Tl was annealed at 280 °C, which is a condition for the (1×1)-Tl formation with negligible desorption (see the (1×1) surface with no indication of desorption in Fig. 2a). The Tl coverage measured from STM images was in good agreement with the deposited amount within the range of thickness monitoring error (±5%).

The experimentally obtained dependence of coverage Θ on annealing temperature T is plotted in Fig. 3 by squares. The fitting solid line in Fig. 3 was obtained as follows. First, we assume that the observed structural changes (Fig. 2) are induced by a thermally activated desorption of the first order. Second, we assume that the desorption energy E_{des} does not depend on Θ, i.e. E_{des} is the same for Tl atoms in all structures formed during the desorption process. Then the decrease of coverage with time t can be expressed as

$$\Theta = \Theta_0 \exp(-Rt), \tag{1}$$

where Θ_0 is the initial Tl coverage and R is the desorption rate, depending on temperature T:

$$R = \nu \exp(-E_{des}/k_B T), \tag{2}$$

where ν is the frequency prefactor and k_B is the Boltzmann constant. The initial coverage Θ_0 and time t were set $\Theta_0 = 0.97$ ML (the initial Tl coverage is lower than unity due to the presence of intrinsic defects, see Fig. 2a) and $t = 120$ s (from the experiment). The frequency prefactor ν and the desorption energy E_{des} were found from the linear fit of Arrhenius dependence of $\ln(R)$ vs. $1/T$, shown in Fig. 4. The values of R were calculated from the experimentally obtained values of Θ using Eq. (1). The parameters obtained by the fitting are $E_{des} = (2.1\pm0.3)$ eV and $\nu = 5\times10^{14\pm2}$ s^{-1}.

The total Tl coverage Θ can be divided into two components Θ_1 and $\Theta_{\sqrt{3}}$, corresponding to fractions of atoms in the (1×1) and the $\left(\sqrt{3}\times\sqrt{3}\right)$ structures, respectively. For simplicity we assume that the $\left(\sqrt{3}\times\sqrt{3}\right)$ structure is formed only by desorption from the (1×1). Then, taking into account desorption from both structures, rate equations can be written:

$$\frac{d\Theta_1}{dt} = -1.5\times\Theta_1 R_1 \tag{3}$$

$$\frac{d\Theta_{\sqrt{3}}}{dt} = 0.5\times\Theta_1 R_1 - \Theta_{\sqrt{3}} R_{\sqrt{3}}, \tag{4}$$

where R_1 and $R_{\sqrt{3}}$ are the desorption rates from the (1×1) and the $\left(\sqrt{3}\times\sqrt{3}\right)$ structures, respectively. Factors 1.5 in the first and 0.5 in

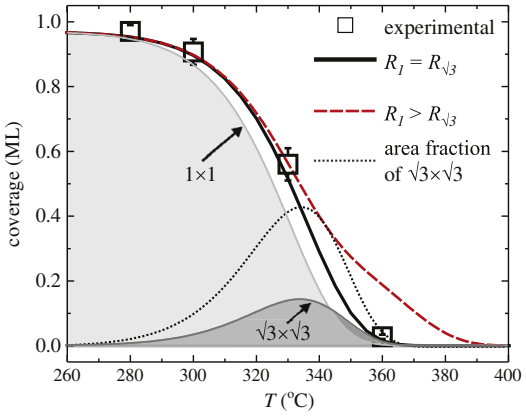

Fig. 3. Experimental dependence of Tl coverage (squares) on annealing temperature, fitted by first order desorption model with single desorption rate $R_1 = R_{\sqrt{3}}$ (solid line) and with two desorption rates $R_1 > R_{\sqrt{3}}$ (dashed line). The curves distinguished by light gray-shaded and dark gray-shaded areas underneath are (1×1) and $\left(\sqrt{3}\times\sqrt{3}\right)$ components of Tl coverage with the same desorption energy. The dotted line corresponds to the area fraction of the $\left(\sqrt{3}\times\sqrt{3}\right)$ structure.

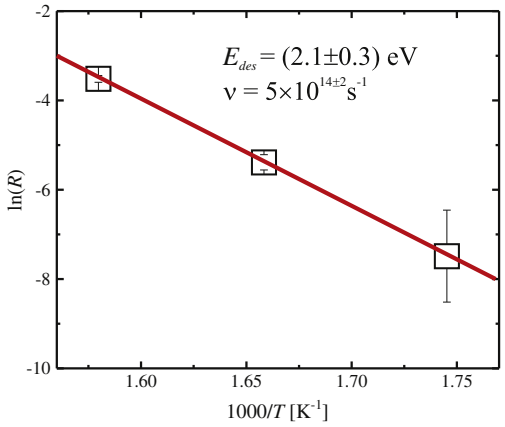

Fig. 4. Arrhenius plot of desorption rate R (squares) obtained from Tl coverage Θ using Eq. (1). The solid line is a linear fit.

the second equation ensure that desorption of two atoms from the (1×1) structure effectively removes three atoms from the (1×1) and adds one atom to the $\left(\sqrt{3}\times\sqrt{3}\right)$ structure. If $R_1 = R_{\sqrt{3}}$, the sum of Θ_1 and $\Theta_{\sqrt{3}}$ represents a one-component first-order desorption (FOD), which gives the same result as plotted in Fig. 3 by the solid line. To test how would a higher desorption energy of atoms in the $\left(\sqrt{3}\times\sqrt{3}\right)$ structure influence the total coverage, a result of the kinetic equations with energies of desorption set to 2.2 eV and 2.1 eV for the $\left(\sqrt{3}\times\sqrt{3}\right)$ and the (1×1) structures, respectively, is plotted in Fig. 3 by the dashed line. The frequency prefactor is set to $5\times10^{14}\,s^{-1}$ for both structures. For coverages >0.6 ML, both models give the same results, because the fraction of the $\left(\sqrt{3}\times\sqrt{3}\right)$ structure is small. However, as desorption continues, a significant difference between the curves is observed. The declination from the original dependence (solid line) is evident and does not fit to the experiment. The successful fitting of the experimental dependence $\Theta(T)$ using a single parameter E_{des} for the desorption from both (1×1) and $\left(\sqrt{3}\times\sqrt{3}\right)$ suggests that a bonding mechanism in both structures is similar.

With respect to the good agreement of the experimental data and their fitting described above we propose a model of structural transformations on the Tl/Si(111) surface. Starting from the (1×1) structure, the $\left(\sqrt{3}\times\sqrt{3}\right)$ is locally formed by decreasing Tl coverage by desorption. Because the activation energy of Tl desorption in both structures is similar, Tl desorbs from both structures with a similar probability. The Tl atoms desorbed from the $\left(\sqrt{3}\times\sqrt{3}\right)$ are replaced by Si adatoms in order to lower the total energy, as discussed below. As a result, the mosaic phase is formed. By further desorption, Si adatoms dominate and Si metastable adatom structures are observed.

We continue by discussion of a stabilizing mechanism of the mosaic $\left(\sqrt{3}\times\sqrt{3}\right)$-Tl structure. In the proposed scenario, the substitutional Si adatoms in the $\left(\sqrt{3}\times\sqrt{3}\right)$ structure are intrinsic, in agreement with proposals in Ref. [13]. In the (1×1)-Tl structure, which covers the surface almost perfectly after heating to ~280 °C, a character of bonding is strongly ionic. It is due to a charge transfer from the monovalent [10] Tl atoms to Si dangling bonds of the bulk-terminated Si(111) surface. Ratio of the Si dangling bonds and Tl atoms is 1:1. If the same mechanism of bonding is applied to the ideal $\left(\sqrt{3}\times\sqrt{3}\right)$ structure (Fig. 1b), where the ratio is 3:1, the charge provided by *monovalent* Tl atoms is not sufficient to saturate Si dangling bonds completely. On the other hand, each Si adatom can provide four electrons to the structure. The Si adatoms are available on the surface from the Si-rich (7×7) reconstruction and from step edges. Furthermore, the Si adatoms are highly mobile at elevated temperatures, otherwise the well shaped 2D islands of Si bilayers would not be formed (see Fig. 2a). Hence the $\left(\sqrt{3}\times\sqrt{3}\right)$-Tl structure is likely stabilized by the Si substitutional atoms, resulting in the mosaic structure (the model is shown in Fig. 1c).

Here we note that the $\left(\sqrt{3}\times\sqrt{3}\right)$-Tl is formed only as a result of desorption of Tl from the (1×1). If ~0.3 ML of Tl is deposited to the (7×7) reconstruction of Si(111) and heated to ~300 °C (or deposited on the hot surface), the $\left(\sqrt{3}\times\sqrt{3}\right)$ structure is not observed by STM. Instead, the (7×7) structure remains on majority of the surface with Tl clusters inside half unit cells of the reconstruction. Minor parts of the surface, preferentially at step edges or domain boundaries, are covered by the (1×1)-Tl structure [5]. This observation, confirmed by our experiments (not shown), suggests that a low concentration of Tl is not sufficient to destroy the (7×7) reconstruction and that (1×1) is preferred in comparison to the $\left(\sqrt{3}\times\sqrt{3}\right)$ structure, which is formed only as a product of the desorption. When the surface with ~0.3 ML of Tl is annealed to Tl desorption temperature, the original (1×1) areas follow the same evolution as in the case of the surface completely covered by the (1×1). Tl is desorbed from the (7×7) areas leaving clean (7×7) reconstruction.

In previous LEED studies of the Si(111)/$\left(\sqrt{3}\times\sqrt{3}\right)$-Tl surface, high intensity LEED spots were observed [4,10,9,14]. By the intuitive interpretation, the maximum intensity LEED pattern was supposed to correspond to the maximum $\left(\sqrt{3}\times\sqrt{3}\right)$ area fraction and to Tl coverage of 1/3 ML. Using our simple model, the Tl coverage Θ from Eqs. (1) and (2) can be divided into components Θ_1 and $\Theta_{\sqrt{3}}$ (the corresponding fractions are shaded by light gray and dark gray in Fig. 3, respectively). The fractions are obtained from Eqs. (3) and (4) using values $R_1 = R_{\sqrt{3}} = R$. The area fraction of the $\left(\sqrt{3}\times\sqrt{3}\right)$ is three times higher than $\Theta_{\sqrt{3}}$, because Tl adatom concentration in this structure is ideally 1/3 ML. This area fraction is plotted by a dotted line in Fig. 3. Maximum of the $\left(\sqrt{3}\times\sqrt{3}\right)$ fraction is 43% at $T=335$ °C, which corresponds to STM observation — the surface is never entirely covered by the $\left(\sqrt{3}\times\sqrt{3}\right)$ during desorption. We propose, that the sharp LEED pattern [4,10,9,14] corresponds to the mosaic $\left(\sqrt{3}\times\sqrt{3}\right)$ structure (Fig. 2d) with about 0.15 ML Tl coverage. We note that in case of the $\left(\sqrt{3}\times\sqrt{3}\right)$ mosaic phase of Pb on the Si(111) surface a sharp LEED pattern was observed as well [15].

Finally we compare our results obtained for Tl with desorption of other group III metals from the Si(111) surface. In general, different techniques used in experiments discussed below gave not only different combinations of frequency prefactors and desorption energies, but also different order of desorption. To allow comparison across the results we introduce a critical temperature T_C defined as a temperature, at which one half of the initial coverage desorbs from the surface after fixed time, which we choose 120 s.

Among the group III elements, Al desorbs from the Si(111) surface at the highest temperatures. In Ref. [16], desorption from the $\left(\sqrt{3}\times\sqrt{3}\right)$-Al structure is studied by the Auger electron spectroscopy, the obtained values of the FOD energy and prefactor were $E_{des}=(3.8\pm0.1)$ eV and $\nu=5.3\times10^{15}\,s^{-1}$, with resultant $T_C=790$ °C. For submonolayer coverages of Ga, the FOD was observed by the Rutherford backscattering technique [17] with the activation energy of desorption $E_{des}=(2.0\pm0.3)$ eV and prefactor $\nu=10^{(10\pm3)}\,s^{-1}$. Resultant T_C is 550 °C. In the case of In desorption in a submonolayer regime, values of E_{des} between 2.5 and 2.9 eV were reported by several techniques (see [18] and references therein) with ν between 10^{12} and $10^{16}\,s^{-1}$, considering the FOD and T_C is in the range from 510 to 620 °C. Interestingly, the zeroth order desorption (ZOD) was reported in contrast to the earlier works. Minami et al. used the fluorescent X-ray spectroscopy and the reflection high energy electron diffraction (RHEED) to study isothermal desorption of In from the Si(111) surface, reporting ZOD with rate of desorption dependent on superstructures formed during the desorption [19]. E_{des} for the $\left(\sqrt{3}\times\sqrt{3}\right)$ superstructure was reported to be 1.9 eV and prefactor 4.6×10^8 ML/s, the resultant T_C is 605 °C. The ZOD usually indicates an existence of a 2D gas phase in equilibrium with a solid phase, which represents a reservoir of atoms for the 2D gas [20]. However, the existence of the 2D gas phase was not confirmed by RHEED, which shows sharp patterns during desorption, corresponding to the solid phase [20]. In the case of

Ga, ZOD was also reported by King et al. using temperature programmed desorption [18]. With initial coverage of 1.5 ML, a single desorption peak was fitted by the zeroth order kinetics with $E_{des} = (2.0 \pm 0.1)$ eV and a ZOD prefactor of $1.0 \times 10^{12 \pm 0.5}$ ML/s, giving T_C of 435 °C.

Our results show that desorption of Tl can be described by the kinetics with a simple bond-breaking mechanism. The value $E_{des} = (2.1 \pm 0.3)$ eV is close to the activation energy of Ga desorption and smaller than E_{des} of In, when considering the first order desorption. The rather high value of prefactor $\nu = 5 \times 10^{14 \pm 2}$ s^{-1} results in desorption at significantly lower temperatures, compared to both Ga and In. The value of $T_C = 350$ °C is the lowest among the compared group III elements. This can be explained by a qualitatively different bonding mechanism, in which only single valence electron per adatom is active.

4. Conclusion

Particular stages of thallium desorption from the Si(111) surface were observed by STM, i.e. formation of the $\left(\sqrt{3} \times \sqrt{3}\right)$ structure by desorption of Tl from the (1×1) surface and formation of Tl-free Si metastable structures by desorption of Tl from the $\left(\sqrt{3} \times \sqrt{3}\right)$ structure. Once the (1×1) structure is canceled, the $\left(\sqrt{3} \times \sqrt{3}\right)$ mosaic phase is formed, while ideal Tl-$\left(\sqrt{3} \times \sqrt{3}\right)$ without Si substitutional atoms has been never observed. It is concluded that a significant amount of the substitutional Si atoms is necessary to stabilize the $\left(\sqrt{3} \times \sqrt{3}\right)$ structure, resulting in the mosaic phase. By fitting the observed temperature dependence of the amount of residual Tl on the surface by means of a first order desorption, we obtained the desorption energy (2.1 ± 0.3) eV for Tl in both (1×1) and $\left(\sqrt{3} \times \sqrt{3}\right)$ structures. From successful fitting by the single desorption energy we derive that a nature of Tl bonding in both (1×1) and $\left(\sqrt{3} \times \sqrt{3}\right)$ structures is similar.

Acknowledgment

This work was supported by The Grant Agency of the Czech Republic, Project No. 202/09/P033 of GACR.

References

[1] K. Sakamoto, T. Oda, A. Kimura, K. Miyamoto, M. Tsujikawa, A. Imai, N. Ueno, H. Namatame, M. Taniguchi, P.E.J. Eriksson, R.I.G. Uhrberg, Phys. Rev. Lett. 102 (2009) 096805.
[2] Y. Bychkov, E. Rashba, JETP Lett. 39 (1984) 78.
[3] K. Yaji, Y. Ohtsubo, S. Hatta, H. Okuyama, K. Miyamoto, T. Okuda, A. Kimura, H. Namatame, M. Taniguchi, T. Aruga, Nat. Commun. 1 (2010) 17.
[4] S.S. Lee, H.J. Song, N.D. Kim, J.W. Chung, K. Kong, D. Ahn, H. Yi, B.D. Yu, H. Tochihara, Phys. Rev. B 66 (2002) 233312.
[5] V.G. Kotlyar, A.A. Saranin, A.V. Zotov, T.V. Kasyanova, Surf. Sci. 543 (2003) L663.
[6] T. Noda, S. Mizuno, J.W. Chung, H. Tochihara, Jpn. J. Appl. Phys. 42 (2003) L319.
[7] N.D. Kim, C.G. Hwang, J.W. Chung, T.C. Kim, H.J. Kim, D.Y. Noh, Phys. Rev. B 69 (2004) 195311.
[8] S. Özkaya, M. Çakmak, B. Alkan, Surf. Sci. 602 (2008) 1376.
[9] K. Sakamoto, P.E.J. Eriksson, N. Ueno, R.I.G. Uhrberg, Surf. Sci. 601 (2007) 5258.
[10] K. Sakamoto, P.E.J. Eriksson, S. Mizuno, N. Ueno, H. Tochihara, R.I.G. Uhrberg, Phys. Rev. B 74 (2006) 075335.
[11] Prepared for publication.
[12] M. Koike, Y. Einaga, H. Hirayama, K. Takayanagi, Phys. Rev. B 55 (1997) 15444.
[13] A. Visikovskiy, Structural investigations of thallium adsorption on Si(100) and Si(111) surfaces, Ph.D. thesis, Kyushu University, Japan (2006).
[14] A. Visikovskiy, S. Mizuno, H. Tochihara, Surf. Sci. 600 (2006) L189.
[15] E. Ganz, H. Ing-Shouh, X. Fulin, S.K. Theiss, J. Golovchenko, Surf. Sci. 257 (1991) 259.
[16] A. Saranin, E. Khramtsova, V. Lifshits, Surf. Sci. 302 (1994) 57.
[17] M. Zinke-Allmang, L. Feldman, Surf. Sci. Lett. 191 (1987) L749.
[18] S. King, R. Davis, R. Nemanich, Surf. Sci. 602 (2008) 405.
[19] N. Minami, Y. Machida, T. Kajikawa, T. Sato, K. Ota, S. Ino, Surf. Sci. 524 (2003) 1995.
[20] K. Nagai, T. Shibanuma, M. Hashimoto, Surf. Sci. 145 (1984) L459.

PHYSICAL REVIEW E **88**, 022403 (2013)

Desorption-induced structural changes of metal/Si(111) surfaces: Kinetic Monte Carlo simulations

Pavel Kocán,* Pavel Sobotík, and Ivan Ošt'ádal
Charles University in Prague, Faculty of Mathematics and Physics, Department of Surface and Plasma Science, V Holešovičkách 2, 180 00 Prague 8, Czech Republic
(Received 29 May 2013; published 14 August 2013)

We used a configuration-based kinetic Monte Carlo model to explain important features related to formation of the $(\sqrt{3}\times\sqrt{3})R30^\circ$ mosaic of metal and semiconductor atoms on the Si(111) surface. Using first-order desorption processes, we simulate the surprising zero-order desorption spectra, reported in some cases of metal desorption from the Si(111) surface. We show that the mechanism responsible for the zerolike order of desorption is the enhanced desorption from disordered areas. Formation of the $\sqrt{3}\times\sqrt{3}$ mosaic with properties of a strongly frustrated antiferromagnetic Ising model is simulated by a configuration-sensitive desorption. For substitution of desorbed metal atoms by Si adatoms, fast diffusion of the adatoms on top of a 1×1 layer is proposed as the most probable. Simulations of desorption-induced structural transitions provide us a link between underlying atomistic processes and the observed evolving morphologies with resultant macroscopic desorption fluxes. An effect of the desorption sensitivity on a configuration of neighboring atoms is emphasized.

DOI: 10.1103/PhysRevE.88.022403 PACS number(s): 81.15.Aa, 68.35.bg, 68.55.ag, 64.60.De

I. INTRODUCTION

Deposition of metals on the Si(111) surface together with an appropriate thermal activation results in re-organizing of surface atoms to a variety of ordered structures, often with interesting properties. Special attention has been paid to mosaic phases of two-dimensional (2D) alloys with $(\sqrt{3}\times\sqrt{3})R30^\circ$ symmetry (hereafter denoted as $\sqrt{3}\times\sqrt{3}$ for simplicity). These structures are usually induced by desorption of metal atoms (Pb [1–3], Sn [4,5], Tl [6,7]) together with their substitution by Si atoms.

A significant amount of experimental work published on the topic can be divided into two categories. First, studies concerning flux of desorbing atoms, represented mostly by the thermal desorption spectroscopy (TDS), and second, studies focused on the morphology of resultant structures mostly by means of the scanning tunneling microscopy (STM) and the low energy electron diffraction (LEED).

A surprising feature observed repeatedly when monitoring a flux of some metal atoms desorbing from semiconductor surfaces was a zero-order desorption (ZOD) [1,8–12], meaning in general that the desorption flux is not dependent on the surface coverage of desorbing particles. Usually the ZOD indicates the existence of a 2D gaseous phase (in equilibrium with the solid phase) from which the desorption is activated [13], or desorption from defect sites with constant concentration and accessed via fast diffusion. However, in the case of metal desorption from the Si(111) surface, none of the explanations seems to be valid.

Structural properties of mosaic phases and their formation have been studied both theoretically by *ab initio* and Monte Carlo methods and experimentally using STM and LEED. The experimentally obtained locally ordered mosaic phases have been explained as a result of a repulsive interaction of the same-element nearest neighbors [2,5]. Such situation is an analog of a two-dimensional antiferromagnetic Ising model in a hexagonal lattice, which is strongly influenced by a geometrical frustration of the system. Even though the mosaic phases are usually prepared by a desorption from phases with higher coverages of metal atoms, the relation of the mosaic phase formation to the desorption processes has not been addressed so far.

In this paper, we study a desorption-induced evolution of Pb and Tl structures on Si(111) surface, representing model examples sufficient to study general phenomena of the transition from the (1×1) to the $(\sqrt{3}\times\sqrt{3})$ phase which further evolves to the mosaic phase. Kinetic Monte Carlo (KMC) simulations allowed us to provide an explanation of experimentally obtained features using a straightforward atomistic model.

II. KMC MODEL OF DESORPTION

A solid-on-solid KMC implementation of the standard activation dynamics [14] was used for the simulations. In the model, the (111) surface is represented by a hexagonal network of adsorption sites. Atoms of two species (metal and silicon) are allowed to diffuse within this network. Only hops to unoccupied nearest positions are allowed. In addition, the metal atoms are allowed to desorb. Both diffusion and desorption processes are thermally activated. Desorption of silicon atoms is prohibited, because of much higher desorption energy, compared to the metal atoms.

For simulations we developed a code in which all possible combinations of occupations of nearest and next-nearest positions are divided into groups of configurations. Each group is associated with "configurational" energy E^c (metal and Si atoms) and with desorption energy E^{des} (metal atoms only). While E^c represents a local minimum of the surface potential, E^{des} represents directly a configuration-specific activation energy of desorption. The configurations and the corresponding energies must be defined with respect to the simulated problem while the number of configurations (ruling the number of model parameters) must be kept as low as possible. For the studied problem we defined the following configurations, examples of which can be found in Fig. 1: (1) 1×1—at least three atoms of the same and no atom of the opposite chemical

*pavel.kocan@mff.cuni.cz

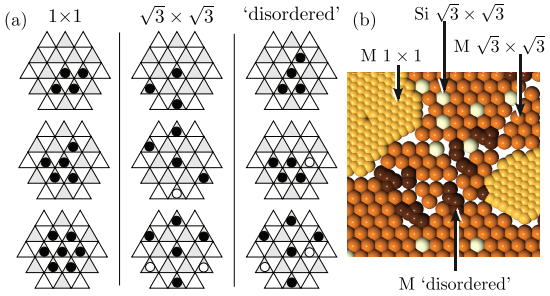

FIG. 1. (Color online) (a) Examples of configurations (with respect to the central adatom) belonging to groups named 1×1, $\sqrt{3}\times\sqrt{3}$, and "disordered" in text. The black and gray circles denote positions occupied by a metal and Si adatom. (b) Selected configurations of metal (M) and silicon (Si) atoms considered in the model are distinguished by colors (grayscale) in a simulated morphology.

species are in the nearest-neighboring positions in the 1×1 grid ($NN_{1\times1}$), forming a compact group; (2) $\sqrt{3}\times\sqrt{3}$—no atoms in $NN_{1\times1}$ and at least two atoms in nearest-neighboring positions in the $\sqrt{3}\times\sqrt{3}$ grid ($NN_{\sqrt{3}\times\sqrt{3}}$) positions; and (3) "disordered"—plain configurations not belonging to the above groups, representing atoms in transitional positions without a favorable arrangement. The group of $\sqrt{3}\times\sqrt{3}$ configurations is further divided into subgroups with respect to the number of atoms of the same chemical species in $NN_{\sqrt{3}\times\sqrt{3}}$ positions in order to allow simulation of effective repulsion in the Ising model.

The activation energy $E_{\rm act}$ for hopping takes into account the diffusion energy $E_{\rm dif}$ (corresponding to diffusion of an isolated atom) and both the initial and the final configuration energies E_i^c and E_f^c, respectively, with parabolic potentials [15],

$$E_{\rm act} = E_{\rm dif} + \frac{\Delta E}{2} + \frac{\Delta E^2}{16E_{\rm dif}}, \quad \Delta E = \left(E_i^c - E_f^c\right). \qquad (1)$$

Rates of the hopping processes are obtained as $R = \nu \exp(\frac{-E_{\rm act}}{kT})$, where ν is the frequency prefactor, k is the Boltzmann constant, and T is the temperature.

An important process during mosaic phase formation is the incorporation of a substrate (Si) atom into the $\sqrt{3}\times\sqrt{3}$ structure, called substitution. As the interface between adatoms and substrate remains in plane according to STM experiments, the substituting atoms are likely to originate from step edges. The atom from the step edge may diffuse to the substituting position either *through* the adlayer by an exchange diffusion mechanism, or *on top* of the adlayer. Our simulations revealed (not shown here) that barriers allowing diffusion through the layer result in poorly ordered domains of (1×1) and $(\sqrt{3}\times\sqrt{3})$ structures, in contrast to experimental observations. On the other hand, fast diffusion on top of the adlayer results in rapid occupation of the site in the $\sqrt{3}\times\sqrt{3}$ grid after desorption of a metal atom. The fast diffusion on top of the adlayer can be awaited because the potential energy surface is smoothed by saturation of Si dangling bonds.

In order to minimize the number of model parameters, we have tested a limit case of infinite diffusion on top of the adlayer—an artificial substitution, in which an atom desorbed from the $\sqrt{3}\times\sqrt{3}$ grid is immediately (with probability of unity) replaced by a Si adatom. Both mechanisms—diffusion on top of the adlayer and the artificial substitution—give statistically the same results. Therefore, the latter is used in the simulations presented in this work.

III. RESULTS AND DISCUSSION

A. Simulations of desorption

Applicability of the model to reproduce experimentally obtained data was tested on two examples—desorption of lead and thallium from the Si(111) surface. In both cases, transition from the (1×1) to the mosaic $(\sqrt{3}\times\sqrt{3})$ phase during desorption has been observed [1,6,7,10,11].

The initial point for simulations discussed here was a complete 1×1 monolayer of the fully occupied network in the case of Pb (which is possibly a minor simplification compared to real Pb structures; see Ref. [16], and references therein). In the case of Tl we introduced experimentally obtained defects [17] within the monolayer, lowering the initial coverage to 0.97 ML.

First we will discuss the case of Pb/Si(111). The desorption spectra at constant temperatures have been published [1,9–11] using different experimental techniques: the low-energy ion-scattering spectroscopy [9], the photoemission spectroscopy [10], and the Rutherford backscattering [1,11]. Even though the data are difficult to compare quantitatively (e.g., Pb desorption rate is higher at 460 °C in Ref. [1] than at 480 °C in Ref. [10]), characteristic features are reproduced. At coverages corresponding to phase transitions, a fast change of desorption rate is observed. The desorption rate is almost constant before the transition, suggesting the ZOD. In the following, we will show that the zerolike order of desorption can be obtained as a result of the configuration-specific desorption from the surface.

In Fig. 2 we plot the simulated decrease of coverage during desorption at constant temperatures (solid lines). The desorption-related parameters used in the simulation are listed in Table I. A value of the prefactor was set to 10^{10} s^{-1}, and values of desorption energies were adjusted to correspond to

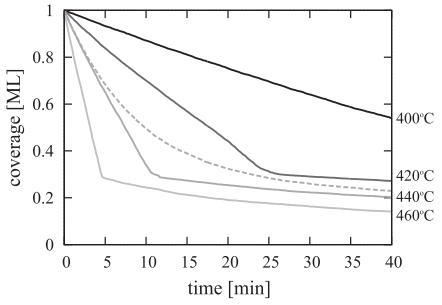

FIG. 2. Simulated isothermal desorption spectra of Pb at several temperatures. Zero-order desorption in the range 1–0.3 ML is reproduced. The dashed line is a simulated spectrum at 440 °C without enhanced desorption from disordered positions.

TABLE I. Model parameters used in simulation of Pb desorption. n denotes the number of atoms of the same chemical species in $NN_{\sqrt{3}\times\sqrt{3}}$ positions.

ν (s^{-1})	$E^{des}_{1\times1}$ (eV)	$E^{des}_{\sqrt{3}\times\sqrt{3}}$ (eV)	E^{des}_{dis} (eV)
10^{10}	1.82	$2.05 - n \times 0.025$	1.57

isothermal desorption reported in Ref. [8].[1] The overall shape is in very good agreement with experimental data [1,9–11], reproducing the fast change of the desorption rate at 0.3 ML related to $\sqrt{3}\times\sqrt{3}$ formation and an almost constant desorption rate for the coverages from 1 to 0.3 ML. The constant desorption rate at the constant temperature is an indication of an apparent ZOD. We proceed by discussing the driving force of the zerolike order of desorption. In the simulation, desorption of atoms in the disordered configuration has been enhanced by decreasing the desorption barrier from these positions by 0.25 eV compared to the 1×1 configuration (see Table I). The dashed line in Fig. 2 shows a simulated decrease of coverage at 440 °C without enhanced desorption from the disordered configurations, $E^{des}_{dis} = E^{des}_{1\times1}$. In such case, the knee at 0.3 ML disappears and almost exponential decay is obtained as in the case of the first-order desorption.

Another indication of the apparent ZOD is the characteristic sharp peak in TDS, caused by an exponential increase of the desorption rate (with temperature growing linearly) followed by a rapid drop off when all material has desorbed. The simulated TDS spectrum using the same model parameters as in Fig. 2 is shown in Fig. 3 by the black solid line, clearly showing the ZOD features. The exponential part is fitted by the theoretical dependence (red dashed line) with parameter $E_{eff} = 1.78$ eV. The desorption rate of atoms in the disordered configurations is plotted by the blue dash-dotted line in Fig. 3. It is evident that the desorption rate of these atoms increases during the structural transition and vanishes when the surface reaches coverage allowing incorporation of all atoms in a stable structure (in our case the $\sqrt{3}\times\sqrt{3}$). In other words, an enhanced desorption of atoms in disordered configuration is responsible for the ZOD behavior in our model.

Snapshots of the morphologies obtained by the simulation of the desorption at 460 °C are shown in Fig. 4. Two phases can be found on the snapshots corresponding to $\sim 2/3$ of ML [Fig. 4(a)]: the "smooth" 1×1 coexisting with islands of the $\sqrt{3}\times\sqrt{3}$ phase. Several Pb atoms (light balls) in the $\sqrt{3}\times\sqrt{3}$ structure are substituted by Si atoms (dark balls). Figure 4(b) shows the surface with $\sim 1/3$ of Pb ML, completely reconstructed to the $\sqrt{3}\times\sqrt{3}$ phase. A small fraction of substituted atoms can be found. After further desorption, this fraction increases, resulting in the $\sqrt{3}\times\sqrt{3}$ mosaic phase at $\sim 1/6$ ML coverage.

[1]Please note that exact fitting of experimental data was not the aim, since desorption characteristics [1,9–11] do not coincide together due to different techniques used. Because of the rather small range of temperatures allowing reasonable observation of desorption, an impact of the prefactor value is rather small, in other words, after adjusting desorption energies different values of prefactors could be used as well.

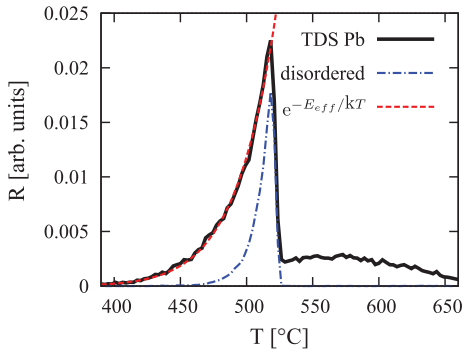

FIG. 3. (Color online) Simulated thermal desorption spectrum of Pb, temperature increasing with rate 1 K s^{-1}. Black solid line, total desorption flux; red dashed line, exponential fit; blue dash-dotted line, desorption flux corresponding to desorption from disordered positions.

In the case of desorption of thallium from the Si(111) surface, a different kind of experimental data is available [7]. In Fig. 5, Tl coverages obtained from STM morphologies after 2 min of desorption at various temperatures are plotted by squares. Contrary to Pb desorption case, the $\sqrt{3}\times\sqrt{3}$ structure without substitutional Si atoms has not been observed. Instead, the mosaic phase is formed immediately from the 1×1 phase by desorption. Previously we have demonstrated that the observed desorption characteristics can be explained using a single desorption energy in all adsorption positions, and the values $E_{des} = (2.1 \pm 0.3)$ eV, $\nu = 5 \times 10^{14\pm2}$ s^{-1} were obtained by fitting [7]. Results of the simulation using the same parameters are plotted in Fig. 5 by the solid line. Not surprisingly, good agreement is obtained, since KMC and rate equations (Ref. [7]) are solutions of the same problem. The advantage of KMC simulations is that morphologies of simulated and experimental data can be directly compared. The simulated morphologies of layers after 120 s of desorption at 300 °C, 330 °C, and 350 °C are shown in Fig. 6. Compared to the STM data [7] a nice agreement is obtained. At a temperature of 300 °C corresponding to the desorption onset, only small islands of the originating $\sqrt{3}\times\sqrt{3}$ structure are formed [Fig. 6(a)]. By the desorption at 330 °C [Fig. 6(b)], islands of $\sqrt{3}\times\sqrt{3}$ structure are formed. A significant amount

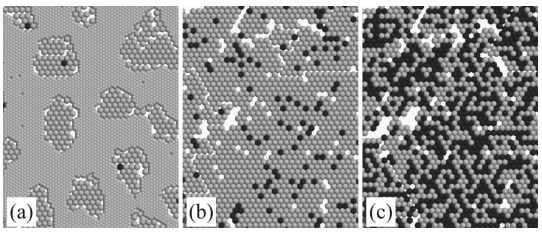

FIG. 4. Snapshots of simulated Pb morphologies during desorption from the initial 1×1 structure at 460 °C. light (dark) gray balls represent Pb (Si) atoms. (a) $\sim 2/3$ ML, coexisting 1×1 and $\sqrt{3}\times\sqrt{3}$ structures. (b) $\sim 1/3$ ML, $\sqrt{3}\times\sqrt{3}$ with several substituted atoms. (c) $\sim 1/6$ ML, mosaic $\sqrt{3}\times\sqrt{3}$ phase.

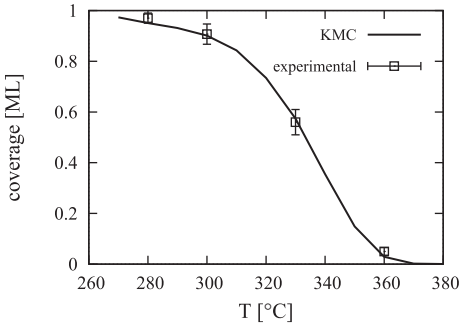

FIG. 5. Residual Tl coverage after 120 s of desorption as a function of temperature. Experimental data (squares) are taken from Ref. [7]; the simulated curve was obtained using the desorption rate independent on atomic configurations.

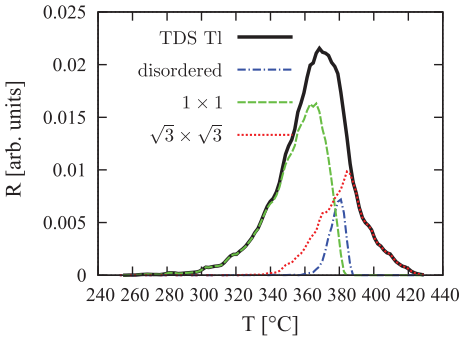

FIG. 7. (Color online) Simulated thermal desorption spectrum of Tl (black solid line), temperature increasing with rate 1 K s^{-1}. Green dashed, red dotted, and blue dash-dotted lines show desorption from 1×1, $\sqrt{3}\times\sqrt{3}$, and disordered configurations.

of Si substitutional atoms in the $\sqrt{3}\times\sqrt{3}$ structure is caused by the same probability of desorption from all structures, in agreement with experiments. The desorption at 350 °C results in the surface being completely covered by the $\sqrt{3}\times\sqrt{3}$ mosaic phase, as shown in Fig. 6(c).

A TDS curve calculated for Tl desorption (plotted in Fig. 7 by the black solid line) has clearly a first-order character. The green dashed, red dotted, and blue dash-dotted lines show desorption from 1×1, $\sqrt{3}\times\sqrt{3}$, and disordered configurations, respectively. The contribution of the disordered configuration reaches maximum when amounts of atoms in dense and sparse structures are comparable.

B. Simulations of the mosaic phase ordering

Ordering of the $\sqrt{3}\times\sqrt{3}$ mosaic phases has been studied in several works as an example of a 2D antiferromagnetic Ising system with the hexagonal symmetry [2,5,18]. In the case of the 1 : 1 ratio of metal and substitutional atoms, the highly degenerated ground state of the system is represented by an infinite number of configurations with two same-element nearest neighbors (SENNs) on average [5]. A geometric frustration, caused by impossibility to reach zero SENNs on average, results in only local ordering. Previously, the ordering has been studied by means of Monte Carlo simulations using a nonrealistic dynamics based on an exchange of atoms in neighboring $\sqrt{3}\times\sqrt{3}$ positions [5].

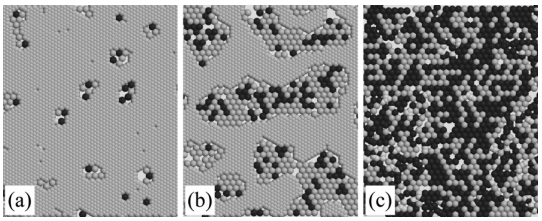

FIG. 6. Snapshots of simulated Tl morphologies obtained after 120 s of desorption at (a) 300 °C, (b) 330 °C, and (c) 350 °C. Light (dark) gray balls represent Tl (Si) atoms.

Since our model is based on hopping within the 1×1 network, an exchange of neighboring atoms can be realized in a close-to-realistic way and probability of the exchange can be tested. Considering in-plane hopping limited to the 1×1 network, the process itself consists of several steps, as depicted in Fig. 8: (1) hopping of an adatom out of a stable $\sqrt{3}\times\sqrt{3}$ position "A" to a first transitional position "B," (2) a neighboring atom leaving its position, resulting in the second transitional configuration "C," and (3) hops of atoms to final positions "D." The schematic energy potential profile of the exchange is shown on the right-hand side in Fig. 8. Since the activation energies of hops are calculated using Eq. (1), the barrier of hopping from the stable $\sqrt{3}\times\sqrt{3}$ position to the transitional position (A to B) is high. Moreover, to realize an exchange, two such events must appear concertedly before the atom collapses to the initial position. The energy barrier for such collapse (B to A) is small. Therefore, in the frame of our model, a direct exchange can be supposed to be very rare. Our simulations of the surface covered by 1/6 of Pb ML and 1/6 of Si ML with the prohibited desorption revealed that if E_{dif} in Eq. (1) is sufficiently low (otherwise no changes are observed), rather whole domains of surface rearrange instead of a pairwise exchange of atoms. Introducing diffusing vacancies [19] facilitates and speeds up kinetics of the system. However, the obtained morphologies are less ordered (average number of nearest neighbors of the same species is higher) than those observed experimentally [2,5]. The reason is probably related to a high level of system frustration [20].

In order to provide a mechanism of the observed local mosaic ordering, we have tested a model utilizing a selective

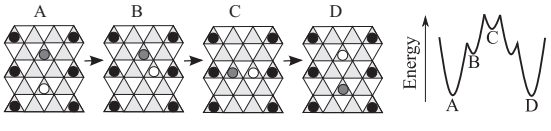

FIG. 8. Step-by-step exchange of two atoms (white and gray circle) in the $\sqrt{3}\times\sqrt{3}$ network via the 1×1 grid. Right-hand side: A schematic potential profile along the kinetic pathway of the exchange. A–D mark local potential minima and corresponding configurations.

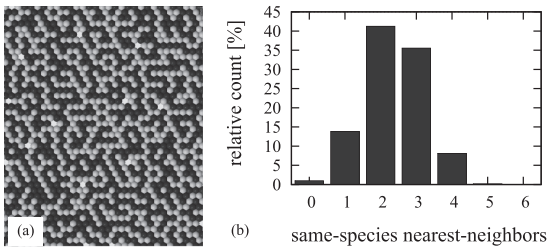

FIG. 9. (a) Simulated morphology of the mosaic phase (1 : 1 ratio Pb : Si) formed by desorption from the $\sqrt{3}\times\sqrt{3}$ phase with 1/3 ML of Pb atoms, with prohibited diffusion. (b) A histogram of the same-species nearest-neighbors occupancy.

desorption. In this model, the desorption energy depends linearly on the number of same-species nearest neighbors. In the simulations further discussed, we started from the $\sqrt{3}\times\sqrt{3}$ lattice fully occupied by metal atoms. During the simulations, events of desorption with the artificial substitution by Si atoms were generated. Hopping of atoms was suppressed in the simulations in order to separate diffusion and desorption effects. Figure 9(a) shows the simulated morphology corresponding to the 1 : 1 ratio of metal and Si atoms. The desorption energy was calculated as $E^{\mathrm{des}}_{\sqrt{3}\times\sqrt{3}} = (2.05\,\mathrm{eV} - NN^{\mathrm{SE}}_{\sqrt{3}\times\sqrt{3}} \times \Delta E_{\mathrm{des}})$, where $NN^{\mathrm{SE}}_{\sqrt{3}\times\sqrt{3}}$ denotes a number of same-species nearest neighbors in the $\sqrt{3}\times\sqrt{3}$ grid. Since we select the structure corresponding to the 1 : 1 ratio of metal and Si atoms, the only important parameter is $\Delta E_{\mathrm{des}}/kT$. At the given temperature of 530 °C [21], the best agreement with the morphology published in Ref. [2] was obtained for a value $\Delta E_{\mathrm{des}} = (0.09 \pm 0.03)$ eV. A histogram of the same-species nearest neighbors calculated from the morphology obtained under such conditions is shown in Fig. 9(b) and a nice agreement is obtained with the morphologies observed experimentally [2].

A rough estimate of the value of ΔE_{des} can be obtained from Ref. [2], where the total energies E_{tot} of selected mosaic configurations of Pb and Si atoms with the 1 : 1 ratio are calculated using the density functional theory. Assuming E_{tot} can be separated to the bonding energy to the substrate (the same in all studied cases) and to the energy of adatom-adatom interactions, the repulsive term ΔE_{tot} can be estimated from the slope of the dependence of E_{tot} on the number of same-element neighbors in the structure [21]. By this procedure, a value $\Delta E_{\mathrm{tot}} = (0.12 \pm 0.02)$ eV per pair is obtained, which is close to the value used in our simulations.

The above result demonstrates that local ordering can be achieved without exchange or diffusion processes, solely as a consequence of the selective desorption and substitution. However, we note that under experimental conditions the diffusion cannot be ruled out at elevated temperatures, at which the mosaic structures are formed. In such case, both the desorption and the diffusion are likely to influence the level of ordering.

IV. CONCLUSIONS

A configuration-based KMC model of desorption-induced structural transitions was used to reproduce experimentally observed morphologies. We have demonstrated that the selective desorption can explain two important features. First, the zero-order-like desorption observed in several cases can be obtained as a result of lower desorption energy of atoms in disordered configurations. Concentration of these atoms increases during the transition from the 1×1 to the $\sqrt{3}\times\sqrt{3}$ phase. Second, a local ordering of the mosaic $\sqrt{3}\times\sqrt{3}$ phase can be achieved by setting the activation energy of the substitution linearly dependent on the number of the same-element nearest neighbors.

[1] E. Ganz, F. Xiong, I. S. Hwang, and J. Golovchenko, Phys. Rev. B **43**, 7316 (1991).
[2] M. Švec, P. Jelínek, P. Shukrynau, C. González, V. Cháb, and V. Drchal, Phys. Rev. B **77**, 125104 (2008).
[3] B. Ressel, J. Slezák, K. C. Prince, and V. Cháb, Phys. Rev. B **66**, 035325 (2002).
[4] C. Törnevik, M. Göthelid, M. Hammar, U. Karlsson, N. Nilsson, S. Flodström, C. Wigren, and M. Östling, Surf. Sci. **314**, 179 (1994).
[5] L. Ottaviano, B. Ressel, C. Di Teodoro, G. Profeta, S. Santucci, V. Cháb, and K. C. Prince, Phys. Rev. B **67**, 045401 (2003).
[6] V. G. Kotlyar, A. A. Saranin, A. V. Zotov, and T. V. Kasyanova, Surf. Sci. **543**, L663 (2003).
[7] P. Kocán, P. Sobotík, P. Matvija, M. Setvín, and I. Ošt'ádal, Surf. Sci. **606**, 991 (2012).
[8] N. Minami, Y. Machida, T. Kajikawa, T. Sato, K. Ota, and S. Ino, Surf. Sci. **524**, 199 (2003).
[9] M. Saitoh, K. Oura, K. Asano, F. Shoji, and T. Hanawa, Surf. Sci. **154**, 394 (1985).
[10] J. A. Carlisle, T. Miller, and T. C. Chiang, Phys. Rev. B **45**, 3400 (1992).
[11] E. Ganz, H. Shouh, X. Fulin, S. Theiss, and J. Golovchenko, Surf. Sci. **257**, 259 (1991).
[12] S. King, R. Davis, and R. Nemanich, Surf. Sci. **602**, 405 (2008).
[13] H. Kreuzer and S. Payne, Surf. Sci. **200**, L433 (1988).
[14] C. Ratsch and J. A. Venables, J. Vac. Sci. Technol. A **21**, S96 (2003).
[15] E. S. Hood, B. H. Toby, and W. H. Weinberg, Phys. Rev. Lett. **55**, 2437 (1985).
[16] S. C. Jung and M. H. Kang, Phys. Rev. B **84**, 155422 (2011).
[17] P. Kocán, P. Sobotík, and I. Ošt'ádal, Phys. Rev. B **84**, 233304 (2011).
[18] J. M. Carpinelli, H. H. Weitering, and E. Plummer, Surf. Sci. **401**, L457 (1998).
[19] E. Vives and A. Planes, Phys. Rev. B **47**, 2557 (1993).
[20] G. H. Wannier, Phys. Rev. **79**, 357 (1950).
[21] M. Švec (private communication).

Závěr

Cílem této habilitační práce bylo na čtyřech příkladech odlišných fyzikálních problémů demonstrovat efektivitu kombinace experimentální techniky poskytující lokální informaci na atomární úrovni s kinetickými Monte Carlo simulacemi. Společným prvkem všech studovaných problémů je využití uspořádaného povrchu monokrystalu křemíku jako podložky pro růst nanostruktur - kvantových teček, jednodimenzionálních řetízků a tenkých vrstev různých morfologií. Ve všech zahrnutých oblastech opakuji podobné schéma - nejdříve je třeba pomocí řádkovacího tunelového mikroskopu (STM) získat dostatečnou představu o základním chování atomů konkrétního prvku na daném povrchu. Detailní studium pomocí STM dále poskytne dostatečný objem experimentálních dat především statistického charakteru. Na základě těchto poznatků je následně navržen kinetický model růstu, zahrnující pouze procesy důležité pro daný problém. Tento model je implementován do Monte Carlo simulací, výsledky výpočtů jsou porovnávány s experimentálními daty. Model může být na základě porovnání zavržen nebo upraven. Fitování jeho parametrů poskytne kvantitativní popis fyzikálního systému na úrovni jednotlivých, i když obvykle efektivních, interakcí. Uvedená kombinace dvou technik tudíž umožňuje popsat mechanismy vedoucí k pozorovaným morfologiím a strukturám. A tato znalost zpětně dovoluje cílenou přípravu nanostruktur s vlastnostmi požadovanými pro jejich aplikaci - např. s co nejvyšším uspořádáním stříbrných klastrů na povrchu Si(111)7×7 nebo s co nejnižší koncentrací defektů v případě růstu MnSi vrstvy na povrchu Si(111).

A. Princip a technika kinetických Monte Carlo simulací

V tomto dodatku budou velmi stručně popsány algoritmy, které jsou výchozími body konkrétních programů použitých ve výše uvedených pracích. Pro detailnější informace odkáži čtenáře na přehledovou literaturu [1, 2].

A.1 Monte Carlo

Metoda Monte Carlo (MC) zahrnuje širokou škálu algoritmů, založených na využití sekvence náhodných (nebo pseudonáhodných) čísel. Uplatňuje se v řadě oborů - matematice, fyzice, biologii, technických vědách, ekonomii apod., především v situacích, které neumožňují deterministické řešení, např. z důvodu velkého počtu vzájemných vazeb ovlivňujících chování systému.

Za historicky první řešení problému pomocí MC algoritmu bývá považována tzv. Buffonova jehla z 18. století - výpočet Ludolfova čísla pomocí náhodného dopadu jehly (generátor) a statistiky, kdy jehla překříží některou ze sítě rovnoběžných přímek. Název Monte Carlo byl zaveden Johnem von Neumannem a Stanislawem Ulamem při řešení difuze neutronů v pevné látce v rámci projektu Manhattan v roce 1946.

Fyzikální aplikace často vycházejí z Metropolisova algoritmu z roku 1953, který je založen na Markovově řetězu událostí, ve kterém náhodná procházka vede k vybranému stavu S s pravděpodobností danou Boltzmannovým faktorem $exp(-E(S)/kT)$. Algoritmus je postaven na opakování následujících kroků:

1. vyber náhodně částici,
2. vyber náhodnou změnu stavu této částice,
3. uskutečni tuto změnu s pravděpodobností

$$p = min(1, exp([E(S') - E(S)]/kT), \tag{A.1}$$

kde $E(S')$ a $E(S)$ jsou energie systému před a po vybrané změně stavu.

A.2 BKL algoritmus

Algoritmus uvažující neuskutečněné události může být velmi pomalý, především v případech, kdy je pozorovaný problém založen na současné realizaci událostí

s velmi odlišnými pravděpodobnostmi realizace. Bortz, Kalos a Lebowitz (BKL) [3] navrhli efektivnější algoritmus, použitý původně pro řešení Isingova modelu, ale využívaný často i pro simulace růstu tenkých vrstev. Na rozdíl od Metropolisova algoritmu není losováno, zda se vybraná událost uskuteční, ale losuje se, která z uskutečnitelných událostí bude realizována. BKL algoritmus je následující:

1. Spočítej celkovou četnost všech uskutečnitelných událostí $\sum R_i$, kde R_i je četnost $i-$tého uvažovaného procesu. Četností je zatím rozuměna pouze četnost relativní, nezahrnující nutně reálný čas.
2. Vygeneruj náhodné číslo s rovnoměrným rozdělením $0 < r < \sum R_i$,
3. vyber událost j pro kterou platí $\sum_{i=1}^{j} R_i \geq r$ a zároveň $\sum_{i=1}^{j-1} R_i < r$,
4. uskutečni událost j a aktualizuj soubor uskutečnitelných událostí.

A.3 Maksymův algoritmus

Dalšího zefektivnění BKL algoritmu docílil Maksym [4] rozdělením uskutečnitelných událostí do skupin S_i tak, že všechny události ve skupině mají stejnou četnost, tedy odpovídají událostem stejného typu. V každém kroku je

1. spočtena celková četnost všech uskutečnitelných událostí $\sum R_i$,
2. vygenerováno náhodné číslo s rovnoměrným rozdělením $0 < r < \sum R_i$,
3. je vybrána skupina událostí s taková, že $\sum_{i=1}^{s} R_i^{kum} \geq r, \sum_{i=1}^{s-1} R_i^{kum} < r$, kde $R_i^{kum} = N_i \times R_i$ je kumulativní suma všech událostí $i-$té skupiny a N_i počet událostí v i-té skupině.
4. V rámci skupiny je náhodně vybrána a realizována konkrétní událost,
5. aktualizují se seznamy uskutečnitelných událostí.

A.4 Zavedení časového kroku

Po zavedení časového kroku do MC algoritmu se hovoří o kinetickém MC (KMC). Každé uvažované události (změně systému) je třeba přiřadit četnost R_i (pravděpodobnost realizace v čase dt).

Výchozí možností je zvolit konstantní časový krok Δt, a v každém cyklu pro všechny realizovatelné procesy i spočítat pravděpodobnost uskutečnění $p_i =$

$1 - exp(R_i \Delta t)$. Tento postup je ovšem výpočetně neefektivní, proto se používá proměnný časový krok

$$\Delta t = \frac{-\ln(a)}{\sum R_i}, \tag{A.2}$$

kde a je náhodné číslo $0 < a < 1$. Tento časový krok potom odděluje dvě realizace procesů vybraných náhodně s pravděpodobností úměrnou jejich četnosti. Protože takto počítaný časový krok vychází z Poissonova rozdělení, kumulativní čas přibližně odpovídá času reálnému.

A.5 Implementace KMC pro růst tenkých vrstev

Tenké vrstvy a obecně nanostruktury rostou na površích podle rozličných schémat a výsledkem je pestrá paleta možných morfologií, od lineárních řetězců přes dvoj-dimenzionální ostrůvky různého tvaru po kompaktní troj-dimenzionální objekty. Dimenzionalita objektů nemusí být ani celočíselná, jako například u dendritických ostrůvků. Růst může být prakticky rovnovážný, nebo naopak od rovnováhy velmi vzdálený. Nicméně ve všech uvedených případech bývají postačující pro simulaci růstu a relaxace pouze následující procesy:

- přeskok atomu mezi dvěma pozicemi v obvykle pevně definované síti, přeskoky umožní náhodnou procházku simulující difúzi po povrchu. Četnost přeskoku z dané pozice je určena konfigurací okolních atomů, tím je rozlišeno např. to, jakým způsobem je atom vázán k ostatnímu adsorbátu.

- depozice atomu - na náhodnou pozici je deponován nový atom, pokud to náhodně vybraná pozice neumožňuje, je vybrána některá ze sousedních pozic.

- desorpce atomu - odebrání atomu z povrchu, četnost opět závisí na konfiguraci okolí daného atomu.

Přeskoky a desorpce jsou procesy teplotně aktivované, pro jejich četnost platí Arrheniovský vztah

$$R_i = \nu \exp(-E_i/kT), \tag{A.3}$$

kde ν je frekvenční prefaktor, k Boltzmannova konstanta, E_i energetická bariéra na koordinátě mezi konfigurací před a po realizaci procesu, a T je teplota systému. Frekvenční prefaktor bývá často zjednodušeně považován za nezávislý na teplotě a stejný pro všechny teplotně aktivované procesy.

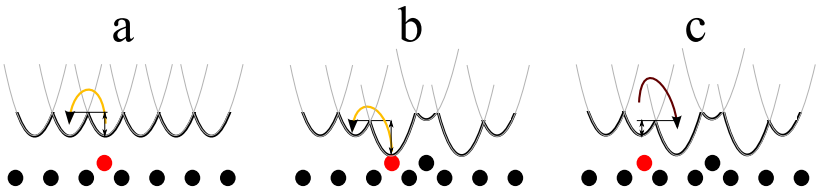

Obrázek A.1: Náčrt 2D bariér pro přeskok atomu (označený červeně) v rámci harmonické aproximace. a - volný atom na povrchu, b,c - přitažlivá interakce s adsorbátem: b(c) - zvýšená (snížená) bariéra pro přeskok směrem od (k) adsorbátu.

A.6 Konfiguračně orientovaný model

Zbývá tedy vyřešit, jak určit hodnoty potenciálních bariér v rovnici A.3 v aproximaci dostatečné pro řešený problém. Uvažujme, že každé konfiguraci atomů lze přiřadit určitou celkovou energii. Tuto energii lze rozdělit mezi jednotlivé atomy na povrchu, každému atomu potom náleží konfigurační energie E_c určená většinou dostatečně přesně obsazeností a strukturou blízkého okolí. Každá v rámci modelu uskutečnitelná událost (např. přeskok atomu) je potom definována konfiguracemi před a po realizaci této události. V harmonické aproximaci je každá částice uvězněná v parabolické potenciálové jámě, energetické bariéry jsou pak dány průsečíky těchto parabol. Za předpokladu přeskoků o konstantní posunutí platí [5]:

$$E_{act} = E_{eq} + \Delta E/2 + \Delta E^2/16E_{eq}, \quad \Delta E = (E_c^i - E_c^f), \tag{A.4}$$

kde E_{eq} je bariéra pro přeskok mezi ekvivalentními pozicemi, E_c^i a E_c^f jsou výchozí a výsledné konfigurační energie. Příklady výpočtu energetických bariér jsou uvedeny na obr. A.1.

V rámci takto definovaného modelu stačí pro daný systém zadat konfigurace lišící se energií, dále potom uvažované způsoby změn mezi konfiguracemi. Fitovanými parametry jsou potom právě konfigurační energie - je proto potřeba zjednodušit model tak, aby jejich počet byl co nejnižší a už dostačující k popsání fyzikálně podstatných vlastností systému. Právě vhodné nalezení minimálního fyzikálního modelu bývá klíčové při KMC simulacích.

A.7 Postup využití KMC simulací

Obvykle bývá cílem KMC simulací 1) získat co nejvěrnější fyzikální model a 2) kvantifikovat jeho parametry. Běžně používané schéma je následující [1]:

1. Na základě dostupných experimentálních dat je definován pravděpodobný fyzikální model,

2. tento model je implementován do KMC kódu.

3. Fitováním parametrů je hledána co nejvěrnější schodu s experimentem,

4. na základě výsledků je model buď potvrzen nebo dále upravován.

Literatura

[1] M. Kotrla, "Numerical simulations in the theory of crystal growth," *Comput. Phys. Commun.*, vol. 97, pp. 82–100, 1996.

[2] C. C. Battaile, "The Kinetic Monte Carlo method: Foundation, implementation, and application," *Comput. Methods Appl. Mech. Eng.*, vol. 197, pp. 3386–3398, July 2008.

[3] A. Bortz, M. Kalos, and J. Lebowitz, "A new algorithm for Monte Carlo simulation of Ising spin systems," *J. Comput. Phys.*, vol. 18, pp. 10–18, 1975.

[4] P. A. Maksym, "Fast Monte Carlo Simulation of MBE Growth," *Semicond. Sci. Technol.*, vol. 3, p. 594, 1988.

[5] E. Hood, B. Toby, and W. Weinberg, "Precursor-mediated molecular chemisorption and thermal desorption: The interrelationships among energetics, kinetics, and adsorbate lattice structure," *Phys. Rev. Lett.*, vol. 55, no. 22, p. 2437, 1985.

Seznam použitých zkratek

KMC	kinetic Monte Carlo
MC	Monte Carlo
DFT	density functional theory
STM	scanning tunneling microscopy
LEED	low-energy electron diffraction
SFET	spin field-effect-transistor
FET	field effect transistor
RF	rozdělovací funkce
0D	nula-dimenzionální
1D	jedno-dimenzionální
AES	Augerova elektronová spektroskopie
QL	quadruple layer
ML	mono-layer
BKL	Bortz, Kalos a Lebowitz
AFM	atomic force microscopy